UNIVERISTY OF SOUTHAMPTON

SCHOOL OF ENGINEERING SCIENCES

MATERIALS RESEARCH GROUP

Thesis Submitted for the Degree of Doctor of Philosophy

FATIGUE OF FRICTION STIR WELDED AA2024-T351 PLATE

By Diccon Philip Paul Booth

November 2003

UNIVERSITY OF SOUTHAMPTON

ABSTRACT

SCHOOL OF ENGINEERING SCIENCES
MATERIALS RESEARCH GROUP

Doctor of Philosophy

FATIGUE OF FRICTION STIR WELDED AA2024-T351 PLATE

By Diccon Philip Paul Booth

The fatigue crack initiation and propagation characteristics of Friction Stir Welds (FSW) in 13mm gauge 2024-T351 Al alloy have been studied. Two failure locations have been identified: outside the weld nugget region and over the nugget region. The study shows that when failure occurs outside the nugget, fatigue crack growth is essentially conventional (mode I dominated), with initiation from S-phase particles. For failures over the nugget region initiations were linked to coarse intermetallics associated with macroscopic discontinuities in the weld flow pattern; with subsequent crack growth being seen to follow the curve of the banded structure within the weld nugget region. A variety of microstructural and micromechanical contributions to fatigue failure have been identified, including the roles of local matrix ageing characteristics, intermetallic particle size and distributions, local flow stress characteristics and the residual stress distributions.

The effect of varying the welding parameters has also been studied in partial penetration 25mm gauge 2024-T351 Al alloy. Again, two failure locations have been identified: outside the weld nugget region and over the nugget region. Outside the nugget exhibited essentially conventional (mode I dominated) crack growth, with initiation occurring at S-phase particles. Failure over the nugget only occurred in samples from the slower of the two welding speeds, initiation was identified with linear defects at, or just below, the surface. Again a variety of microstructural and micromechanical facts were identified as having an influence on the subsequent growth, in particular the marked deflection from a conventional mode I path. The failure location however did not appear to significantly alter fatigue lives.

Contents

ABSTRACT i
Contents ii
Preface vii
Acknowledgement viii

Chapter 1: Introduction 1
1.1 Introduction 1

Chapter 2: Literature Review 3
2.1 Aluminium alloys 3
2.1.1 Heat-treatable alloys 3
2.1.2 Precipitates in heat-treatable aluminium alloys 3
2.1.2.1 Constituent particles 4
2.1.2.2 Dispersoids 4
2.1.2.3 Strengthening Precipitates 5
2.1.3 Fabrication of Aluminium Alloys 5
2.1.3.1 Casting 5
2.1.3.2 Homogenisation of DC ingots 5
2.1.4 Thermomechanical Processing 6
2.1.5 Age Hardening in Aluminium Alloys 7
2.1.6 Strengthening Mechanisms 10
2.1.6.1 Deformation Modes 11
2.1.7 2024-T351 12
2.1.7.1 2xxx series alloys 12
2.1.7.2 Tempers 13
2.1.8 Crack initiation in aluminium alloys 13
2.1.8.1 Slip Band Initiation 13
2.1.8.2 Particle Initiation 15
2.1.8.3 Grain Structure Effects 16
2.1.9 Short crack propagation in aluminium alloys 17
2.1.9.1 Grain Structure Effects 17
2.1.9.2 Particle Effects 19

2.2 Friction Stir Welding 24

2.2.1 The Friction Stir Welding (FSW) process 24

2.2.2 General Weld Structure 27

2.2.3 Material flow developed in the welding process 29

2.2.3 Heat Input 33

2.2.4 Microstructure 40

2.2.4.1 Grain Structure 40

- *Dynamic Recrystallisation 41*

2.2.4.2 Precipitate Structure 47

2.2.4.3 Texture 49

2.2.4.4 Nugget Banding 51

2.2.5 Mechanical Properties 53

2.2.5.1 Hardness/Strength Profile 53

2.2.5.2 Tensile Behaviour 57

2.2.5.3 Fatigue in Friction Stir Welds 59

- *Fatigue Crack Propagation 59*
- *Crack Closure 60*

Plasticity Induced Crack Closer (PICC) 60

Roughness Induced Crack Closer (RICC) 61

- *Short Crack Fatigue 61*

Definition of short cracks 62

- *Fatigue of Friction Stir Welds 63*

2.2.6 Residual Stresses 68

Chapter 3: Experimental Procedure 86

3.1 Specimen Preparation 86

3.1.1 Mechanical Polishing 86

3.1.2 Electro Polishing 86

3.2 Microscopy 86

3.2.1 Optical Microscopy 86

3.2.2 Electron Microscopy 87

3.2.3 Image Analysis 87

3.2.4 Electron Backscattered Diffraction (EBSD) 87

3.2.4.1 Principles 87

3.2.4.2 Experimental 89

3.3 Micro Hardness Testing 90

3.4 Differential Scanning Calorimetry (DSC) 91

3.5 Fatigue Testing 92

3.5.1 Sample Preparation 92

3.5.2 Specimen Geometry 93

3.5.2.1 13mm Gauge Weld 93

3.5.2.2 25mm Gauge Weld 93

3.5.3 Testing 93

3.6 Residual Stress Measurements 94

Chapter 4: 13mm Gauge Weld 100

4.1 Materials 100

4.1.1 Macrostructure: 13mm weld 100

4.1.2 Hardness Characteristics 101

4.1.3 Differential Scanning Calorimetry: 13mm weld 102

4.1.4 Microstructure: 13mm weld 104

4.1.5 Summary 108

4.2 Results 122

4.2.1 Fatigue Life Results 122

4.2.2 Crack Growth Rates 123

4.2.3 Fractography 124

4.2.3.1 Failures outside the nugget region 124

- *Macroscopic Failure Behaviour 124*
- *Initiation and Propagation Behaviour 124*

4.2.3.2 Failure over the nugget region 125

- *Macroscopic Initiation Behaviour 125*
- *Microscopic Initiation Behaviour 125*
- *Macroscopic Flow Arm Propagation Behaviour 126*
- *Microscopic Flow Arm Propagation Behaviour 126*
- *Macroscopic Nugget Crack Propagation Behaviour 127*
- *Microscopic Nugget Crack Propagation Behaviour 127*

4.3 Discussion 144

4.3.1 Failure Outside the weld region 144

4.3.1.1 Initiation 144

4.3.1.2 Propagation 148

4.3.2 Failure over the nugget region 149
4.3.2.1 Initiation 149
4.3.2.2 Propagation 152
4.3.3 Fatigue crack growth life 158

Chapter 5: 25mm Gauge Welds **168**

5.1 Materials **168**

5.1.1 Weld Conditions 168
5.1.2 Macrostructure: 25mm welds 169
5.1.3 Hardness Characteristics 170
5.1.4 Differential Scanning Calorimetry: 25mm welds 172
5.1.5 Microstructure: 25mm welds 173
- *Grain Structure* 173

5.1.6 Summary 175

5.2 Results: Crown Surface Tests **194**

5.2.1 Fatigue Lives 194
5.2.2 Failure Outside the Weld Region 195
- *Macroscopic Behaviour* 195
- *Fatigue Crack Growth Rate* 196
- *Microscopic Behaviour* 196

5.2.3 Failure Over the Weld Region (slow weld) 196
- *Macroscopic Behaviour* 196
- *Fatigue crack growth rates* 197
- *Microscopic Behaviour* 198

5.2.4 Residual Stress Measurements 201

5.3 Results: Weld Root Tests **202**

5.3.1 Fatigue Lives 202
- *Macroscopic Behaviour* 202
- *Fatigue Crack Growth Rates* 203
- *Microscopic Behaviour* 203

5.3.2 Residual Stress Measurements 203

5.4 Discussion **221**

5.4.1 Microstructure 221

5.4.2 General Fatigue Behaviour *223*
5.4.2.1 Failure Outside the Weld Region 224
- *Initiation* *224*
- *Propagation* *226*

5.4.2.2 Failure over the Weld Region 228
- *Initiation* *228*
- *Propagation* *234*

Chapter 6: Conclusions **242**

6.1 13mm Weld **242**

6.2 25mm Welds **243**

5.3 Overall Conclusions **244**

Chapter 7: Future Work **246**

Appendix 1: Linear Elastic Fracture Mechanics (LEFM) **247**

A1.1 Linear Elastic Fracture Mechanics **247**

A1.2 Linear Elastic Stress Analysis of Cracks *250*

A1.3 Crack Tip Plasticity *252*

A1.3 Crack Tip Opening Displacement (CTOD) *253*

A1.4 Plastic Zone Shape *254*

References **259**

Preface

This dissertation is submitted for the degree of Doctor of Philosophy. The research was carried out in the Materials Research Group, School of Engineering Sciences, University of Southampton, under the supervision of Dr. I. Sinclair from October 1999 to September 2003.

Except where acknowledgement to previous work is made, this dissertation is the results of my own work. Neither this dissertation, nor any part of it, has been submitted for a degree or diploma at any other university.

Acknowledgement

Thanks must first of all go to my supervisor Ian Sinclair, without his supervision this thesis would never have been produced. Thanks also go to Philippa Reed for her help. The help and support of the Engineering Materials technical and support staff is gratefully acknowledges, in particular Eric Bonner and David Becket, for their help with specimen preparation, rig manufacture and general good humour. The support of the other PhD students and post doctorial researchers is much appreciated, particularly the members of the office who always manage to lighten the mood.

I would also like to thank the EPSRC and Airbus UK for their finical support. Airbus UK also provided the welded plates without this support this work could never have been undertaken.

The residual stress measurements in this work were obtained at the Open University by Supriyo Ganguly and Lyndon Edwards. I'd like to take this opportunity to thank them for their help.

Outside the Materials department I must thanks the Learning Difference Department at Southampton University, in particular Geraldine Price for her help in the last 2 years of my PhD. Also the Special Need Department at King Henry VIII Comprehensive School in particular Christine Davies, without their help with my dyslexia I may never have got to start this project let alone completed it.

Thanks must also go my parents, dad for reading several drafts of this thesis, but particularly mum for her tireless campaigning to get my dyslexia acknowledged at school. I really do appreciate all the time and effort that you put in. Thank you.

Chapter 1: Introduction

1.1 Introduction

Currently within the aerospace industry there is a drive for larger, cheaper, and more economic aeroplanes. This has led to significant interest being shown in the use of advanced welding techniques for airframe structures. Welding has a number of significant advantages over established mechanical joining methods[1], in particular in relation to design and manufacturing. Whilst a variety of welding methods have been identified for airframe structures, friction stir welding (FSW) is seen as an important candidate technique that is distinctive in being a low energy, solid state process[2].

A key factor in the exploitation of FSW techniques in primary airframe structures will of course be the associated fatigue characteristics. It may be noted that various aspects of established airframe design are closely linked to the intrinsic interactions between cracks and mechanically fastened components (such as the incidence of crack initiation at rivet holes and the inherent damage tolerance associated with the multiple load paths in riveted structures). The extensive use of welded airframe components (via FSW techniques or otherwise) therefore represents an important shift in the treatment of damage tolerance in airframes requiring an understanding of cracks initiation characteristics and corresponding implications for crack growth. Whilst several reports within the literature have commented on fatigue performance in friction stir welds, FSW micromechanical details are as yet unavailable.

Recently the first airframe with a significant amount of friction stir welding has started flight tests. The use of friction stir welding has enabled the manufactures of the Eclipse 5000, a 5 seat private passenger jet, to sell the finished aircraft for less than $1,000,000. This saving has been possible due to the significant reduction in the number of rivets in the airframe. The fuel economy of the aircraft is also expected to be very good due to the weight saving afforded by the use of welding over conventional joining techniques.

Given the obvious advantages that welding of airframes clearly gives, it is not surprising that the major companies in the aerospace sector such as Airbus and Boeing are undertaking large amounts of research into welding of aluminium alloys. Of particular interest is friction stir welding, with the current aim being to use the technique on the next generation of wide body aircraft.

Chapter 2: Literature Review

2.1 Aluminium alloys

The following section provides a general review of the physical metallurgy of wrought, high strength aluminium alloys. Use has particularly been made of the following reference material: Aluminium Alloys-Contemporary Research and Applications[3], edited by A.K. Vasudevan and R.D. Doherty, Light Alloys[4], 3rd edition, I.J. Polmear and the ASM Specialty Handbook, Aluminium and Aluminium Alloys[5]. Other sources are referenced in the text as necessary.

2.1.1 Heat-treatable alloys

Aluminium alloys for structural aerospace applications depend on age-hardening to develop their required strength levels. Overall, the heat-treatable class of wrought aluminium alloys is covered by the following three International Alloy Designation Series (IADS) series: 2xxx (Al-Cu and Al-Cu-Mg), 6xxx (Al-Mg-Si), and 7xxx (Al-Zn-Mg and Al-Zn-Mg-Cu). Given the present interest in 2xxx type alloys the following review will tend to focus on this compositional group.

2.1.2 Precipitates in heat-treatable aluminium alloys

There are three basic classes of precipitates present in age-hardenable aluminium alloys:

1. Coarse intermetallics (constituent particles), typically 0.5-10 μm in size
2. Submicron particles (dispersoids), typically 0.05-0.5μm in size
3. Fine precipitates (strengthening precipitates), up to 0.1μm in size

2.1.2.1 Constituent particles

There are two groups of constituent particles; the first is made up of virtually insoluble compounds; predominantly formed from the impurities in the aluminium. Examples are $Al_6(Fe,Mn)$, Al_3Fe, $\alpha Al(Fe,Mn,Si)$ and Al_7Cu_2Fe, which form interdendritically during solidification by eutectic decomposition and are only altered by subsequent deformation, where they tend to fracture and become aligned into "stringers". The second group of constituent particles are soluble compounds formed from the major alloying elements; examples include Al_2Cu, Al_2CuMg and Mg_2Si. Ideally these are dissolved in the solutionising treatment of the material. Both types of constituent particle form as lacy networks around grain boundaries during casting; in most cases they perform no useful function (accepting that soluble particles may contribute to strength if they are dissolved by subsequent treatment/processing).

2.1.2.2 Dispersoids

These are usually formed from transition elements that have very low solubility in aluminium. They are formed in the homogenisation of cast ingots by solid-state precipitation. The dispersoids resist coarsening or dissolution due to the low diffusivity of the associated transition elements. Example phases include $Al_{20}Mn_3Cu_2$, $Al_{12}Mg_2Cr$ and Al_3Zr. Their purpose is to control grain growth and retard recrystallisation during thermo-mechanical processing. They also affect the dislocation structure during deformation by blocking dislocation motion. The dispersoids may be either coherent (Al_3Zr), or semi coherent/incoherent ($Al_{20}Mn_3Cu_2$ and $Al_{12}Mg_2Cr$); with coherent dispersoids being thought to have a greater effect in controlling grain size during deformation.

2.1.2.3 Strengthening Precipitates

These are formed during the ageing treatment in heat treatable alloys. Important strengthening phases associated with commercial Al-alloys include S' (Al_2CuMg) in 2xxx alloys, andη' (Mg_2Zn) in 7xxx alloys. Further details of strengthening precipitates and their formation are considered later.

2.1.3 Fabrication of Aluminium Alloys

2.1.3.1 Casting

Most aerospace aluminium alloys are used in the wrought form. For a good quality product it is essential to have a uniform ingot structure, with current commercial production favouring direct-chill (DC) casting. A key factor for casting is the solidification rate, with faster rates producing a finer dendritic structure. At higher cooling rates the intermetallic compounds formed are also smaller, along with the grain size being finer and more uniform. Small amounts of master alloy of Al-Ti, Al-Ti-C or Al-Ti-B are usually added to the melt to control the grain size (providing nucleation sites during solidification).

2.1.3.2 Homogenisation of DC ingots

This part of the processing of DC ingots involves heating to between 450°C and 600°C. The aim of this treatment is to reduce the effects of microsegregation, remove non-equilibrium low melting point eutectics, and to precipitate dispersoid phases. The time required for homogenisation depends on the alloy and the grain size or dendritic arm spacing, but is typically in the range of 6-24 hours. This is a critical process for the higher strength alloys because of the effect it has on the dispersoids. The solubility of the

dispersoid forming elements is low, and they tend to supersaturate during the cooling of DC ingots. The dispersoids ultimately control the grain structure in wrought materials; for the most effective control, dispersoids need to be uniformly distributed through the ingot before hot working. For the precipitation of dispersoids, careful control of time, temperature and heating rate of the homogenisation is important. Dispersoids may be nucleated heterogeneously at the surfaces of other precipitate particles, which form during the heating phase, but are then redissolved leaving stable dispersoids.

2.1.4 Thermomechanical Processing

Thermomechanical processing is carried out both to fabricate a desired product form from an ingot, and to control alloy structure. Thermomechanical processing can take several forms: hot rolling, forging and extrusion, in conjunction with controlled heating cycles and cold forming processes.

Deformation processing changes the grain structure developed in the casting stage of an alloy. Subgrains may form, constituent particles are fractured and crystallographic texture changes take place. The constituent particles are typically fractured at strains of less than 0.1, into fragments, which are typically <5μm. Particle fracture may be avoided by working the material above $0.8Tm$ and using low strain rates[6]. Precipitation at subgrain boundaries and re-crystallisation may also occur. Observation of the hot rolled precipitate morphologies of some aluminium alloys suggests that dynamic precipitation can occur. A suggested mechanism is that during climb, dislocations drag solute atoms from the solid solution; this is followed by rapid diffusion along the dislocation core to form precipitates. Dynamic re-crystallisation may also be significant during the hot working process.

Thermal processing can be specifically used to control the grain size. This is due to the effect of particles on recrystallisation; a deformation zone is formed around large particles when a hot deformation process is applied. These consist of networks of dislocations with a high level of misorientation. These may transform into high angle recrystallisation fronts that sweep through the matrix. Small particles however (dispersoids in particular) retard the migration of such boundaries. As such, careful control of recrystallisation driving force and particle retardation influences may be used to manipulate ultimate microstructures.

2.1.5 Age Hardening in Aluminium Alloys

Age hardening in high strength Al-alloys has three main stages: solution treatment followed by quenching to develop a super saturated solid solution (SSSS) of solutes and vacancies and then controlled decomposition of the SSSS.

Solution treatment, This involves heating the alloy in to a single-phase region on the phase diagram. Typical solution temperatures for 2xxx series alloys are 500°C, and 480-490°C for 7xxx series alloys.[5] It is important that the temperature remains below the solidus temperature to avoid liquation of the eutectic compounds at grain boundaries, which has an adverse effect on mechanical properties. This is of particular importance in the Al-Cu-Mg alloys where the solutionising temperature is only a few degrees below the solidus. ΔT_1 in Figure 1 shows the temperature range over which solution treatments may be carried out in the particular system shown. When a hot worked product is solutionised it may be important to minimise the temperature and time at temperature to avoid the growth of re-crystallised grains

Quenching is the rapid cooling from solution treatment temperature to room temperature to maintain the maximum supersaturation of alloying elements. Distortion is a significant problem with very rapid cooling of thin sheets, while residual stresses maybe introduced in thicker gauges. These problems can be overcome by subsequent stress relief by stretching, or, for thinner gauges, a levelling rolling pass maybe implemented. Some stress relief will also occur in the ageing treatment. For commercial heat treatable alloys the critical temperature range for quenching is typically between 290-400°C. There are several techniques that are used to maximise the cooling rates in this region while still enabling residual stresses to be minimised. The simplest is to immerse the alloy into a salt bath at an intermediate temperature, and hold it there for a time before cooling to room temperature.

Reducing the cooling rate can reduce the stresses introduced in quenching; this does however reduce the response of the alloy to subsequent ageing, as there is a lower percentage of alloying elements in solid solution. Figure 2 shows the effect of cooling rate on tensile strength for several heat-treatable aluminium alloys. Quench sensitivity is increased by the presence of dispersoids, as they can act as nucleation sites for coarse precipitates. In 7xxx alloys it is commonly noted that chromium containing dispersoids have a greater effect on quench sensitivity, whilst zirconium containing dispersoids have a significantly smaller effect. When the quench rate is slow, grain boundaries are particularly adversely affected by heterogeneous precipitation; this may reduce toughness and increase susceptibility to intergranular corrosion in service.

Decomposition of SSSS (ageing) is typically a complex process involving several stages that depend on the temperature at which it is carried out. Below the zone solvus line shown in Figure 1, Guinier-Preston (GP) zones form. These consist of small regions of atoms that are coherent and solute rich; they are usually only a few atom planes thick. Although they are coherent, there is usually a significant lattice strain. The formation of GP zones requires atoms to diffuse over small distances, with zones being very finely dispersed through the matrix (densities as high as 10^{17} to 10^{18} m^{-3}).

The next stage of decomposition is the formation of the intermediate precipitate. These are normally larger than GP zones and can nucleate at the GP zones or heterogeneously at lattice defects. Intermediate precipitates are typically partially coherent.

Overall the decomposition sequence may be identified as:

SSSS → clusters → intermediate precipitate → equilibrium precipitates

For Al-Cu alloys the sequence is typically given as:

SSSS → Cluster of Cu atoms → Semi coherent θ` (Al_2Cu) (θ`` may also exist) → Incoherent θ (Al_2Cu)

For Al-Cu-Mg alloys the sequence is typically given as:

SSSS → Cluster of Cu and Mg atoms → Semi coherent S' (Al_2CuMg) → Incoherent S (Al_2CuMg)

Al-Cu precipitates may also form when the Cu:Mg ratio is high (i.e. atom ratios ≥1:1).

It should be noted that the very early stages of decomposition are still relatively poorly understood, with advanced imaging techniques such as 3D atom probe microscopy ("3DAP") revealing valuable new insights.

In various systems precipitate free zones (PFZ) are often found next to high angle grain boundaries. This may be a result of diffusion of solute atoms to the grain boundaries where larger equilibrium precipitates form. A second cause is the depletion of vacancies close to the grain boundaries, which then prevents nucleation of precipitates. Lowering the aging temperature may decrease PFZs widths by increasing the driving force for homogeneous nucleation and reducing diffusion rates. This may be beneficial in duplex aging treatments of 7xxx alloys for example: firstly a low temperature treatment is used to encourage homogenous precipitation, followed by a higher temperature treatment to coarsen the precipitates to a given size. Typical heat treatments for 2xxx series alloy are in the range of 160-200°C for 8-18 hours.[5]

2.1.6 Strengthening Mechanisms

There are a variety of mechanisms that may operate in a precipitation-hardened system. These particularly depend on the nature of the precipitates and surrounding matrix, e.g. degree of coherency between the two, see Table 1.

Mechanism	Description
Coherency Strain Hardening	If the lattice parameter for a coherent precipitate is slightly different from that of the matrix then, an elastic misfit strain occurs[7,8].
Surface or Chemical Hardening	When a particle is deformed or cut by a dislocation, the particle/matrix interface area increases. This requires energy to create the interface. This mechanism has a greater effect with small particles[9].
Elastic Modulus Hardening	There is some debate as to the exact mechanism of modulus hardening which is beyond the scope of this review. The basic principle is that the dislocations experience a force when moving from the matrix, which has a particular modulus and Poisson's ratio, to the particle which has a different set of properties[9].
Stacking Fault Hardening	This type of hardening occurs when there is a difference in stacking fault energy between the particle and the matrix. This difference may affect the motion of the dislocation[8].
Order Hardening	When a dislocation cuts an ordered coherent particle an antiphase boundary is formed which requires additional energy. The dislocations in this mechanism usually move in pairs. It may be an important mechanism for Nimonic alloys for example, and more recently has been related in some detail to the Al-Li alloys[8,9].
Orowan Looping	When individual particles are too strong to be sheared by dislocations (typically identified with incoherent particles), strengthening arises from the looping of dislocations between pinning points (particles). The looping process and build up of dislocation loops then contributes to material strength.

Table 1 Mechanisms of strengthening of heat treatable aluminium alloys

2.1.6.1 Deformation Modes

When a dislocation shears a particle, the resistance to successive dislocation motion is reduced. This leads to the concentration of slip and the formation of slip bands, which may be beneficial for certain forms of fatigue crack propagation as it promotes non-planar crack growth; this is discussed in more detail later. When strengthening particles are

however looped by dislocations during deformation, resistance to further dislocation motion on a given slip plane is increased (i.e. contrary to shearable particles). This has a converse influence on deformation mode, with more homogeneous slip then being favoured.

2.1.7 2024-T351

2.1.7.1 2xxx series alloys

2xxx series alloys represent the "original" heat-treatable aluminium alloys, being based on the binary Al-Cu system. Such alloys respond to natural ageing: with the discovery that the degree and rate of aging could be improved by the addition of Mg, the basic Duralumin composition type was developed.

The alloy of interest in this work is 2024; this alloy is commonly used in the aerospace industry for lower wing structures and other damage tolerant applications. The alloy is commonly used in the naturally aged temper, offering an attractive balance of damage tolerance and structural properties. Typical mechanical properties and composition details of the alloy are shown in Table 2 and Table 3:

Temper	Yield Strength (MPa)	Tensile Strength (MPa)	Elongation (% in 50mm)
0	75	185	20
T3	324	469	18
T4, T351	345	483	20
T6	395	475	10
T8	450	480	6

Table 2 Typical mechanical properties for 2024 in different tempers.[5]

Alloy	Si	Fe	Cu	Mn	Mg	Zn	Cr	Ti	Other
2024	0.50	0.50	3.8-4.9	0.30-0.9	1.2-1.8	0.25	0.10	0.15	0.20Zr+Ti

Table 3 Composition specification of 2024 Al Alloy (Compositions are in % maximum by weight unless shown as a range or a minimum)[4].

2.1.7.2 Tempers

The current work was carried out on plate in the T351 temper, i.e. solution heat-treated, cold worked and naturally aged to a substantially stable condition. The cold working (typically a 1.5-3% stretch) in this case is applied to improve strength and provide stress relief after the solution heat treatment.

2.1.8 Crack initiation in aluminium alloys

2.1.8.1 Slip Band Initiation

When a material is cyclically loaded, any plastic deformation that results typically produces fine slip markings, called slip lines, on the free surfaces. Slip occurs along the most favourable slip planes, which, under certain conditions, can lead to an intense form of slip localisation, termed 'persistent slip bands' (PSBs). Fatigue cracks may initiate as fine cracks along the most intense of these bands. PSB formation is a mode of fatigue crack initiation that has been observed for both 2024-T4 and 2124-T4 by Kung and Fine[10]. Their study involved direct observation of the cracks at the base of a notch. They observed that for high stresses (above 0.25 σ_y for 2124-T4, and 0.44 σ_y for 2024-T4) cracks initiated from coarse slip lines in the matrix that were not near any constituent particles or etch pits. As stress levels are lowered below a transition level, almost all of the cracks in the 2024-T4 case and half the cracks in the case of 2124-T4 initiated at constituent particles; the proposed explanation was that as the slip bands develop within the matrix they impinge on the constituent particles and are pinned leading to local stress concentrations. In the Kung and Fine[10] work, the grain size of the 2124 was larger than that of the 2024. This was considered to give more rapid crack initiation in the former

alloy as the active slip length for slip bands is effectively increased. 2124 is a high purity version of 2024; as such there are less intermetallics in 2124. Whilst intermetallics may participate directly in the crack initiation process, it may also be noted that they may also disperse slip, slowing the formation of coarse slip bands and hence delaying the onset of cracks initiation[4].

Zabett and Plumtree[11] studied 2024-T351 using plain sided (i.e. un-notched) specimens at $0.45\sigma_t$ (where σ_t is the tensile strength) in all three principal loading orientations. They saw no evidence of slip band initiation in the samples loaded in the L direction, however in the S and T samples persistent slip bands developed and initiation in the surface grains occurred. Kung and Fine[10] would have classed the stresses that were used in this study as being close to, but slightly above, their transition stress. The lack of slip band initiation in the L orientation was attributed to the relatively easy crack initiation at cracked particles that were present. In the S and T orientations, the particle lamina that are aligned normal to the rolling direction and parallel to the S and T loading direction are not favourable for crack initiation, therefore a change in mechanism occurs. There were less cracks in the T loading orientation compared to the S, however both orientations had substantially less cracks than the L orientation (1-5 cracks, 10-20 cracks and more than 100 cracks respectively (cracks greater than 100μm at 100,000 cycles over the whole specimen gauge length)). The cracks in the T orientation showed a tendency to form in the largest surface grains, whereas those in the S orientation showed no preference.

In a study performed by Mulvihill and Beevers[12] on an experimental Al 4.0 wt% Cu alloy, tested in 3 point bending at a relatively high stress levels in the solution-treated and

quenched condition, slip band formation and crack initiation was observed. When the material was subsequently peak aged, initiation was seen to occur at large intragranular intermetallic inclusions.

Morris[13] found that in 2219-T851 (near peak aged), crystallographic cracking due to persistent slip was rare, even at high stress levels ($0.8\text{-}0.9\sigma_y$). The absence of slip band crack initiation in this work is in agreement with the work carried out by Mulvihill and Beevers[12] for peak aged material.

Overall it may be seen that relatively high stress levels in materials that are underaged favour slip band initiation of fatigue cracks. Peak aged materials and high intermetallic contents may be seen to favour particle initiation of fatigue cracks.

2.1.8.2 Particle Initiation

Particle cracking can occur in thermomechanical processing stages[11,14]. Langford[14] also reported that intermetallic particles may break in the early stages of cycling prior to matrix crack initiation. Kung and Fine[10] noted that in 2024 and 2124-T4 materials, cracks present in the intermetallic particles did not initiate matrix fatigue cracks (however they did see slip band initiation at the intermetallic particles, as reported in the previous section). Both Langford[14] and Mulvihill and Beevers[12] suggest that some initiation occurred from the cracked intermetallic particles. Zabett and Plumtree[11] noted that all cracks in the L orientation initiated from broken intermetallic particles.

Several authors have noted that intermetallic particle size is important; notably Kung and Fine[10] found that the probability of slip band initiation at particles decreased rapidly when

the size decreased below 6μm and was quite small below 2μm. They suggest this is a result of the decreased probability that a coarse slip band will impinge on an intermetallic particle. Lankford[14] also noted a similar trend in 7075-T6; it was found that cracks initiated from intermetallic particles in the size range of 3-10μm.

Wanhill and Schra[15] found for 2024-T3, tested using SENT (Single edge notch tension) specimens and a Fokker 100 reduced basic gust spectrum load sequence, that crack initiation was from the interfaces between inclusions and the aluminium alloy matrix.

The evidence presented above shows that particle initiation is common in many aluminium alloys. This mechanism is only reported for particle sizes above 2-3μm. There seems to be a number of possible mechanisms for the crack initiation process specifically: debonding, slip band/particle interaction, cracks already present in the particles or cracks that develop during testing.

2.1.8.3 Grain Structure Effects

Various authors have noted grain size effects on fatigue crack formation. In slip band initiation it was seen that the larger the grains the more easily cracks were able to form, hence the shortened life in the case of the 2124 compared to the 2024 tested by Kung and Fine[10]. Zabett and Plumtree[11] also attributed the position of cracks in T orientation test specimens to the largest grains.

Mulvihill and Beevers[12] observed crack initiation at grain boundaries in their experimental higher copper alloy (4.5%Cu) in the peak-aged condition. After observation of the grain boundary region using TEM they noted the presence of precipitate-free zones (PFZ).

Elongated θ precipitates were seen to decorate the grain boundaries, with a PFZ of 0.2μm surrounding them (the matrix was θ`` and θ` strengthened). The grain boundaries were not judged to be inherently weak, with initiation being thought to occur at micro-notches on the surface caused by severe deformation within the grains, which subsequently initiated fatigue cracks.

2.1.9 Short crack propagation in aluminium alloys

Microstructural features are widely recognised to influence the propagation of short cracks. The following sections review these effects with respect to heat-treatable aluminium alloys.

2.1.9.1 Grain Structure Effects

As was stated earlier, grain size may have clear effects on crack initiation, with initiation being preferred in larger grains. There is general agreement that grain boundaries may slow or even stop subsequent short crack growth[11,14,13]. Zhang and Edwards[16] note that the rate of crack growth begins to decrease as the plastic zone impinges on the grain boundary, before the crack tip gets there. Figure 4 shows a illustration of the situation. In A, a fully developed plastic zone is present at the crack tip; moving to B, the plastic zone shape is distorted and effectively limited as it impinges on the grain boundary, slowing the crack growth rate. However, before the crack impinges on the boundary; the plastic zone (in this case) has been "initiated" in the neighbouring grain (shown in part C) and the crack growth rate accelerates along a different growth plane, D.

Zabett and Plumtree[11] tested samples of 2024 in all three principal plate orientations. Although for the direction with the smallest grain dimension in the direction of crack

growth, the L test orientation, very few crack arrests were seen; attributed to the bridging effect of the cracked particles occurring across the grain boundaries. In the S and T orientations however, numerous crack arrest events were seen (more in the S orientation than the T). This was identified with initiation occurring in smaller surface grains in the S orientation, so cracks encounter more grain boundaries per unit length. This did not lead to a longer life in the S orientation, which was thought to be due to the short distance in the depth direction cracks were able to grow in the T orientation before encountering a grain boundary (38μm compared to 350μm for S-L cracks and 110μm for S-T cracks).

The crystallographic orientation of neighbouring grains has been identified in several studies as being key to the amount of deceleration seen as a crack propagates across a grain boundary[14,16]. Figure 5 taken from Langford's[14] results shows a series of traces for a number of cracks in 7075. The graph shows the effect of orientation on growth rates: the flat trace is for a crack that was not arrested moving from one grain to the next as the orientations were favourable (grain-grain mis-orientation was low). As the mis-orientation is increased, then the amount of deceleration increases, and hence the dip in growth rates increases. If the amount of mis-orientation is too high for the size of the crack (i.e. indicative of crack driving force), arrest can occur.

Mulvihill and Beevers[12] found that grain boundaries had a two-folded effect on crack growth. Their work concentrated particularly on triple points. Not only is the crack growth rate slowed or arrested in agreement with the above work, but there is also a growth mode change in 50% of cases, from intergranular to transgranular propagation.

Some growth mode changes were observed remote from surface triple points but these are thought to have occurred at sub-surface features.

Results reported in Morris's[13] study were obtained for the 2219 alloy, measuring crack tip opening displacements (CTOD), and relating them to the crack tip plastic zone size r_p. Both *CTOD* and r_p were identified as relatively large for cracks just beginning to propagate in a large grain. It was also noted that the r_p size was dominated by grain boundaries, being largely independent of crack length, but dependent on the distance of the crack tip to the next grain boundary (as illustrated in Figure 4). In their work, some crack tips were observed that, due to the close proximity to grain boundaries, exhibited an essentially elastic crack tip opening behaviour. This held for surface stresses approaching the yield stress. It was accepted that there was some plasticity at the crack tip but this was too small to measure. It is assumed for CTOD's larger than the elastic bound (see Figure 6), then a contribution of plastic deformation has occurred, and hence cyclic damage and propagation can occur.

2.1.9.2 Particle Effects

Zabett and Plumtree[11] saw very few crack arrests in L orientation test specimens of 2024-T3. This was identified with the cracked particles that caused the crack initiation in this orientation also proving "bridges" across the grain boundaries. As they are an abundant source of cracks, there is a high probability for crack coalescence to occur. Zabett and Plumtree[11] also suggest that the cracked particles may effectively increase the plastic zone size in front of a crack, and hence increase growth rate.

Kung and Fine[10] also noted that short cracks grow through or around intermetallic particles. For β (Al-Mg) phase it was found that the preferred method of propagation was through the particle, while for S (Al-Cu-Mg) phase debonding was preferred.

Mulvihill and Beevers[12] reported that only intermetallics greater than 5μm have an effect on propagation, and then only if the crack length is less than 500μm. The effect was attributed to the blocking of slip at the crack tip.

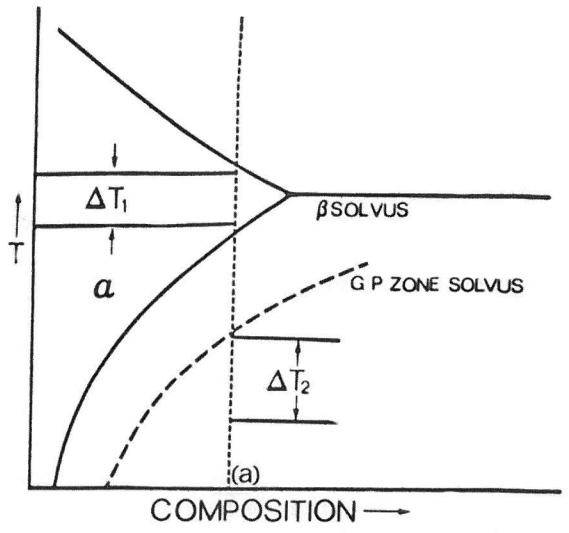

Figure 1 Phase diagram of hypothetical system A-B showing the β solvus and the GP zone solvus. For composition (a), the ΔT_i temperature range for solution heat treating, whilst the ΔT_2 temperature range may be used for a precipitation heat treatment.[7]

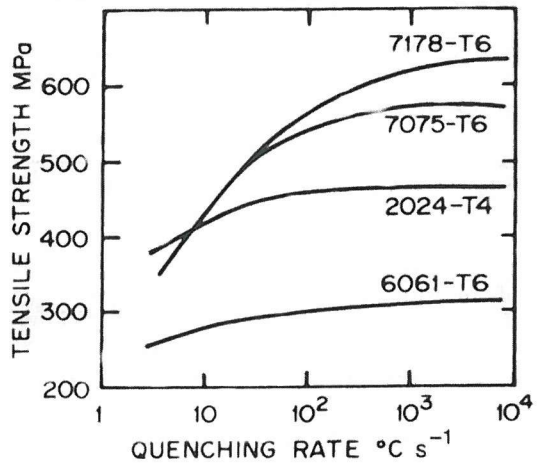

Figure 2 Tensile strengths of various commercial alloys as a function of quenching rate in the critical temperature range 400-290°C.[4]

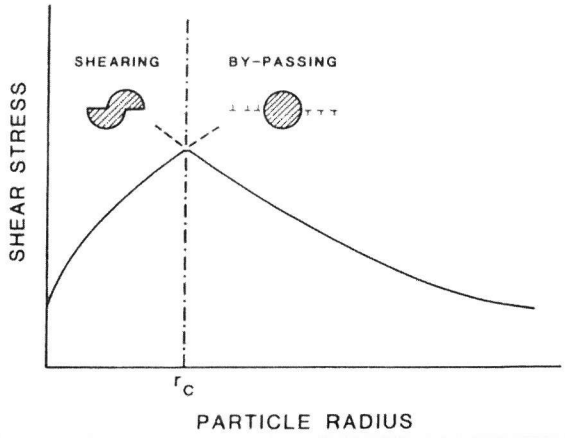

Figure 3 Schematic of the resolved shear stress as a function of particle radius when the particles are sheared or bypassed by dislocations[7].

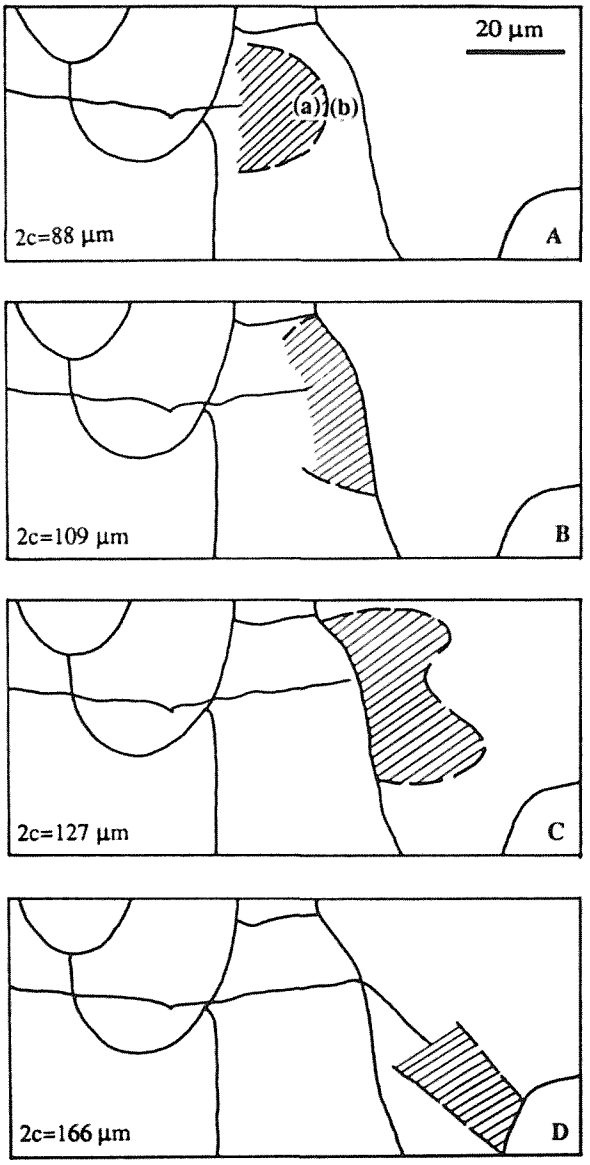

Figure 4 Plastic zones (hatched area is plastic zone and dashed line delineates plastic zone boundary) measured using selected area channelling patterns, grain boundary positions are also delineated[16].

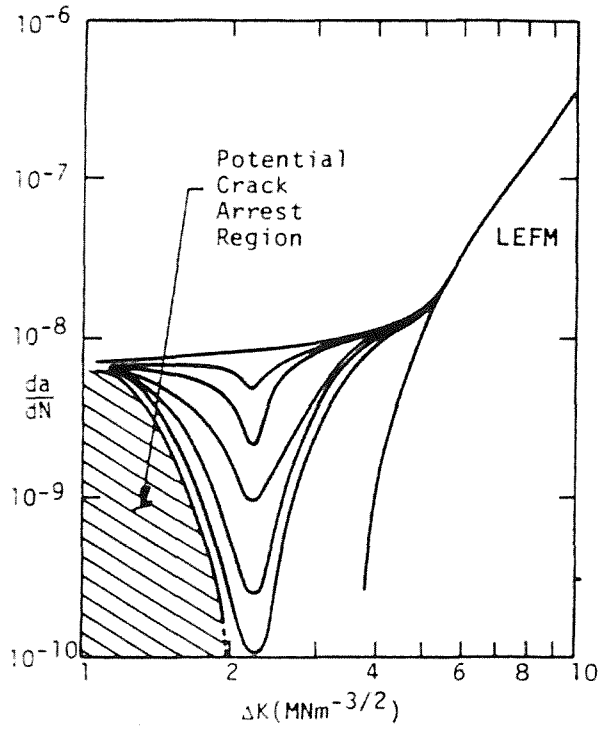

Figure 5 Growth of short and long cracks, Schematic idealisation of results[13].

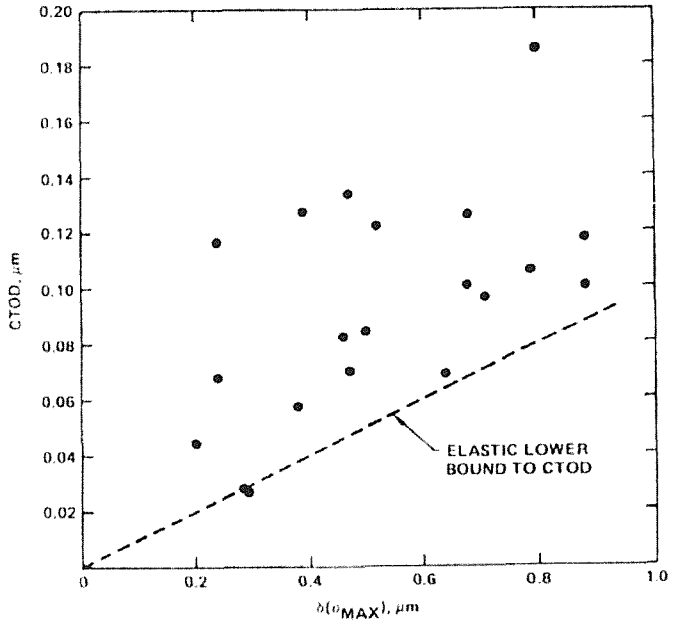

Figure 6 Comparison of CTOD to opening in crack centre

2.2 Friction Stir Welding

2.2.1 The Friction Stir Welding (FSW) process

- **General Issues**

Friction has been used as a heat source for welding for many years, see Figure 7[17]. The process usually involves rotating one or both of the work pieces and then forcing them together, with at least one of the parts having a circular cross section. Friction stir welding was developed from friction welding by The Welding Institute (TWI) in Cambridge with a fundamental shift in the mechanics via the introduction of a rotating 3rd body to the joining process, allowing non-rotating parts to be joined (patented in 1991[18]). The weld is achieved using a cylindrical tool with a profiled pin (commonly threaded) in the centre; the pin diameter is usually comparable to the work piece thickness. The tool is rotated and plunged in to the joint line until the tool shoulder has just penetrated the surface of the material with the work pieces being fixed rigidly to a backing plate or bar. Heat is generated by friction between the tool and the work piece; the heat and rotation plasticizes the material in front of the tool. The plasticised material is transported around the tool as the tool is traversed along the joint line, and the joint is formed by the mechanical mixing/interpenetration of the parent plate material[19]. Figure 8 shows a schematic diagram of the process.

The development of friction stir welding has lead to a number of other process being developed that are based on friction stir welding: Orbital friction stir welding[20], lap joints[21] and Skew-Stir welding[22]. More information on each of these techniques can be

found in the references given; the present work is focussed on butt joints made via friction stir welding only.

The process has been identified with a variety of advantages over other welding methods as a means of airframe construction; such as;

- Energy efficient (about half the energy required for MIG welding[23])
- Suitability for automation
- No filler metal or shield gas required
- Oxide removal prior to welding is not necessary
- The joining of dissimilar materials is possible
- The solid state character of the process may facilitate the welding of "difficult" composition types
- High strength joints have been demonstrated for heat-treatable Al-alloys
- Very low porosity/defect levels
- Low distortion

In terms of airframe design, it has been noted that the replacement of mechanical joints with high integrity welds (such as friction stir welds) offers a wide variety of weight saving and design optimisation opportunities[24,25]. In a first step towards using welding in airframe construction a central wing box structure was produced out of 10mm gauge 7055-T7511 and 7349-T6511 AA, the friction stir welded structure showed a 4% reduction in properties over the equivalent rivet structure[26]. The process has also been identified for the potential use in the manufacture of tailor welded blanks[27,28].

A significant portion of the on going research work is aimed at increasing the gauge and range of alloys that can be successfully friction stir welded. Currently welds in up to 25mm gauge plate have been achieved in a range of heat treatable aluminium alloys (2024, 7050, 7075 and 7449) using single and double pass welding techniques[27,26,29].

Friction stir welding (like all welding techniques) may be considered to have a number of disadvantages:

- Single pass welding speed is slower than in other welding techniques
- Parts must be rigidly clamped (this is a particular problem for corner joints[29])
- A weld keyhole is typically left at the end of a weld run (several techniques have been developed to overcome this problem; a comparison of the main techniques was produced by Engelhard *et al*[30])
- There is a lack of understanding of damage tolerance of associated welds and welded structures

Whilst there is ongoing development work to overcome the difficulties, the lack of damage tolerance information must be regarded as a critical factor in the use of friction stir welding in primary airframe structures[31], with little information as yet being available within the literature on micromechanical and microstructural contributions to fatigue in friction stir welds.

Subsequent sections address a variety of microstructural and performance aspects of friction stir welded joints that have been reported. Whilst a general advantage of friction stir welding may be identified in its applicability to various metals (and indeed dissimilar

metal joints) the present document focuses on work carried out in medium to high strength Al-alloys, in keeping with the aerospace technology driver of the project.

2.2.2 General Weld Structure

There is general agreement about the transverse macroscopic structure of friction stir welds[32,33,34]. This is commonly broken down into three main regions: the Heat-Affected Zone (HAZ), the Thermal Mechanically Affected Zone (TMAZ) and the weld nugget (which is sometimes identified as part of the TMAZ). The HAZ is the region that is only subject to thermal effects; HAZ will of course be present after any process where a heat source is applied to an area of the material, e.g. fusion welding. The TMAZ is the region that is subjected to thermal effects due to the welding process, along with relatively mild plastic deformations, and is a characteristic of the friction stir welding process. The weld nugget is generally identified as the region of the weld experiencing the highest plastic strains due to the joining process, with the associated recovery and/or recrystallisation processes then giving rise to a region of characteristically fine grain size.

Figure 9 shows a schematic overview of a friction stir weld structure. The nugget is perhaps the most striking of the various regions, with its widely reported macroscopic "onion ring" structure (see below), see Figure 10; this region is severely deformed and heated to a relatively high temperature during the welding process. Reynolds *et al*[35] found it useful to divide the TMAZ into three regions (flow arm, nugget and the TMAZ). In the weld that they studied, the area directly underneath the weld tool shoulder was identified as the "flow arm", this region is the hottest part of the weld and has the highest strain input. Norman *et al*[36] refer to this region as "the shoulder contact zone"; they suggest that

the region is close to melting, with incipient liquation in this region potentially limiting heat input.

The "onion ring" structure is generally thought to be a 3 dimensional feature of many friction stir welds. Some works have reported the structure as consisting of a number of concentric hemispheres which when cut transverse to the welding direction result in a ring pattern commonly observed.

It is significant to note that the features produced by the friction stir welding process are asymmetric due to the rotational and linear motions involved. It is therefore important to clearly identify the sides of the weld. The sides of the weld are either described as "advancing" or "retreating", depending on the direction of rotation of the weld tool and the direction of travel of the work piece [35]. The advancing side is defined as the side where tool rotation and weld direction coincide; with these directions being opposite on the retreating side, see Figure 11 (inset). Low magnification metallographic observations commonly show the advancing side of the nugget to be more clearly defined from the TMAZ, and hence maybe referred to as the 'sharp side', whilst the retreating side often appears relatively diffuse. Others have referred to the two sides of the weld depending on the flow mechanism; the advancing side is then referred to as the "shear" side and the retreating side as the "flow" side[37]. In this work the sides of the weld are referred to as either advancing or retreating.

Given the autogeneous constrained solid state nature of the process, limited dimensional changes are associated with the weld region, however Bussu and Irving[25] highlight minor

surface features they called 'weld toes'. These may be formed on either side of the weld tool shoulder by material being forced out from under the tool shoulder, at the edges of the flow arm, see Figure 9.

2.2.3 Material flow developed in the welding process

A range of techniques have been used to visualise the flow of material that occurs during the friction stir welding process. Colligan[38] and Reynolds *et al*[39] used embedded markers to establish material flow. Other workers have used etch contrast between different alloys to visualise flow. Colligan[40] and Yang [41] studied keyholes left at the end of welds and the surrounding material to establish the weld forming process. Colegrove *et al*[42] and Bendzsak *et al*[44] have modelled the weld flow process via finite element (FE) methods.

Based on their embedded marker studies, Reynolds *et al*[39] have described the material flow in 8mm gauge friction stir welds in 2195-T8 AA as an in-situ extrusion process; where the backing plate, the cold parent plate material and the weld tool shoulder form the extrusion chamber. Colligan's[38] work with 6.4mm gauge friction stir welds in 6061-T6 AA supports this idea, particularly for the material that is towards the bottom of the joint; however it was found that the rest of the material is chaotically mixed around the tool.

There is general agreement that the material near the weld top surface ('crown') is mainly affected by the action of the shoulder. Colligan[38] found that material as far as 1mm below the top surface may be swept around to the retreating side of the tool by the shoulder, well ahead of the pin. The material may then be deposited in a scattered manner on the advancing side of the weld. Reynolds *et al*[39] found that the most pronounced material transport in "cold" welds (welding parameters were varied in their work to develop

relative hot and cold welding conditions) was close to the top surface, where material is moved from the retreating side to the advancing side of the weld, with the vacant area left being filled with material moving in the opposite direction lower in the weld. In a relatively hot weld the flow was more chaotic; also, material at a greater depth through the plate was moved from the retreating side to the advancing side of the weld.

Yang[41] also found that the material close to the crown surface in friction stir welded 3.2mm gauge AA 7050 is moved to the retreating side of the weld by the shoulder. The welds that Yang used were not full penetration; the following observations were made on the weld tunnel left below the weld tool pin when welding had been stopped and the weld tool removed. Successive removal of layers of material by grinding vertically down through the keyhole region, indicates that the amount of deformation of the joint line left below the weld tool pin increases moving closer to the centre of the pin from the front edge of the shoulder, i.e. the degree of bending of the joint line towards the retreating side of the weld increases. Behind the pin, the joint line is bent from the retreating side to the advancing side due to the rotation of the weld pin and the travel direction of the plate. London *et al*[43] arranged a number of thin sheets of aluminium lying parallel to the welding direction and the weld pin to study material transport, finding that the most significant deformation in front of the tool occurs at the edge of the shoulder on the advancing side where material is swept across to the retreating side of the weld. The 3D FE model of Bendzsak *et al*[44] for 7mm thick 6061-T6 aluminium alloy showed that material close to the crown surface (<2.5mm) is rotated around the pin from the advancing side to the retreating side, which is supported by a 600μm transition zone from the rest of the material which is extruded around the weld tool (c.f. observations of Colligan). Bendzsak

et al[44] also noted that as tool rotational speed is increased, the depth of the transition zone for material swept by the shoulder from one side to the other also increases, this can lead to voiding.

Vertical (through-thickness) material movement has been identified within friction stir welds. Colligan[40] proposed a mechanism for transport of material along the thread of their screw type tool pin based on experimental observations of the weld keyhole when welding is abruptly stopped and the weld pin is unscrewed to leave the keyhole intact. Material near the weld top surface on the front edge of the weld pin begins to curl into the thread; this material does not rotate around the pin but is forced down into the weld. When the thread profile is full, the material rotates around with the pin but at a slower speed than the pin, and is deposited behind the tool. In this way there is material flow down into the weld from the surface. Material at the bottom of the weld is then extruded around the tool and upwards. Colegrove *et al*[42] found a similar result from the modelling of 5083-0 12mm gauge welds; it was found that material around the weld bulk moves vertically upwards, except that in the threads, which moves downwards. Reynolds *et al*[39] noted material movement down through the weld, particularly at higher welding speeds. Dalle Donne *et al*[45] clarified the effect of the threads on the weld pin using 2024-T3 and 6013-T6 welds in 4mm gauge plate welded with two tools. The first tool had no threads; producing no downwards movement of material. This was seen to obviate the incidence of "onion rings" within the weld, but left voids at the root of the weld. The second tool had a threaded pin; this produced material movement down into the weld, along with an "onion ring" structure in the nugget and lower defect content (in both alloys). London *et al*[43] using a continuous marker placed at the mid plane of the plates prior to welding

however saw material movement up through the weld to a position approximately 1/3 of the plate thickness below the crown surface; this may be the result of the individual tool upwards flow was related to the tilt angle of the weld tool, larger tilt angles (up to 3°) give more upwards movement.

Bendzsak *et al*[44] noted swirls in the flow pattern, where the material flow in a small local region does not follow the global flow, rather it forms small whirlpool like features, these are developed on the advancing side of the weld within the transition zone between the material that is swept around with the pin, and material that is extruded past the pin, the material flow in the transition region is more chaotic. Flow swirls were also studied by Ying *et al*[47] using alloys with different etch characteristics to visualise the material flow. They found that the final weld structure had linear striations through the weld zone (sectioned parallel to the welding direction and through thickness) that correspond to the pitch of the thread on the weld tool pin, consistent with Colligan's linking of material flow to the thread of the weld tool and results from London *et al*[43]. Ying *et al*[47] also noted flow markings parallel to the welding direction. Ying *et al*[47] and Reynolds *et al*[39] both experimented with a range of welding parameters. Both groups noted that for higher rotational speeds material flow patterns became less well defined with more chaotic mixing occurring.

The understanding of weld flow is the subject of ongoing research with new tool designs being developed to increase the amount of material flow. The "onion ring" structure

32 Diccon Booth

characteristic of the weld nugget as stated previously is related to the pitch of the thread on the weld tool as such, it is difficult to reach detailed conclusions at present, with new tool types clearly potentially having marked influences on weld characteristics, e.g. the latest fluted tool designs which aim to maximise the amount of material flow do not produce the same clear "onion ring" structure in the weld nugget as noted above[48].

2.2.3 Heat Input

Temperature distributions will of course have a defining influence on many features of a given FSW. This is particularly significant for the precipitation strengthened aluminium alloys. Various works in the literature have measured and modelled the temperature profiles associated with friction stir welds, although it must be noted of course that there are experimental difficulties associated with the high level of plastic deformation around the weld zone.

The friction stir welding process is not generally reported to involve melting. The maximum temperatures reported by most workers for Al-alloy welds are in the range 450-500°C, which is typically less than ~0.8 Tm [42,49,50], but close to the incipient melting temperature in many high strength alloys (~505°C for 2024). Due to the difficulty of producing accurate maximum temperature results for the weld centre line of a friction stir welds, North *et al*[51] have used "plunge" testing, simulating the initial plunge of the weld tool pin by forcing a smooth rotating pin without a shoulder into an aluminium plate and measuring the temperatures reached. The maximum temperature recorded in such experiments however was 582°C, temperatures reached in any one weld will of course vary with exact weld conditions and material properties. It is worth noting however that

in friction stir welding the majority of the heat input is reported to be from the shoulder (see below).

However as the temperature increases the viscosity of the weld region may be expected to decrease[49], along with the effective coefficient of friction, and therefore the heat input mechanisms reach a peak value. Reynolds *et al*[35] studied a number of alloys 5083-0, 6061-T6, 2024-T3, 2219-T87, 7050-T73, and 7075-T73, for many of the alloys tested a saturation in temperature was found. The most significant effect on temperature however was in fact the alloy rather than the welding parameters, it is therefore clear that care must be taken with the selection of welding parameters and weld tool material for the different aluminium alloys to ensure that a good quality weld is produced.

The nature of the friction stir welding process makes temperature measurements in the weld centre difficult hence the majority of thermal data that has been reported for friction stir welding is for the regions outside the weld centre. Mahoney *et al*[32] produced a map of peak temperatures for a friction stir weld in 6.35mm gauge 7075-T651AA, shown in Figure 12. The peak temperature obtained was 475°C at the edge of the weld nugget, close to the crown surface. Other workers have reported similar results for a range of heat treatable aluminium alloys[50,52,53]. The thermal gradient through the thickness of the HAZ/TMAZ suggests that most of the heat input is from the weld tool shoulder. This is supported by the modelling results of Colegrove *et al*[42] and Russell and Shercliff[50]. Russell and Shercliff[50] estimated the heat input from the weld tool pin (for welding 6.5mm gauge 2014-T6 plate) to be 10-20W from pin contact, and 10-20W from material shear, while the shoulder contributes 1-2kW of the weld energy (i.e. orders of magnitude

greater). Modelling results obtained by Dong *et al*[54] agree that the maximum temperature recorded is under the tool shoulder; however they also identify a similar temperature immediately underneath the base of the pin. Tang *et al*[49] suggest that there is no thermal gradient through the thickness in the region close to the weld centre. This is based on thermocouple readings at three depths, and an observed lack of grain size gradient through the weld thickness.

While there is agreement that large scale melting of the work pieces does not occur during "conventional" friction stir welding processes, some workers have suggested the possibility of local melting at the weld surface. Bjørneklett *et al*[55] studied the phenomenon of local melting. They found that local melting may be significant for friction stir welding as it may limit the maximum heat input due to molten eutectic effectively lubricating the shoulder. This point was also suggested by Norman *et al*[36] in section 2.2.2 to be a possible factor governing the heat input in a friction stir weld.

Obviously there will be a thermal gradient across the weld which drops quickly outside the weld shoulder[49]. Russell and Shercliff[50] report values of ~100°C at 40mm from the weld centre for example for a 2014-T6 weld in 6.3mm gauge plate[50], with Leonard[53] suggesting that maximum temperatures are still above 100°C at 50mm (see Figure 13) from the weld centre line for the same alloy and gauge; differences may of course be attributed to differences in weld tool shape, size and/or welding parameters (details not supplied by Russell and Shercliff[50]). The temperature distribution across a friction stir weld in 6.35mm gauge 7075-T651 was reported by Mahoney *et al*[32] and is shown in Figure 12 for the region within 11mm of the weld nugget. Tang *et al*[49] tested welds in

6.4mm gauge 6061-T6 AA; they measured temperatures above 300°C at over 12mm from the weld centre line, in reasonable agreement with Mahoney *et al.* Most workers agree that there is little difference in thermal profiles between the advancing and retreating side of the weld[49,52].

As noted above, the primary mechanism of heat generation in friction stir welds has been identified as friction between the shoulder and the work piece. Evidence for this has been produced by several models; Colegrove *et al*[42] reported very good correlation between experimental and modelling results using only frictional heating from the shoulder, as did Frigaard *et al*[52]. The experimental results obtained by Colegrove *et al*[42] were obtained using thermocouples embedded 3mm below the top surface in 12mm gauge 5083-O friction stir welds, for the modelling result the tool was assumed to only consist of a tool shoulder. North *et al*[51] based their assessment of heat generation during friction stir welding on the more established process of rotary friction welding. Using this approach, they found that in the initial stages of the welding process, friction is the primary heat source; however they suggest that once the plastic zone is established the primary heat generation method is "churning" of the plasticised material, i.e. heat generation is by viscous dissipation of mechanical energy. Gould and Feng[56] suggest that there are two mechanisms for heat generation in friction stir welds: firstly, friction from the shoulder contact as seen by others, and secondly heat is generated by the plastic deformation in the vicinity of the tool pin (similar to North *et al*[51]). Gould and Feng[56] suggest that aluminium may bond to the surface of the weld tool shoulder and that heat is generated by continuous extrusion of the sub-surface aluminium layers, although this has not been particularly identified by others. Dong *et al's*[54] model agrees that friction induced heating is

important in the upper portion of the weld, however they suggest that plastic work induced heating is dominant at the bottom of the weld. It is clear that the exact mechanism of heat generation is complex, the scope of which is beyond the present work; however good correlation between experimental data and modelling results has been shown when considering friction as the only heat source, this would appear to confirm the critical role of the shoulder/work piece contact.

Several workers have studied traverse speed effects on weld temperature. In the absence of any other changes, increasing the traverse speed reduces the weld temperature, in keeping with the primary heat input arising from tool rotation. Similarly, increasing the rotational speed is seen to increase the temperature. Reynolds *et al*[35] have particularly identified the use of a 'weld pitch' parameter (defined as rotational speed/traverse speed) in friction stir welds in a range of alloys (including 2024-T3 and 7075-T73). In all cases, as the weld pitch increases, so does the temperature. As a result of the increase in temperature the time at an elevated temperature also increases.

Along with peak temperature levels, heating and cooling times are clearly important. Leonard[53] produced temperature history traces for distances between 6 and 100mm from the weld centre line for 6.35mm gauge friction stir welded 2014-T651 and 7075-T651, as shown in Figure 13. In keeping with a variety of other reports, a general heating/cooling cycle of the order of 100 seconds for the temperature to return to below 150°C is reported for friction stir welds of Al alloys of intermediate gauge (up to 12mm) [42,49]

Boundary conditions for the welding process should of course incorporate the backing plate, which may have a significant effect on the cooling rate of the welds; in keeping with this, Colegrove *et al*[42] and Frigaard *et al*[52] found that the temperature distribution outside the weld tool gets narrower towards the weld base, see Figure 14. Midling and Røruik[57] particularly note the significant heat sink effect of the backing material in reducing the width of the HAZ; they report that the same width of HAZ is achieved at a 15mm/s welding speed with a zirconia (insulating) back plate, compared to a 5mm/s weld speed with a steel backing plate (other parameters being maintained).

The effect of the tool shoulder pressure has been noted to be similar to the effect of rotational speed; as the pressure increases so does the temperature. A limit above which increasing the pressure has little effect has been reported. Too little pressure has been identified with plasticised material of the weld not being contained and excessive flash being produced (i.e. material flow into the weld toes)[49,57].

The results of Midling and Røruik[57] are shown in Figure 15 for the relative effect of individual weld parameters on the heat input, calculated by estimating the heat input from the theoretical net power input and the width of the HAZ. It can be seen that the traverse speed has the greatest range of influence on heat input, (i.e. the other parameters have a limit below which they have no effect) with increasing transverse speed increasing the width of the HAZ. Reducing the vertical load and rotation speed reduces both the width of the HAZ and the estimated heat input but the effect has a limit below which reducing the parameters no longer affects the heat input or HAZ width. The theoretical net power,

q_o, was calculated using the following equation; the equation can be used to compare the amount of power involved in the welding process when varying the welding parameters:

$$q_0 = \tfrac{2}{3}\mu F v_{\max} \qquad \textbf{Equation 1}$$

Where μ is the friction coefficient (fixed arbitrarily at 0.2)

F is vertical load (N)

v_{max} is shoulder peripheral speed (m/s)

The only report on different weld tool shoulder materials is provided by Midling and Røruik[57]. It was found that zirconia was more efficient at generating heat than the other materials tested by between 30% and 70% (Inconel 718, Nimonic 105, Hard metal and hot worked tool steel (Orvar)).

As stated above, the heat generation mechanism in friction stir welds may be complex and may arise from a combination of friction and plastic working. The effect of the various weld parameters is complex, furthermore temperature, as mention previously, is dependent on the alloy as well as welding parameters. Gould and Feng[56] have demonstrated the effect of incorrect welding parameters on friction stir welds of 6062-T6 6mm gauge. If the weld is too hot then excess flash is produced, while a weld that is too cold may exhibit porosity, i.e. in the cold weld material is not sufficiently plasticised to form a weld. It has also been shown by Dong *et al*[54] that if the rotational speed is too high, over-stirring (mixing becomes chaotic) has been identified with turbulent material flow which can lead to void formation.

2.2.4 Microstructure

2.2.4.1 Grain Structure

A distinctive feature of FSW microstructures is the grain structure of the nugget; this region has been studied by a number of workers. The region typically exhibits a very fine equiaxed grain structure, with grains in the range of 1-10μm[33,58,59]. Norman *et al*[36] have used EBSD (Electron Back Scattered Diffraction) to provide a detailed analysis of the grain structure within the nugget for 6mm gauge 2024-T351 friction stir welds. They found grain sizes within the nugget of ~2.5μm and they estimate the strain during welding that is required to produce this fine a grain size to be between 5 and 10. Juričić *et al*[60] report the grain size in the nugget region as independent of the original temper for friction stir welds performed in 4mm gauge 6013-T6 and T4. They also found that the retreating side of the weld had a smaller grain size than the advancing side.

It was noted by Hassan *et al*[61] (6.35mm gauge 7010-T7651) and Tanaka and Kumagai[62] (4mm gauge 5083-H112 and A6N01-T5) that the width of the nugget was affected by the welding parameters; increasing the rotational speed for a fixed traverse speed increased the nugget width. Hassan *et al*[61] suggest that this is due to an increase in energy input causing a rise in the temperature of the weld and this results in a larger plastic zone. They also found that the grain size is generally finer at the weld root than at the crown surface, which they attribute to temperature gradients; this effect was more obvious at slower weld rotational speeds. Sato *et al*[63] reported an increase in grain size with increasing weld rotational speed with other weld parameters kept constant. This was thought to be due to the increased energy input that would result from increasing the rotational speed as

reported in the section 0; the increased energy was thought to lead to static grain growth, see below.

The majority of workers have attributed the fine equiaxed grains found in the nugget region to continuous dynamic recrystallisation. This process is described in detail for friction stir welding by Jata and Semiatin[64] for an Al-Li alloy; however a brief review of the basic principles and mechanisms of dynamic recrystallisation in aluminium alloys, based on Recrystallisation and Related Annealing Phenomena by Humphreys and Hatherly[65], is given below.

- ***Dynamic Recrystallisation***

Dynamic recrystallisation is generally identified with materials exhibiting slow recovery processes, i.e. those with low or medium stacking fault energy. New grains originate at old grain boundaries, but as material continues to deform, the dislocation density of new grains increases, thus reducing driving force for their further growth and the grains stop growing. Nucleation of other grains at the migrating grain boundary may also limit grain growth.

Characteristics of dynamic recrystallisation include

1 The stress-strain curve for a material which undergoes dynamic recrystallisation generally exhibits a broad peak that is different to the plateau, characteristic of a material which undergoes dynamic recovery.

2 A critical deformation (ε_c) is necessary in order to initiate dynamic recrystallisation. This is somewhat before the peak of the stress-strain curve.

3 ε_c decreases steadily with decreasing stress

4 The size of dynamically recrystallised grains (D_g) increases monotonically with decreasing stress. Grain growth does not occur and the grain size remains constant during deformation.

5 The flow stress (σ) and D_g are almost independent of the initial grain size although the kinetics of dynamic recrystallisation may be accelerated in specimens with smaller initial grain size.

6 Dynamic recrystallisation is usually initiated at pre-existing grain boundaries, although for very low strain rates and large initial grain size intragranular nucleation becomes more important.

Bulging of the grain boundaries is frequently observed prior to dynamically recrystallisation. The mechanism is assumed to be close to Strain Induced Boundary Migration (SIBM). Any subsequent growth is thought to depend on the distribution and density of dislocations (both in the form of subgrains and free dislocations).

The evolution of a dynamically recrystallised microstructure structure is shown schematically in Figure 16. Nucleation occurs at old grain boundaries as shown in Figure 16; new grains subsequently nucleate at the boundaries of growing grains. This develops a thickening band of recrystallised grains. A "necklace" structure occurs if a large difference in new and old grain size exists. Eventually a fully recrystallised structure may develop. This process is generally termed discontinuous dynamic recrystallisation, due to the step nature of the process.

An alternative form of recrystallisation may be identified in geometric dynamic recrystallisation. Grain boundaries develop serrations roughly on the wave length of the subgrain size. Subjecting a material to large hot deformations flattens the original grains; if sufficient deformation occurs then the serrations become comparable with the grain thickness. As shown schematically in Figure 17, interpenetration occurs and an equiaxed grain structure appears. A high number of low angle grain boundaries may be linked to this process, however a proportion of high angle boundaries are also formed, proportion of high angle boundaries increases with strain. This mechanism is common in aluminium and aluminium alloys when deformed to high strains

Another possible process for dynamic recrystallisation is by Progressive Lattice Rotation. In this mechanism new grains with high angle grain boundaries may be formed by progressive rotation of subgrains with accompanying boundary migration during straining. Moving from the original grain boundaries towards the centre there is generally a gradient in the misorientation, in the centre of the old grains subgrains may not have developed or the misorientation may be low. This mechanism has been seen in aluminium alloys with sufficient solute additions e.g. Al-Mg and Al-Zn alloys.

Jata and Semiatin[64] suggest that the recrystallised grains are in fact high angle subgrain boundaries; the mechanism they propose for this is dislocation glide assisted subgrain rotation. They compared the grain structure in the nugget of a friction stir weld with the structure developed in other hot deformation processes where continuous dynamic recrystallisation occurs, such as hot forging and found that the result is within the scatter band of the other processes. Norman *et al*[36] agree that dynamic recrystallisation occurs in

the nugget, however the mechanism they suggest is different; they suggest the process occurs by strain induced grain boundary migration and geometric dynamic recrystallisation; this is supported by Hassan *et al*[61] for 7010-T7651. It is worth noting that no grain growth is associated with such mechanisms, therefore grains will be of the order of the sub-grain size. Murr *et al*[66] have attributed the formation of the fine weld region grain structure to dynamic recrystallisation and (limited) static grain growth; the evidence for this was produced by welding dissimilar metals (6061 to copper), producing a complex vortex-like/swirl-like intercalated microstructure within the weld zone with no dendrite structure or other characteristic solidification features present. The complex structures formed must have done so simultaneously with the friction stir welding process; hence dynamic recrystallisation is thought to be the most likely mechanism for this to occur. A lack of twinned boundaries in copper welds was noted as an indication of recrystallisation.

Flores *et al*[67] produced friction stir welds in a 6.3mm plate of a modified 1100 aluminium alloy (modified to form an equiaxed, dendritic cell structure in the as-cast condition with an average size of 28μm). This was welded in the as-cast condition, and after 50% cold rolling. The recrystallised weld zone grain size was ~15μm in both cases, but a higher dislocation density was left in the cold rolled sample, suggesting that the recrystallisation process is intimately connected with the instantaneous plastic flow associated with the welding process rather than the stored energy of prior deformation. This result contributes to the notion that slip deformation leading to dynamic recrystallisation (sub-grains form and incur a continuous increase in misorientation and hence absorb dislocations) is the principal mechanism of grain structure evolution in the weld nugget. This is supported by

the remaining dislocation difference between the two welds; other mechanisms would be expected to leave the same dislocation density in both cases.

The report of Yang[41] does not agree that the fine grain structure found in the nugget region is due to dynamic recrystallisation; instead it is suggested that it is the result of dynamic recovery. This suggestion is due to the instability of the microstructure when subjected to high temperature heating cycles (500°C for 10 minutes), followed by a low temperature aging treatment. Yang suggests that the associated changes in grain structure cannot be the result of grain growth during the thermal treatment, but are the result of recrystallisation during the heat treatment. It is therefore suggested that the welded structure is dynamically recovered, which may or may not be stable during post weld annealing depending on the stored energy and the temperature and time of heat treatment. Frigaard *et al*[52] suggested that dynamic recovery is a possible cause of the structure found in the weld nugget region of friction stir welds in 6082-T6 and 7108-T79. This was also linked to the response of the weld region to post weld heat treatments similar to those used by Yang. The flow arm and weld root regions were seen to recrystallise during heat treatment to form regions with finer sub-grains than the un-recrystallisied region. Sato *et al*[68] used the changes seen after post-weld heat treatment to argue that dynamic recrystallisation does occur. They argue that if the recrystallisation occurs statically, then the grains' structure would not change during post weld heat treatment due to a lack of a driving force. They however found that a change does occur, suggesting that recrystallisation must have occurred during the welding process for a driving force to be present, the driving force results from limited deformation continuing after recrystallisation has occurred.

Broadly speaking, the flow arm has not been studied in as much depth as the weld nugget region. Norman *et al*[36] have identified a similar grain size to the weld nugget, however the grains are more elongated than those seen in the nugget, and there are fewer high angle grain boundaries. This was thought to be due to the lower strain intensity in the region and the higher heat input. Hassan *et al*[61] found a similar grain structure in the flow arm to Norman *et al*[36], particularly at low tool rotation speeds where the flow arm had larger grains that were slightly more elongated than those found in the centre of the nugget and contained a greater proportion of low angle boundaries.

In terms of the grain structure in the TMAZ, significant distortions are identified, although the region is essentially defined by an absence of recrystallisation; as temperatures and strain levels fall off moving out from the weld line. Svensson *et al*[69] report the grains as being bent around the nugget, i.e. the parent plate grains are deformed to fit around the weld nugget that develops. Mahoney *et al*[32] identify a similar grain deformation, where the grains adjacent to the weld nugget are bent upwards toward the top of the weld nugget. Denquin *et al*[70] (using 6mm gauge 6056-T4) and Normal *et al*[36] (using 6mm gauge 2024-T351) found that the grains in the TMAZ on the advancing side of the weld were rotated by as much as 90°, so that the grains lie vertically through the thickness. In keeping with increasing strain levels, the grains get thinner moving towards the nugget; eventually the grains are only one subgrain wide. Leonard[53] also found grain rotations of ~90° close to the interface between the TMAZ and nugget. A transition region between the two regions was also reported, where larger grains have grain boundaries decorated with very fine equiaxed grains, referred to as a necklace which is often the first stage in dynamic

recrystallisation, however there is no indication of which side of the weld Leonard is referring to. Juričić *et al*[60] found that the grain boundaries in the TMAZ were serrated, and that a few fully recrystallised grains were present, Von Stombeck *et al*[34] also note that whilst TMAZ grains are predominantly distorted and rotated around the weld nugget, some limited recrystallisation may be seen in a range of alloys, including 2024-T31, 6061-T6 and 7020-T6. Sato *et al*[71] indicate that the TMAZ of friction stir welds in 6063-T5 may contain a high density of low angle sub grain boundaries, i.e. a recovered structure.

The HAZ is only subjected to a thermal cycle, which is generally well below the solutionising temperature for aerospace aluminium alloys. Therefore, as would be expected, Pao *et al*[72] report that processes such as recovery and growth grain do not affect this region (consistent with Denquin *et al*[70]).

2.2.4.2 Precipitate Structure

For heat treatable aluminium alloys, the thermal cycle associated with welding will of course have a significant effect on the precipitates present and hence the mechanical properties. Given the temperatures involved, strengthening precipitates may be expected to undergo a degree of ageing/coarsening, resolutionising and/or reprecipitation, depending on the position in the weld and the point in the weld cycle.

The weld nugget may of course be expected to be the hottest region of the weld. A number of workers have reported finding none of the very fine hardening precipitates associated with artificial ageing of heat treatable aluminium alloys in this region[33,73,71]. Precipitates that may not be directly imaged may of course be present as zones and/or clusters which may be expected to make a significant contribution to strength in this

region[50]. Norman *et al*[36] have however reported θ (Al_2Cu) and S (Al_2CuMg) phase particles present in the weld zone of 2024-T351 friction stir welds. They believe that some of the S phase is the remains of constituent particles broken up during the welding process; hence their distribution closely follows the material flow; while some of the S and θ appears to have formed during the weld thermal cycle[36].

As reported above, some of the intermetallics present in the parent plate are stirred into the weld nugget and may be fractured in the process; this is supported by several other workers[60,74,75,76]. It has also been noted that the density of such debris increases with depth through the nugget. Strangwood *et al*[77] suggested that while some intermetallics will be fractured during the welding process, there may also be some dissolution; this is supported in a model produced by Russell and Shercliff[50], which will of course depend on the alloy chemistry and prior treatment (i.e. presence of soluble intermetallics).

Hassan *et al*[61] note that the 2nd phase particles in a 7010-T7651 weld were affected by variations in welding speed; at low rotational speed the larger 2nd phase particles (0.5 - 1μm in length) were found mainly at the grain boundaries with some finer particles (~0.2μm) within the grains. Whilst for higher rotational speeds coarse 2nd phase particles (0.5 -1μm) were still present but the volume fraction had reduced and a higher density of finer precipitates (~0.2μm) was found within the grains. They also noted the presence of density gradients for a given set of weld parameters, with a higher concentration of 2nd phase at the weld root compared to the crown. This variation was seen to be less significant with increasing rotational speed, this is thought to be due to a more uniform

through thickness temperature profile at higher rotational speed for the same traverse speed.

The TMAZ region experiences a range of temperatures and some mechanical deformation. This region has been reported in many alloys as essentially being overaged[53,59,69]. A duplex population of hardening precipitates has been reported by some workers which may be consistent with a degree of re-precipitation occurring during cooling[58]. PFZ's around large matrix particles and grain boundary precipitates have also been reported[58,61,72]. Russell and Shercliff's[50] model suggests that close to the weld nugget the temperature is sufficient in the TMAZ for dissolution to occur; moving further away from the nugget the drop in temperature gives rise to coarsening. Further details of the precipitation processes associated with friction stir welds are discussed in section 2.2.5.1.

2.2.4.3 Texture

The texture within the regions of a weld may of course have an influence on the strength and mechanical behaviour. Whilst lacking Orientation Distribution Function (ODF) data, the most detailed texture study that appears to have been produced to date has been that of Sato *et al*[68] for 6063-T5 friction stir welds in 4mm gauge plate. The parent plate was identified with a <100> fibre texture, with the most dominant component close to the Goss Orientation ((110)<001>). This is a typical recrystallised texture in aluminium alloys: the coarse grain structure of the plate. The actual weld zone had no obvious nugget in this work, but the advancing side was more clearly defined than the retreating side, with the grain size of the weld region being reported to be ~8μm, compared to 65μm in the parent plate. Pole figures obtained at intervals through the weld centre thickness indicate that the material close to the surface has a different texture to that deeper into the weld. Between 0

and 0.5mm from the top surface the texture contains a component with a 110<001> orientation which is rotated by ~9° around the weld direction (WD) and ~14° around the normal to the plate (ND). For depths greater than 0.8mm, regions exhibit both {110}<001> and {114}<221> components. Sato *et al*[68] related the texture in the weld centre to stresses and strains at the backside of the tool: these are generated by both the tool shoulder and pin rotation. It can be shown that both {110}<001>and {114}<221> have a common plane {111} and a common direction <110>: behind the tool these are roughly parallel to the pin surface and perpendicular to the weld direction. As such the tool surface and rotational direction are in a maximum shear orientation, suggesting that at a depth over 0.8mm, the texture is dominated by plastic flow arising from the shear stress along the pin surface. The shoulder may then be responsible for the inclination of the sheared material direction, from the WD to the ND directions.

Pole figures produced by Sato *et al*[68] for the vertical centre of the welded plate at different horizontal distances from the weld centre line indicate that for 2.5, 3.3 and –2.5mm from the weld centre, the pole figure is similar to the centre line, with clockwise rotation of -30°, -42° and 44° respectively around the ND direction. The shear stresses become more complicated moving away from the weld centre, as shown in Figure 18: it is a composite stress induced by the rotation of the weld tool and the traverse direction of the tool. On the advancing side, the two stresses are similar in sense, whilst on the retreating side they vary to the point where they are opposite. This produces the more complex texture pattern; however, since both sets of shears still operate perpendicular to the ND direction, the resultant composite plastic flow produces one of the <111> directions roughly perpendicular to the ND.

It is clear from the work of Sato *et al*[68] that, for the majority of the weld, textures are relatively moderate (maximum pole figure intensities ~4 times random). There was a stronger texture around 0.8mm from the crown of the weld on the weld centreline (corresponding to ~7 times random) and also 4mm from the weld centre line (advancing side), but at –4mm (retreating side) it is very weak ~2. Other studies that have also concentrated on the weld nugget agree that this region has a generally weak texture[36,64]. Field *et al*[78] found that there was a texture gradient moving from the crown to the root in a 6.35mm gauge weld in 1100 and 6061-T6, they agree that the strongest texture is on the advancing side for all depths and that there is a significant difference between the advancing and retreating side of the weld.

2.2.4.4 Nugget Banding

The presence of an onion ring structure is dependent on the weld parameters used, as stated previously: for example, when the rotational or lateral speed is increased beyond a limiting point the bands may disappear[35]. Many groups have studied the nature of the bands that may be seen within the weld nugget: it is generally agreed that the bands are related to threads on the weld tool pin (as stated previously, in the absence of a thread no bands are formed). Sutton *et al*[79] (using 6.35mm gauge 2024-T351) and Krishnan[80] (using 6061 and 7075, gauge and heat treatment not given) found that the spacing of the bands in the nugget is equal to the tool advance per revolution; they suggest that it should therefore be possible to control the nugget structure. Biallas *et al*[81] described the bands as being concentric tube shapes (parallel to the weld line); they however only looked at transverse sections. More recently they have been shown to be concentric hemispheres[80,53] , i.e. shells like an onion. Norman *et al*[36] (studying 2024-T351) and Larsson *et al*[59] (studying

2014-T651 and 5083) both found no difference in grain size between the bands, however Mahoney *et al*[32] did find a variation in grain sizes between the bands in 7075-T651. Mahoney *et al*[32] reported the bands as being either fine (5-10μm) or very fine (2-5μm) grained. Leonard[53] also reported a slight grain size difference for 2014-T651 and 7075-T651 welds, with the "coarse" bands exhibiting grains of ~6μm, and the "fine" bands corresponding to ~5μm. However, this was not evident on the transverse sections: only longitudinal sections and in-plane sections.

Some authors believe that there is no variation in particles between the bands, while others have reported clear differences. Norman *et al*[36] linked the bands to an abrupt change in density of coarse 2nd phase particles. They suggest that this is indicative of large local differences in deformation conditions. Sutton *et al*[79] also attribute the bands to a change in particle density (particles ≤1μm), where Energy Dispersive X-ray (EDX) analysis showed that the particle chemistry is consistent with the constituent particles found in aluminium alloys. It was suggested that the particle segregation between the bands is possibly caused by entrainment of particles in the region that corresponds to a high strain rate gradient. If the particles are large relative to the distance over which the strain rate changes appreciably, then the particles may tend to roll towards the low strain region, resulting in clearly defined bands of high and low particle density. Leonard[53] noted changes in particle distribution between the bands, suggesting that coarse grain areas have fewer particles and hence less grain boundary pinning. Krishnan[80] suggests that there may be an oxide film between the bands due to the void that is thought to form behind the weld tool pin during welding. While there has been little evidence of oxide found in friction stir welds of aluminium alloys Larsson *et al*[82] did note lines of oxide particles, that are ≤2μm

in size, decorating the interfaces between the two materials in a dissimilar alloy weld (5083-H12 to 6082-T6); this interface is thought to correlate to the original joint interface. They suggest the reason why this is not seen in like alloy welds is the difficulty in finding the original interface.

Svenson *et al*[69] reported that there were grain orientation differences present between bands, based on optical imaging of anodised samples. They noted that the misorientation within the bands is relatively low compared to the surrounding grains. Jata and Semiatin[64] used EBSD to measure misorientation more quantitatively across the weld zone, showing a uniform distribution of grain boundary miss-orientations across the weld region. Also using EBSD, Norman *et al*[36] found no texture change between the bands in 2024-T351 welds. It is clear that further work is required to clarify the nature of banding within the FSW microstructure.

2.2.5 Mechanical Properties

2.2.5.1 Hardness/Strength Profile

Friction stir welds in heat treatable aluminium alloys exhibit a characteristic transverse hardness profile, the form of which appears remarkably independent of the alloy, temper prior to welding and the welding parameters. This profile is illustrated schematically in Figure 19. The typical features are the plateau region in the weld centre, with a steep drop to minima on either side, followed by a more gentle rise to parent plate hardness[52,53]. The minima are located close to, but outside the nugget region. Depending on the temper condition of the parent plate, a slight rise in hardness may occur moving from the parent plate towards the minima. Murr *et al*[66] note that the hardness trace may be significantly

different if an annealed alloy was welded; they suggest that the weld hardness would be more similar to that found in non-heat treatable alloy welds; however no evidence of this is provided.

In heat treatable alloys, the distance of the hardness minima from the weld centre is commonly reported as being close to the width of the weld tool shoulder[53,76]. The temperature at this point has been reported to be in the range of 350-450°C [32]. Through-thickness hardness properties have been reported by several groups. Heinz *et al*[73] found that the hardness minima about the weld centre in 6013 friction stir welds in 4mm gauge plate formed a "V" shape through the thickness, similar to the grain structure, i.e. giving a wider hardness plateau at the crown surface than the root. This was also seen by Leonard for 6mm gauge 2014-T6 and 6.35mm gauge 7075-T6. Jata *et al*[33] found that hardness profiles close to the root side of the weld in 6.35mm gauge 7050-T7451 had a dip in their centre, while the trace close to the crown surface did not. The origin of the dip was not clear. Bussu and Irving[25] found no clear plateau region for 2024-T351, but this may be due to the scatter evident in their results.

The basic potential effect of welding parameters has been discussed previously with respect to weld process conditions and microstructure; it therefore follows that the hardness characteristics may also be altered by the welding parameters. Frigaard *et al*[52] have reported the distance between the hardness minima in heat-treatable alloy welds reduces with increasing weld traverse speed due to a reduction in weld temperature. Hassan *et al*[61] also found a change in the hardness properties with welding parameters. They reported that close to the crown surface there is little effect when the rotational speed

is increased for a fixed traverse speed, this is due to this region being dominated by the shoulder. However at the mid thickness and root, the width of the central plateau region is affected by increasing weld tool rotational speed due to increased energy input.

Russell and Shercliff[50] proposed a model for the characteristic hardness trace seen in friction stir welded 2014-T6 alloys based on the effects that the thermal cycle will have on the hardening precipitates. They note that when metastable precipitates coarsen on exposure to the thermal cycle, there may be a loss in strength. Close to the weld centre however, the temperature maybe sufficient for effective resolutionising to occur, with re-precipitation being possible by natural ageing after cooling (within the constraints of the cooling rate during the weld cycle). The associated strength recovery at the weld centre then contributes to the characteristic strength plateau. Further out from the weld centre temperatures are lower and coarsening (overaging) becomes the dominant effect on strength. The overall hardness profile is a balance between re-precipitation and coarsening, depending on the region of the weld. In terms of non-heat-treatable alloys Murr *et al*[2] noted that the hardness characteristics of friction stir welds in 1100 AA are a balance between: grain size, dislocation cell size, dislocation density and secondary phase inter-particle spacing. However, such effects are of a generally lower order than those due to precipitation.

As noted previously, some hardness recovery may be expected to arise from natural ageing of heat-treatable alloy welds[52]. Leonard[53] reported significant natural ageing in 2014-T651 for 5 days after welding and 7075-T651 for the first 2 months after welding. Several groups have investigated artificial post weld ageing treatments. There are

generally two types of post-weld heat treatment (PWHT) applied: these are either (a) ageing type treatments, or (b) solution treatments followed by ageing. Solution treatment of welds is not thought industrially realistic for the aerospace applications of interest to this work due to the size of components envisaged, however post weld aging treatments are thought to be possible in some cases. Most groups have reported significant hardness recovery in the weld region on PWHT, but little improvement in the HAZ region[33,73]. This is clearly a result of the resolutionising and coarsening "balance" across the weld, with the HAZ only being able to overage further during post weld treatment, i.e. no hardness recovery occurs, whilst the weld centre starts in an effectively underaged condition with little or no precipitates present after welding; it is therefore expected that this region should respond to aging[73].

Strangwood *et al*[77] also found that ageing treatments had little effect on HAZ hardness. However when they applied a solutionising treatment of 505°C for 65 minutes for the 2014-T6 friction stir weld followed by an ageing treatment the result was uniform hardness across the weld.

The majority of workers have concentrated on macroscopic hardness trends for whole welds with little information being presented on more microscopic details. Svensson *et al*[69], working on 6082-T6 friction stir welds, also noted a general hardness trace similar to that reported above (i.e. a central hardness plateau with sharp adjacent minima), however they also studied the hardness of the individual bands found within the nugget region of the weld, noting no clear difference in hardness between the bands. However Sutton *et al*[83] noted a distinct hardness variation between the bands for a 6.35mm gauge weld in

2024-T351. The high particle density (particles ≤1μm) bands (as reported in Section 2.2.4.4) were found to be harder than the low particle density bands.

2.2.5.2 Tensile Behaviour

The tensile properties of friction stir welds have been assessed by a number of workers. In general, tensile properties are found to be good in comparison with other welding techniques. Literature reports indicate joint efficiencies transverse to the welding direction in the as-welded condition as ~70-90% for a wide variety of aluminium alloy welds (including 2024-T3, 6013-T4, 6061-T6, 7020-T6, and 7475-T76[34,84]). However, whilst tensile strengths are generally good, transverse extensions to failure have been reported to be low[33,34]. It is generally agreed that, in the absence of coarse weld defects, transverse tensile tests tend to break at the minimum in hardness at the interface between the TMAZ and the HAZ[85,86]. Failure has been seen to occur at 45°, running from the crown surface, getting closer to the weld centre line at the weld root[32,60,73]; this fits with the hardness results reported in Section 2.2.5.1 where the hardness minimum was seen to be closer to the weld centre at the weld root than the weld crown surfaces. The particular loss in ductility of transverse weld specimens may be linked to strain localisation into the soft region of the weld[60,70]. Mahoney *et al*[32] demonstrated this for a friction stir weld in 7075-T651; their results are shown in Figure 21. It is clear that the effective gauge length of the specimen is then reduced for the welded specimens and hence a low nominal elongation results.

Longitudinal tensile tests carried out by Mahoney *et al*[32] found that the weld nugget region of a 7075-T651 weld had higher UTS than the overall transverse tests. The extension to failure was found to be greater than for parent plate tests. This was also found for welds

in 6061-T6 and 7020-T6 tested by Stombeck *et al*[34]. These increases are probably a result of the unusual temper condition found in the weld region and the absence of a dislocation structure. The elongation in the nugget of 2024-T351 weld has been reported to be comparable to parent plate[34]. Micro tensile testing has shown that the tensile properties closely follow the hardness traces, with dips in strength coinciding with the minima in hardness, as would be expected[34,70].

As noted earlier several groups have experimented with the effect of post welding heat treatments. It has been found that post weld aging may reduce the transverse tensile strength of welds and has a detrimental effect on elongation[32,33]. This is not unreasonable; since the TMAZ/HAZ interface region shows little or no recovery after ageing whilst the material surrounding may recover in strength, potentially enhancing strain localisation effects. Magnusson and Källman[84] found that when a friction stir weld in 7475-T76 was resolutionised and then subsequently aged, some weld strength recovery was achieved (heat treatment details not given). This is not surprising as hardness results noted for 2024-T6 welds in the previous section show a uniform hardness distribution after solution treatments[73]. Magnusson and Källman[84] found 2024-T3 weld samples did not show an improvement in strength, however the failure location did move closer to the weld centre line and the fracture surface morphology changed due to the coarsening of the grain structure that resulted from the heat treatment. Such potential interactions between post weld heat treatment and grain structure may of course be seen as a potential complication to any proposed resolutionising of friction stir welds.

2.2.5.3 Fatigue in Friction Stir Welds

Before discussing friction stir weld fatigue results it is necessary to introduce general concepts relating to fatigue. Basic elements of related fracture mechanics are also noted in Appendix 1.

- ***Fatigue Crack Propagation***

A key assumption in the use of linear elastic fracture mechanics when applied to fatigue (and indeed any fracture process) is that similitude applies. Similitude occurs when the crack tip conditions can be uniquely defined by the stress intensity factor. It does not strictly take into account any load history effects, and/or the effects of crack closure (see below). Figure 22 is a plot of typical fatigue crack growth rate data, as conventionally plotted against ΔK, where $\Delta K = K_{max} - K_{min}$ (K_{max} is the maximum applied stress intensity factor and K_{min} is the minimum applied stress intensity factor). The graph shows three distinct regions of crack growth. There is a notional linear portion of the growth curve in region II. The growth in this region is described by the well know Paris Law:

$$\frac{da}{dn} = C\Delta K^m \qquad \textbf{Equation 2}$$

Where C and m are both scaling constants dependent on material, microstructure, loading frequency, testing environment, and R-ratio (i.e. K_{min}/K_{max}).

From Figure 22 it may also be seen that there is a threshold value in region I where the crack driving force (i.e. ΔK) falls below a critical value for growth to occur. It is also evident that the growth rate accelerates towards K_{crit} (the "cyclic" fracture toughness) in region III.

- ***Crack Closure***

The discovery of crack closure is commonly attributed to Elber and may be seen to compromise the fundamental notion of similitude. He argued that premature contact between fatigue crack faces may result in a reduction in cyclic crack driving force. From this an effective stress intensity factor can be defined,

$$\Delta K_{eff} = K_{\max} - K_{cl} \qquad \textbf{Equation 3}$$

where K_{cl} is the stress intensity factor when the two crack faces first contact. The assertion here is that if crack faces contact prematurely during unloading, the crack tip does not experience the full cyclic 'damage' of the applied loads. Elber obtained experimental evidence for the incidence of closure via displacement gauges attached to the crack wake. The incidence of closure was rationalised in terms of plastic stretching in the crack wake due to propagation having occurred. This leads to a modification of the Paris law (c.f. equation 21),

$$\frac{da}{dN} = C\left(\Delta K_{eff}\right)^m \qquad \textbf{Equation 4}$$

Since Elber's original work, many mechanisms for crack closure have been suggested, however for aerospace applications Plasticity Induced Crack Closure (PICC) and Roughness Induced Crack Closure (RICC) have been generally identified as being most significant. A basic analysis of each mechanism can be found in Suresh[88]: the key points of the two relevant mechanisms are given below.

Plasticity Induced Crack Closer (PICC)

When a crack grows under cyclic loading in a ductile material, the material at the crack tip undergoes plastic deformation. Despite the reverse plastic deformation that occurs when

the specimen is unloaded, there will still be some remaining plastic deformation at the crack tip, i.e. crack tip blunting. When on subsequent cycling the crack tip advances, the plastically deformed material forms the crack wake, resulting in an effective reduction in crack opening which can lead to premature crack closure, as seen in Figure 23.

Roughness Induced Crack Closer (RICC)

This may be considered to result from fatigue cracks growing in a ductile material where the crack path is deflected, and permanent shear occurs (due to local mixed mode displacements). This leads to an offset between the asperities on opposing faces. Hence on unloading the surface can come into contact under a tensile load, see Figure 23. Walker and Beevers first identified this mechanism when studying fatigue crack growth in titanium. This mechanism is commonly judged to have more influence on low *R*-ratio/near threshold growth where crack opening levels are low, and is more pronounced where a large grain size is present (due to increasing surface asperity sizes and propensity for planar slip).

- ***Short Crack Fatigue***

Much of the early work on the growth of fatigue cracks was concentrated on relatively large cracks, with the initial component or test piece of interest containing a macroscopic flaw, and hence LEFM can readily be applied. A significant body of literature from the 1980s however identified that growth rates characterised in "large" cracks via LEFM methods, significantly under-predicted growth rates seen for cracks approaching the microstructural scale of typical metallic alloys (dimensions below 1mm). This so-called "short crack" effect has been identified with a variety of physical causes, a number of which are considered below.

Definition of short cracks

There is no precise definition of what constitutes a short crack, however some clarification of the term "short" may be made as follows:

1. A fatigue crack that is comparable in length to the microstructural features such as grain size may be defined as a *microstructurally small crack.*
2. Cracks on a smooth specimen for which the near tip plasticity is comparable to the crack size, or cracks that are fully engulfed by the plastic strain field of a notch, can be defined as *mechanically small cracks*.
3. Fatigue cracks which are large compared with the micro-structural features and the local plasticity but less than 1-2 mm in length may be seen as simply *physically small cracks*.
4. Cracks that would normally be analysed using linear elastic fracture mechanics but exhibit anomalies in propagation rates below a certain crack size as a result of the dependence of environmental effects on crack dimensions, may be referred to as *chemically small cracks*.

Various other authors have reported on conditions where crack size effects may arise[87,88,89], depending upon material, load conditions and microstructure. Depending on the physical mechanism, the main issue may be identified with small cracks which propagate at a rate that cannot be predicted from 'normal' (large crack) LEFM based test data, i.e. they do not fit the similitude requirements of LEFM for cyclic loading. As stated before, for LEFM to be applied, there must be limited plastic deformation, such that the elastic singularity dominates crack tip behaviour. It has been reported that the plastic zone

size should be less that 1/50 of the crack length; this places an upper bound below which LEFM cannot be applied.

A common feature of short cracks is the incidence of arrests in growth that may occur prior to the transition to the long crack regime, as shown in Figure 24.

Many microstructural features are seen to affect the propagation of short fatigue cracks, such as grain boundaries and the presence of shearable or non-shearable particles.

- ***Fatigue of Friction Stir Welds***

The fatigue life of as-welded friction stir welds (no heat treatment and no surface machining) has been shown to be relatively poor compared to the parent plate. Bussu and Irving[25] (tension-tension loading, R=0.1) for example reported a 50% reduction in stress range (for a given fatigue life) compared to parent plate for 2024-T351 welds in 6.35mm gauge plate in both the longitudinal and transverse direction in the as-welded condition. The initiation sites were linked to surface stress raising features left by the welding process. Longitudinal specimens failed from the curved marks left on the weld surface by the tool shoulder. Initial growth following these marks, while the transverse specimens failed from 20-70μm oxide particles located within the over lap of the weld toe. Magnusson and Källman[84] also produced transverse fatigue life time data for friction stir welds (tension-tension testing, R=0.1) for a range of alloys (2024-T3, 2mm gauge, 6013-T4, 1.6mm gauge and 7475-T76, 2mm gauge). They compared the fatigue life of the friction stir welds to two sets of parent plate results with different stress concentrations (Kt =1 and Kt=2.5 (open hole)). The as-welded friction stir weld fatigue results were all found to be below the Kt=1.0 parent plate data, but above the Kt=2.5 curve. Both the

2024 and 7475 weld results were closer to the Kt=2.5 data than the Kt=1.0, while the 6013 results were approximately halfway between the two. All initiations were seen to occur on the weld top surface. Shinoda *et al*[90] also found that the fatigue life of friction stir welds in 6N01-T5 (Japanese grade) were below the parent plate values but were better than Metal Inert Gas (MIG) welds and Laser Beam welds in the same alloy.

Ericsson *et al*[76] found that, for 6082-T6 friction stir welds with the surface skimmed and no heat treated, the initiation location had an effect on the fatigue life (tension-tension loading, R=0.5). Specimens with a higher number of cycles to failure initiated on the weld root surface while tests with lower cycles to failure initiated on the crown surface. The load level also had an effect on failure location: for low loads most failures occurred in the low hardness region of the interface between the TMAZ/HAZ of the retreating side of the weld, however for high load levels initiation sometimes occurred in the weld region, slightly to the inside of the retreating side of the weld. Propagation then deflected rapidly to outside the weld zone. All cracks were reported to initiate at the edge of the specimens. There is no explanation of this given, but it may be related to the residual stresses present, or to machining marks left by the milling process (the final stage of specimen preparation before testing).

Biallas *et al*[81] found that the fatigue strength of 2024-T3 friction stir welds (tension-tension loading, R=0.1) was close to that of the parent plate. Furthermore they found that increasing the rotational speed and traverse speed of the weld tool increased the fatigue life of the welds almost back to parent plate levels. This was thought to be due to the increasing weld speed increasing the distance between the hardness minima and increasing

the strength of the weld nugget region. Crack initiation for 1.4mm gauge welds was found to occur at ripples caused by the weld tool in the minimum thickness region in the centre of the weld; while 4mm welds were seen to fail at the steps caused by the weld tool shoulder at the edge of the weld zone. Since the crack initiation is over the nugget increasing the hardness in this region is thought to make crack initiation more difficult. Moving the hardness minima further out increases the hardness in the regions around the edge of the weld shoulder.

It is clear from the work reported above that the weld surface features may directly influence fatigue crack initiation[25,84]. It is therefore not surprising that surface skimming of the weld surface before testing may influence the fatigue life. Bussu and Irving[25] skimmed both weld surfaces (root and crown) by 0.5mm, removing surface geometrical features. The resultant fatigue lives (tension-tension loading, R=0.1, 2024-T351) are shown in Figure 25: the weld fatigue lives are significantly improved and are in fact comparable to the parent plate. As noted earlier, crack initiation for transverse samples was reported to occur at near-surface oxide particles (20-50μm), trapped by the welding process. Longitudinal samples failed in the parent plate well away from the weld. It is interesting to note the identified cause of the initiation in the transverse samples (i.e. from trapped oxides) is perhaps unexpected, as little other evidence for large oxide particles within similar alloy welds has been reported, although this may be due to microstructural investigations concentrating on material deeper into the plate rather than near the weld surface. The studies of Magnusson and Källman[84] found that surface skimming by 0.1-015mm returned 6013-T4 and 7475-T76 friction stir welds fatigue performance to levels close to parent plate levels. Equivalent assessment of welds in 2024-T3 however showed

less significant recovery in properties. For all of the 6013-T4 surface skimmed specimens, crack initiation was located on the crown surface; while the 2024-T3 and 7475-T76 welds showed no preference (i.e. failure was from the weld crown or root). The crown surface failure of the 2024-T3 and the 6013-T4 alloy welds all occurred either on the retreating side of the weld, or in the weld centre, while the 7475-T76 showed no preference in crown surface initiation location, however the location of the initiation does not appear to significantly affect the fatigue life of the specimens from the three alloys tested.

Ericsson *et al*[76] found that a post weld ageing treatment (185°C for 5 hours) did not improve the fatigue strength of a 6082-T4 friction stir weld above that of a 6082-T6 friction stir weld. It did however change the initiation location: the original T6 welds failed outside the weld region, however half of the post treated welds failed in the weld area (near the centre, or half way towards, the TMAZ border on the retreating side of the weld), with the rest failing in the TMAZ or parent plate. (They do not report the mechanism for fatigue crack initiation or the effect that failure location has on the fatigue life.)

Fatigue crack growth resistance of friction stir welds has been studied by a number of workers. Dalle Donne *et al*[45](using compact tension (CT) specimens, R=0.1and 0.7 for 2024-T3 welds, and R=0.1 and 0.8 for 6013-T6 welds, tested in the T orientation) found that for low R-ratios, fatigue crack propagation rates for the welds were better than those for the parent plate at low ΔK values, as can be seen in Figure 26 for both 2024 and 6013. For higher R-ratios friction stir weld crack growth rates are very close to parent plate values. It is suggested that the residual stresses present in the weld cause the lower growth

rates via closure for R=0.1; at higher R-ratios cracks are of course less sensitive to closure, hence the residual stresses have a limited effect, see Figure 27. Dalle Donne *et al*[45] also produced data for centre cracked plates, where fatigue crack growth rates were found to be faster than the parent plate. This result was attributed to residual stress fields, as explained further in Section 2.2.6. It is also evident from Figure 26 that the defects reported in the weld root for "tool A" did not significantly affect crack growth rates.

Jata[91] used an Al-Li-Cu alloy to study as-welded fatigue crack growth rates (CT specimens, R=0.33 and 0.7, crack growth direction parallel to the welding direction and rolling direction), examining crack growth in the parent plate, in the weld centre, and growth 7mm from the weld centre in the HAZ. Both regions of the friction stir weld were seen to have better fatigue crack resistance than the parent plate, with the weld centre showing slightly better results than the HAZ. The HAZ was identified as having a compressive residual stress that pulled the crack out of the normal growth plane, accounting for the good properties. The good crack growth results in the weld region could be explained by the residual stresses, although no "explanation" is given.

Long crack growth results obtained for a 7050-T7451 weld with a post weld heat treatment of 121°C for 24 hours by Jata *et al*[33] (crack growth direction parallel to the welding direction and the rolling direction) indicated that the nugget had a worse fatigue crack resistance than the parent plate, while the HAZ had a better fatigue crack resistance than the parent plate. This was explained by closure in the HAZ region, linked to the compressive residual stresses present. The fracture surface of the nugget was examined

and found to have surface features of the order of the recrystallised grain structure, which were thought to be due to intergranular failure.

Pao *et al*[72] (using CT specimens with deep side groves to enhance constraint, R=0.1) used the same alloy and aging treatment as Jata *et al*[91] and found a similar result. The nugget had a lower fatigue crack resistance than the parent plate, which was lower than the HAZ. This can be seen in Figure 28. Pao *et al*[72] also agree (with Jata *et al*[33]) that this is the result of increased closure in the HAZ caused by the residual stress. The measured ΔK_{th} for the weld region and the parent plate was ~2MPa$\sqrt{m}$ while the ΔK_{th} for the HAZ was 5MPa$\sqrt{m}$. At high ΔK levels crack growth rates are seen to merge.

In summary; the fatigue properties of friction stir welds can be improved significantly by surface skimming the welds, to remove the surface features left by the welding process that act as stress concentration points. The cause of fatigue crack initiation in friction stir welds after surface skimming has not been fully investigated; the only mechanistic suggestion to date has been oxide particles. Post-weld heat treatments have been shown to improve fatigue properties and can change the location of crack initiation. In terms of the growth rate of fatigue cracks in friction stir welds, performance appears to be influenced by the residual stresses present and loading conditions/geometry.

2.2.6 Residual Stresses

Residual stresses are clearly a significant issue in welded structures, being developed when a body is heated unevenly and then cooled. In some senses friction stir welding may be expected to generate relatively low residual stresses due to the relatively low temperatures involved, however it is clear that this point requires experimental validation.

A number of techniques have been used to analyse the residual stresses present in friction stir welds. These include: hole drilling, cut compliance, conventional x-ray diffraction, synchrotron x-ray analysis and neutron diffraction.

Dawes *et al*[92] have used centre hole rosette strain gauging near the mid-length of welds, with the residual stresses then being determined using air abrasion drilling. This was performed on 2014-T651, 6mm gauge plate and 7075-T651+PWHT, 6.35mm gauge plate (PWHT of 220°C for 5 minutes plus re-aged at 120°C for 24 hours). The results indicated a tensile residual stress within the weld parallel to the welding direction, and a much lower compressive residual stress normal to the weld. They also found the residual stress on the crown face to be higher than the root; this is thought to be due to the increased temperature and mechanical deformation on the crown compared to the root surfaces. The residual stress in the 2014 weld was higher than the 7075 weld, but still less than 30% of the parent plate yield stresses (σ_y). The differences between the two welds were attributed to the post weld heat treatment in the 7075 (i.e. may have given some stress relief).

Dalle Donne *et al*[45] used a cut compliance method to calculate residual stresses. This method involves introducing an incremental saw cut into the plate in the desired crack plane and measuring the resulting strain (using strain gauges). Dalle Donne *et al*[45] used a saw cut parallel to the welding direction of 2024-T3 and 6013-T6 in 4mm gauge plate. The nominal weld stress distribution based on simple force balance concepts is shown in Figure 29 for the two fatigue crack coupons that were examined by Dalle Donne *et al*[45] as part of this work. The results showed that for edge cracks growing in the welding direction, the 2024 had the highest compressive residual stress at the crack tip. When a

centre crack/defect was used, the residual stresses experienced became tensile for both alloy cases.

James *et al*[93] have used X-ray diffraction to calculate the residual stresses in a 6.35mm gauge 7050-T7451 weld. There are some questions about the accuracy of X-ray measurement made on the complex microstructure developed during friction stir welding. This is illustrated by the large amount of potential error reported in James *et al*[93] results; however the general trend is important. Generally the residual stresses are low; in the welding direction there is a tensile stress in the weld, while the transverse direction stresses are reported to be compressive.

Synchrotron X-ray diffraction represents a more advanced technique and is thought to produce more accurate results than standard X-ray analysis. The only results reported using this technique has been for 6mm gauge 7108-T79 friction stir welds[94]. The results agree with other workers, in that residual stresses are generally low; the maximum stress measured in the longitudinal direction (parallel to the welding direction), see Figure 30(a), was 140MPa, which is ~47% of the σ_y for the parent plate and ~57% of σ_y for the weld region[94]. The root face residual stress was found to be roughly symmetrical, while the crown face showed a higher residual stress on the retreating side of the weld. The results also indicate that the tensile stress tapers through the thickness. The transverse (normal to the weld direction) stresses, see Figure 30(b), are relatively low. The distribution of the stresses again shows a tapering towards the root surface. The minimum longitudinal stress measured on the crown surface was a compressive value of ~50MPa; this appears to be located slightly sub-surface, ~5mm from the weld centre (on either side); corresponding to

the approximate width of the weld pin. In another report by the same group, again using Synchrotron X-ray diffraction, they suggested that the pattern of residual stresses is ~6mm wider than the shoulder of the weld tool in both directions, and is offset by 0.5mm due to the differences between the two sides of the weld[95].

The only way to obtain through thickness residual stresses from bulk specimens is to use neutron diffraction; this is also thought to be the most accurate method of calculating residual stresses (the error reported for the following results is ±4MPa). The only systematic study carried out to date on friction stir welds using neutron diffraction appear to be that of Sutton *et al*[96] for a 2024-T351AA friction stir weld in 7mm gauge plate. The largest tensile stress was found to be 150MPa in the longitudinal direction (parallel to the welding direction) on the advancing side, ~7.5mm from the weld centreline and at the plate mid thickness, see Figure 31 (the circles on the map indicate data points). The largest compressive stress was found in the through thickness direction with the minimum being -40MPa located near the root side at (-2.7mm below the plate mid thickness) at ~12mm from the weld centreline on either side of the weld. The maximum transverse stress was a tensile stress of 70MPa near the plate mid thickness; see Figure 32 (the circles on the map indicate data points). All three components of residual stress were found to be asymmetric with respect to the weld centreline. The largest residual stress gradient was found on the advancing side of the weld, this is speculated to be due to a higher thermal gradient in the region. Close to the specimen edge the residual stresses were found to be lower due to relaxation.

Jata *et al*[33] report residual stress measurements for single edge tension specimens with the longitudinal component in the direction of the weld and crack growth. Data are quoted for friction stir welds in 7050-T7451+PWHT (PWHT 121°C for 24 hours); the technique used to calculate the residual stress was not given. They found that the residual stress in the longitudinal direction was compressive on the crown surface, while the root surface had a higher compressive residual stress than the crown surface, that then became tensile ~20mm from the weld centre. The residual stresses perpendicular to the welding direction were reported to be negligible. A possible explanation for the different results is the PWHT used, however Dawes *et al*[92] also applied at PWHT and did not find the same residual stress distribution features.

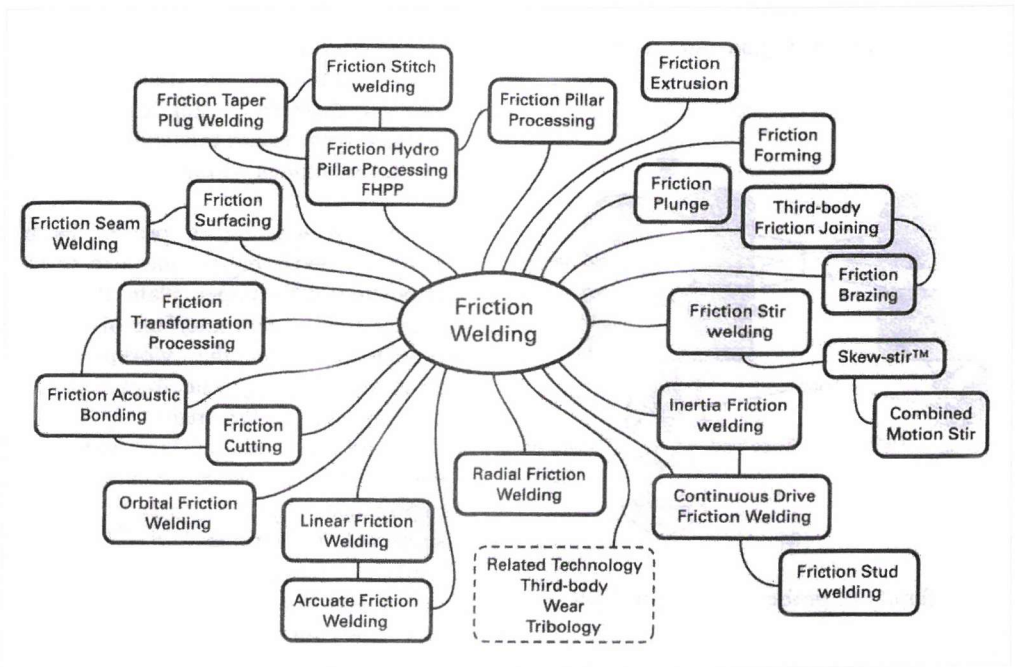

Figure 7 Friction processing technologies[17]

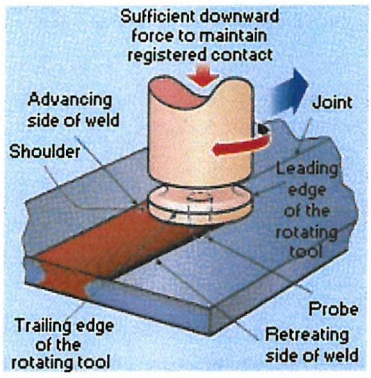

Figure 8 FSW Schematic diagram of the friction stir welding process for producing a butt joint[19].

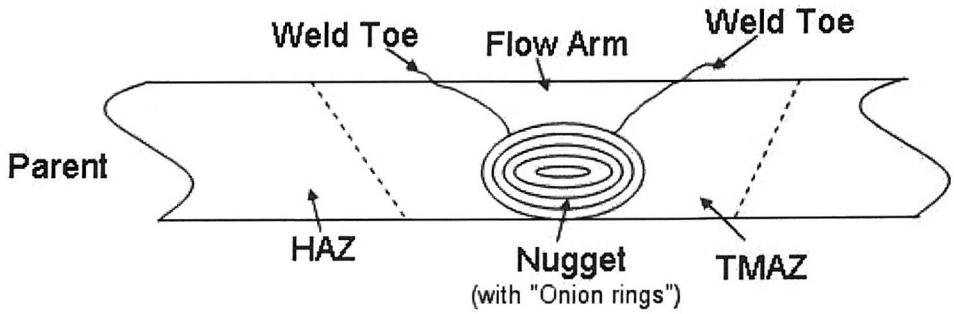

Figure 9 Schematic view of a typical FSW weld with weld zones labelled

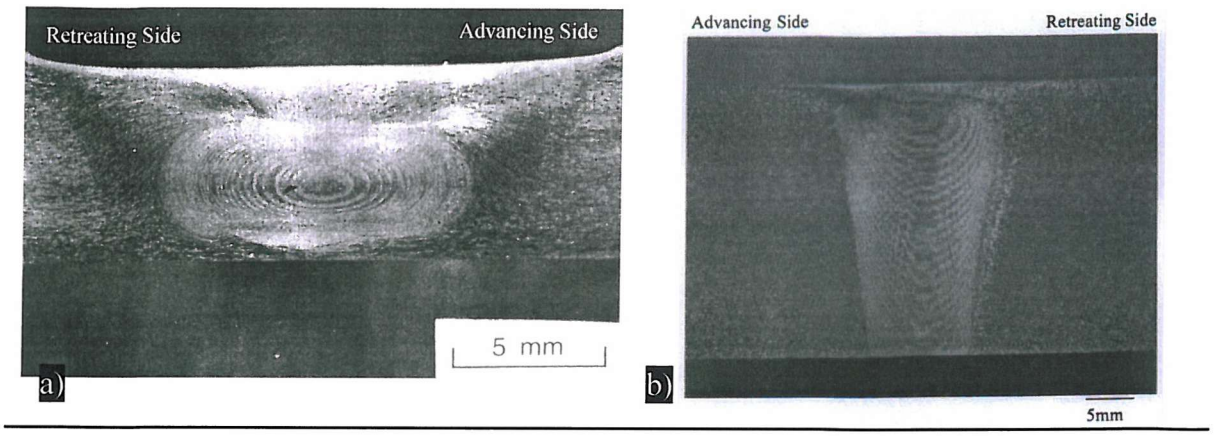

Figure 10 Nugget "onion ring" structure from; a) 6.35mm gauge, 7075-T6 weld[58] and b) 25mm gauge , 2195-T8 weld[48].

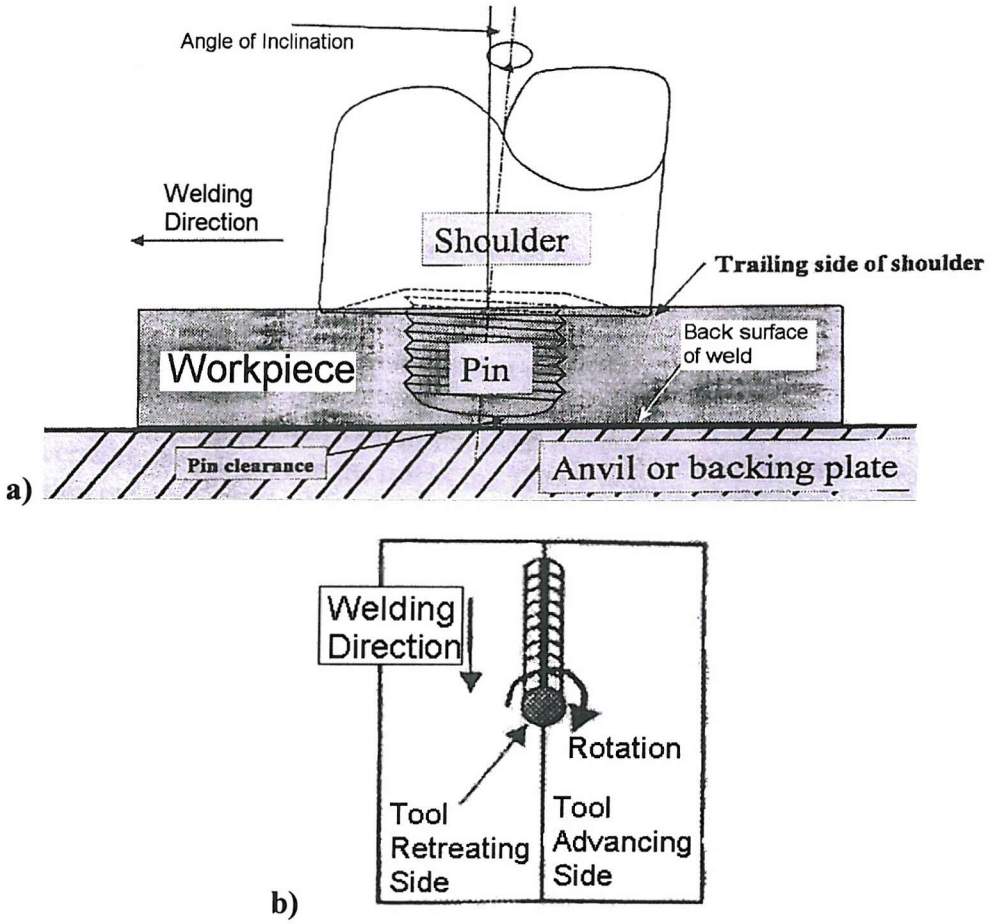

Figure 11 a) Schematic illustration of FSW process and b) associated terminology[35]

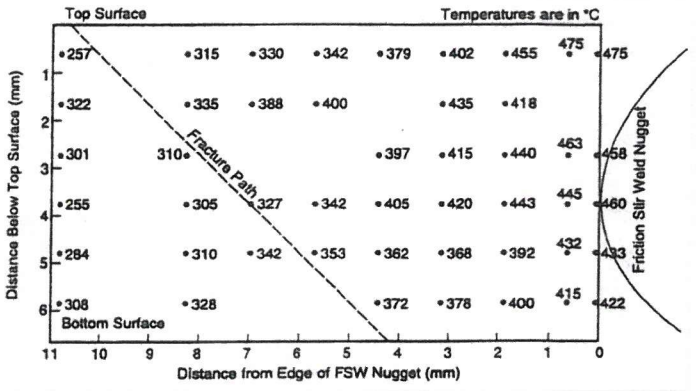

Figure 12 Peak temperature distribution adjacent to a friction stir weld in 7075-T651[32]

a)

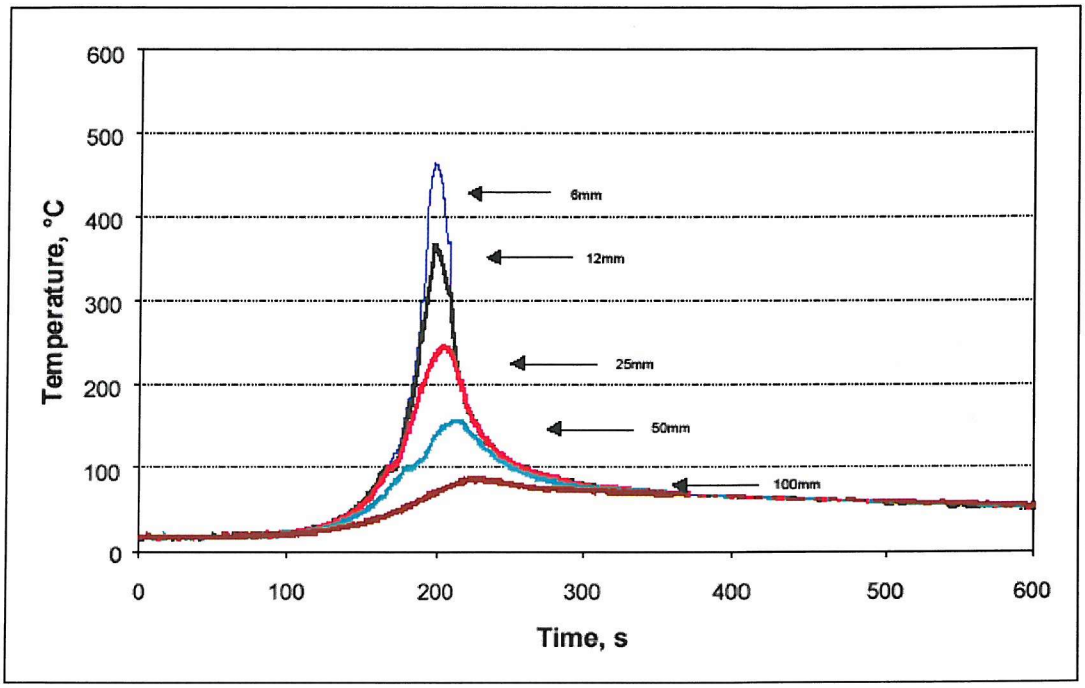

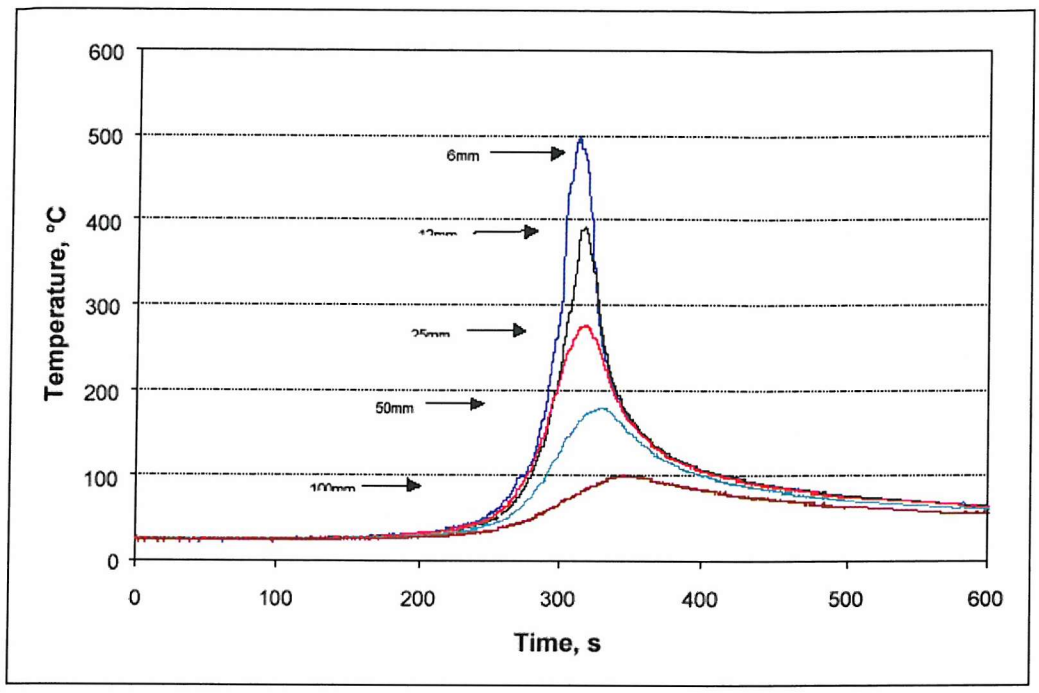

b)

Figure 13 Temperature distribution during friction stir welding of; a) 2014-T651 and b) 7075-T651. Curves relate to distance from the weld centreline.[53]

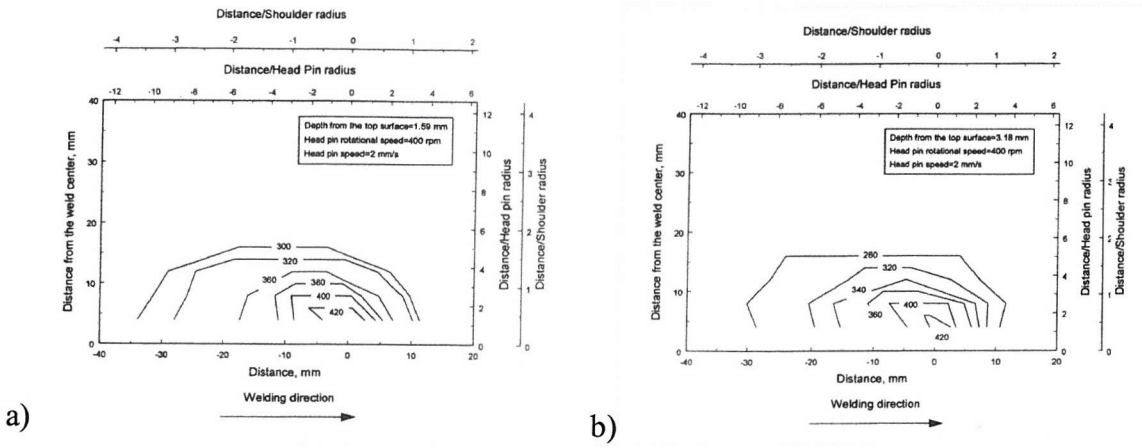

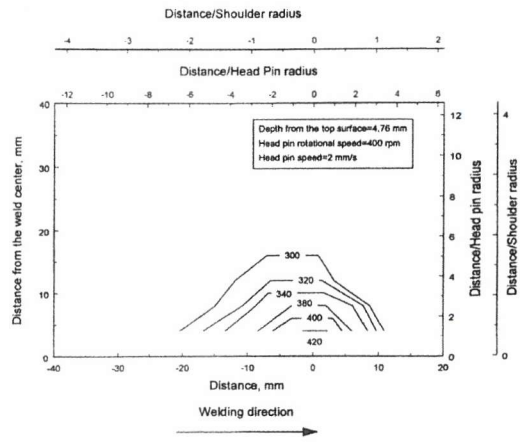

Figure 14 Isotherms at different depths below the work piece surface: (a) depth = 1.6mm, (b) depth = 3.2mm and (c) depth =4.8mm[52]

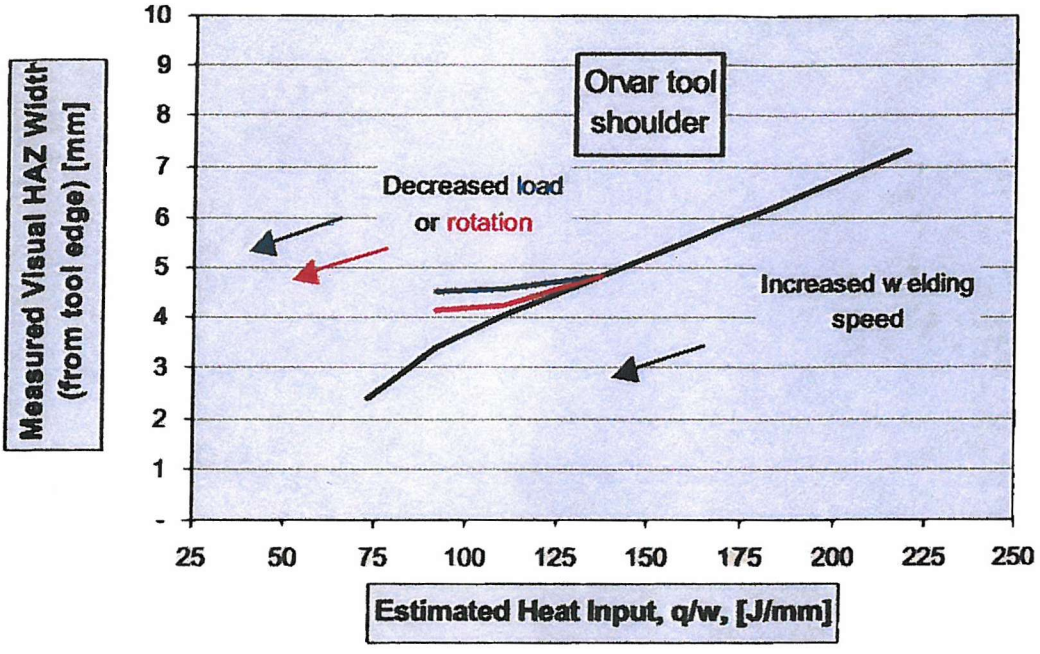

Figure 15 Effect of varying weld parameters on heat input vs. measured visual HAZ width, Orvar (hot work tool steel) tool shoulder, results are shown for varying welding speed, load and rotation.[57]

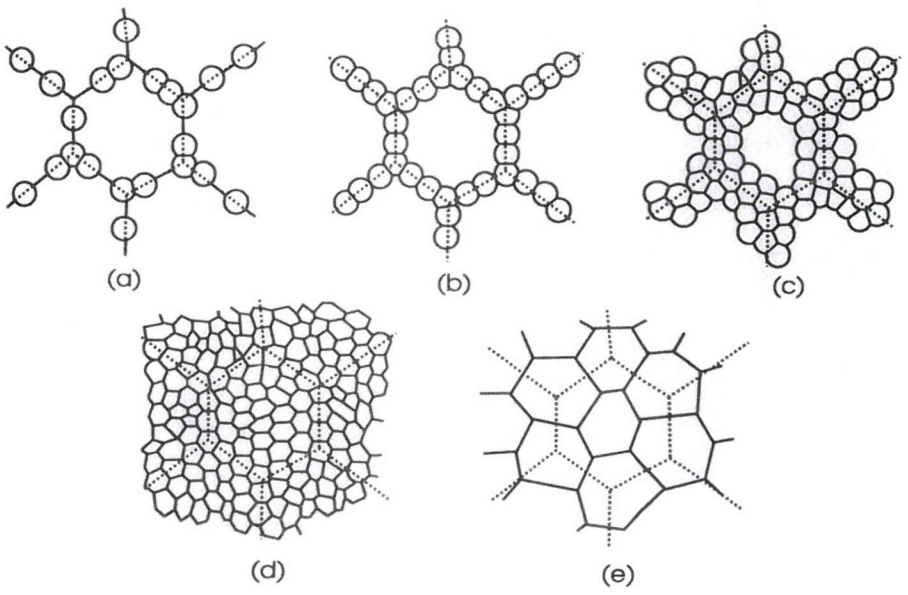

Figure 16 The development of microstructure during dynamic recrystallisation. a-d) Large initial grain size. e) Small initial grain size.

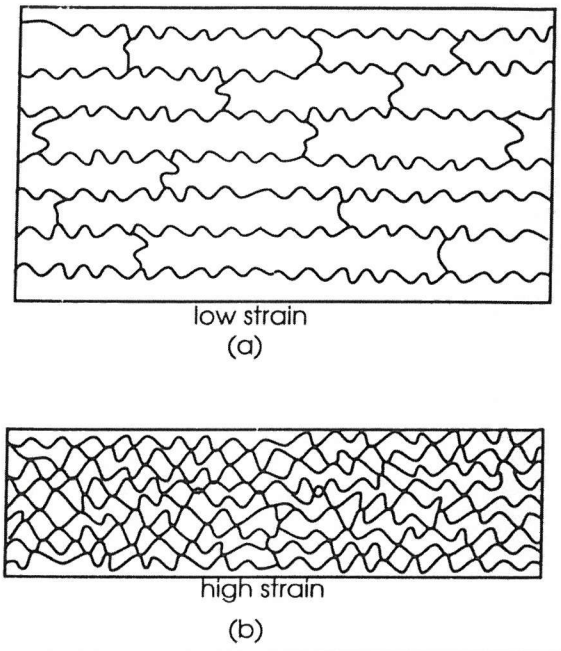

Figure 17 Geometric dynamic recrystallisation. a) Low strain. b) High strain.

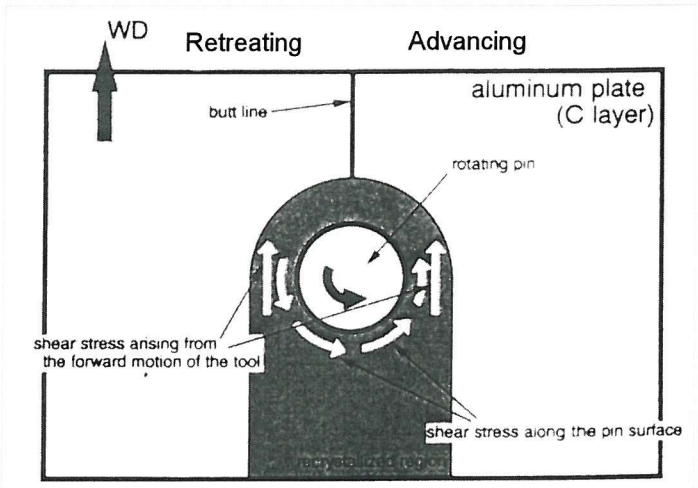

Figure 18 Schematic illustration of shear stresses induced by the forward motion of the rotating pin. Regions apart from the weld centre experience the shear stress arising from the forward motion of the tool, besides the shear stress along the pin surface[68].

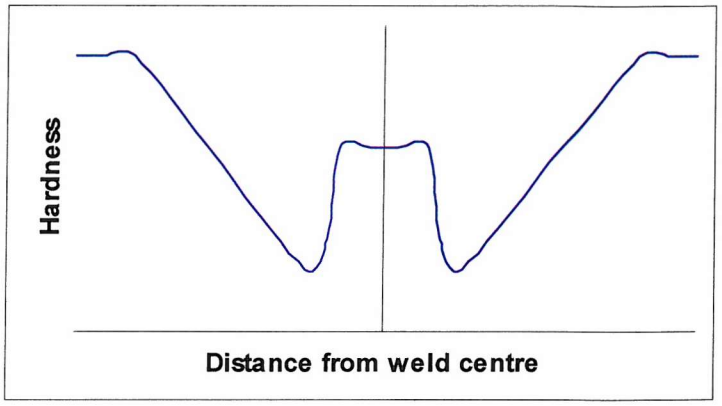

Figure 19 Schematic hardness trace for heat treatable aluminium alloy friction stir weld.

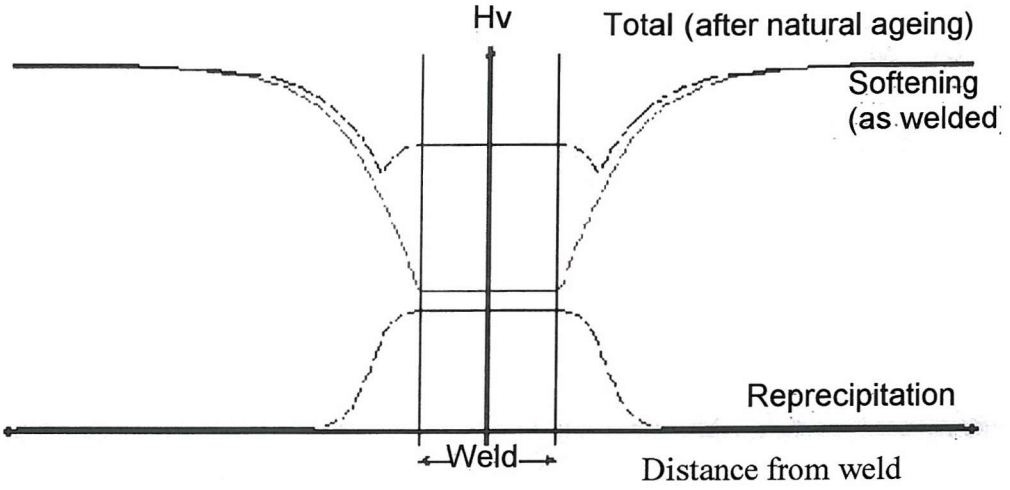

Figure 20 Suggested weld hardness trace caused by dissolution and re-precipitation. The lower trace in the figure represents the strength contribution, post-welding, due to re-precipitation of solute solutionised by the welding process. The middle trace represents softening from the parent plate condition due to coarsening/overaging, whilst the top trace represents a conceptual summation of the two effects50.

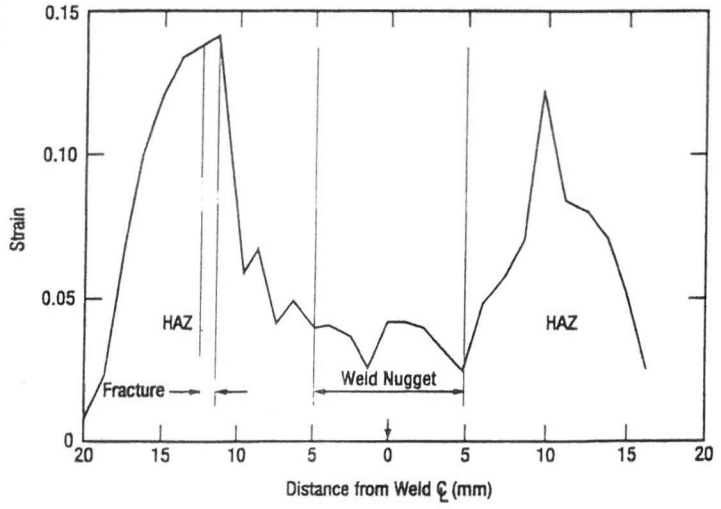

Figure 21 Tensile strain distribution within the HAZs and weld nugget of a friction stir weld when loaded transverse to the weld line[32].

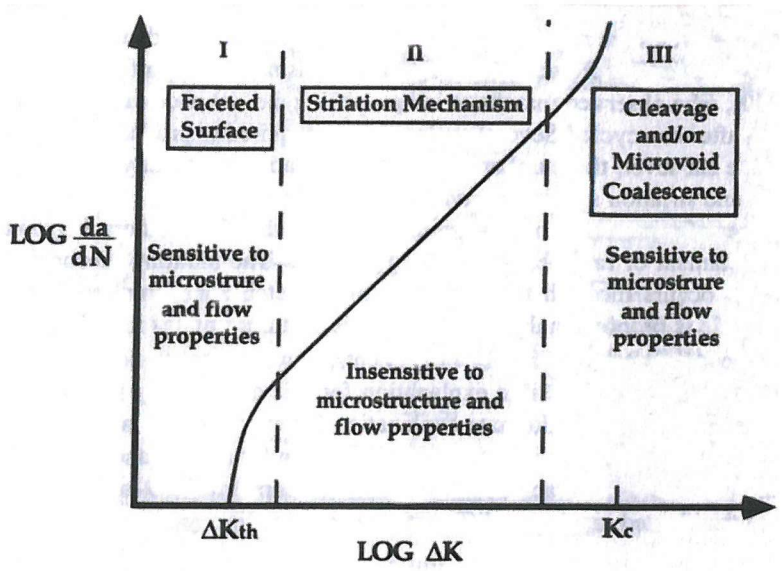

Figure 22 Fatigue crack growth regimes.[97]

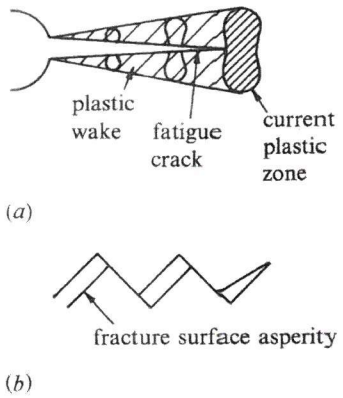

Figure 23 A schematic illustration of the mechanisms which promote retardation of fatigue crack growth in constant amplitude fatigue. a) plasticity induced crack closure: b) roughness induced crack closure.[88]

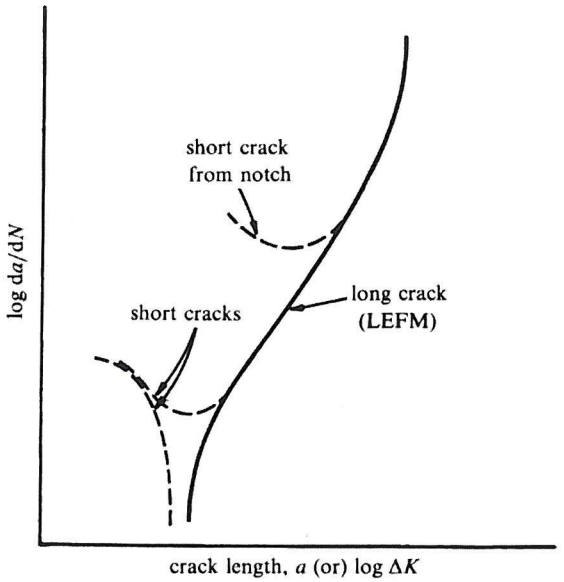

Figure 24 Schematic illustration of the typical crack growth behaviour of long and short cracks at constant values of imposed cyclic range and load ratio.[88]

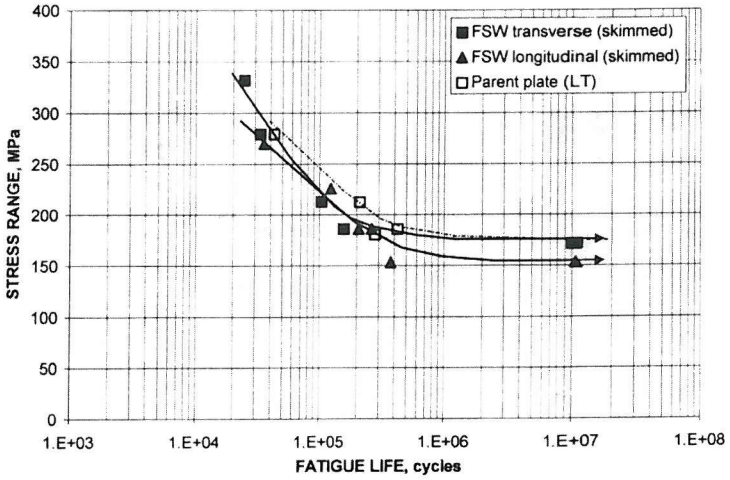

Figure 25 S-N curves (R=0.1) of parent and FSW joints in the surface skimmed condition (0.5mm from both surfaces)[25]

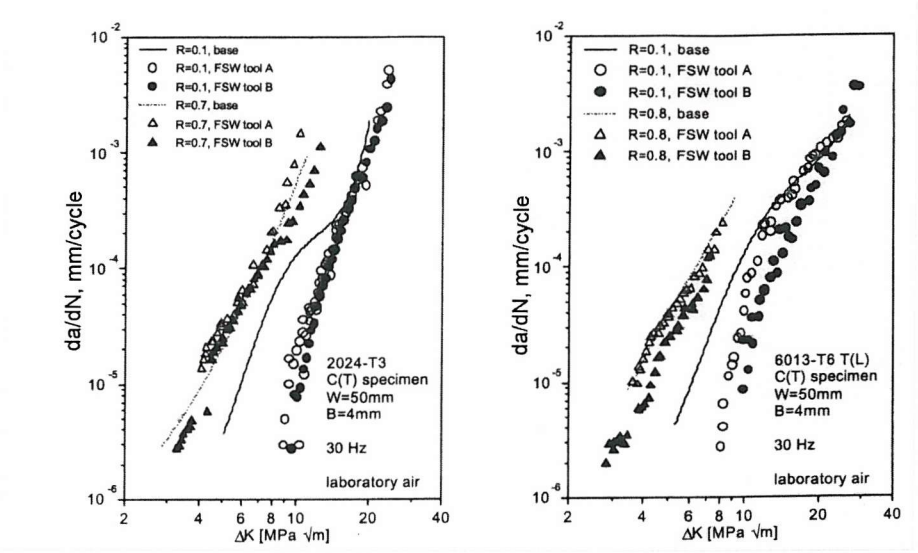

Figure 26 Fatigue crack propagation curves of joints containing pores (tool A) compared to defect free joints (tool B) and to the base materials, (C(T) specimen in 2024-T3 and 6013-T6, crack growth parallel to the welding direction and rolling direction)[45]

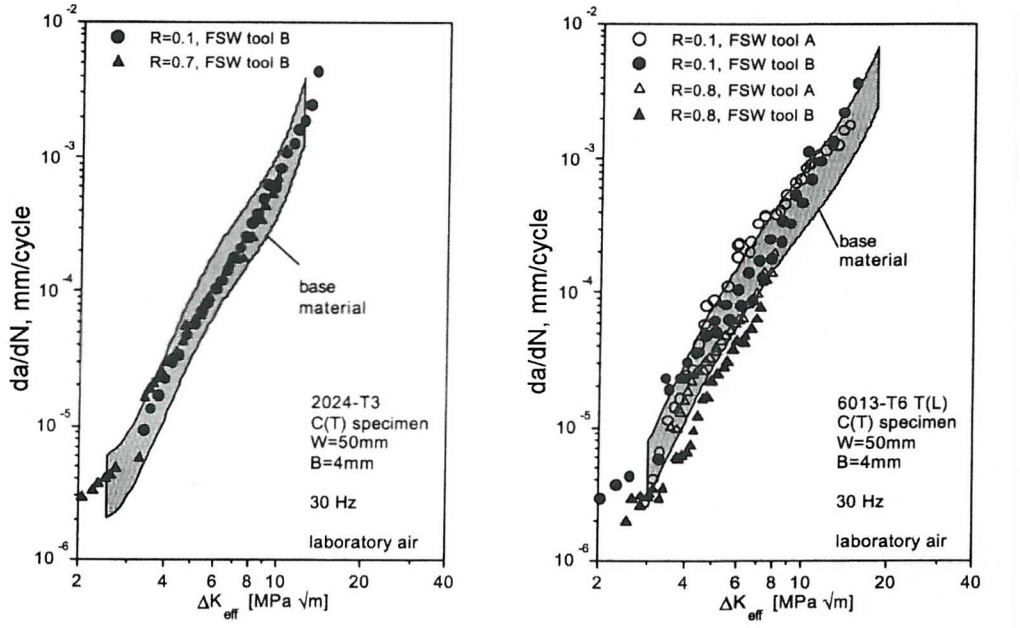

Figure 27 Effective crack propagation curves of the welded specimens compared to the base material scatter-bands, (C(T) specimen in 2024-T3 and 6013-T6, crack growth parallel to the welding direction and rolling direction)[45]

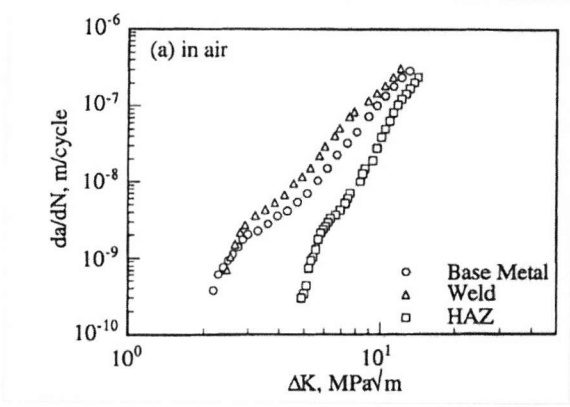

Figure 28 Fatigue crack growth in air through the base metal, weld and HAZ (C(T) specimens in the L-T orientation in 7050-T7451)[72]

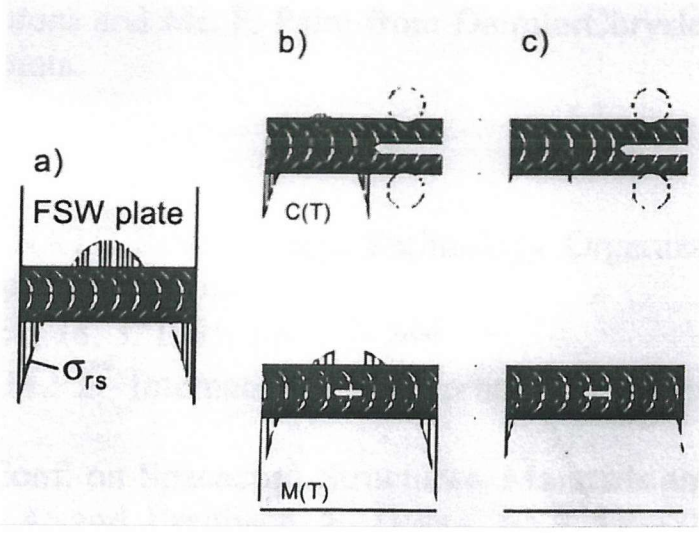

Figure 29 Schematic of residual stress distribution in friction stir welded plate a), stress re-distribution after machining of C(T) and M(T) fatigue specimens b) and during crack growth c) [45] (M(T) is centre cracked specimen.)

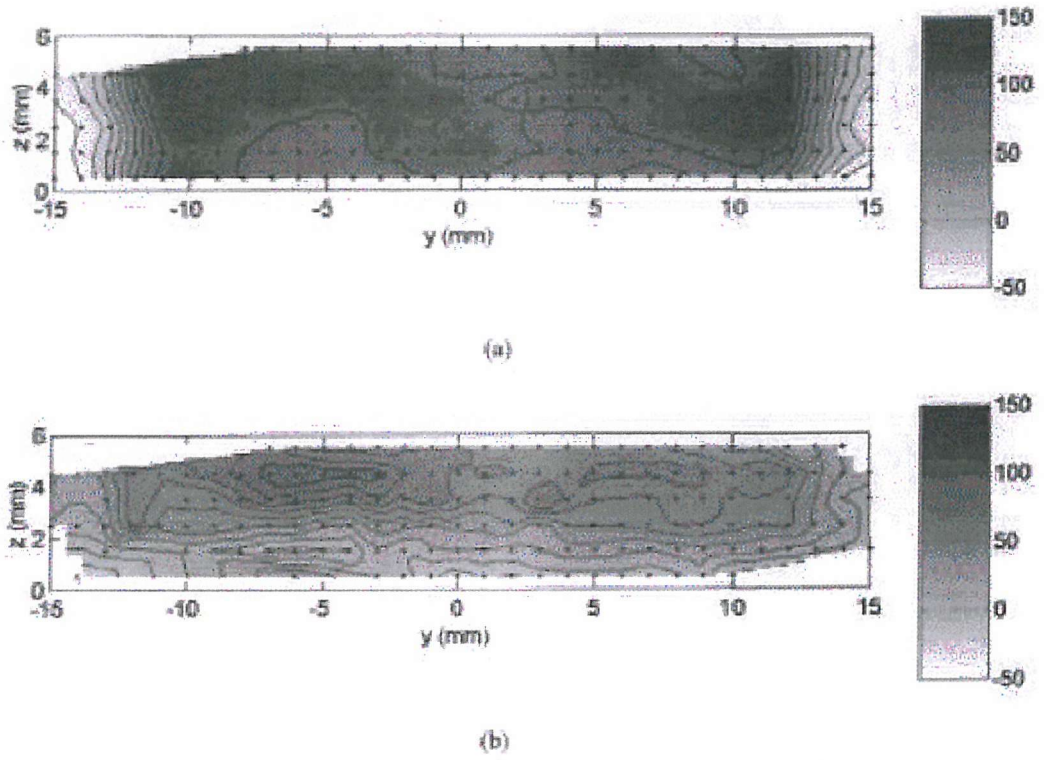

Figure 30 Residual stress contour for the FSW: (a) *Longitudinal*-orientation; b *Transverse*-orientation (units, MPa; contour intervals, 20MPa)[95]

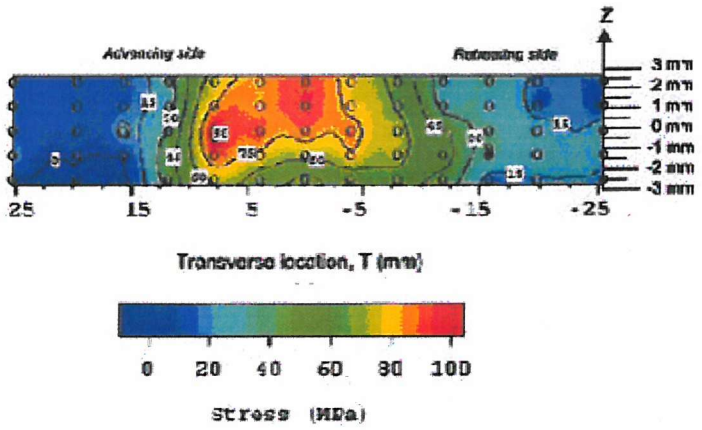

Figure 31 Longitudinal residual stress distibution[96]

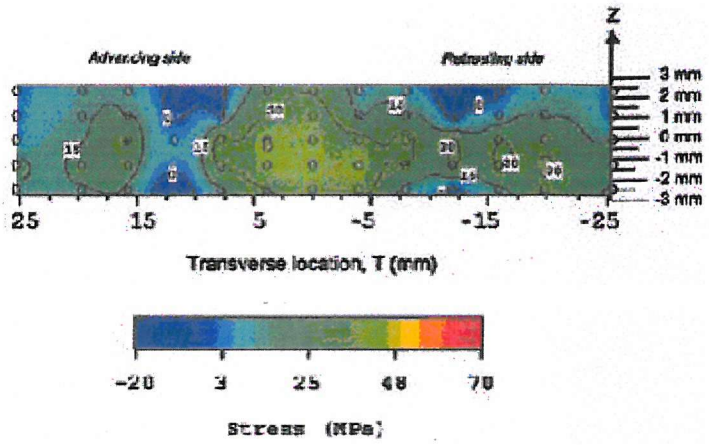

Figure 32 Transverse residual stress distribution[96]

Chapter 3: Experimental Procedure

3.1 Specimen Preparation

3.1.1 Mechanical Polishing

Unless stated, all specimens were prepared in the same way for metallographic examination. The specimens were ground using successively finer Silicon Carbide paper up to 4000 grit. This was followed by mechanical polishing with 1μm diamond paste using Struers Red lubricant, and 0.02μm OPS solution (Alumina suspension).

3.1.2 Electro Polishing

Specimens were firstly mechanically polished to 0.02μm OPS as described above. The specimens were then immersed in a 10% nitric acid in methanol solution cooled to -30°C: polishing was carried out at 30V for between 3 and 5 seconds. This technique was only used on some of the Electron Back Scattered Diffraction specimens, as a deformation free surface was required for a high quality mapping, see section 3.2.4.

3.2 Microscopy

3.2.1 Optical Microscopy

A range of optical techniques was used to analyses the microstructure of the welds and the fatigue failures. A portable handheld digital camera was used extensively for the macroscopic photographs of the fatigue failures. A Wild M420 Macroscope was also used for more detailed images of the failure surfaces and macroscopic images of the weld microstructures. More detailed optical microstructural studies were carried out using an

Olympus BH-2 microscope with a digital camera and image acquisition software. Polarising filters were also used for some of the weld microstructure imaging.

3.2.2 Electron Microscopy

High magnification analysis was carried out using a range of Scanning Electron Microscopes (SEM). (i) a Joel T300 SEM, fitted with a standard film camera and a back scattered electron detector (BEI). (ii) a Joel 6500, equipped with a digital camera, BEI detector and Energy Dispersive X-Ray detector (EDX), and (iii) a Joel 8500 Field Emission Gun (FEG) SEM, with a digital camera, windowless EDX detector, BEI detector and Electron Back Scattered Diffraction (EBSD) system (see section 3.2.4).

3.2.3 Image Analysis

Image analysis was carried out using the commercial KS300 image analysis software. Primarily this software was used to measure crack lengths on the fatigue crack replica record (see section 3.5.3). KS300 was also used to measure some of the grain sizes from the EBSD data. This was done using maximum and minimum Ferret approach measurements.

3.2.4 Electron Backscattered Diffraction (EBSD)

3.2.4.1 Principles

The EBSD process, like most bulk specimen diffraction techniques, is based on the use of Kikuchi patterns. Kikuchi patterns arise when a primary incident electron beam enters a crystal and is inelastically scattered in all directions. Some of the scattered electrons may impinge on crystal planes at the Bragg angle. This results in elastic scattering of the electrons through the Bragg angle in all directions. The result is a diffraction cone, which

extends about the normal to the reflecting planes. Each family of planes gives rise to two cones, one from either side of the imaginary source[98], see Figure 33. The Kikuchi pattern consists of pairs of parallel lines where each pair of lines is known as a Kikuchi band. Each band has a distinct width and corresponds to a distinct crystallographic plane. The bands intersect at the zone axes (pole). It is therefore clear that the Kikuchi pattern embodies all the angular relationships in a crystal, and implicitly the crystal symmetry.

The depth of penetration of back-scattered electrons is relatively high compared to secondary electrons[99], see Figure 34, this results in a relatively low number of electrons being emitted from the specimen surface, leading to a low contrast level. This can be significantly improved by tilting the specimen; this reduces the path length of the electrons, which are backscattered by the lattice planes[100]: for EBSD the sample is typically titled to between 60° and 70°.

The EBSD technique can be used with a standard SEM with the addition of a phosphor screen and a means of recording the images from this screen (either photographic film or more commonly now a low light CCD camera)[101]. However better spatial resolution is achievable using a Field Emission Gun SEM (FEGSEM).

In order to use EBSD as a technique to analysis a large number of points, an automatic pattern recognition system is required. The first stage is to extract the bands from the pattern using the Hough transform. The usual form of the Hough transform applied to lines is normal parameterisation[102], which describes the position of a line by its distance, ρ, from the origin and the direction of its normal vector, θ, (see Figure 37), with:

$$\rho = x\cos\theta + y\sin\theta \qquad \textbf{Equation 5}$$

Where ρ is the perpendicular distance from the origin

θ is the direction of the normal vector pointing from the origin

x and y are a set of pixel coordinates

Figure 38 shows how the lines are converted first to a series of sinusoidal curves, which for any given line will have a common intersection. This intersection gives rise to a high intensity peak in the Hough transform see Figure 39. The grey level value at each point in the pattern is then added to the grey level at the corresponding point in Hough space; the straight-line segments in the original image space can be identified by choosing the local maximum of the pixel intensity in the (ρ,θ) plane. Figure 39 shows an image of Hough space produced by applying the Hough transform to a real EBSD pattern where the "butterfly" contrast profiles are seen in the ρ direction of the Hough peaks, these may function as an additional recognition feature[98].

Automatic indexing of Kikuchi patterns is now available in commercial software such as Channel 5 from HKL. The ability to automatically analyse the Kikuchi patterns together with the ability for the software to control the beam position and/or the stage position enables large amounts of data to be collected and mapped automatically[103]. It is therefore possible to map the surface of the sample.

3.2.4.2 Experimental

To obtain an EBSD pattern the surface of the specimen must be free from deformation. The highest pattern quality is obtained from an electro-polished surface. Therefore the technique for electro-polishing outline in section 3.1.2 was adopted for all of the EBSD

specimens, except for those where a sharp edge was required, such as maps taken at fracture surfaces. The specimens that had a fracture surface involved were polished using the standard mechanical route as outlined in section 3.1.1, except slightly more time was taken at each stage, particularly the OPS final polishing stage.

The EBSD mapping was carried out using a Joel FEG-SEM 8500 with the HKL Channel 5 system fitted. An accelerating voltage of 20KeV was used and a probe current setting of 17-18. The specimen was tilted to 60°, the working distance was 30mm and the step size was 0.5μm. All quoted results achieve 'successful' indexing rates of ≥60%, with pattern quality maps being used as a cross reference.

When the EBSD maps of the edge views of the fracture surfaces were created, the extrapolation process used to complete the missing data resulted in some enlargement of the edge grains beyond the original fracture edge. The original crack edge was identified using the pattern quality maps and a line marking the edge of the fracture was added to the EBSD grain maps reported.

3.3 Micro Hardness Testing

All hardness testing was carried out using a Matsuzawa MHT-1 micro hardness machine with a load set to 1kg and a dwell time of 15s (unless otherwise stated). All testing was carried out on specimens polished to 0.02μm OPS finish. A limited amount of testing was carried out on lightly etched samples.

3.4 Differential Scanning Calorimetry (DSC)

In the first instance systematic Differential Scanning Calorimetry (DSC) assessment was made of the friction stir welds and surrounding materials. Firstly strips running transverse to the weld direction (with a cross section 6mm x 6mm) were machined from various locations through the depth of the specimens; see Figure 40 illustrating the location of the strips from the 13mm weld. Micro hardness measurements were carried out on the strips to identify the regions of interest. 1mm thick slices where then cut using a Buehler Isomet 4000 linear precision saw using a silicon carbide abrasive disk. Specimens were then ground using silicon carbide paper into disks 3-4mm in diameter which could be fitted into the DSC furnaces. A Perkin Elmer Pyris 1 heat compensation DSC was used with a block reference temperature of -30°C. The reference was an empty pure aluminium sample pan. In all tests a Nitrogen gas shield was used. The typical heating cycle that the specimens underwent was as follows:

- Equilibrate at 5°C
- Heat to 540°C at 10°C/min
- Cool to 5°C at 300°C/min

The curves were corrected for baseline, linear deviation and sample weight. Minor temperature compensations were also made on the basis of multiple high temperature measurements, with fluctuations of ~±3°C being noted in the DSC results. Such variations are somewhat beyond the nominal specifications of the DSC equipment, but do not have any bearing on the conclusions drawn in the present work.

A second set of DSC tests was carried out to assess the effect of a short exposure to high temperature in the parent metal. A strip of parent plate 2024-T351 was prepared in the same way as above (but without a micro hardness trace). The stages of the thermal cycle for each specimen are shown in Table 4; these were all followed by a rapid cool to 0°C and hold for 5 minutes, the cooling rates that were achieved were in excess of 200°C/min to below 300°C, the cooling rate then slowed: all specimens had reached a temperature below 200°C within 4 minutes. A normal DSC run was then performed, as reported above. The significance of such measurements will be considered in Chapter 5.

Run number	First stage	Second Stage
Parent	-	-
1	5-480°C at 200°C/min	480-490°C at 20°C/min
3	5-500°C at 200°C/min	500-510°C at 20°C/min
5	5-520°C at 200°C/min	520-530°C at 20°C/min

Table 4 Thermal cycles for high temperature exposure tests.

3.5 Fatigue Testing

3.5.1 Sample Preparation

The fatigue specimens were all cut transverse to the welding direction. The crown surface of all specimens was skimmed by 2mm to remove any weld features: this was carried out using a standard milling machine taking very small amounts of material off in each pass to minimise any residual stress that may be introduced by the deformation associated with machining.

The testing face of each of the fatigue specimens was polished using the method outlined in section 3.1.1 and lightly etched in Keller's reagent.

3.5.2 Specimen Geometry

3.5.2.1 13mm Gauge Weld

As previously stated the crown surface all specimens were skimmed by 2mm, as was the root surface to give a total specimen thickness of 9mm. The length of the specimens was 300mm, see Figure 41; this enabled the entire weld affected region to be tested. Specimens were tested with a range of widths, from 25→50mm.

3.5.2.2 25mm Gauge Weld

Again the crown surface of all specimens was skimmed by 2mm. The root faces of the specimens were skimmed by 7mm. This gave a total sample thickness of approximately 16mm in all cases. When the root faces were to be fatigue tested, the same slow machining procedure as outline for the crown surface in Section 3.5.1 was employed. The sample width varied from 15→30mm to take advantage of available material. As with the 13mm welds all samples were 300mm long, see Figure 42.

3.5.3 Testing

All tests were carried out in four point bend at 10Hz with a centre roller spacing of 90mm, with the outside rollers another 40mm beyond that, see Figure 41 and Figure 42. The applied load for each specimen was calculated using Equation 6. An Instron 8500 Plus Servo Hydraulic test machine was used for all of the tests, fitted with a 100kN load cell. For some of the tests replication was used to study fatigue crack growth rates. This was done by stopping the test at regular intervals. Pieces of acetate were softened in acetone and then pressed onto the surface of the specimen, allowed to dry and then removed. The crack length was measured on an optical microscope using the KS300 image analysis

software. The crack growth rates were established and plotted against the cyclic stress intensity factor (ΔK) where appropriate. ΔK values were calculated using the Scot and Thorpe analysis assuming a semi-circular crack profile.

$$P = \frac{\sigma B W^2}{3S} \qquad \textbf{Equation 6}$$

Where P is applied load
σ is top surface stress
B is specimen width
W is specimen thickness
S is roller span

3.6 Residual Stress Measurements

Residual stress measurements reported in this work were carried out on both fast and slow specimens from the 25mm gauge welds at the Open University. A single line of measurements were carried out transverse to the welding direction, for both the fast and slow welds, at the centre of a 30mm wide standard fatigue specimen that had been electro-polished. The measurements were carried out every 1mm along the length of the specimen using an X-ray system. The data from outside the weld region was binned (a number of points were averaged) ever 3mm to reduce the amount of noise caused by the texture present in 2024 parent material.

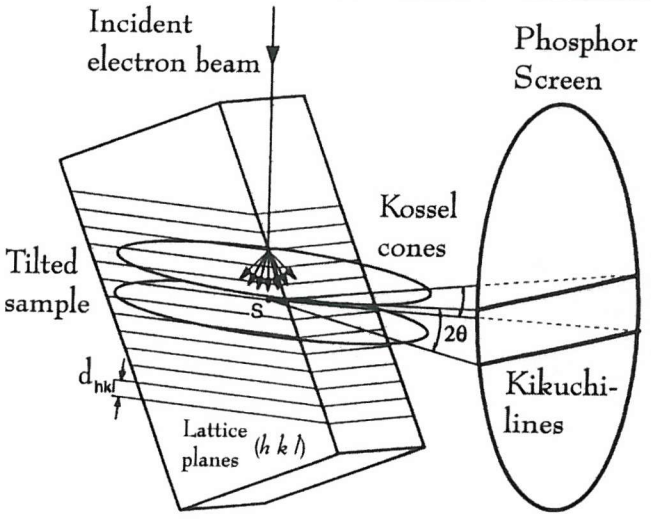

Figure 33 In-elastically scattered electrons from specimen generating Kikuchi-lines on a fluorescent screen[98].

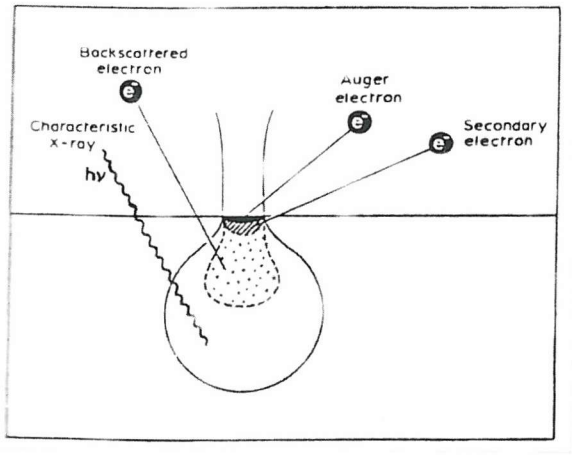

Figure 34 Schematic diagram illustrating the volume of material that is probed by an incident beam together with the volumes from which X-rays and backscattered Auger and secondary electrons emanate[105].

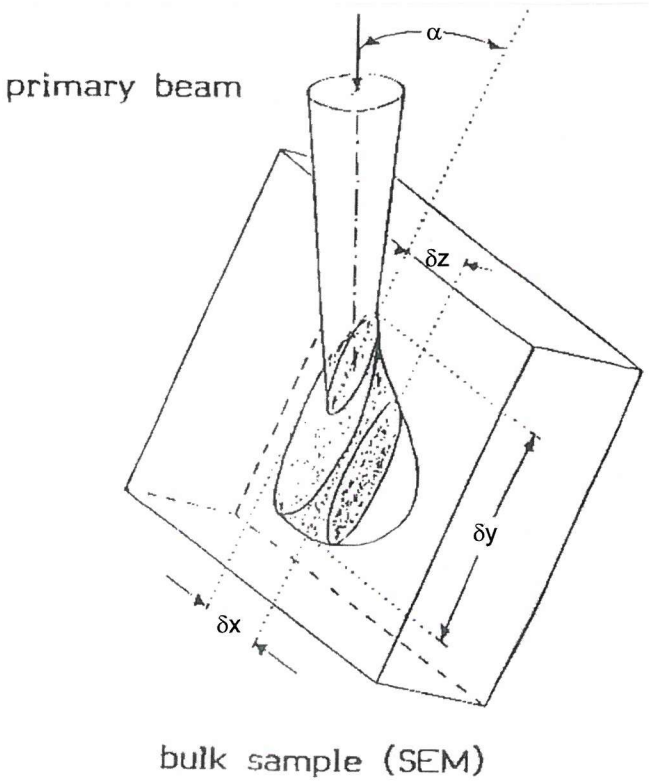

Figure 35 Schematic diagram showing the specimen-beam interaction volume in a specimen titled to 60-70° [105].

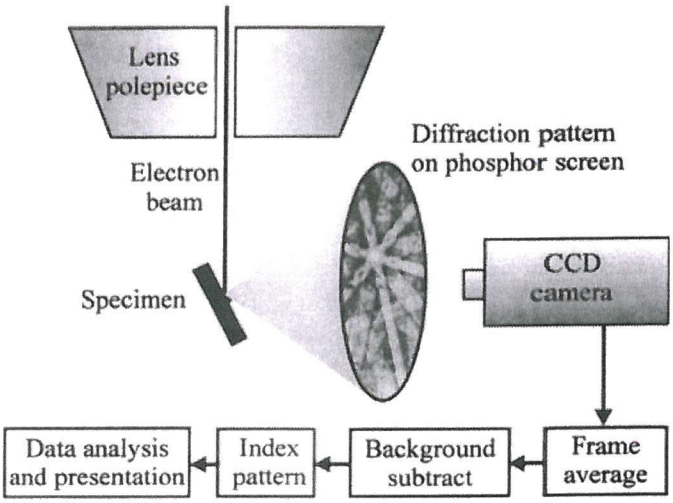

Figure 36 Schematic diagram of a typical ESDB installation[101].

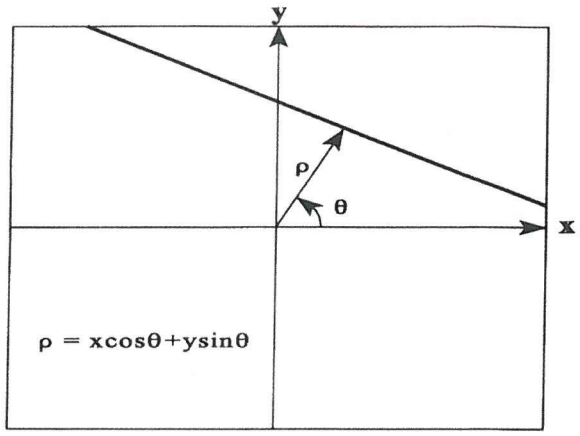

Figure 37 Illustration of the normal parameterisation of lines: ρ parameter describes the distance of the line from the origin, and θ describes the direction of the normal vector pointing from the origin to the line[102].

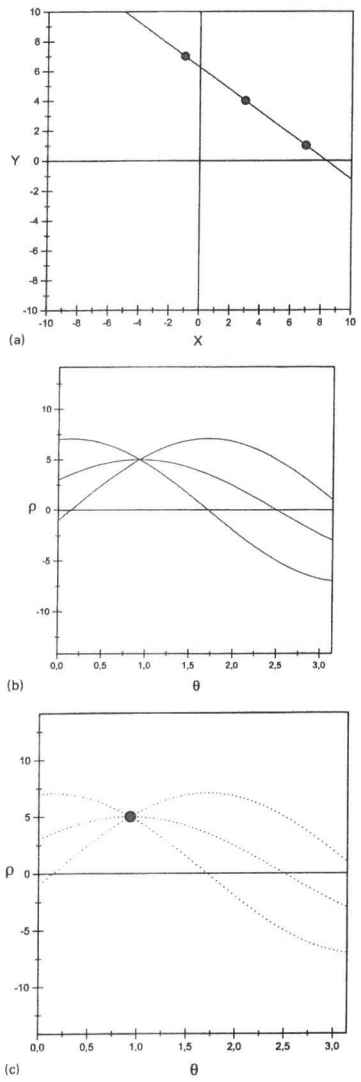

Figure 38 Principle of the Hough transform and back mapping. (a) Three collinear points in image space. (b) Each of the three collinear points in image space is mapped to a sinusoid curve in parameter space. (c) Each of the three collinear points in image space is mapped to the common intersection point in parameter space of the three (dotted) sinusoid curves[102].

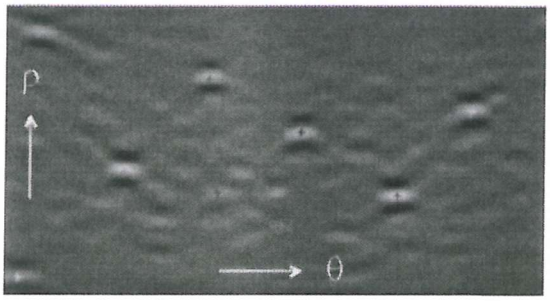

Figure 39 Hough space image of an EBSD pattern[109].

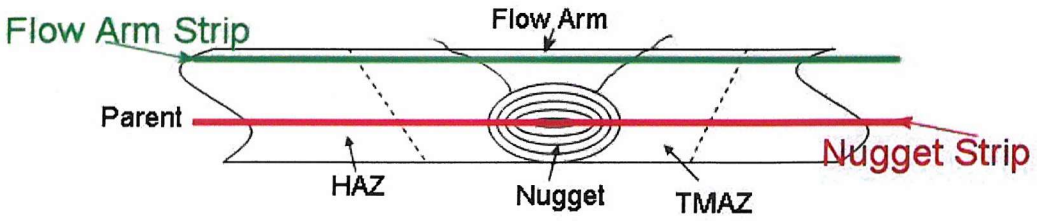

Figure 40 Schematic illustration of the location of the DSC strip specimens for the 13mm weld: Green is from the flow arm (2mm below crown surface) and Red is through the weld nugget (7mm below crown surface).

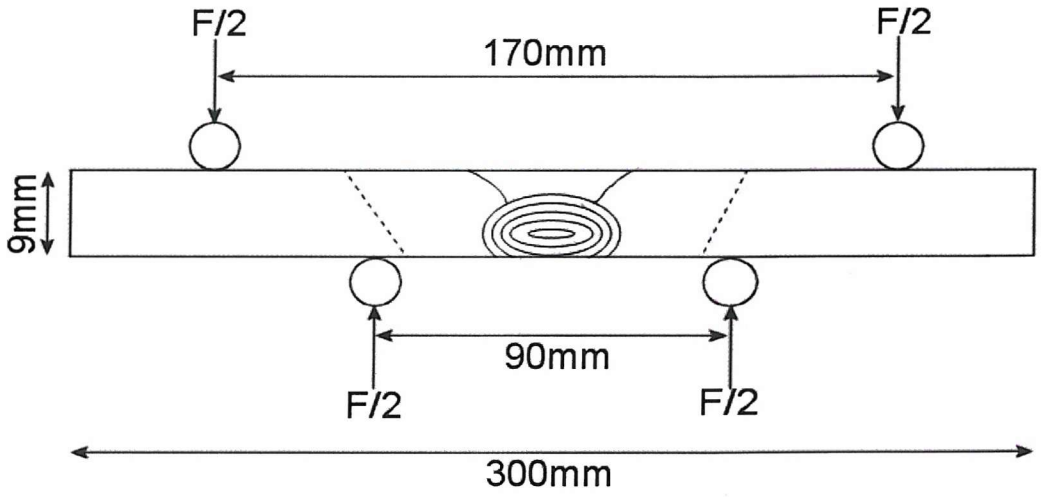

Figure 41 Schematic illustration of 13mm weld fatigue specimen.

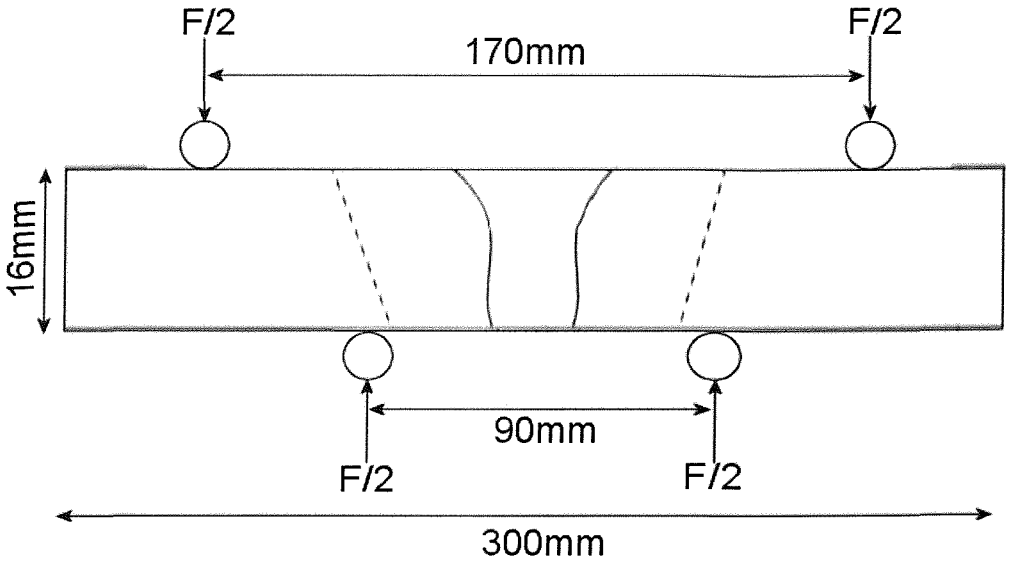

Figure 42 Schematic illustration of 25mm weld fatigue specimen.

Chapter 4: 13mm Gauge Weld

4.1 Materials

Work in the present thesis has been based on 3 batches of welded 2024-T351 plate supplied by Airbus UK. The first batch corresponded to 13mm gauge parent plate, whilst the remaining 2 batches were based on 25mm gauge parent plate. The present chapter is specifically concerned with the 13mm gauge material.

4.1.1 Macrostructure: 13mm weld

A single-pass friction stir welded panel (600mm x 300mm) of the conventional airframe aluminium alloy 2024-T351 in 13mm gauge plate form was provided by Airbus UK (Filton) in the as-welded condition, with welding being carried out parallel to the longitudinal direction of the plate. The overall transverse weld structure is illustrated by the photo-montage in Figure 43. A well defined central nugget exhibiting a distinct annular banded (or 'onion ring') structure may be seen, in keeping with various reports within the literature[58,104]. It is also possible to identify a 'flow arm' region between the nugget and the surface on which welding was carried out penetrating to a depth of ~5mm below the weld crown; it should be noted that this is deeper as a proportion of the overall thickness than seen in most of the thinner welds found in the literature[48,58].

Further out from the weld line the thermomechanically affected zones (TMAZ) and heat affected zones (HAZ) may be identified on each side of the weld. The characteristic deformation of the parent plate grain structure associated with the TMAZ region is illustrated in Figure 43 for the entire width of the weld region, and, in particular, for the

retreating side of the weld in Figure 44 (i.e. the side of the weld where the direction of probe rotation and the work piece traverse direction are opposite). In addition to the flow of the parent grain structure in and around the weld nugget that may be seen in Figure 43 and Figure 44, a small region of grain flow upwards into the weld toe may also be identified (circled in Figure 44), extending some 1 – 2mm into the main body of the plate.

4.1.2 Hardness Characteristics

Figure 45a) shows an optical macrograph of the overall weld structure, along with Figure 45b) which is a 2-dimensional hardness map of the same region at the same scale. The general outline of the weld is delineated in the hardness map, with both the weld nugget and flow arm being associated with a central plateau in hardness levels. The line traces shown in Figure 45c) correspond to individual hardness profiles through the weld nugget (near its centre) and through the flow arm (approx. 2mm below the plate crown surface). Going from the parent plate towards the weld line, both traces exhibit a small initial rise from the parent plate hardness level, which is followed by a gradual decline in hardness to a minimum either side of the weld line. There is then a steep rise in hardness to a central plateau of intermediate hardness. The hardness trace through the weld nugget in Figure 45c) shows a small but distinct dip in the central plateau region that is also evident in the weld nugget region of the map in Figure 45b). The plateau region in the weld flow arm (identified as 11mm from the weld back (or root) in Figure 45b) and c)) is wider than that of the nugget and does not show a dip. The map in Figure 45b) confirms that the slight peak in hardness at the outer edge of the HAZ is indeed consistent through the whole plate thickness.

The apparent edge of the flow arm region in the hardness traces shown in Figure 45b) does not occur at the apparent interface in the grain structure; rather it is extended out into the TMAZ. This is highlighted in Figure 46 showing a local region in the transition zone from the HAZ, to the TMAZ, to the flow arm. The hardness indents that may be seen in the micrograph show that the minimum in hardness occurs in the HAZ (below the weld toe) where the parent grain structure has essentially been retained (a mild grain rotation has occurred). The figure shows that whilst hardness levels rise sharply further into the weld, there is little or no variation in hardness as the trace passes the interface in grain structure between the deformed grains of the TMAZ and the very fine structure of the flow arm (see Section 4.1.4).

4.1.3 Differential Scanning Calorimetry: 13mm weld

Differential Scanning Calorimetry (DSC) testing was carried out at various locations across the transverse width of the friction stir welds in 2024-T351 at two depths into the material: firstly, specimens centred at 2mm below the parent plate surface (through the flow arm), corresponding to the fatigue test specimen surface (see Chapter 3), and secondly, through the centre of the weld nugget. The location of each DSC specimen is shown on the transverse hardness trace of the weld in Figure 47a) and Figure 47b) for the flow arm and weld nugget test depths respectively. In both cases position A corresponds to parent plate, B is at the slight peak in hardness seen at the outer edge of the TMAZ, C is approximately half way down the hardness drop towards the weld centre and D is at the hardness minimum immediately adjacent to the central hardness plateau. Position E in the flow arm trace (Figure 47a)) corresponds to approximately the weld centre, while in the nugget trace (Figure 47b)) position E corresponds to the peak in hardness at the edge of the nugget and position F is the actual weld centre.

Figure 48 shows the DSC curves for all of the specimens from the flow arm series of measurements. Looking at the parent plate trace (A) the general trend of the important features can be ascertained[105,106,107,108]. There is little heat flux to approximately 150°C, where there is a endothermic dip is that consistent with GPB/zone dissolution, this is followed by an exothermic peak at about 250°C which may be attributed to the formation of S-Phase. There is a long endothermic region above ~300°C corresponding to dissolution of previous phases. Finally between 500°C and 515°C there are a number of sharp endothermic peaks consistent with the onset of incipient melting.

Looking at the low temperature reactions (up to ~400°C), starting with trace B (which corresponds to the HAZ peak in hardness), a significant amount of S-phase appears to have been precipitated before the run (with a corresponding drop in zone content), accounting for the increase in hardness via a degree of artificial ageing. Trace C (located on the decrease in hardness) shows very little zone dissolution and practically all of the available S-phase appears to have been precipitated. At the hardness minimum (D) there is evidence of some GPB/zone formation, i.e. suggesting a degree of resolutionising and reageing. In the weld centre (E) there is a significant increase in the GPB/zone dissolution peak, (c.f. location (D)). It is also interesting to note a distinct split in the intermediate temperatures exotherm peak (250-350°C) whilst the origins of this effect has not been explicitly checked in this work, recent reports by Lefebvre *et al*[108], Wang *et al*[109] and Reich *et al*[110] suggest the possible formation of Ω (Al_2Cu) under slow cooling conditions in 2024 welds and bulk material, consistent with an apparent additional reaction in the present slow cooled weld region.

High temperature thermal effects are shown in Figure 49 for each position. It is clear from the figure that locations (B) and (C) are essentially the same as the parent plate trace (A) with the onset points of incipient melting occurring in the region of 504°C. However points (D) and (E) show a significant variation, with (e) particularly showing little evidence of incipient melting at the temperature shown

The low temperature DSC results for the centre of the weld nugget are shown in Figure 50. These are essentially the same as for the corresponding traces from the flow arm for positions A, B, C and D. Trace E in this case corresponds to the edge of the weld nugget at the slight rise in hardness: this trace also shows the double exothermic peak seen at intermediate temperatures in the flow arm trace in Figure 48. The weld centre (trace F) in Figure 50 does not have the double peak however it does have a relatively broad exothermic peak extending to high temperatures. The higher temperature portions of the traces are shown in Figure 51; traces B, C, and D are essentially the same as the parent plate. Both of the traces for the weld nugget region (E and F) show the same absence of incipient melting as seen in the weld centre of the flow arm material.

4.1.4 Microstructure: 13mm weld

The characteristically fine grain structures of the flow arm and weld nugget regions are illustrated via optical images in Figure 52 and Figure 53, which show typical structures identified in the flow arm and nugget regions of the 13mm gauge weld. The average grain size was estimated (using an average of the horizontal and vertical linear intercepts) to be of the order of 3-4μm for both flow arm and nugget regions, with the nugget typically showing a slightly finer structure (i.e.~3μm). In terms of the onion ring structure that was

evident macroscopically in the weld nugget (i.e. as in Figure 43), optical microscopy did not show any distinct changes in grain dimensions between the bands. Further analysis of the grain size in the nugget region is illustrated at the location indicated in Figure 54 (this was a region particularly associated with fatigue crack growth for failures over the weld region, see Section 4.2.3.2) using Electron Back Scattered Diffraction (EBSD) mapping was carried out in the FEG-SEM, with the resulting map being shown in Figure 55a) (it may be noted that ~85% of boundaries were noted to be high angle (>12°), in keeping with the results reported by Hassen *et al*[61]). Such imaging revealed no systematic grain size variation that correlated with the bands seen in Figure 43. The grain size for the region shown in Table 5 was calculated using the linear intercept method first parallel and then perpendicular to the x-axis in the figure (i.e. the transverse direction to the weld line) and then at ±45° to the horizontal axis in Figure 55a). From Figure 55a) and the results in Table 5 it is clear that the grains in Figure 55a) are aligned at approximately 45° to the transverse direction. Alignment of the structure is further highlighted when the maximum and minimum feret directions of each of the grains in Figure 55b) and c) correspond to a larger grain size than the darker regions. This variation appears to shows some evidence of patches of varying grain size, however, the scale and consistency of the bands was not obviously connected with the macroscopic onion ring bands seen in Figure 43. The EBSD results reported in Table 5 for the grain sizes taken from Figure 55a) and equivalent EBSD maps of the flow arm support the average grain size measurements reported from the optical observations, with the flow arm having a coarser grain structure than the nugget (average grain sizes via EBSD of 5.1μm and 3.1μm in the flow arm and nugget respectively).

Location	Angle to x-axis in Figure 55	Axis 1 grain dimension (μm)	Axis 2 grain dimension (μm)	Average grain size (μm)	Aspect Ratio
Nugget (Figure 55a)	0°	2.5	2.7	2.6	0.9
	45°	3.9	2.3	3.1	0.6
Flow arm	-	3.5	6.7	5.1	0.5

Table 5 Grain size taken from EBSD map at 0° and 45° to the horizontal axis in Figure 55a) for nugget and for the flow arm.

Figure 56 again shows a transverse section through the 13mm weld region, highlighting the location of the back scattered electron images (BEI) in Figure 57 indicated. Figure 57a) particularly shows the coarse intermetallic particle distribution within the parent plate. Figure 57b), c) and d) are BEI images highlighting the intermetallic particle distributions associated with various regions of the weld. Local flow clearly influences the intermetallic distribution within the TMAZ close to the apex between the nugget and the flow arm in Figure 57b), however the general scale and clustering of particles appears to be retained from the parent material. Within the weld nugget and flow arm regions significant redistribution and break up of the parent particles is evident, particularly in Figure 57c), corresponding to the flow arm.

Backscattered electron imaging at higher magnification particularly identifies the presence of micron-scaled particles in the weld material, see Figure 58. The local distribution/content of particles was seen to vary significantly (compare Figure 58a) and b)), with some regions showing significant evidence of grain boundary decoration, whilst others are relatively particle free. Figure 59 shows a typical etched macroscopic transverse section of the weld nugget region, together with a conventional SEM image of a similarly etched material taken on the advancing side of the weld close to the top of the

nugget, as indicated in the macroscopic image. The SEM image shows distinct local etching differences that were seen to correlate with the macroscopic banding/onion rings. It is evident in the SEM image in Figure 59 that there was a significant variation in the degree of intragranular attack associated with the etching of the microstructure, with most intermetallics appearing to lie on the more heavily etched region of the image. A more detailed study of un-etched and etched specimens was carried out in the FEG-SEM, as illustrated in Figure 60 and Figure 61. The location of Figure 60a) was close to the advancing edge of the weld nugget, approximately level with the nugget centre, with the location of the subsequent images in Figure 60 being marked in Figure 60a). Coarser intermetallic particles are marked in Figure 60a): these are commonly seen to be Fe and Mn containing, presumably remain from the parent intermetallic population. A band in the particle distribution is clearly evident in Figure 60a); in particular, a band of reduced intermetallic content is seen to run vertically, slightly to the left of centre in the image. At higher magnification (Figure 60b) and c)) the presence of fine (≤0.5μm) evenly dispersed intragranular particles is noted in Figure 60b), whilst in Figure 60c) more coarse (~1-2μm) intergranular particles are evident given the scale and morphology of these particles, and their apparent composition (EDX indicates the intergranular particles at least are Cu and Mg rich) these particles are presumed to be precipitates from the weld thermal cycle (probably S/S`, with the present DSC results and the results of Lefebvre *et al*[108] suggesting the possible presence of θ`/Ω phase). Figure 61a) shows the same region as that shown in Figure 60a), etched with Keller's reagent. It was noted that distinct intragranular attack takes place in the central region/band, consistent with preferential etching of the fine particles. Overall it was noted that the macroscopic onion ring structure of the nugget region was closely associated with these local variations in intergranular and intragranular

particle content, with those regions that appear dark in macroscopic images (such as Figure 43) being associated with an increased incidence of the intragranular particle bands and their associated intragranular etching when treated with Keller's reagent.

4.1.5 Summary

From the work reported above it is clear that the weld macrostructure studied in the present work is comparable to many friction stir welds reported in the literature for thinner gauge heat treatable aluminium alloys in that a banded weld nugget is evident, along with the presence of flow arm and TMAZ regions. It has been shown that the grain structure in the weld nugget is reasonably fine, with a grain size of ~3μm, with limited grain elongation parallel to the onion ring bands. No significant change in grain size was associated with the onion ring banding. It has been noted that the intermetallics within the nugget (and flow arm) were much reduced in size and redistributed compared to those of the parent plate, and there is evidence of systematic variation in both size and nature (intergranular versus intragranular location) of the fine intermetallic particles that are associated with the onion rings of the weld nugget. The hardness traces show the expected hardness distribution for a friction stir weld in a heat treatable aluminium alloy, with a central plateau and a minima on either side.

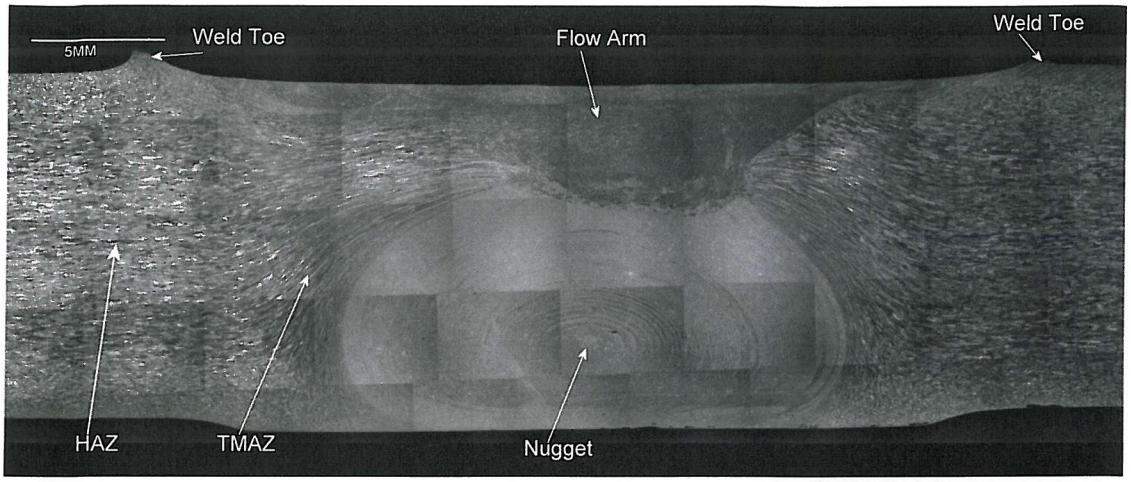

Figure 43 Optical macrograph of friction stir welded 13mm gauge 2024-T351 plate (etched and viewed in crossed polarisers).

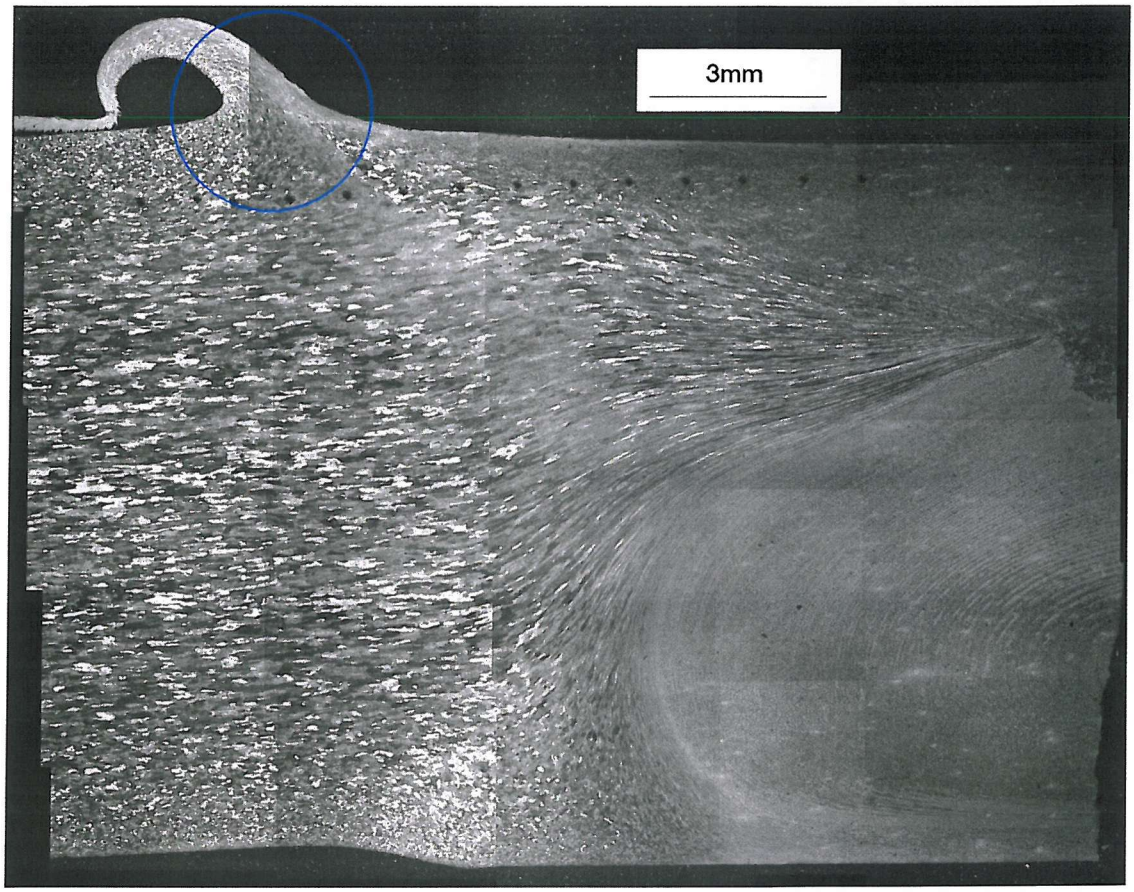

Figure 44 Optical micrograph of the retreating side of weld; circle highlights upward grain flow into weld toe (etched and viewed in crossed polarisers).

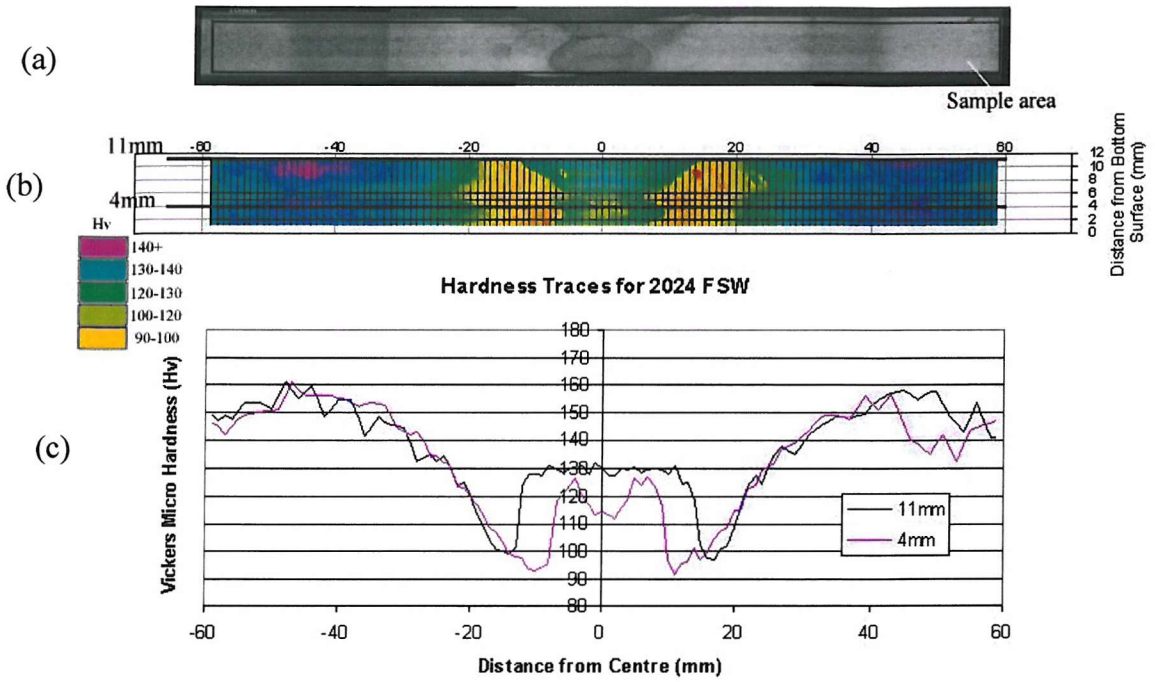

Figure 45 Hardness characteristics for 2024-T351 friction stir welded plate: (a) optical macrograph, (b) hardness map plotted to same scale as (a), and (c) hardness traces at 4 and 11mm from parent plate base, corresponding to traces through the centre of the weld nugget and the flow arm regions respectively (trace positions are highlighted in (b)).

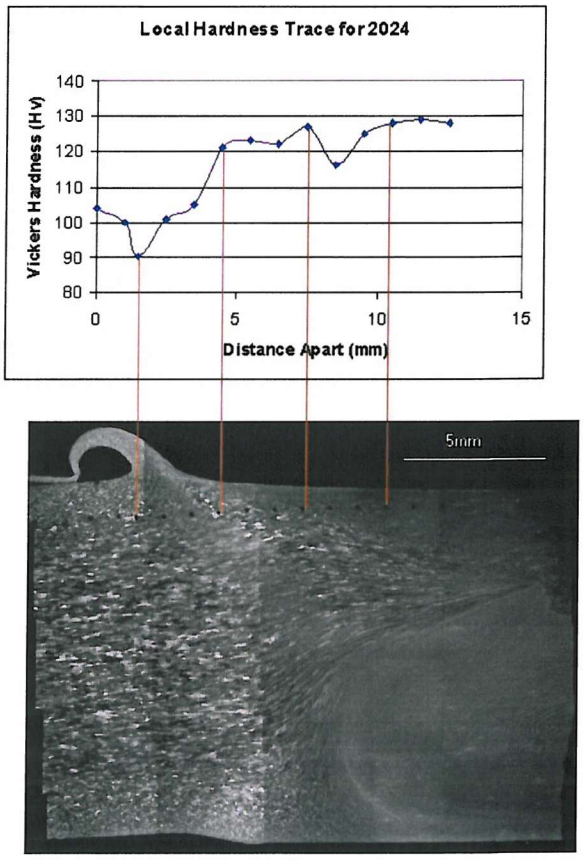

Figure 46 Local micro-hardness variations in relation to the weld flow arm grain structure.

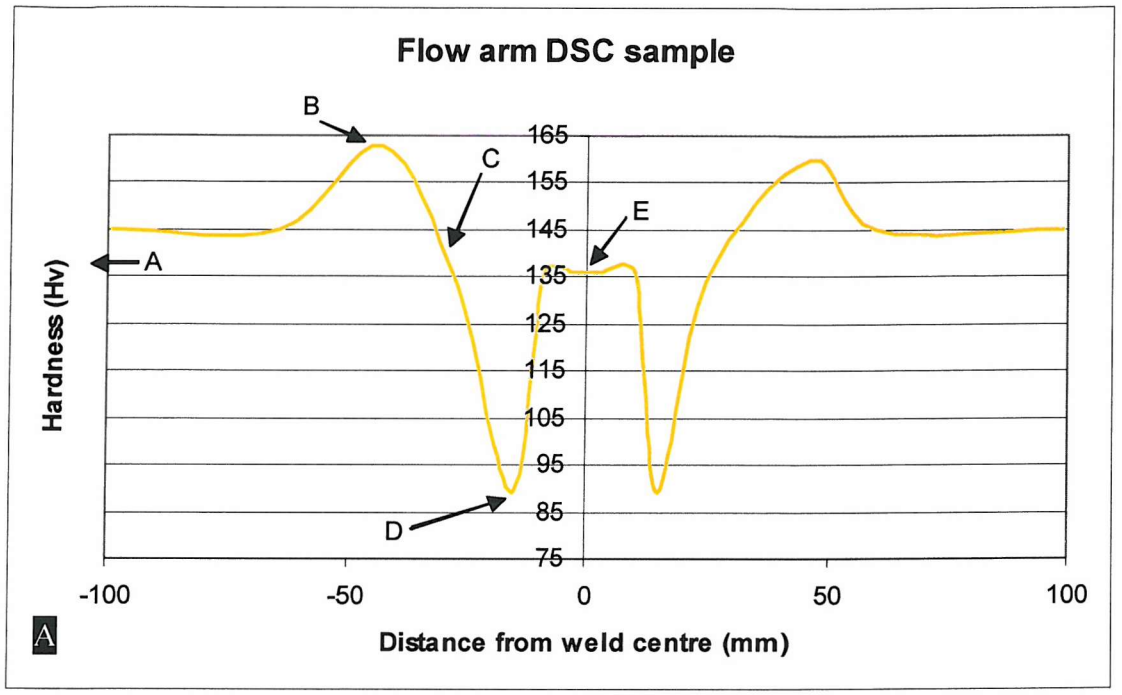

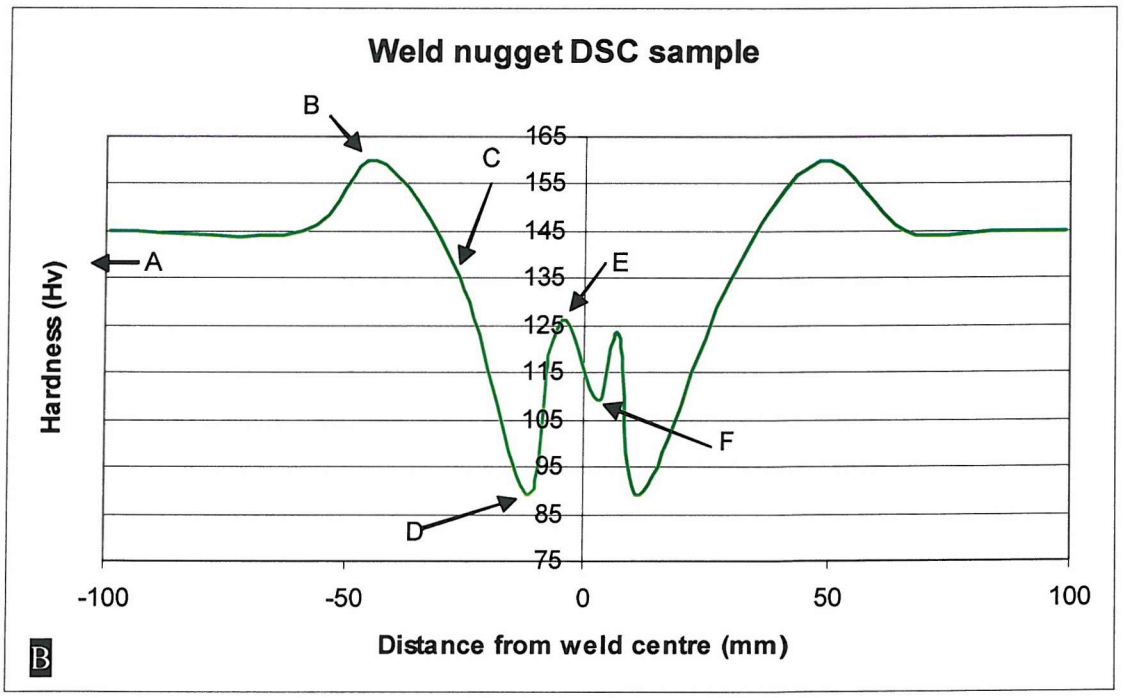

Figure 47 Hardness trace showing location of the DSC samples, a) through the flow arm and b) through the centre of weld nugget.

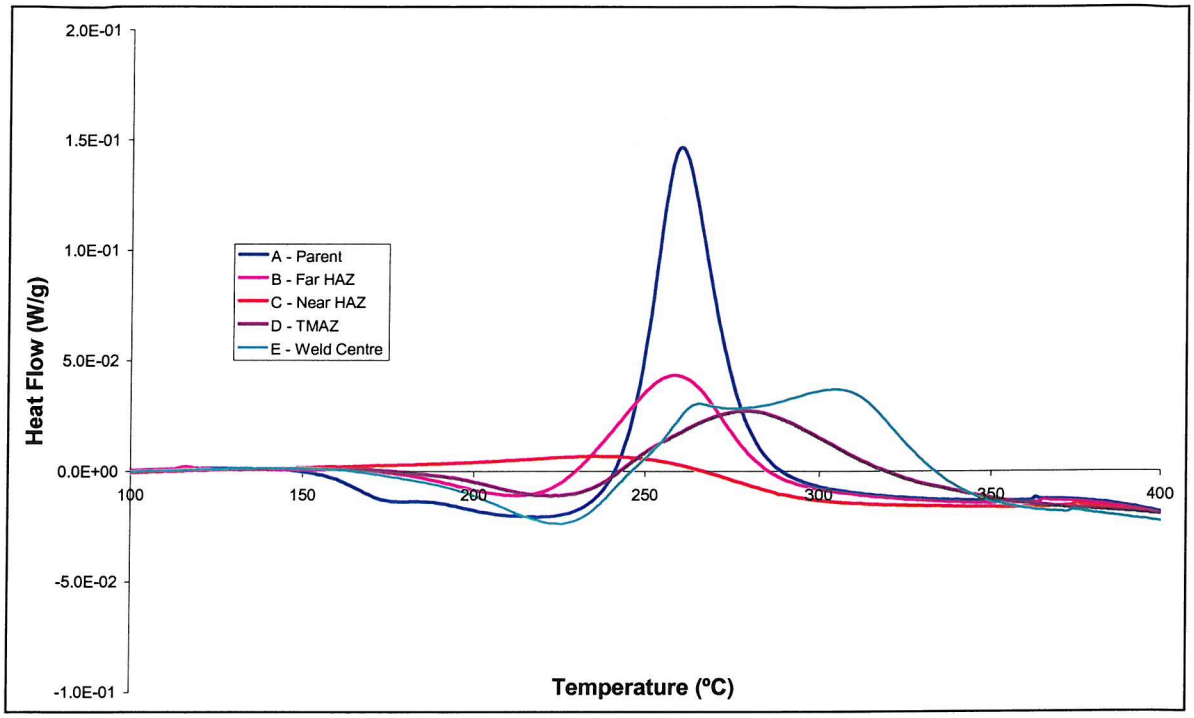

Figure 48 DSC curves for the flow arm series, A = parent plate, B = maximum hardness, C = approximate middle of hardness drop, D = hardness minimum and E = weld centre (100-540°C).

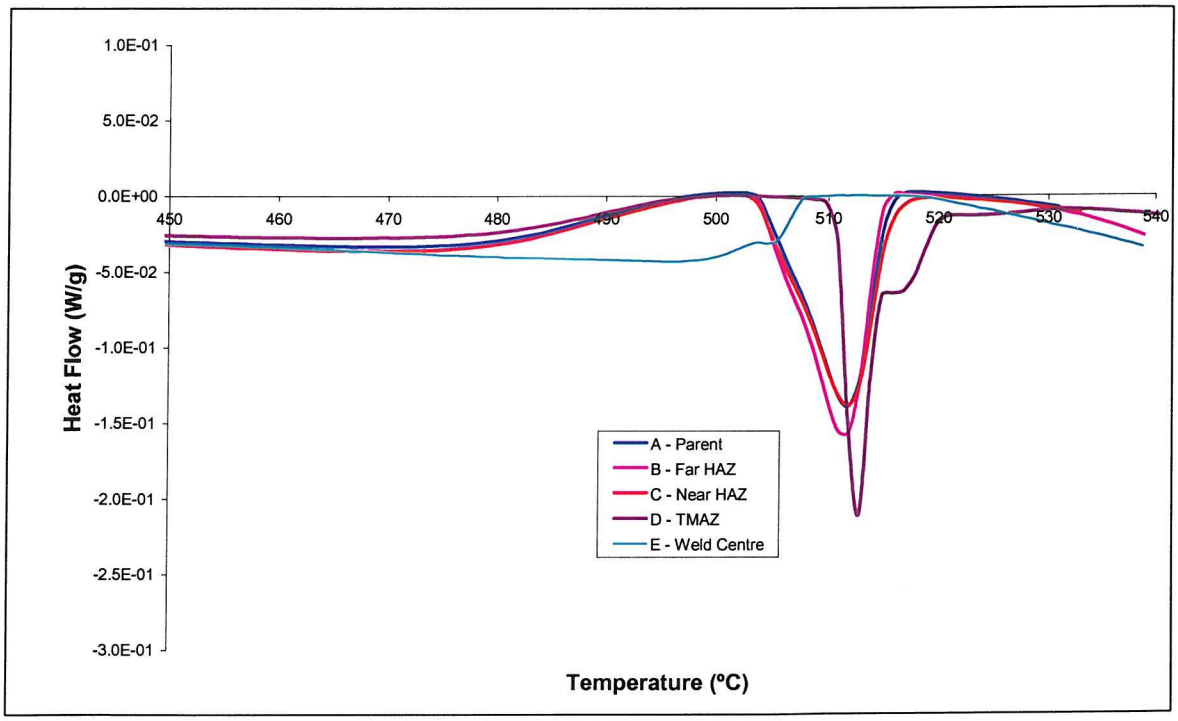

Figure 49 450-540°C part of the flow arm series of the DSC curves shown in Figure 48.

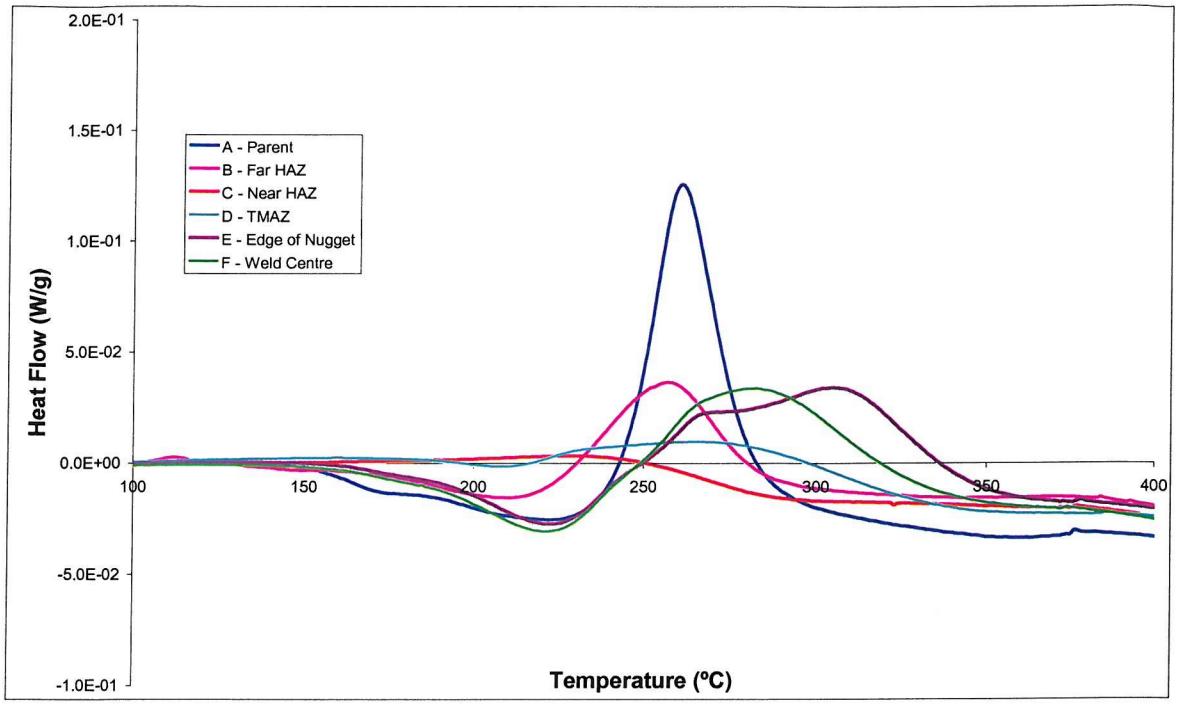

Figure 50 DSC curves for the weld nugget series, A = parent plate, B = maximum hardness, C = approximate middle of hardness drop, D = hardness minimum, E = edge of the weld nugget, and F = weld centre.

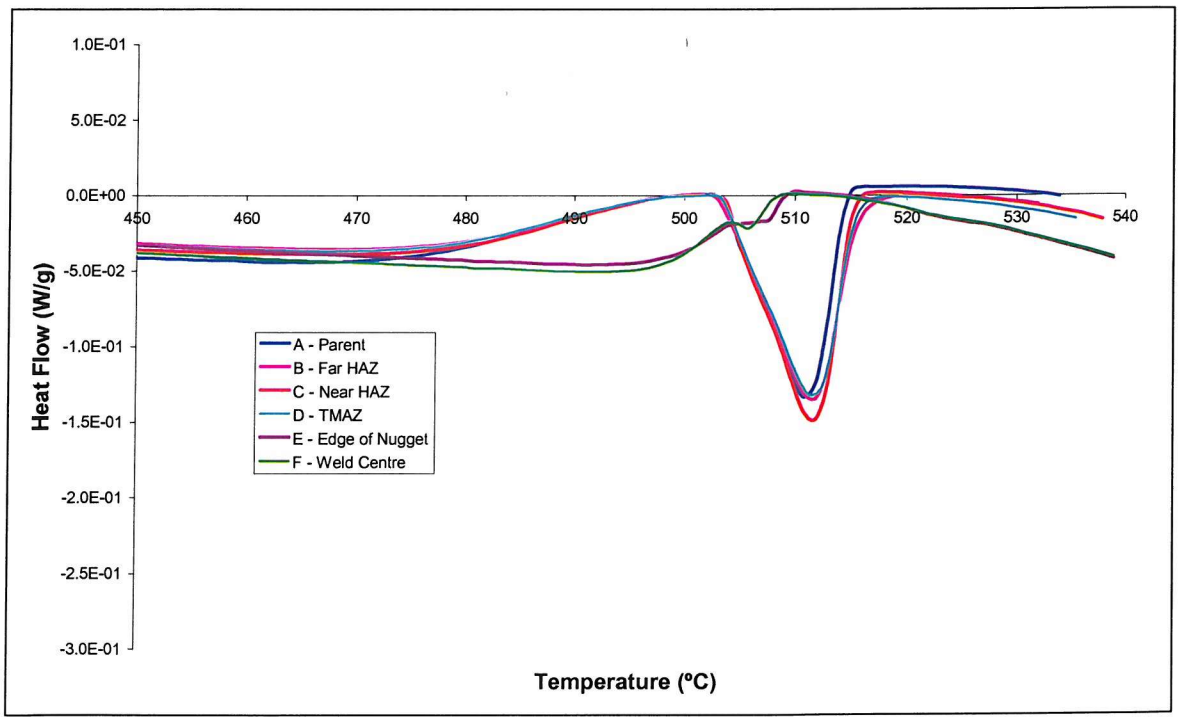

Figure 51 450-540°C part of the weld nugget series of the DSC curves shown in Figure 50.

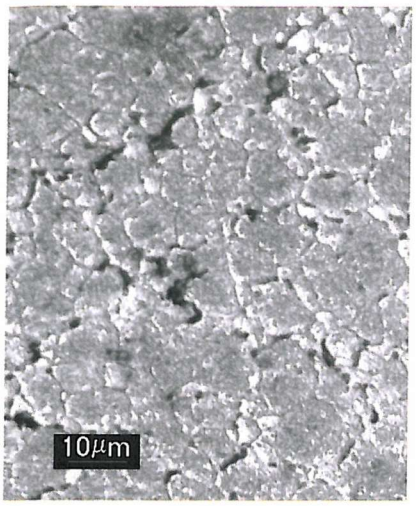

Figure 52 Flow arm grain structure

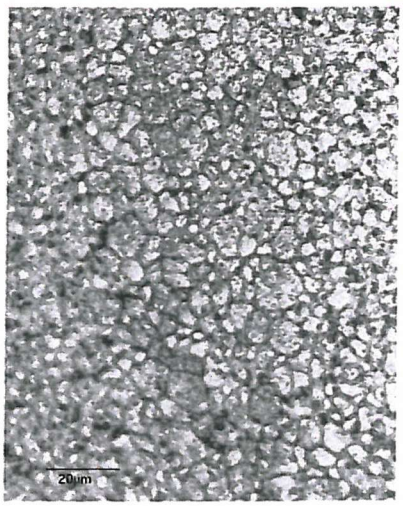

Figure 53 Nugget grain structure

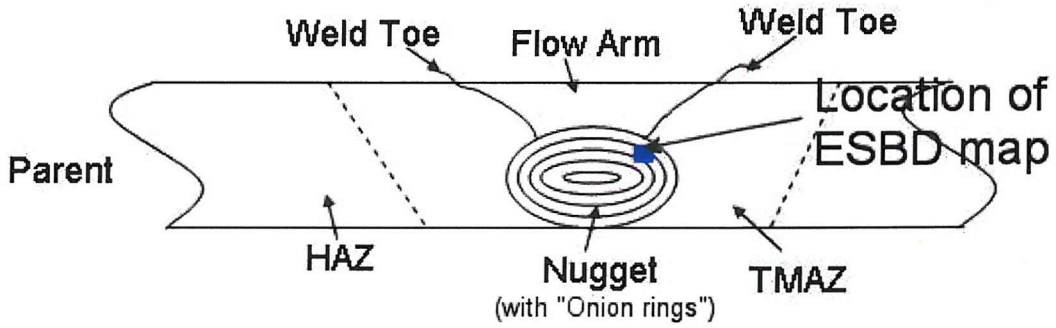

Figure 54 Schematic of 13mm friction stir weld showing approximate location of the EBSD map shown in Figure 55.

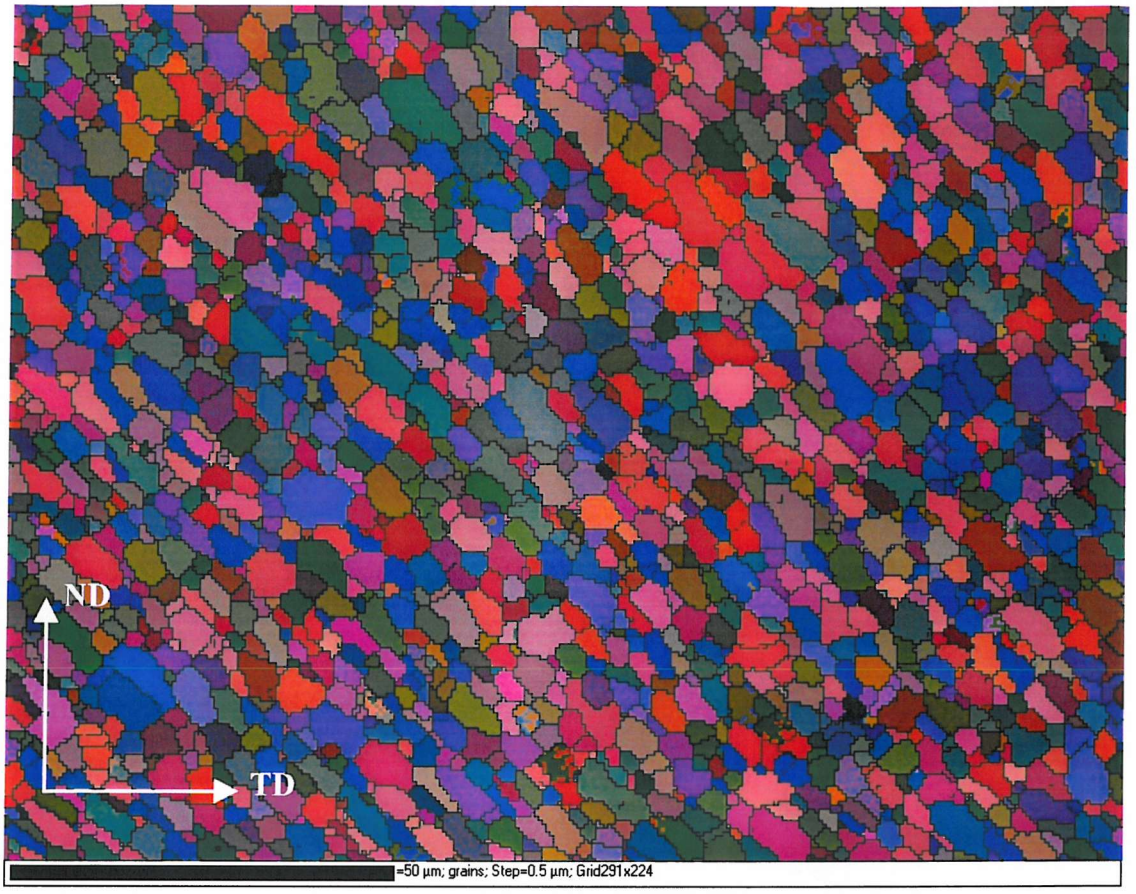

a)

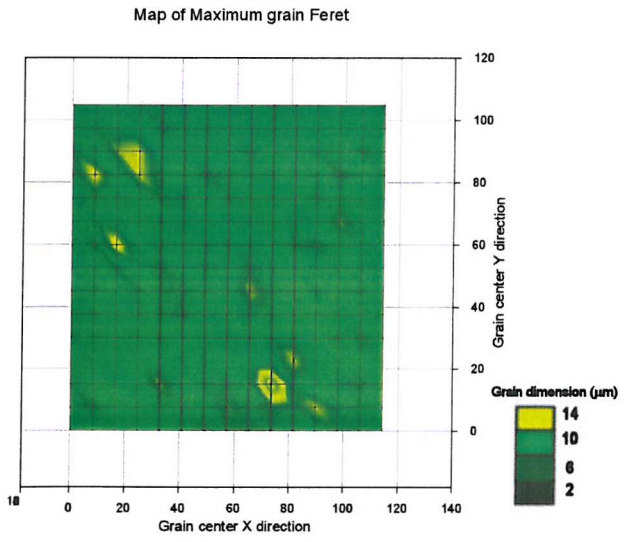

b)

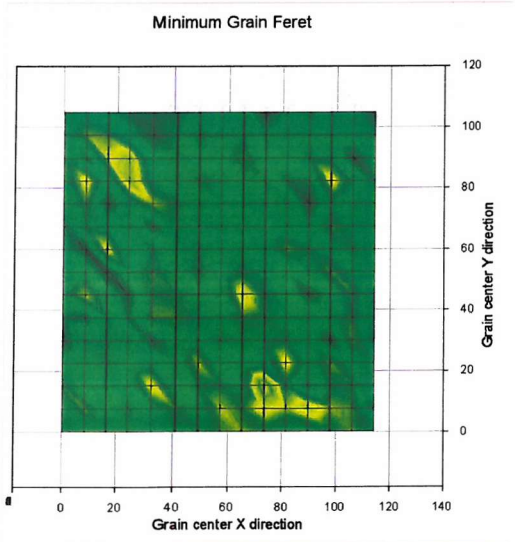

c)

Figure 55 a) EBSD map orientation of nugget region indicated in Figure 54, b) contour map of maximum dimensions grain feret and c) minimum grain feret dimensions

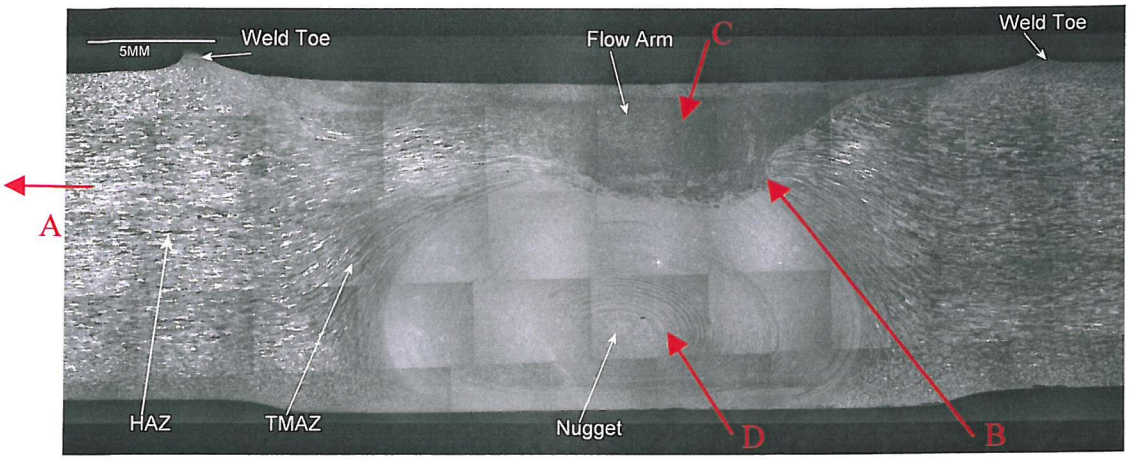

Figure 56 Weld macrograph showing location of BEI images in Figure 57.

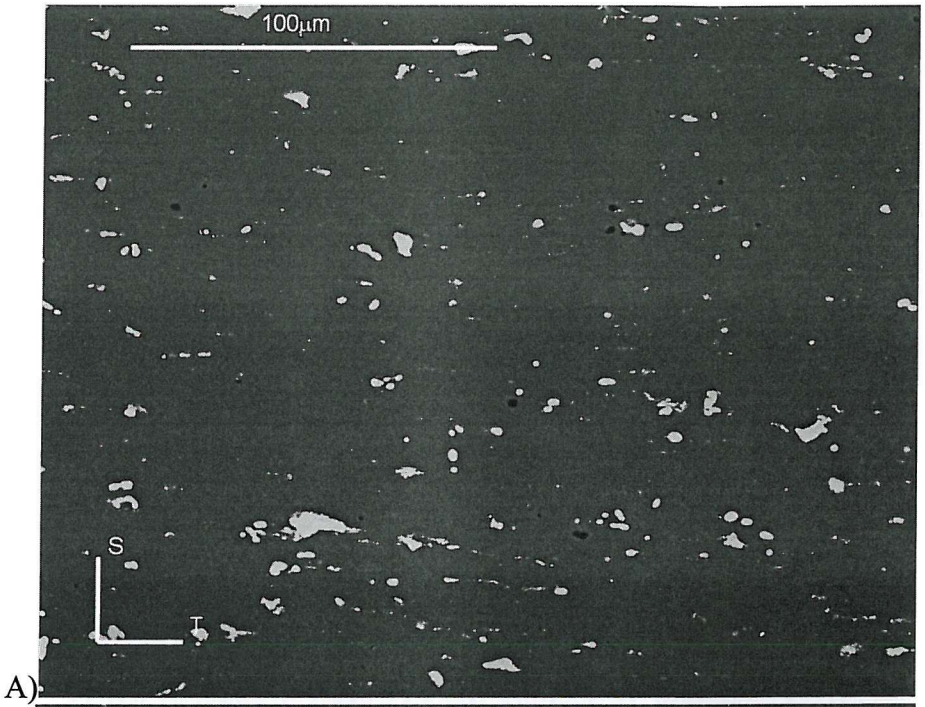

A)

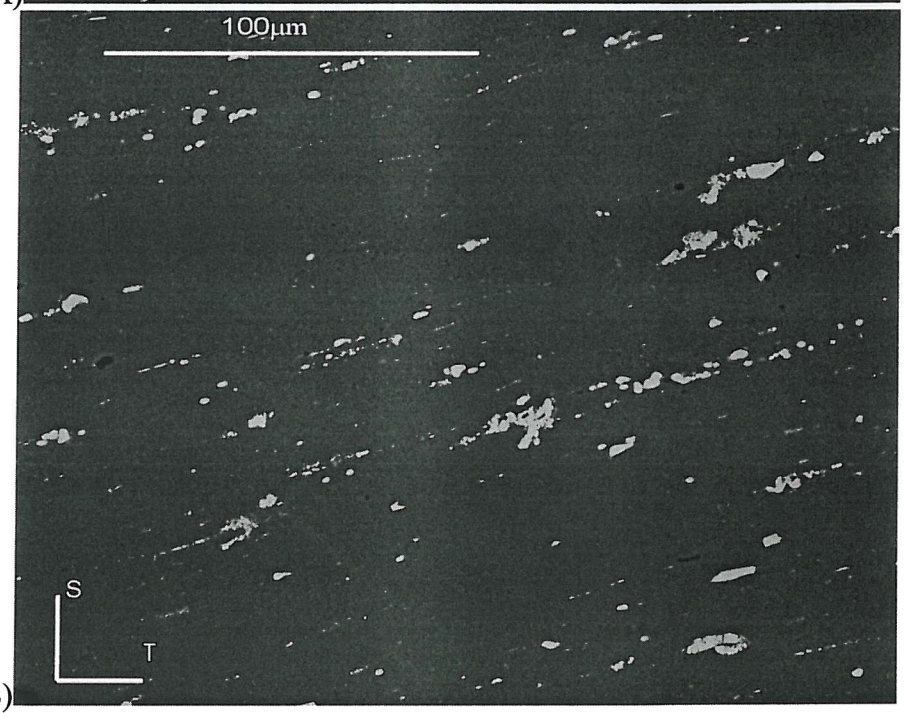

B)

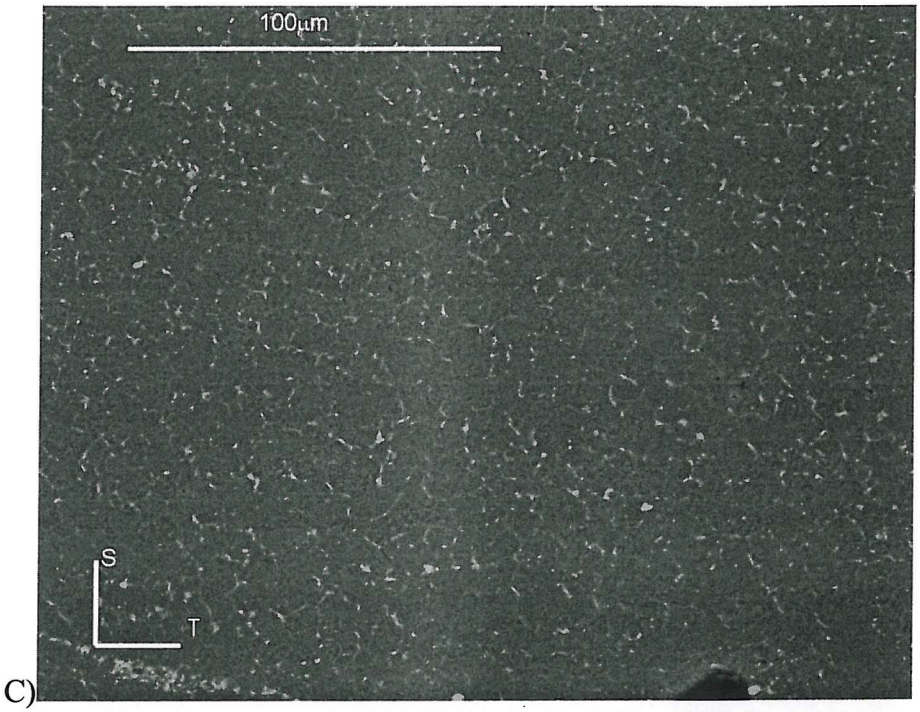

C)

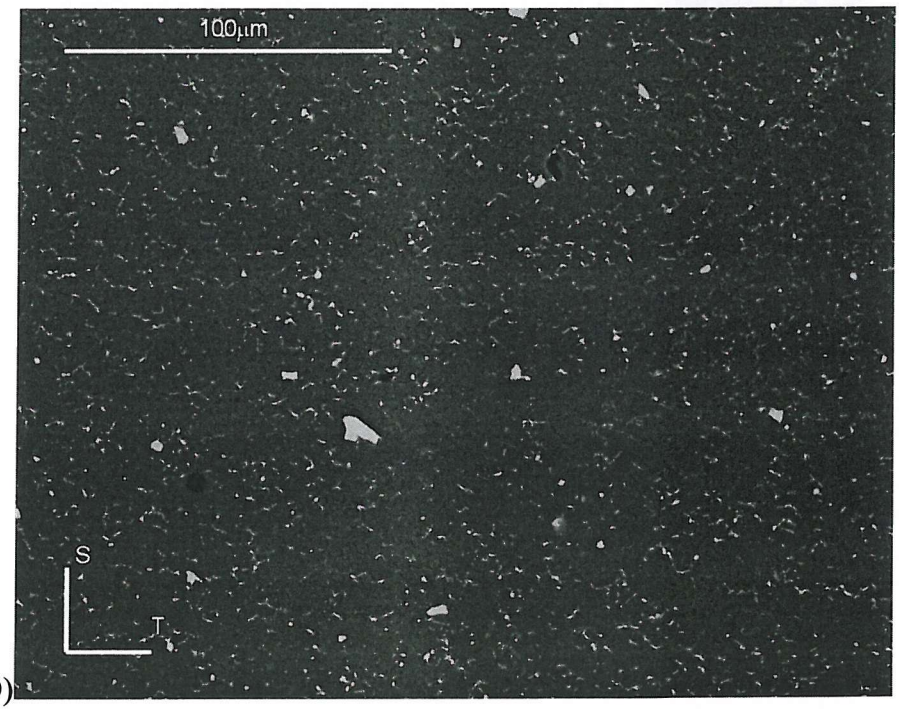

D)

Figure 57 BEI SEM images of the A) parent plate, B) TMAZ (retreating side of weld, 3mm below surface, 5mm from centreline), C) flow arm region, 2mm below weld surface, perpendicular to the weld line, and D) weld nugget, near the weld centreline, perpendicular to the weld line (S and T directions based on parent plate).

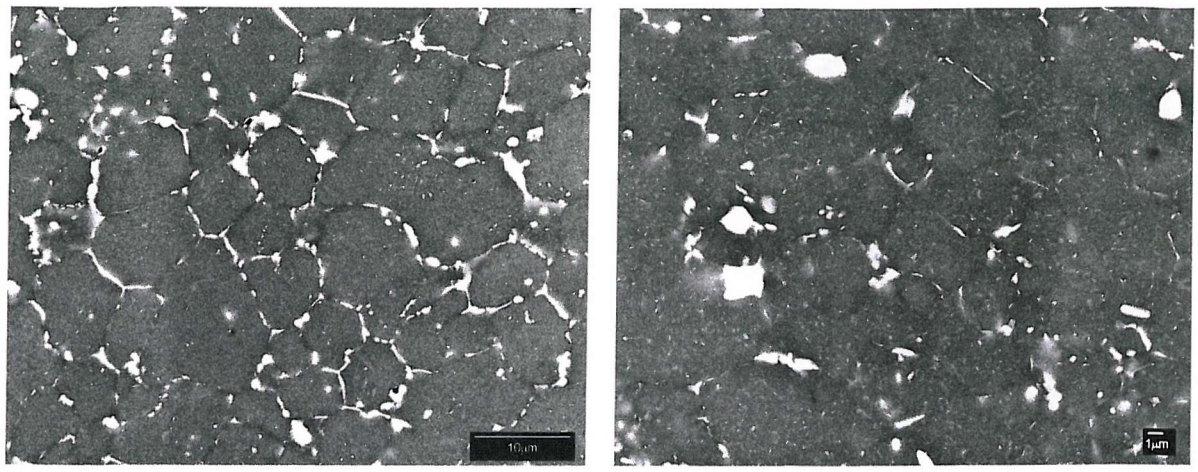

a) b)

Figure 58 BEI images highlighting flow arm heterogeneity; a) high particle content region and b) low particle content region.

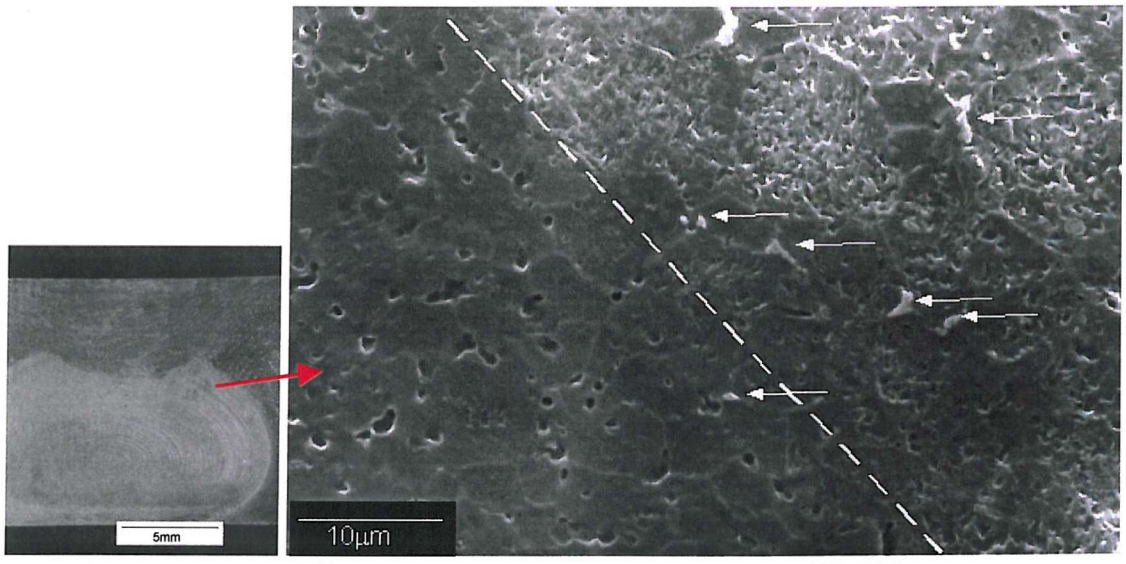

Figure 59 Macrograph showing the location of the SEM image of an interface between two bands making up the 'onion ring' structure within the weld nugget (polished and etched in Keller's reagent): the dashed line highlights a band edge, whilst arrows highlight the locations of larger intermetallics.

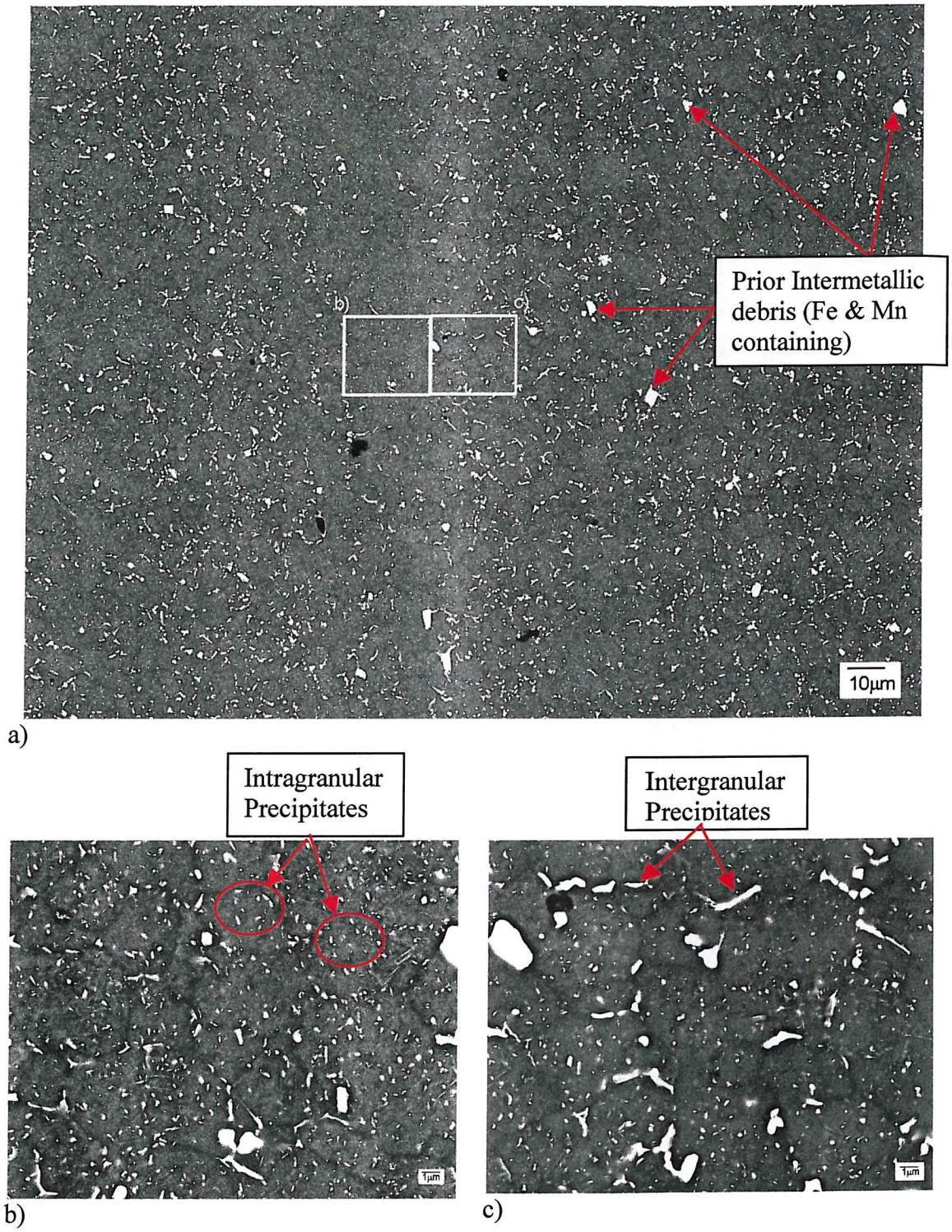

Figure 60 FEG-SEM BEI images across an apparent band in intermetallic density within the weld nugget; a) low magnification image showing location of images b) and c).

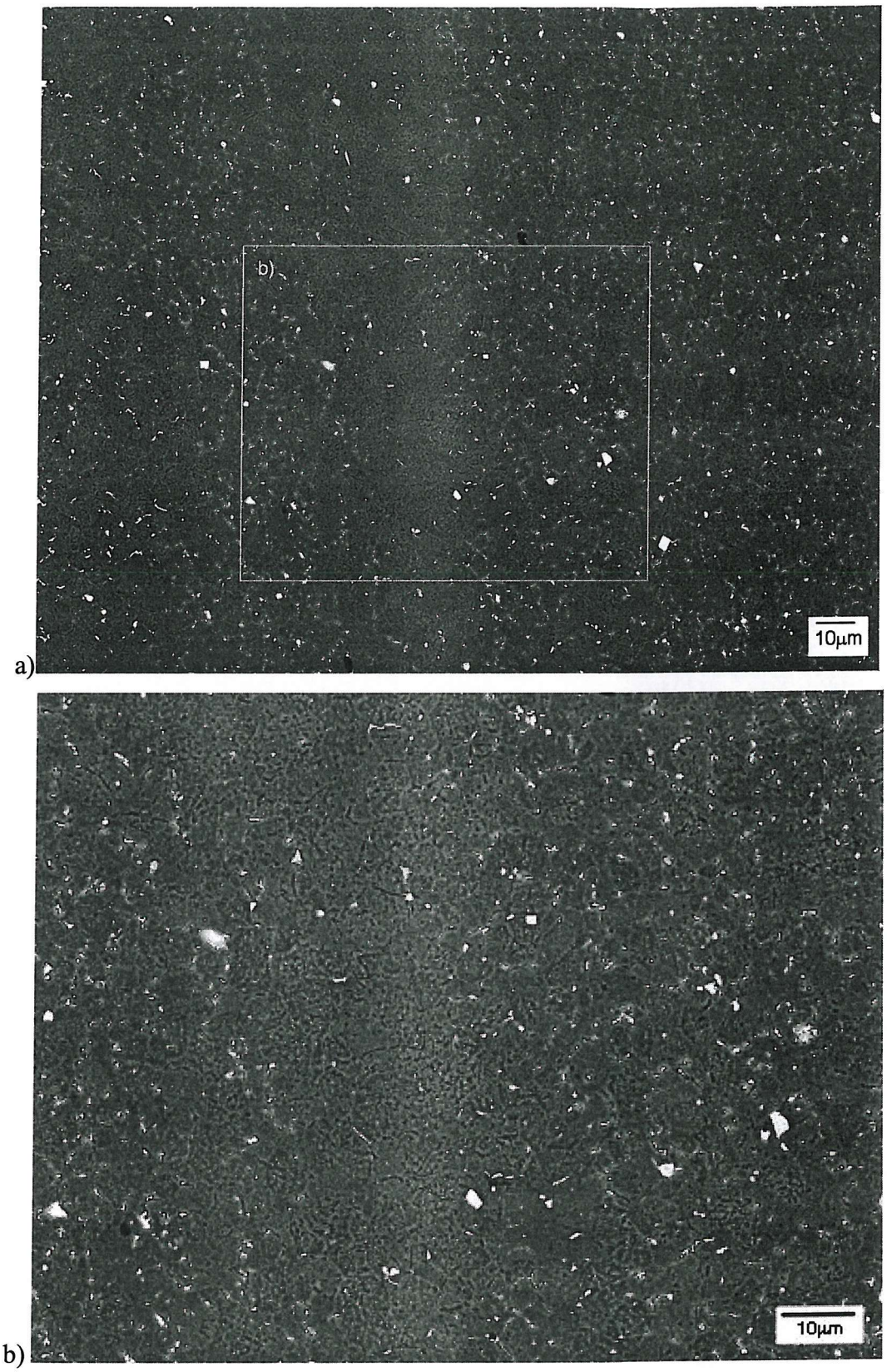

Figure 61 BEI of the etched weld nugget region; a) cover similar area to that shown in Figure 60, the location of the subsequent images is also included and b) as indicated in a).

4.2 Results

4.2.1 Fatigue Life Results

Of the five specimens of the 13mm gauge weld made available for testing, two forms of failure were identified in the present work: (i) tests where failure occurred outside of the flow arm/nugget region, and (ii) tests where failure occurred from within the actual weld material (identified here as 'over' the nugget region). Details of the failure events are considered further in the following sections. In terms of fatigue life it may be seen from Figure 62 that for the two specimens where failure occurred outside of the nugget region and the run out result, fatigue performance is comparable to that found by Bussu and Irving[25] for thinner 2024-T351 friction stir welds (6.35mm gauge) plate. Two failures occurred over the weld nugget region, although accurate fatigue life data is only available for one sample. The fatigue life of this specimen was appreciably lower (by a factor of ~8) than the specimens that failed outside the nugget region. The other specimen that failed over the weld nugget received an accidental overload during testing. Whilst local plastic deformation would have been expected from the overload, no evidence of tensile damage (i.e. cracking) was identified in the specimen and testing was resumed at the original load levels (given the limited material availability). The total fatigue life of this specimen was then recorded as 580,000 cycles, i.e. comparable with the specimens that failed outside the weld nugget. In the first instance this number of cycles maybe identified as an upper bound on the true fatigue life given the residual compressive surface stresses the overload of a bend specimen maybe expected to generate.

Figure 63 indicates the location of the fatigue failures in relation to the transverse weld microstructure. It is clear that the failures over the weld nugget region initiated in the fine grained flow arm region. While the two failures that occurred outside the nugget region occurred in a region of limited grain deformation, i.e. on the HAZ side of the TMAZ. The hardness around each of the failure locations is shown in Figure 64 (the trace consists of a number of indents on either side of the failed specimen close to the initiation location); it is clear from the results that initiation is not linked to any unexpected variation in strength. It is also clear that initiation outside the weld region does not occur at the exact hardness minima, but just inside the minima, on the rise in hardness up to the weld nugget plateau.

4.2.2 Crack Growth Rates

Figure 65 shows crack growth rates obtained for two cracks from the same specimen when failure had initiated outside the weld nugget region, but within the TMAZ/HAZ (see following sections for details). Results are plotted against literature values for long crack growth in standard commercial 2024-T351 plate[111]. The figure represents crack growth from approximately 500μm to 2500μm total crack length. It may be seen that growth trends for the friction stir weld cracks are closely comparable to the commercial plate, although there is a small but consistent offset in growth rates of the order of a factor of 2 (i.e. faster than the commercial plate data). Unfortunately no growth data was obtained for the over nugget failures.

4.2.3 Fractography

4.2.3.1 Failures outside the nugget region

- ***Macroscopic Failure Behaviour***

A typical dominant crack for one of the specimens that failed outside the nugget region is shown in Figure 66. The crack in this case is the result of the coalescence of two small cracks (both formed at a similar distance from the weld centre line on the same side of the weld). Crack growth was predominantly perpendicular to the applied load on both the specimen surface and into the depth of the specimen.

- ***Initiation and Propagation Behaviour***

Crack initiation sites were clearly identified as coarse 2nd phase particles (of the order of 5-10μm); in particular decohesion of S-phase, as illustrated in Figure 67 for a secondary crack that arrested prior to final failure.

Initial crack growth showed characteristic river-lines radiating out from the initiation point, as shown in Figure 68. Early crack growth was transgranular with distinct deflections at grain boundaries, characteristic of a classical Stage I/crystallographic failure mode. Figure 69 shows the crack growth at a latter stage of the failure with a more ductile transgranular failure mode evident, and some evidence of grain boundary splitting.

4.2.3.2 Failure over the nugget region

- ***Macroscopic Initiation Behaviour***

The top surface of one of the specimens that failed over the nugget region is shown in Figure 70 (a). In both instances of such failure over the nugget, initiation was clearly identified with a macroscopic discontinuity in the weld flow patterns, as highlighted in Figure 70(b). The crack path across the sample width was generally more irregular (i.e. deflected) than that seen in the failures outside the nugget region.

- ***Microscopic Initiation Behaviour***

After careful SEM investigation the microscopic cause of crack initiation was unfortunately not considered to be clearly identifiable in these cases: there were no obvious initiating inclusion particles or weld defects as can be seen from Figure 71a) and b), which show the region around the observed initiation site in SEI and BEI mode respectively: no microscopic river line features or facets are seen to radiate from a single point or particle, and no large defects are particularly identifiable at the specimen top surface. A large intermetallic can however be seen towards the centre of Figure 71b) (some 15μm in maximum dimension), however its role in the local crack evolution is unclear. It was noted that at least one secondary crack[1] that was present on the surface of one of the samples, however none were clearly identifiable on the primary crack paths. The initiation location is clearly associated with quite a complex local arrangement of tilted fracture planes; however no clear evidence was obtained to establish a link between the microscopic initiation point and these features.

[1] Overall numbers of crack initiations within the specimens were generally low however, with no more than 4 cracks seen in the nugget region.

The intermetallic particle distribution of the macroscopic flow discontinuity seen in Figure 70 was studied further on the top surface of the test specimen. A clear link to the macroscopic flow feature was identified, as can be seen in Figure 72a), with a coarse intermetallic region containing particles up to approximately 15μm (occasionally up to 20μm), being seen in Figure 72b) appearing to radiate out from the crack initiation region. While on the fine intermetallic side the particle size is typically 3-4μm i.e. typical of the rest of the weld, see Figure 72c). The hardness across the discontinuity was also assessed; a difference of ~3Hv is evident in Figure 73, with the fine intermetallic side appearing to have a slightly higher strength. EBSD analysis revealed that in the coarse intermetallic (Figure 74a)) side of the flow feature the grain size is coarser than the fine intermetallic (Figure 74b)) side varying from ~5μm to ~6μm.

- ***Macroscopic Flow Arm Propagation Behaviour***

Figure 75 shows a general view of the fracture surface of the region close to the initiation point for one of the failures over the nugget region; the crack growth through the weld flow arm (top ~2mm in Figure 75) showed some minor deflections from a nominal mode I path, which is also evident at the top of the fracture surface profile in Figure 76.

- ***Microscopic Flow Arm Propagation Behaviour***

The mixed mechanism nature of crack growth in the flow arm is clearly evident in Figure 77a), with the circled regions showing clear evidence of intergranular failure, while surrounding regions of the fracture surface exhibit a flatter fracture surface characteristic of transgranular failure. Figure 77b) shows that the intergranular fracture regions are linked to regions of continuous grain boundary decoration. The grain structure in the flow

arm region immediately behind the crack path is shown as an EBSD map in Figure 78[2]; with crack growth occurring on the right hand edge of the image. Such imaging showed no unusual grain structure features in the regions of crack growth (e.g. large grains or unusual degrees of elongation).

The top surface view of a secondary crack initiation from a nugget region failure is shown in Figure 79. A predominantly straight crack path is seen indicative of transgranular failure, although local deflections of the order of the grain size are also seen consistent with the images in Figure 77a) and b).

- ***Macroscopic Nugget Crack Propagation Behaviour***

The curved nature of the crack growth around the nugget region can clearly be seen in the lower parts of Figure 75 and Figure 76. The deflection of the crack path forms a curve that closely follows the macroscopic onion ring structure of the nugget region. Sections from both halves of the failed sample showed that crack growth had occurred just within the nugget, rather than at the nugget/TMAZ interface, see Figure 76 and Figure 80 which show each side of the fracture path respectively.

- ***Microscopic Nugget Crack Propagation Behaviour***

Figure 81shows transverse crack profiles imaged in BEI mode in the FEG-SEM highlighting the local distribution of intermetallic particles in the region of curved crack growth around the nugget. Figure 81a) highlights a region of relatively planar crack growth, whilst Figure 81b) shows regions of more irregular apparently intergranular

[2] It should be noted at this point that the data acquired at the very crack edge must to be treated with caution. This is a result of the data processing/enhancement that is preformed by the HKL software after acquisition. At the crack edge this can lead to grains that appear larger than they really are, a line has been added to represent the true crack edge.

failure. In both cases, the coarse intermetallic particle interaction along the crack path appears to be limited, i.e. the crack does not appear to be linked to chains or bands of coarse particles. Figure 81c) shows a local step in the crack path (i.e. a region running perpendicular to the overall banding structure of the nugget). There is evidence this step has occurred across a region of lower intermetallic content, with the dominant growth direction (i.e. following the onion-ring structure) being resumed in a region of higher intermetallic content.

Figure 82a) shows an SEI of the fracture surface 3.5mm below the specimen surface (corresponding to the top of the nugget). The image shows complex fracture morphology with evidence of transgranular, intergranular and local ductile void growth. However there are no large voids obvious on the fracture surface. Figure 82b) is a BEI image of the same region of the fracture surface as seen in Figure 82a). Whilst there is only a limited coverage of the *larger* intermetallic particles, there does however appear to be a high density of intermediate (~0.5-2μm) particles at the fracture surface.

The grain structure near the crack edge in the nugget was further studied using EBSD on sections taken transverse to the welding direction, see Figure 83. The crack growth appears to be parallel to the general alignment in the grain structure; this is consistent with the alignment that was seen in Figure 55.

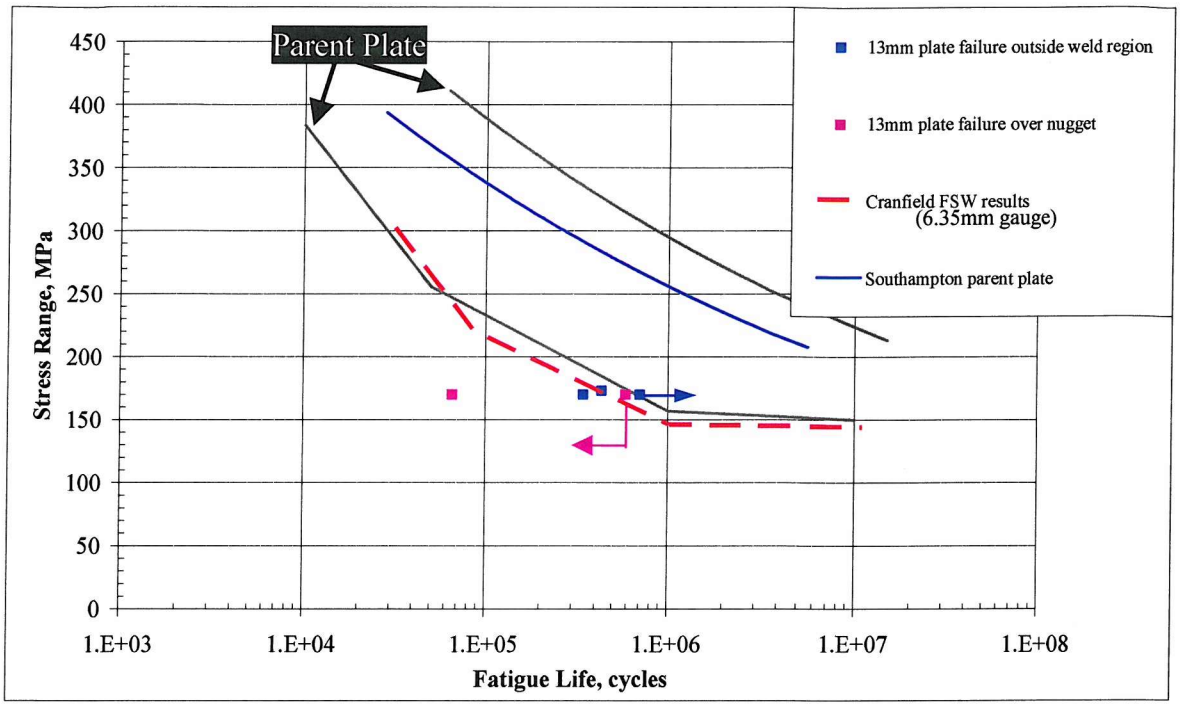

Figure 62 Fatigue life vs. stress level for 2024-T351 friction stir welds plotted with results from Bussu and Irving[25] (all data for R = 0.1).

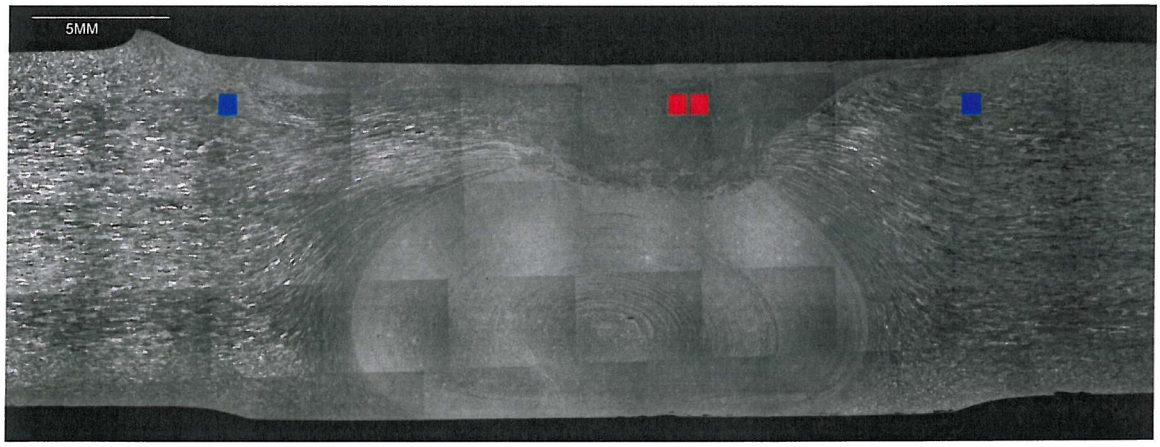

Figure 63 Transverse section of weld showing location of fatigue failures. Squares denote the location of the fatigue initiation sites, blue outside the nugget and red inside the nugget.

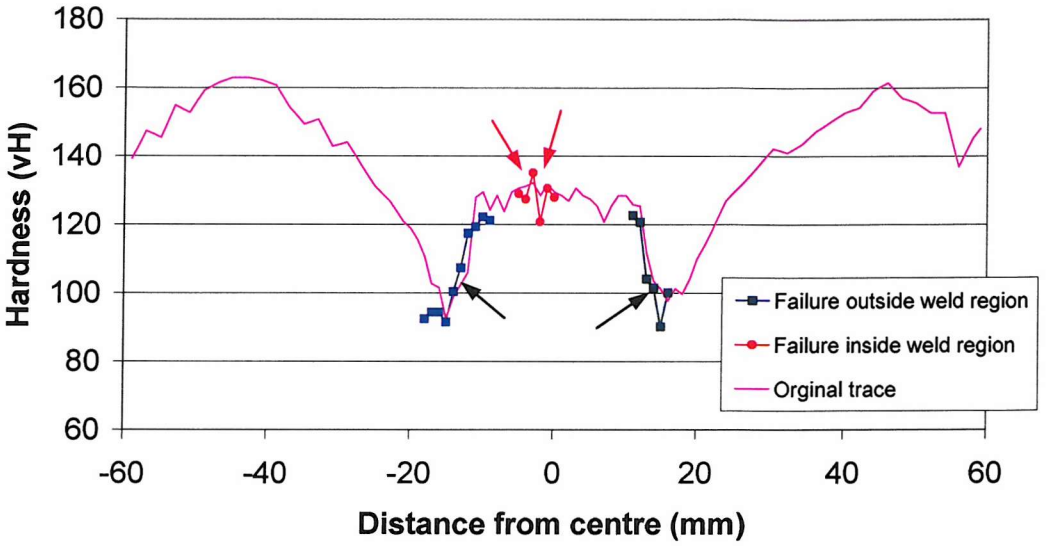

Figure 64 Local hardness traces taken around crack initiation locations, together with a corresponding hardness trace.

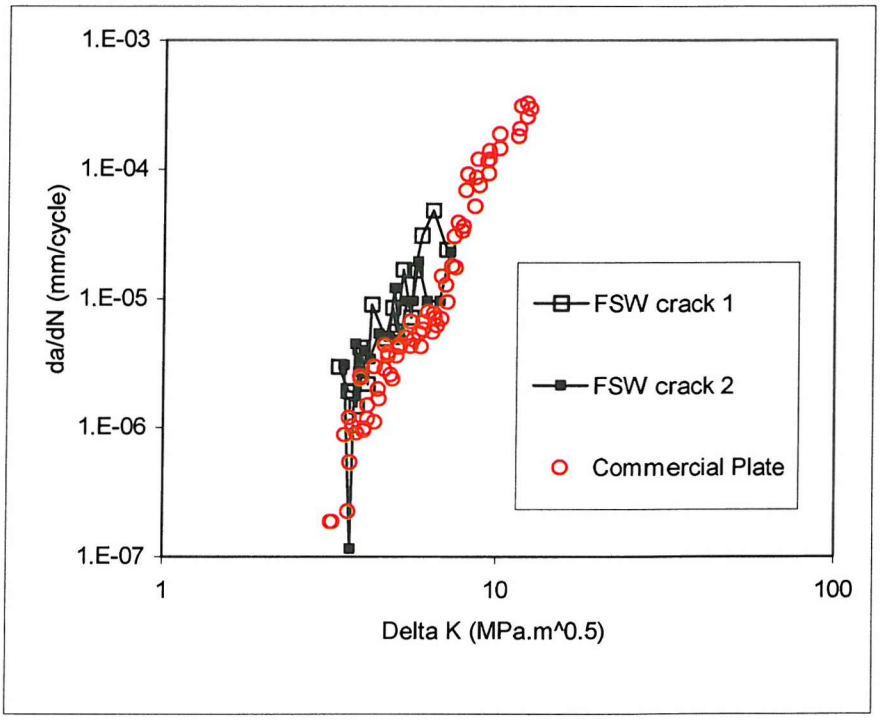

Figure 65 Crack growth rate data obtained for welded samples plotted against commercial 2024-T351 plate results (long crack)[111].

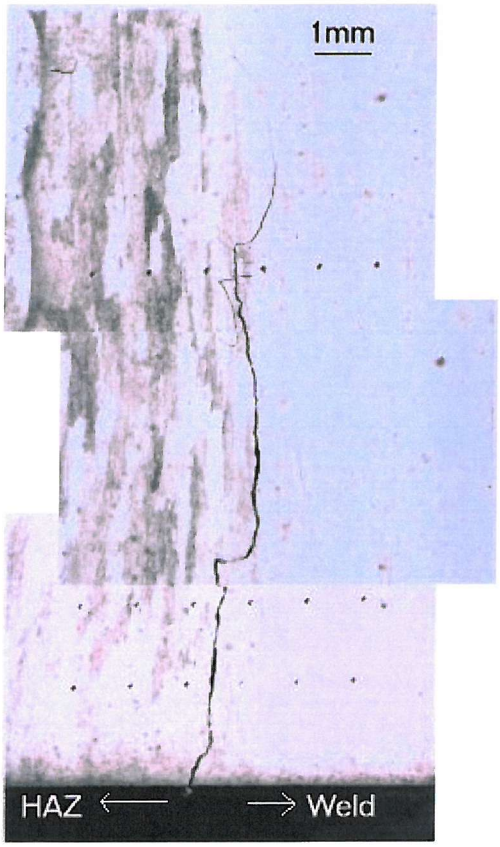

Figure 66 Optical micrograph showing a dominant crack after the coalescence of two cracks in the HAZ/TMAZ region.

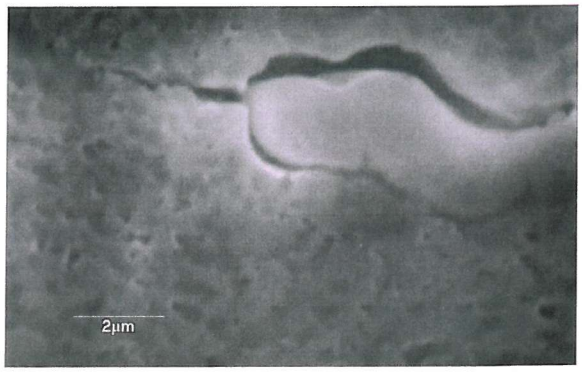

Figure 67 Crack initiation by decohesion at an S particle in the HAZ/TMAZ.

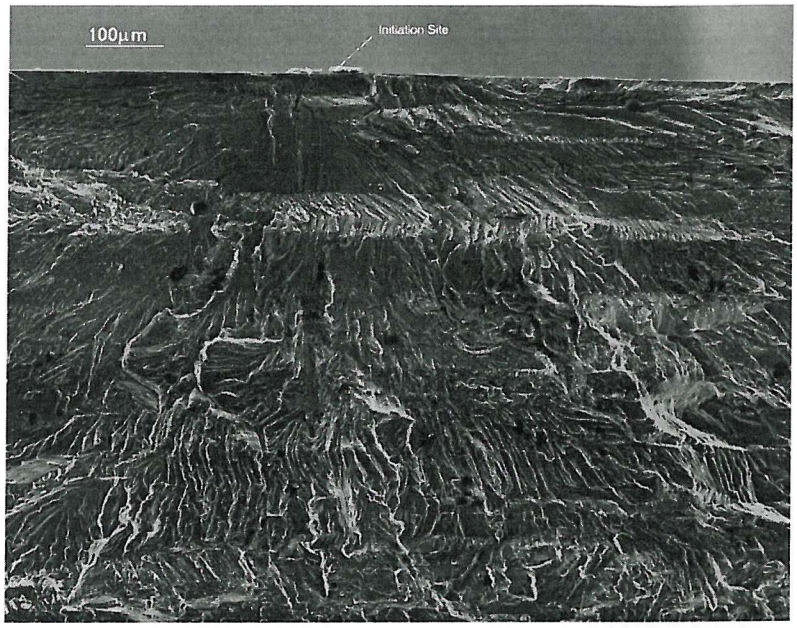

Figure 68 Fatigue surface at the crack initiation site for failure outside the nugget region.

Figure 69 Higher ΔK crack growth for failure outside the nugget region.

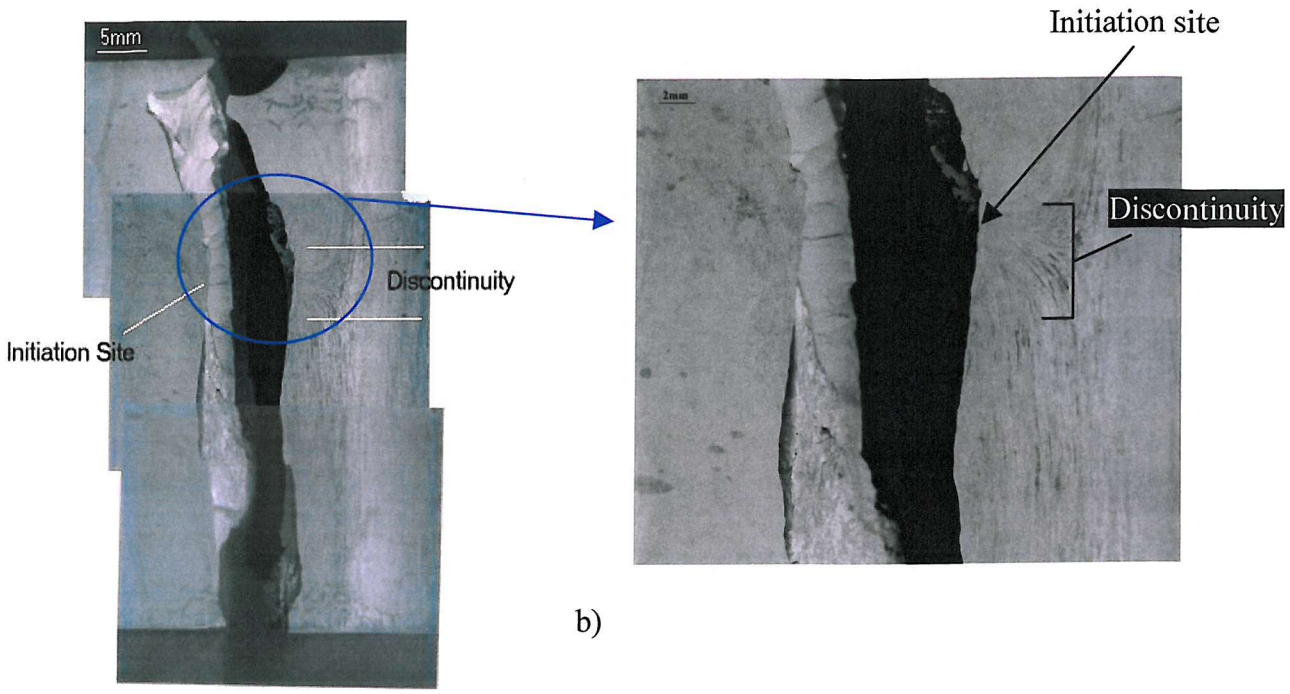

Figure 70 a) Macrograph of the top surface of a specimen that failed over the weld nugget b) Detail of flow discontinuity at the crack initiation site.

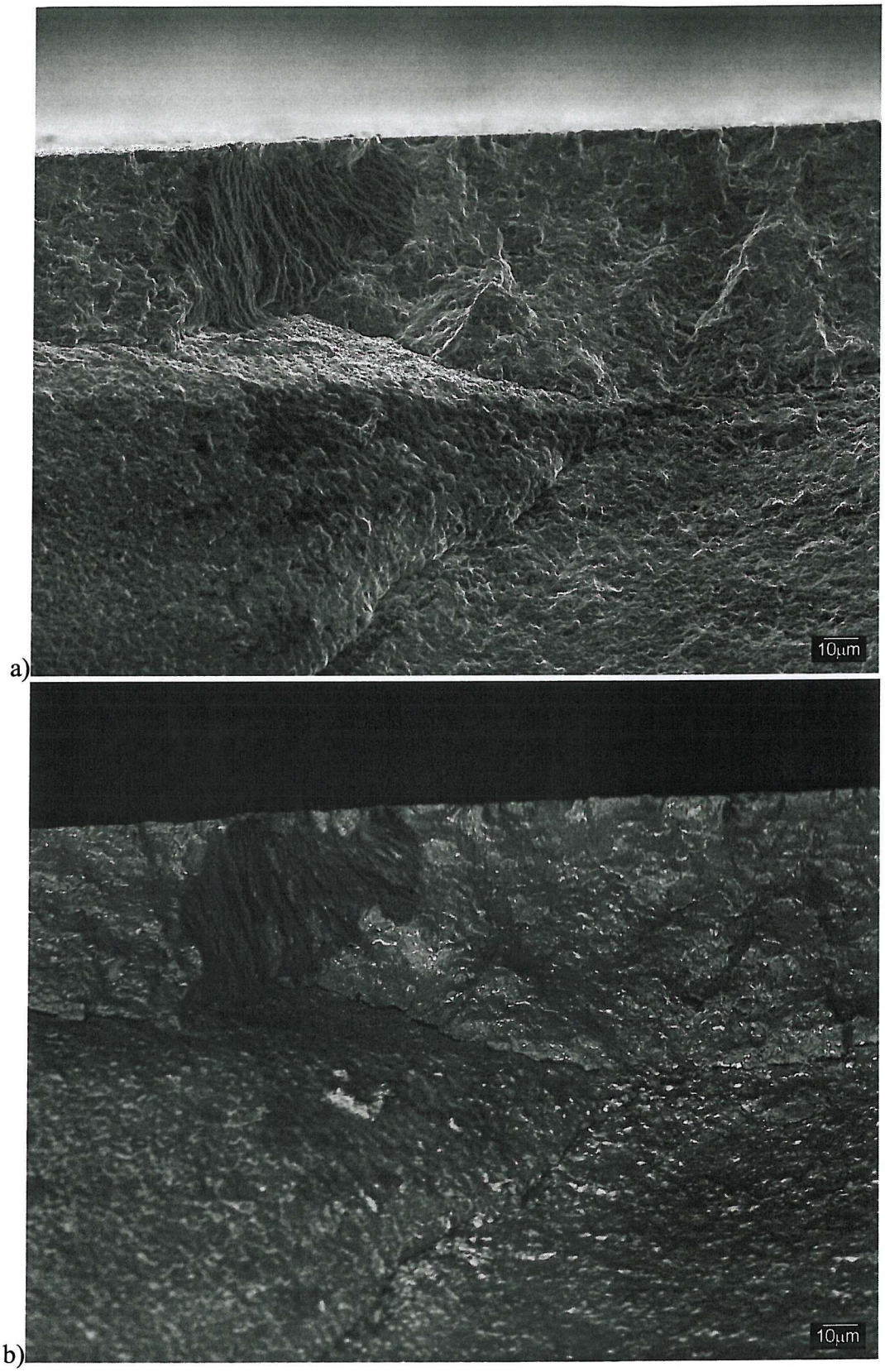

Figure 71 Region around initiation of failure over the nugget region, a) SEI and b) BEI.

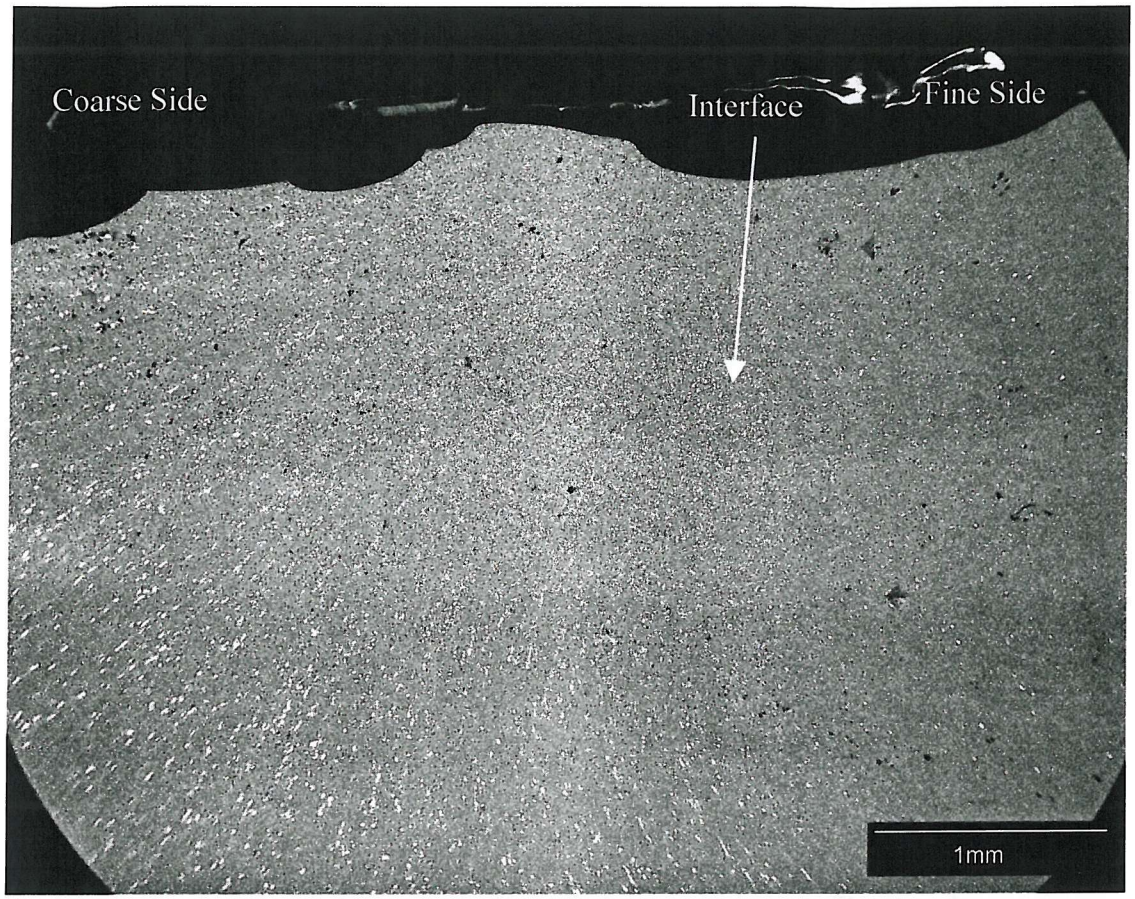

a)

b)

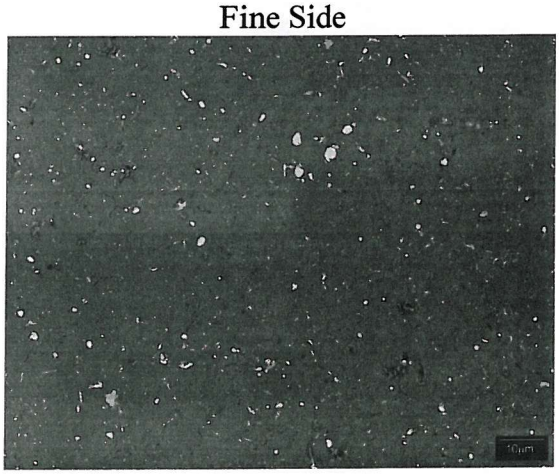

c)

Figure 72 BEI Image of Macroscopic surface discontinuity, a) Low magnification with coarse and fine intermetallic sides labelled together with the interface, b) coarse intermetallic side and c) fine intermetallic side.

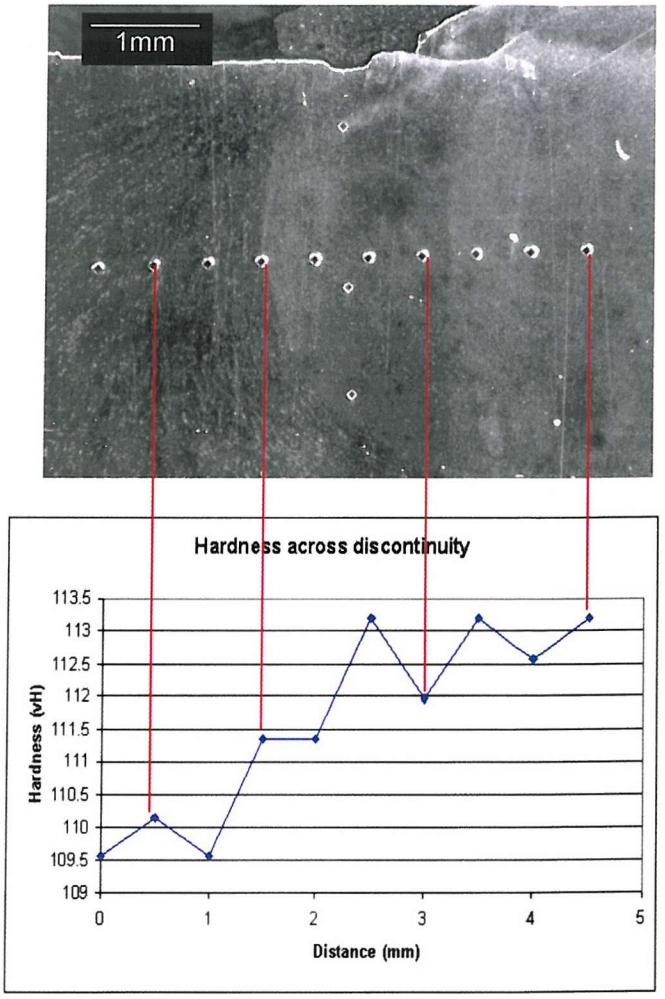

Figure 73 Hardness variation across macroscopic flow discontinuity in an over weld failure specimen.

a) Coarse intermetallic side

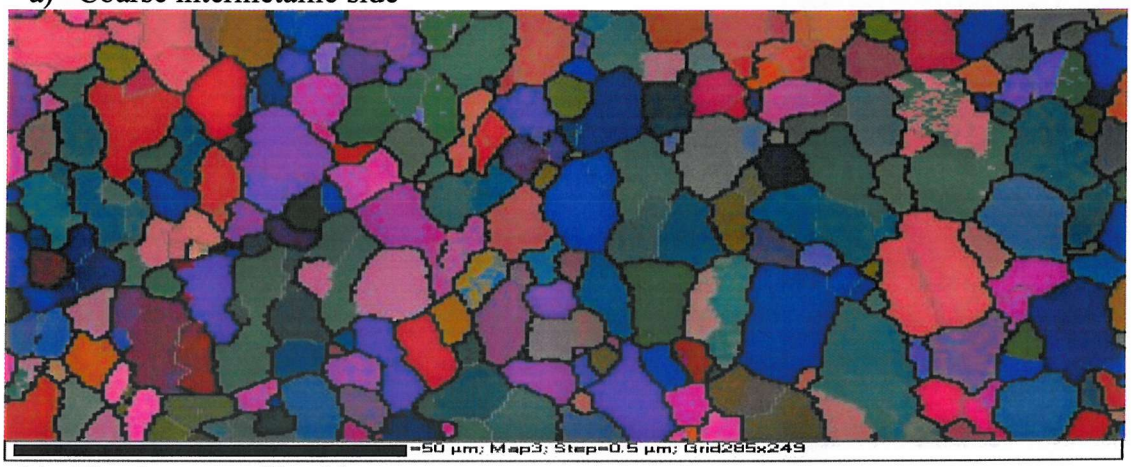

b) Fine intermetallic side

Figure 74 EBSD orientation mapping results for two sides of discontinuity, a) Coarse intermetallic side and b) fine intermetallic side.

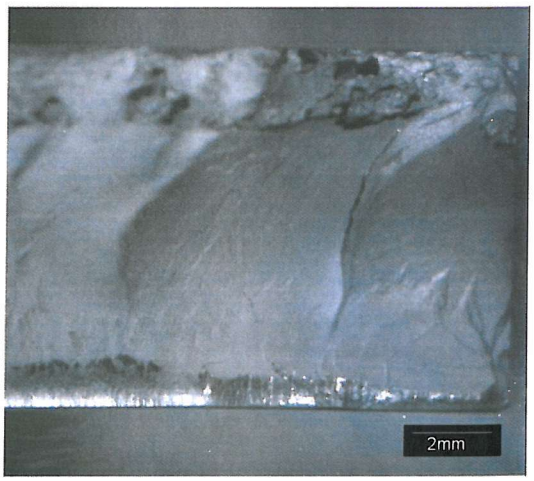

Figure 75 Macrograph showing "head-on" view of fracture surface.

Figure 76 Macrograph showing the fatigue crack path down through the weld region.

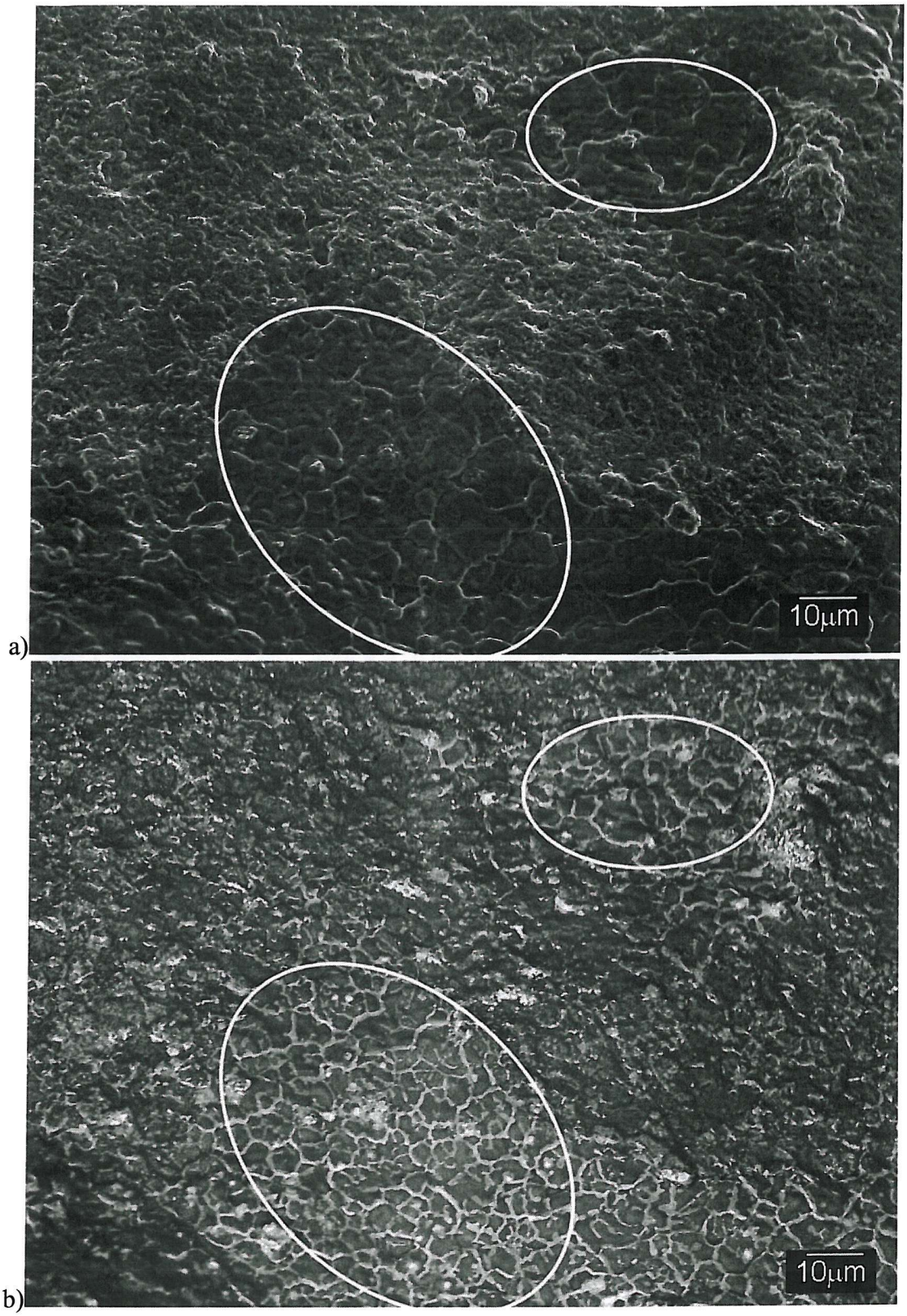

Figure 77 Fracture surface, 0.5mm below the specimen surface (in the flow arm), a) SEI (ellipse marks region of flat growth) and b) BEI.

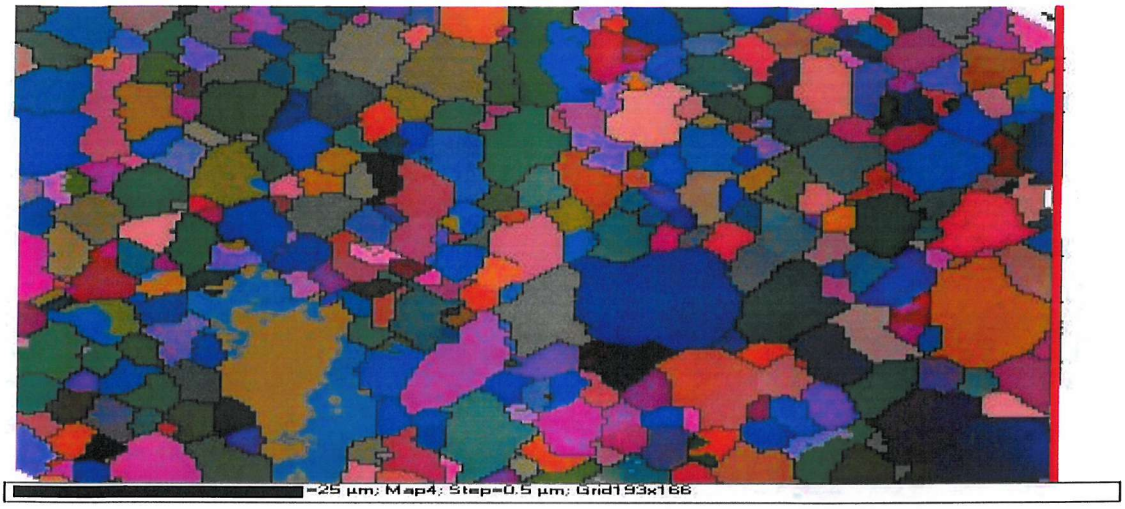

Figure 78 EBSD orientation map of growth through the flow arm, sectioned behind the fracture surface, perpendicular to the normal growth plane (The thick red line to the right marks the approximate crack edge; data beyond this line has been extrapolated in the Channel 5 software).

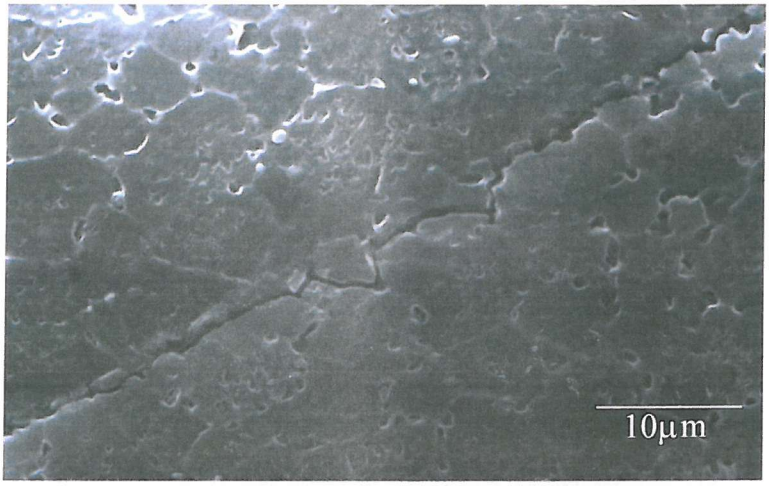

Figure 79 Secondary crack showing predominantly straight growth with some local deflections.

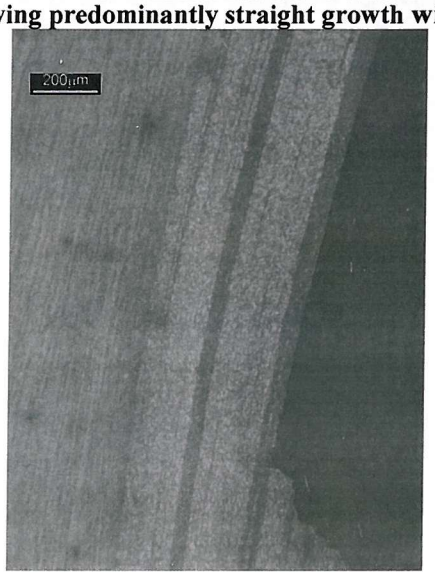

Figure 80 Macrograph showing the outside (towards the TMAZ) of the fatigue path through the weld nugget.

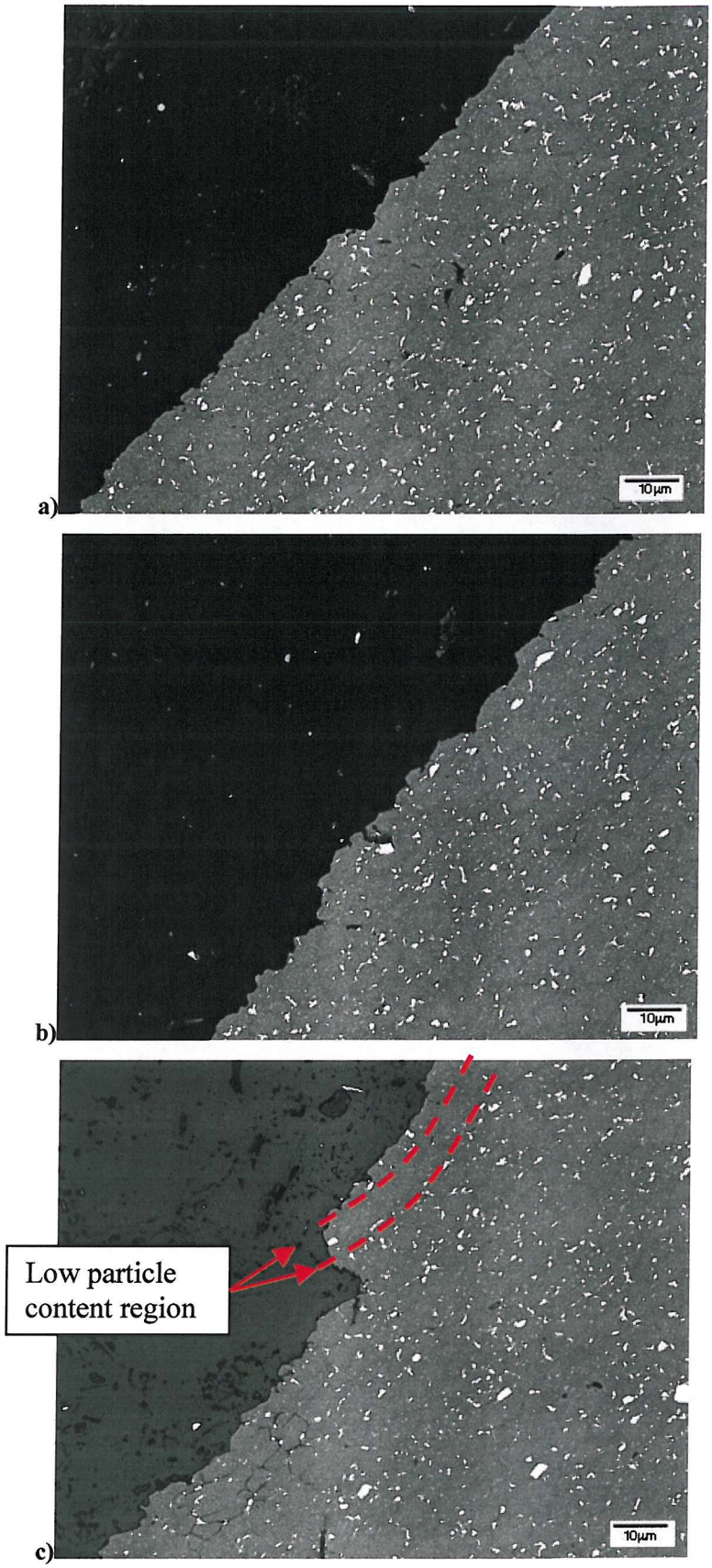

Figure 81 Backscattered SEM image of the curved fracture path at the weld nugget: a) before step, b) after step and c) at step.

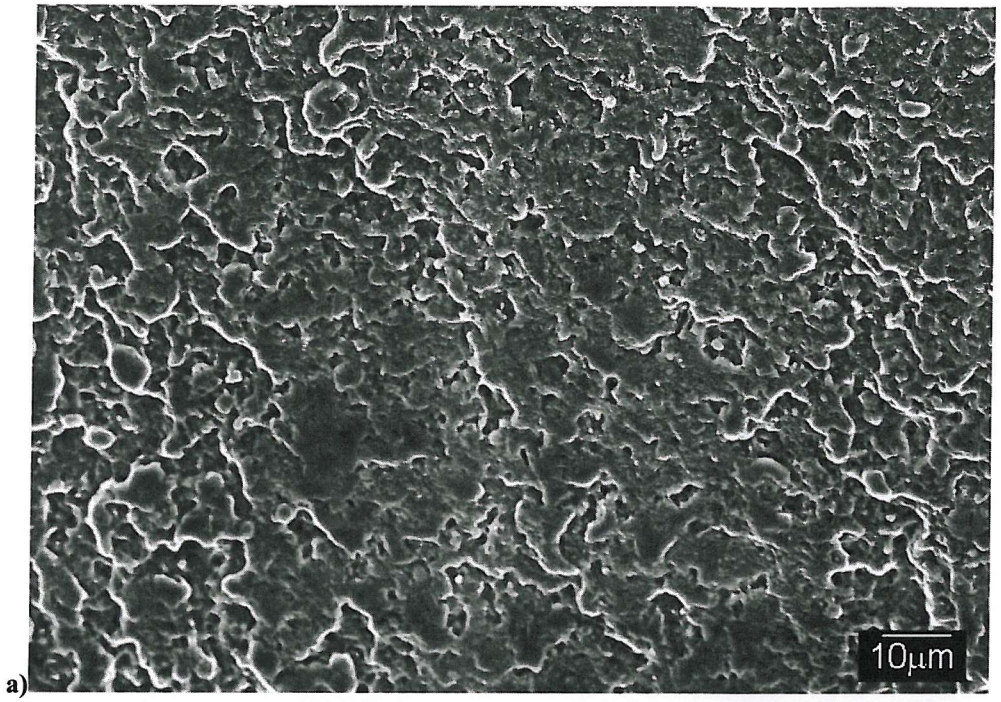

a)

b)

Figure 82 Fatigue crack around the weld nugget region a) SEI and b) BEI.

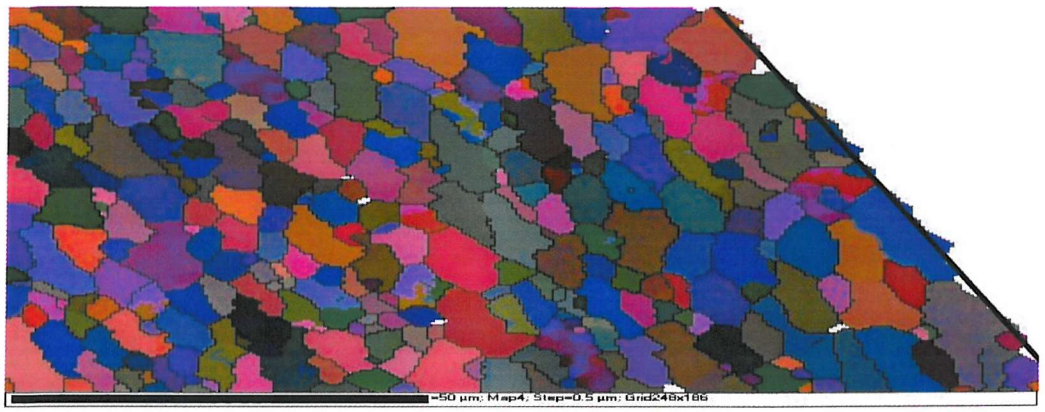

Figure 83 EBSD orientation map of the crack edge for failure over the weld nugget at the top of nugget region (The heavy black line marks the approximate edge of the specimen, data beyond this line has been extrapolated in the Channel 5 software).

4.3 Discussion

4.3.1 Failure Outside the weld region

4.3.1.1 Initiation

It is clear from Figure 63 that the grain structure around the initiation sites for failure outside the nugget are largely un-deformed, with only a very mild grain rotation having occurred during the welding process. It was also noted in the previous section that initiations outside the weld region were seen to occur near the minima in micro-hardness but not actually at the minima, as seen in Figure 64. These facts clearly imply that features other than hardness/local flow and weld grain structure modifications on strength are influencing the initiation behaviour of the cracks, contrary to the observations of Bussu and Irving[25] for 6mm plate for example. Other features that may then be identified as contributing to crack initiation behaviour include:

(1) Potential presence of non-equilibrium melting features adjacent to the weld region,

(2) Local matrix microstructure features, such as grain boundary precipitation and matrix precipitate variation, etc.,

(3) Residual stress states.

The presence of non-equilibrium melting features, as seen adjacent to the fusion zone in fusion welded (MIG, LASER etc.) high strength aluminium alloys[112] has been clearly identified with local failure processes in such welds. Such non-equilibrium melting is identifiable with intermetallic phases elongated along grain boundaries (boundary wetting

occurs). No evidence of such elongated particles was seen, however in the present TMAZ regions, consistent with the lower temperatures associated with friction stir welds (as opposed to fusion processes).

The flow arm-TMAZ interface may be identified with sharp changes in local grain size, shape and orientation, all three of which are identifiable with potential changes in crack initiation processes. In both instances fatigue failure occurred at the rise in hardness towards the weld centre, but this is still some 1-2mm from the flow arm – TMAZ grain structure interface, implying a limited sensitivity to grain structure changes.

In terms of the intermetallics causing crack initiation, the large particle distributions at the observed initiation sites were reasonably equivalent to those of the parent plate (i.e. not heavily broken up or deformed). There is therefore little reason to identify the particles themselves as intrinsically more favourable for fatigue crack initiation over those in the parent plate. Initiation from cracked particles, as seen by Mulvihill and Beevers[12], might have been thought to occur due to deformation during the welding process being sufficient to crack the intermetallics in the TMAZ, however this does not appear to have contributed to failure in the present work, as initiation was dominated by decohesion of the intermetallics and matrix, rather than intermetallic cracking.

In terms of local matrix precipitation effects, the characteristic shape of the hardness trace for a Friction Stir Weld in a heat treatable alloy is clearly dependent on the elevation in temperature caused by the welding process. The predominant drop in hardness from the parent plate into the HAZ/TMAZ has been primarily attributed to the coarsening of

strengthening precipitates (i.e. overaging) during the heat cycle (Russell and Shercliff[50]). This is supported by the Differential Scanning Calorimetry (DSC) results shown in trace C, in Figure 48, taken at the initial drop in hardness moving from the parent plate to the weld line. This shows very little zone dissolution or higher temperature precipitation, indicative of a fully aged structure. Trace D, which is close to the initiation location at the minima in hardness, shows an increased amount of GP zone dissolution and a broad, relatively flat (compared to the parent material trace) precipitation peak at around 250-300°C, indicating that solute was available for precipitation after the weld pass. The low strength at this point must then be attributed to heavy coarsening of S/S' phase and/or heterogeneous precipitation during the welding heat cycle, with the subsequent zone precipitation giving only a limited contribution to strength. Whilst DSC data was not obtained exactly on the rise in hardness between the TMAZ and the central plateau of the weld, it may be presumed that coarse precipitation is still significant at this location, with the increasing hardness indicating increasingly effective resolutionising and subsequent natural ageing of the material, in keeping with the increased zone content seen in the DSC results for the weld centre. The effect of the weld thermal cycle is summarised in the hardness schematic in Figure 84 for the various regions of the weld. The parent plate is in the T351 condition; this initially ages to an effective 'T8' condition (it has been cold worked and naturally aged prior to artificial aging), causing an increase in hardness. Moving closer to the weld centre the plate overages resulting in a drop in hardness, whilst closer to the weld centre resolutionising and natural ageing occurs, although the hardness still continues to decrease due to continued overaging. The increase in hardness which is associated with the weld centre is then the result of resolutionising and natural ageing as the weld temperatures approach those of conventional alloy solution treatments.

In terms of such local ageing effects and crack initiation, the particle decohesion seen at the initiation sites, and the lack of evidence for slip bands at initiation would then appear consistent with overageing/coarsening dominating the slip character of the crack initiation process, with heterogeneous precipitation on the intermetallic interfaces and/or the associated PFZ formation potentially contributing to particle decohesion processes.

In terms of residual stress effects, of the limited work available on residual stresses in friction stir welds, the results of Webster *et al*[95] are perhaps the most significant to date, obtained for 7108-T79 friction stir welds in 6mm gauge plate using synchrotron x-ray diffraction data. It was found that there was a predominantly tensile longitudinal residual stress field that extended just beyond the edge of the weld region[3]. It was also evident that the tensile residual stress field did not strictly follow the shape of the weld nugget. In the transverse direction tensile residual stresses also extended outside the weld region into the TMAZ; they were identified as tensile on the top surface of the weld, becoming compressive moving down through the thickness. In terms of the residual stress fields in the present fatigue specimens, they may of course be expected to be affected by alloy properties, weld parameters and the amount of relaxation that occurs when specimens are machined. As such, the results of Webster *et al*[95] can only be used as a qualitative indication of the stress fields that may be present in the current welds (whilst residual stress measurements have been made as part of the thesis (see chapter 5), limited material supply prevented a reasonable study of the present 13mm gauge welds). On the basis of the Webster *et al*[95] results, it may however be inferred that the crack initiation locations in

[3] A degree of caution must be applied to the Webster *et al*[95] data however as corrections for variations in the strain free lattice parameter across the weld were not made.

all of the present 13mm gauge welds (failures inside and outside the nugget region) occurred in regions of tensile transverse residual stress, which may then be seen as contributing to failure at these location. It is however clear that local microstructural conditions (particularly those associated with the macroscopic flow discontinuities in the flow arm) may still exert a controlling influence on the crack initiation behaviour. Overall it may be seen that crack initiation behaviour in the present welds shows a number of unique features in relation to results from the literature, (particularly in terms of the influence of flow features of the weld and the fact that HAZ/TMAZ crack initiation was not specifically linked to the hardness minima) highlighting the potential complexity of fatigue influences that may exist in friction stir welded structures.

4.3.1.2 Propagation

The grain structure in the regions where crack growth occurred outside the weld region are relatively uniform and undistorted by the welding process, as shown by Figure 63, consistent with the reasonably straight conventional crack path behaviour at a macroscopic scale. There is a moderately crystallographic transgranular propagation mode at low ΔK levels in the short crack range, whilst at higher ΔK levels there is a higher degree of ductile propagation, as generally reported for high strength Al alloys (consistent with increasingly homogenous deformation as crack tip plasticity spreads in relation to the distribution of slip blocking features). The thermal treatment of the welding process may be seen to limit the incidence of planar deformation commonly linked to the incidence of crystallographic features during crack growth (i.e. due to coarsening/overaging of the original T351 microstructure), although the degree of resolutionising and re-precipitation of zones close to the weld (indicated by DSC) may be expected to provide some contribution to slip planarity (i.e. providing shearable precipitate strengthening).

The growth rates reported here are slightly higher than those identified for parent plate in the T351 condition. The growth rate results obtained by Dalle Donne *et al*[45] for long cracks in the TMAZ of 4mm gauge 2024-T351 friction stir welds in the transverse orientation conversely show significantly lower initial crack growth rates than results reported here. The results obtained by Dalle Donne *et al*[45] were for through-thickness cracks with the low apparent growth rates being attributed to crack closure due to compressive residual stresses. Given the nature of the residual stresses as, noted in section 4.3.1.1, compressive stress on the bottom face of the weld may well be expected to contribute to enhanced crack closure in a through thickness defect, lowering crack growth rates, however the net influence of tensile and compressive residual stresses across a whole crack front is not immediately clear. It is significant to note however that the present growth rate data were obtained for relatively small cracks near the weld top surface. As such, only residual tensile stresses are expected to act on the cracks (Webster *et al*[95]), rather than a balance of tensile/compressive stresses across the whole sample thickness. Therefore, residual tensile stresses may indeed be identified as a contribution to the differences in crack growth rates seen here and in the work of Dalle Donne *et al*[45].

4.3.2 Failure over the nugget region

4.3.2.1 Initiation

As noted in 4.2.3.2 the exact microstructural cause of the crack initiation over the weld nugget region in the 13mm weld specimens was not clearly identifiable from the fracture surfaces. Of the common crack initiation mechanisms in wrought high strength Al alloy welds, the basic microstructural features of the flow arm may be seen to have a number of

potential influences. It is clear for example that intermetallics were heavily broken down and redistributed by the welding process, which may be noted to reduce the probability of particle failure[10] with reduced probability of finding a critical defect in a given particle and/or reduced energetic driving force for failure. In terms of slip band crack initiation, the very fine grain structure of the weld region may be expected to strongly inhibit slip band formation; this is consistent with the distinct lack of crystallographic features on the present fracture surfaces (see Figure 77). The weld region of friction stir welds is also generally identified as having a "low" defect content compared with fusion welds, limiting the incidence of initiation from porosity. The residual stresses in the weld centre are relatively low (cf. fusion welds) with results reported in Chapter 5 for X-ray diffraction in the 25mm gauge 2024-T351 friction stir welds indicating that the residual stresses in the weld region are $<\pm 50$MPa, i.e. far less than the residual stress that may be developed during fusion welding[113].

It is clear from the above factors that the weld nugget should be reasonably resistant to crack initiation. This has generally proven to be the case, with crack initiation occurring preferentially outside the weld region (as discussed in section 4.3.1) except when a macroscopic discontinuity in the weld flow features is present. The exact cause of the discontinuity is still unclear, and this type of defect does not appear to have been reported elsewhere in the literature. Establishing the processing conditions that caused the discontinuities is beyond the scope of the current work, but they are presumably related to instability in the material flow pattern around the weld tool and subsequent changes in the local temperatures, strain and strain rate distributions. On the basis of observing relatively large intermetallics, the region is likely to have experienced relatively low strain levels

with such particles being likely to be retained from the parent plate. Of the limited literature on friction stir weld defects, Dong et al[54] have however reported the presence of macroscopic flow instability, in a model of 6000 series weld and actual welds (material details not given), if the rotational speeds are relatively high; this was manifest in occasional irregular flow patterns within the weld that are therefore somewhat analogous to the present flow irregularities. No detailed microstructural assessment of the features was however provided by Dong *et al*[54] for more detailed correlation with the present work.

In terms of the microstructural features of the flow discontinuities that have been studied here, a clear difference in intermetallic particle content was found across the discontinuity as seen in Figure 72. On the coarse intermetallic side of the discontinuity, intermetallics as large as ~20μm were identified, however no microscopically hard interface between the intermetallic regions was apparent. Marginal hardness (~3Hv) and grain size variations were seen across the discontinuity and no significant pore/defect effects were seen on the primary cracks.

Of the likely influences of microstructure on crack initiation Figure 85 shows a relationship between particle size and relative probability of fatigue crack initiation in a 2024-T4 aluminium alloy determined by Kung and Fine[10]. It is clear from these results that the normal flow arm intermetallics are relatively unlikely to initiate fatigue cracks as they fall below the critical 4-5μm particle size. However intermetallics on the coarse side of the flow discontinuity are observed up to ~20μm in size. The significance of intermetallics particle size effects on crack initiation is further confirmed by the results of Laz and Hillberry[122] (for 2024-T351 plate) in Figure 86, showing that no particles smaller

than 5μm give rise to fatigue cracks. Overall it may be seen from the present evidence that whilst the particularly uninformative nature of the fracture surfaces in the fine scaled weld material prevents detailed tracing of crack path evolution, the presence of relatively large intermetallic particles (approaching the size of those initiating cracks in the parent plate) in the macroscopic flow discontinuities of the flow arm is the most likely microstructural cause of their fatigue failure.

4.3.2.2 Propagation

A distinctive feature of crack propagation in the over nugget failures was clearly the macroscopic crack deflection closely following the onion ring pattern of the nugget region. As such, it is evident that such flow features of the weld may represent intrinsic weakness within the welds. Microscopic examination of the failures revealed a mixture of relatively flat transgranular regions, and intergranular failure regions, which appear to be linked to patches of continuous grain boundary decoration (see Figure 77b). At greater crack lengths a more generally ductile failure mode was also evident.

Given the incidence of macroscopic failure paths along the flow patterns of the welds, it is clearly valuable to consider the microstructural features associated with the bands that are seen. In this respect it is possible to identify the following features related to the onion ring features in the literature:

1. Variations in intermetallic particle density between the bands,
2. Variations in grain size/shape.

In terms of the present 13mm welds, it is clear that grain size variation within the weld nugget was quite limited, corresponding to no more than 1-2μm. Whilst not all authors

have reported such variations, these results are consistent with Mahoney *et al*[32]. It may also be noted that the grain structure of the present welds was aligned to some extent with the banding of the weld. The alignment is however relatively mild, with grain aspect ratios of the order of ~0.6, i.e. very much less than those found in common wrought Al alloy products. It should also be noted that the local variations in the grain structure identified in the present welds are not "continuous" features, but are quite patchy compared to the extended nature of the onion rings that the crack appeared to follow.

FEG-SEM observation revealed variations in particle size and distribution across the weld nugget region that are associated with the onion ring features. In particular, 3 populations of particle were identified; i) larger intermetallic debris from the parent material, up to ~3-4μm in diameter, ii) intergranular precipitates of the order of 1-2μm, and iii) intragranular precipitates up to ~0.5μm. Norman *et al*[36] also noted a difference in the intermetallic distribution between the bands in the nugget region consistent with the current findings although only the coarser particles were particularly identified. The intragranular particle observations and differential etching effects noted in Section 4.1.4 do suggest a local variation in matrix precipitate condition between the bands. Slow cooling of 2024-type material may be expected to produce coarse intragranular precipitation of S-phase, particularly on Mn containing dispersoids[5]. Such precipitation would be expected to interact with etching in Keller's reagent, i.e. the more heavily etched bands would be consistent with greater intragranular precipitation.

Given the fine scale of the bands it seems unlikely that variations in precipitation character between bands can arise from heat distribution effects during or after the welding. A

heterogeneous distribution of intragranular nucleation sites may then be identified as a cause of the local hardness and etching effects between the bands. Figure 87 [123] shows the heterogeneous nature of the dispersoid particles in 2024-T351, in commercial DC cast plate form. Whilst the relationship between such parent plate heterogeneity and final weld structure has not yet been reported in the literature, it is clear that significant heterogeneity exists within the parent material (both in dispersoid distribution and the fibring of larger intermetallic particles) that may not be `removed` in the friction stir welding process. It has been reported that such onion ring bands disappear when the rotational speed of the tool is increased[35], consistent with more effective mixing and homogenisation of the weld material.

Further sources of heterogeneity intrinsic to the weld process may be identified with local variations in strain, and strain rates. Whilst the exact local deformation conditions within a given stir weld remain the subject of debate in their own right (particularly with the use of complex threaded or fluted tool shapes), it may be seen that associated bands of dislocation structure and/or distribution of dispersoid and intermetallic particle debris may have a direct influence on the availability of heterogeneous precipitation sites within the material and the subsequent susceptibility to inter-or intra-granular precipitation during cooling. In terms of strain and strain rate variations, it may for example be noted that onion ring bands have been linked by several authors to the forward movement of the weld tool with each individual rotation[35,79,80]. If this is due to material being effectively picked up and deposited in layers that are mechanically coupled to the tool rotation during each cycle, similar to Colligan's[40] proposed mechanism, then variations in deformation condition *within* each band may indeed be identified with material that is closer to, or

farther from, the metal/tool interface. Alternatively, the incidence of adiabatic shear bands (ASBs) may be anticipated in high strength aluminium alloys[114] under conditions of severe temperature and strain rate (of the order 500°C and 10 /s respectively), with clear implications for homogeneity of temperature and deformation process. Such temperature and strain conditions have indeed been reported within the literature in relation to friction stir weld processing[53], but have not as yet been explicitly linked (to the best knowledge of the author) to the presence or absence of ASBs in friction stir welds. Notwithstanding the origins of deformation banding within the nugget, the fact that grain size variations may be limited (as seen here) is consistent with the assertion of Hassan *et al*[61] and Frigaard *et al*[115] that the final nugget grain dimensions must be controlled by growth rather than strain/strain rate, although further assessment and quantification of weld process conditions is clearly required to verify the presence of such complex mechanical and microstructural interactions.

Noting the particle distribution differences between the bands reported above, it is of course interesting to consider the potential strength differences that might arise locally, as heterogeneous precipitation within certain grains or grain boundaries might be expected to limit solute availability for re-precipitation after the weld pass. In Figure 88, a variation in hardness between the light band and the dark bands of the weld nugget region is in fact seen from local microhardness measurements. It is clear from the figure that the light band is consistently harder than the surrounding dark bands by ~7Hv (with an expected σ_y variation of ~30MPa)[4]. The light bands shown here by optical microscopy have a higher incidence of coarse intergranular precipitates while the dark bands contain more of the

[4] It should be noted that this is expected to be a lower bound given the comparative size of the hardness indents to the bands present, therefore some material outside the bands is also likely to be sampled.

fine intragranular precipitates. Sutton *et al*[79] also noted a variation in hardness between the onion ring bands by values of the order of ~6HK (Knoop hardness). It is interesting to note that Sutton *et al*[79] attributed increased hardness in certain band to the presence of coarse intermetallic debris, with no detailed study being carried out on finer precipitation features of their weld structures.

Oxide particles have been reported by Larsson *et al*[116] to be deposited as lines along the original joint interface between regions of different alloys when dissimilar alloy welds are performed, see Figure 89. They suggest that the particles are not seen in similar alloy welds due to the difficulty of identifying the regions of the original plates. In the current work a detailed attempt was made to ascertain if lines of oxide particles were present in the region where crack growth occurred (i.e. linked to the onion ring structure). This was carried out at a higher magnification than Larsson *et al*[116] used to obtain their results, across a 3mm wide region close to the location of crack growth, see Figure 90 (shows the region that was inspected for oxide particles), with no oxide particle bands being detected. However they may still be present on a very fine scale but this would have to be less than ~0.25μm. It should be noted that the continuity of such oxide strings will be a function of the exact weld conditions, and oxide particles were not observed on the transverse crack profiles in the current work. It is therefore reasonable to assume that in the current study that oxide particles bands, such as those reported by Larsson *et al*[116], were not a determining factor in the deflected failure within the nugget region..

Given the current evidence, the deflected nature of crack growth in the weld nugget region may be identified as a consequence of propagation being channelled by variations in matrix microstructure and/or the mechanical influence of crack propagation between

regions of high and low yield stress (cracks tending to deflect back into a soft material on approaching a hard material interface, as the crack tip plastic zone is constrained on entering the harder material). The most prominent, direct microstructural effect would appear to be the presence of intermediate sized intermetallic particles (up to 2μm), as indicated in Figure 82b). Whilst extensive void growth was not seen from these particles at the fracture surface, it may be presumed that they still provided some favourable path for crack growth to occur. The fact that such particles were often intergranular in character does not appear to have been critical however, as much of the deflected crack growth was seen to be transgranular.

In terms of mechanical influences of regions of high and low yield strength, it is valuable to note the work of Suresh *et al*[117], studying the growth of fatigue cracks in a ferritic steel (σ_y = 240MPa), approaching a perpendicular interface with an austenitic steel (σ_y = 340MPa). As shown in Figure 91, sharp crack deflection through angles of ~90° were identified with the mechanical interaction of the soft and hard layers. Whilst the reported difference in yield stress between the steels in Suresh's study is 40%, which is significantly higher than the (lower bound) estimated ~10%[5] change seen in the current work but , it may be seen from Figure 76 and Figure 80 that, deflected crack growth occurs at the interface between dark and light bands, with the crack staying outside of the bands of harder material, analogous to the behaviour in Figure 91.

Monotonic crack propagation along onion ring bands in the weld centre has been reported by Sutton *et al*[79] for 2024-T351 friction stir welds in 6.25mm gauge specimens, under mixed-mode I/II loading with a through thickness pre-crack in the weld centre parallel with the welding direction. Figure 92 clearly shows that the crack deflection was along the bands, as seen on the top surface of the weld, in a similar manner to the deflections seen for the transverse bands in the current work. Sutton *et al*[79] attribute the deflected crack growth along the bands to larger particle (~5μm+) density differences. They suggest

[5] This is thought to be a lower bound due to the macroscopic nature of the hardness indent compared to the bands, resulting in the sampling of surrounding material along with the band

that growth is along coarse particle rich bands consistent with the monotonic load condition as opposed to the cyclic failure of the present work.

Overall it may be identified from the present results that preferential failure/crack deflection at the nugget `onion ring` features may be linked to a combination of failure via the intermediate intermetallic particle distribution formed by heterogeneous precipitation during the weld cycle, and mechanical contributions of strength differentials between the onion ring bands. It may be noted however that these factors are intimately linked, as heterogeneous precipitation process may largely determine local flow strength, with the two factors therefore being difficult to strictly separate.

4.3.3 Fatigue crack growth life

The fatigue life of the non-overloaded specimen that failed over the nugget region is significantly shorter than for the specimens that failed outside the nugget region. This is a concern for lifing predictions. An attempt was made to characterise the fatigue crack growth of the over nugget failure with respect to the typical crack growth rate regimes for 2024 – type alloys. The typical curves are represented schematically in Figure 93, curve A represents conventional short crack behaviour involving microstructural arrest events and a gradual build-up of crack closure, eventually joining the long crack growth curve, curve B represents a typical long crack growth curve and curve C represents a closure and microstructural interaction free behaviour (intrinsic growth). The effects of heat treatment can be considered limited in relation to these relative differing crack growth behaviours. Fatigue crack growth lives can then be estimated for the present welds using a Hobson approach for short cracks in particular.

The model suggested by Hobson[118] assumes that the fatigue crack growth rate is proportional to the distance between the crack tip and the grain boundary. The crack propagation rate can be described by:

$$\frac{da}{dN} = C_1\left(\frac{n}{2}d - a\right)^{1-\alpha} a^{\alpha} \qquad \textbf{Equation 7}$$

Where d is the grain size, n is the number of grain spacings traversed by the crack, a the crack length, C_1 and α constants, (in current work α=0)

The equation above assumes that the crack will be arrested by the grain boundaries. The constants C_1 and α are obtained by experimental fitting. This approach was developed further by Grabowski and King[119] and Bomas et al[120]. They define the boundary conditions of the model in terms of the spread of maximum and minimum growth rates based on experimental data for the material being studied. The growth rate is then assumed to vary in a linear manner between the grain boundaries. Grabowski's model, unlike other models, also takes into account growth rate perturbation within the grains, which may occur when slip orientations change.

An initial defect size of 20μm was selected on the evidence of the intermetallic distribution around the macroscopic flow discontinuity seen in the flow arm and the initiation observed at a decohered intermetallic. In the current work three growth rate regimes are used, A) is a typical short crack regime showing microstructural arrest events and the build up of crack closure, this is based on short crack data obtained for 2024-T351 specimens at Southampton by Lefebvre[113] shown in Figure 94, B) is a typical long crack growth curved obtained from the literature[111] and C) represents closure and microstructural interaction free behaviour, this data was obtained by Xu[121] by careful

crack closure measurements. The results reported in Table 6 clearly show that for the failure over the nugget to have been so short (65,000 cycles), the fatigue growth must have followed the rapid closure and microstructural interaction free growth curve. This is consistent with the reported behaviour of very fine grained materials where the plastic zone size rapidly exceeds the grain size dimension and the limited slip distances limit the build-up of roughness induced closure (RICC). Also the tensile residual stress present in the region may be further reducing closure effects. While it can clearly be seen that for the failure outside the nugget there is good agreement between the calculated life and actual life when a short crack growth curve is used (see Table 6).

Stress (MPa)	Crack growth regime	Predicted growth life to 3mm (cycles)	Actual fatigue life (cycles)
170	Closure and Microstructure free growth	68,000	65,000 (nugget)
170	Short Crack	536,000	431,000 (HAZ)

Table 6 Fatigue growth lives for the nugget and HAZ/TMAZ region failures. (Based on initial 20μm initiation defect)

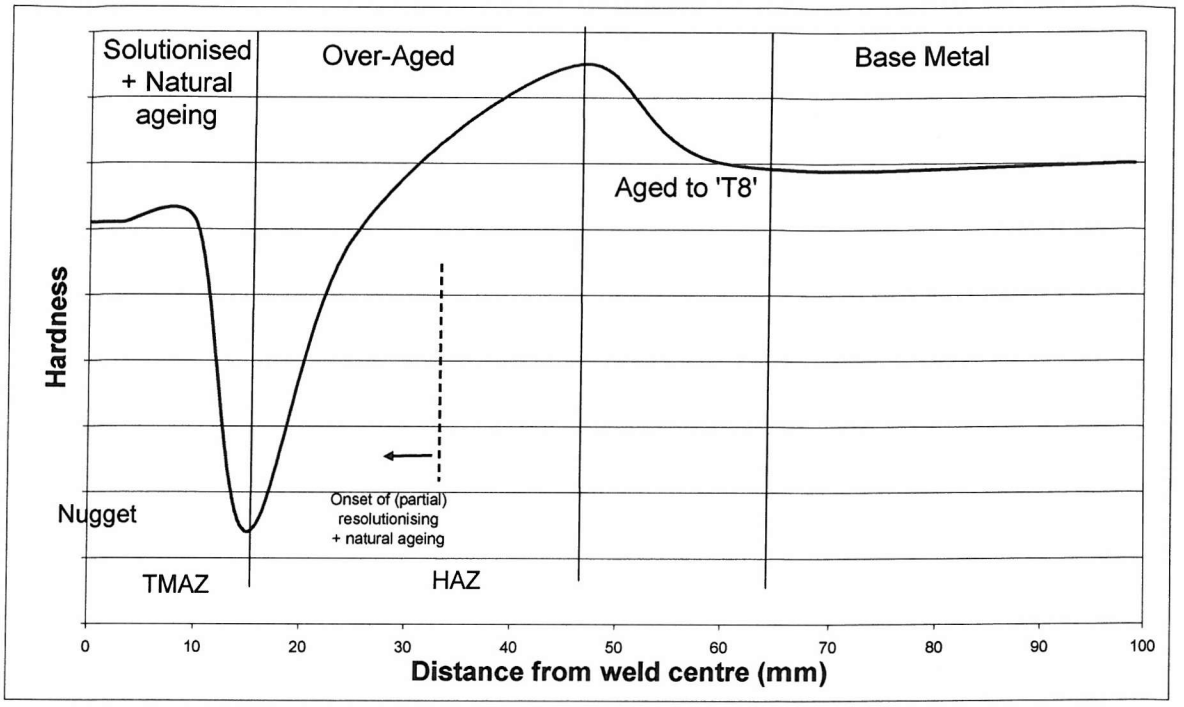

Figure 84 Schematic of hardness variation across a friction stir weld, labelled with approximate heat treatment conditions[36].

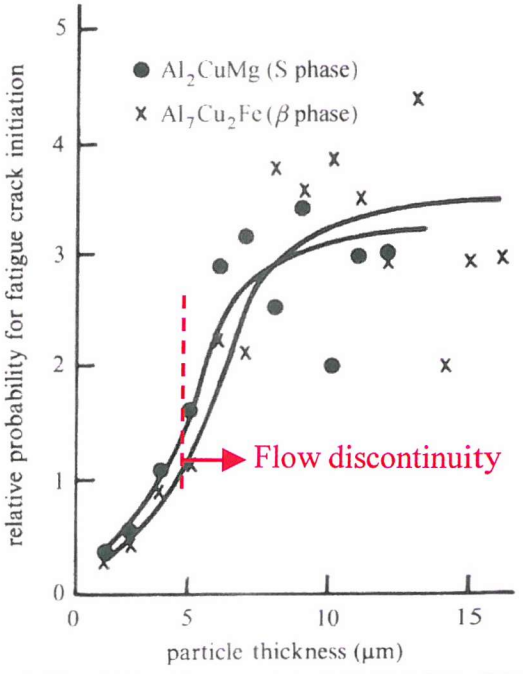

Figure 85 Relative probability of crack initiation versus the constituent particle thickness normal to the stress axis for S and β inclusions in 2024-T4 aluminium alloy[10] (uneasily testing at R=-1 and σ_{maz} = 140-65MPa)

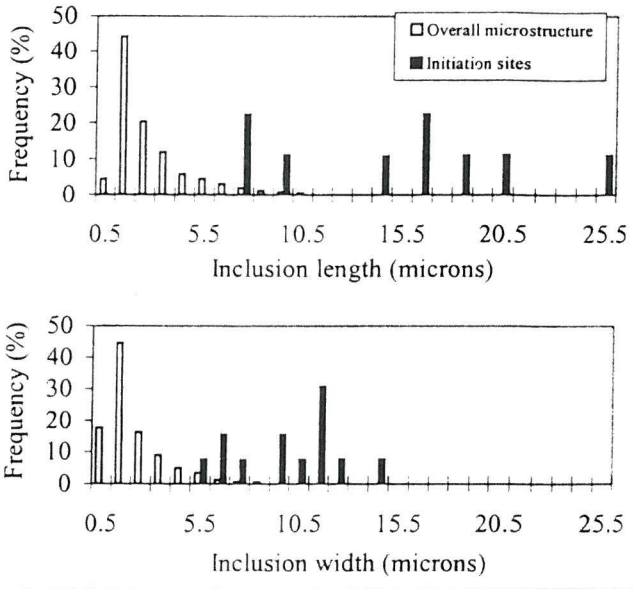

Figure 86 Intermetallic inclusion size distribution, with relative frequency of crack initiation[122] in 2024-T351.

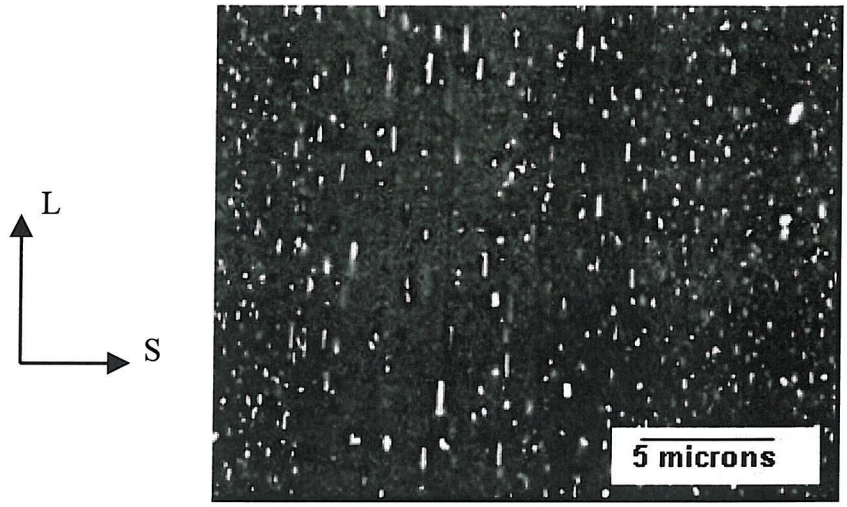

Figure 87 SEM BEI image showing the heterogeneity of dispersoid particle distribution in parent plate 2024-T351[123]

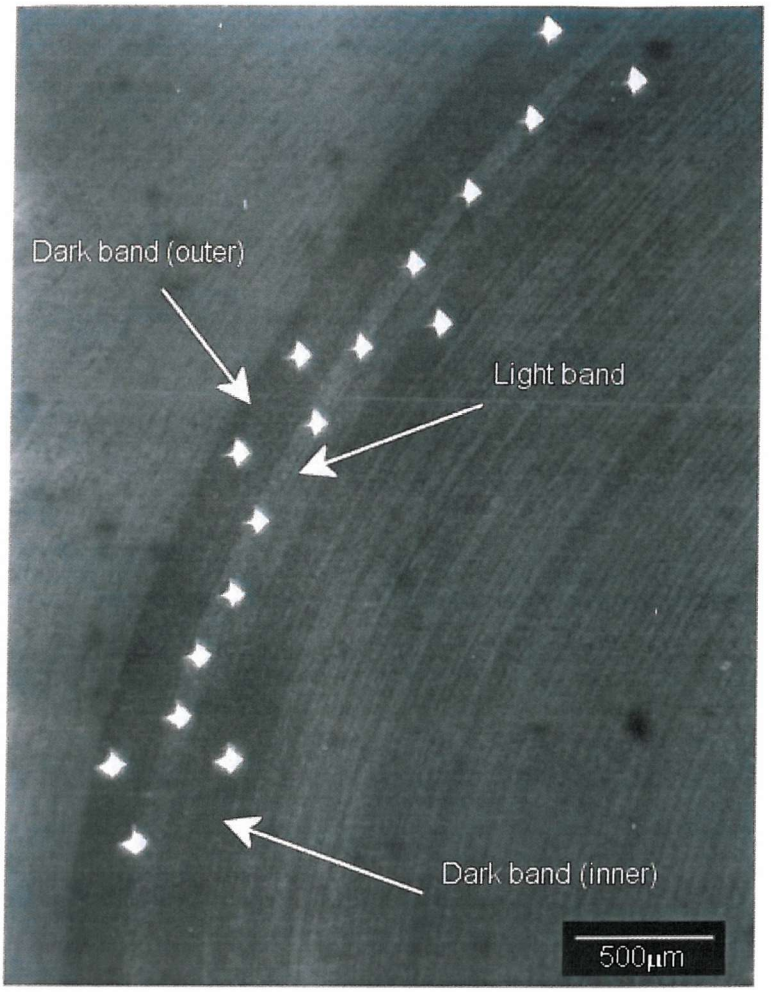

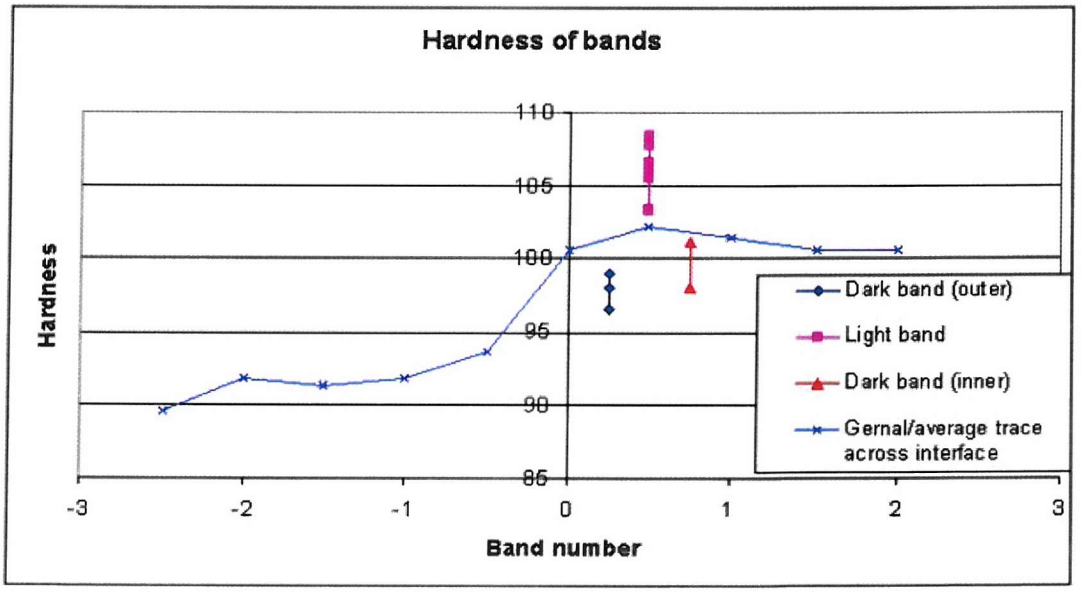

Figure 88 Hardness variation between bands in the weld nugget region

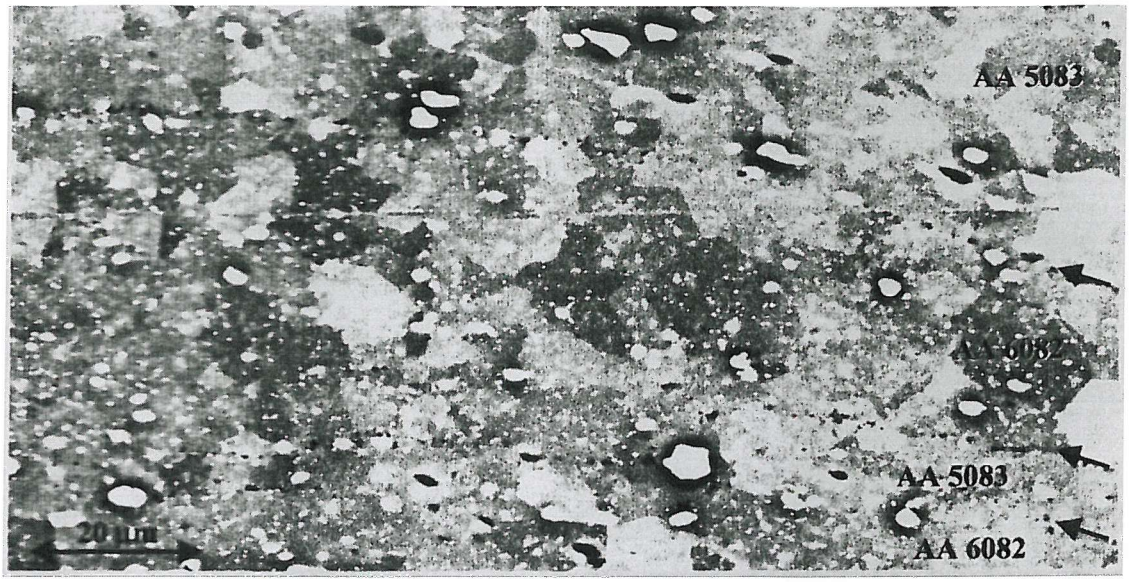

Figure 89 BEI image within the weld nugget in a dissimilar alloy friction stir weld of 5083 and 6082, highlighting dark oxide particles (arrows) delineating boundaries between 5083 and 6082 regions.[116]

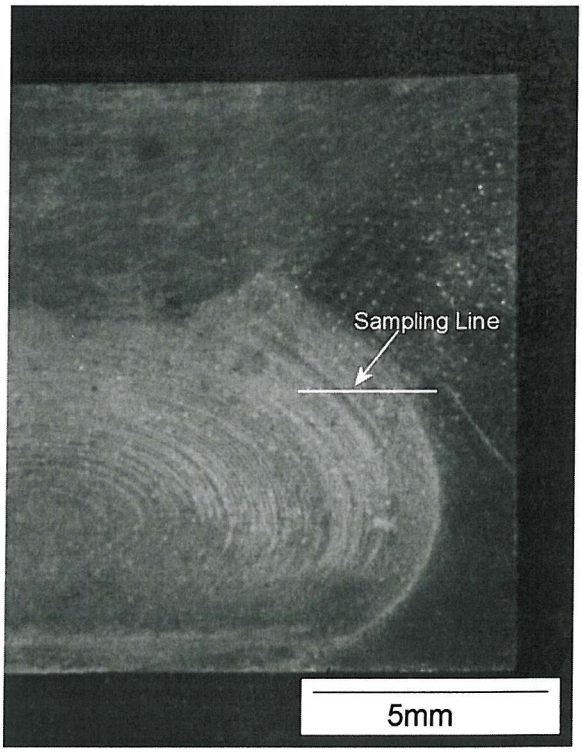

Figure 90 Region examined for oxide particles in the nugget region of the present 13mm gauge weld.

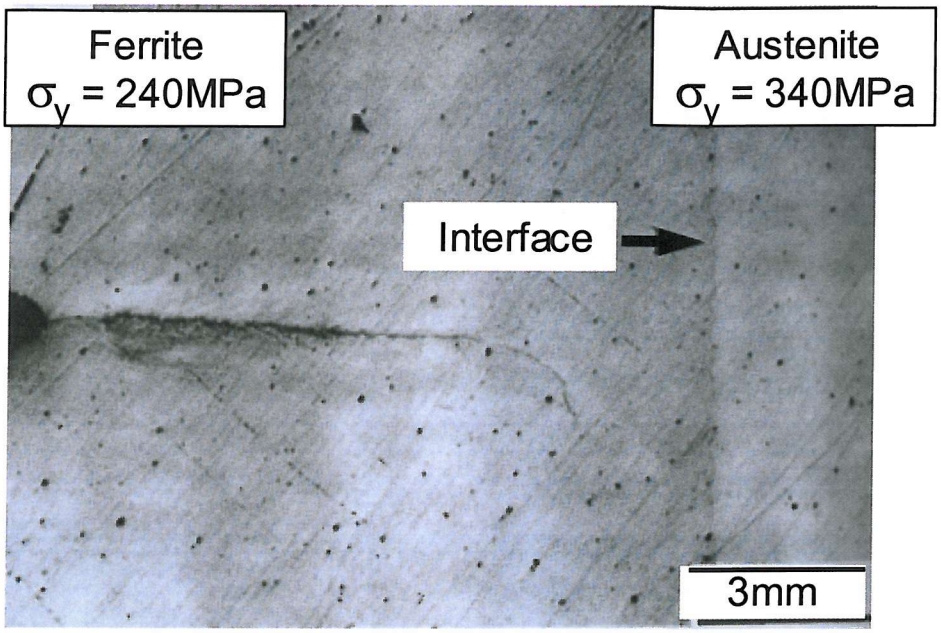

Figure 91 Optical micrograph illustrating the incidence of crack deflection in a nominal mode I fatigue crack approaching a sharp interface between low and high yield strength materials of equal moduli (corresponding to ferritic and austenitic steel) [117]

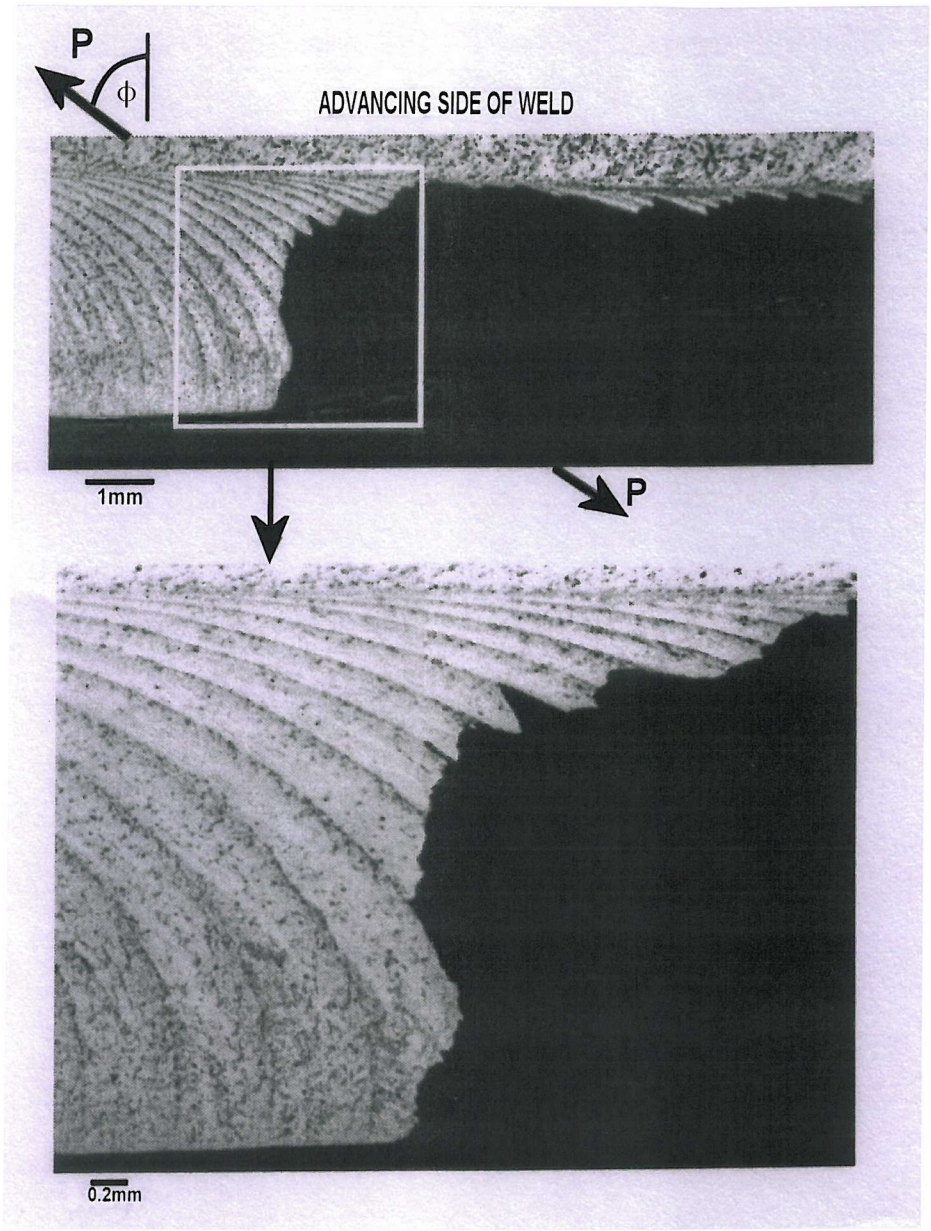

Figure 92 Crack propagation at a friction stir weld in 2024-T351 under monotonic mix mode I/II loading. Φ=60° where Φ is the angle between the normal to the welding direction and the loading direction.[79]

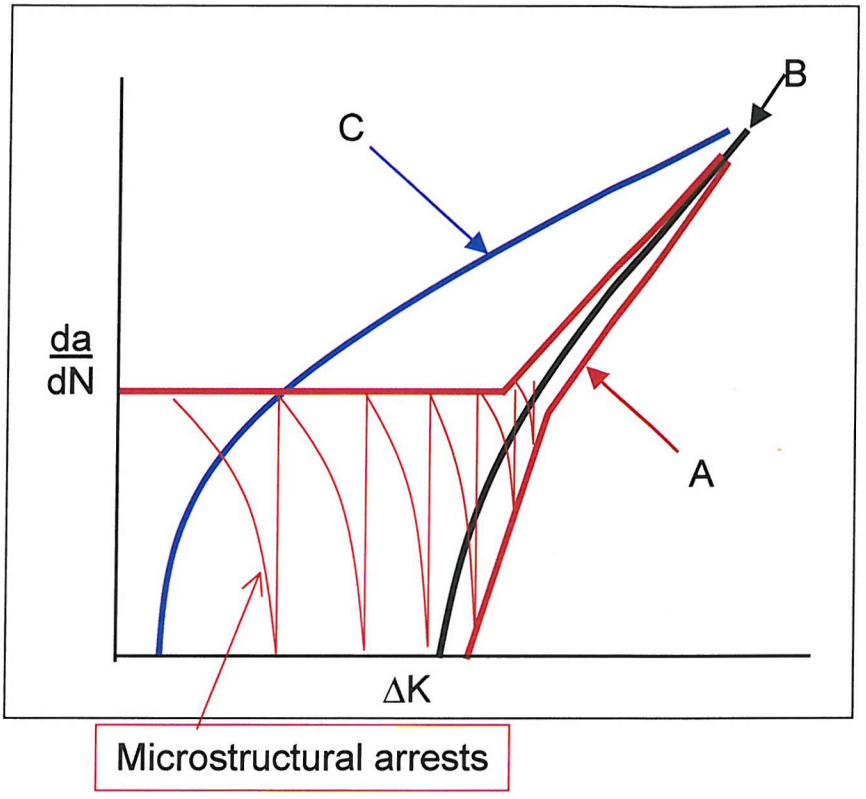

Figure 93 Schematic fatigue crack growth regimes for 2024-type alloys, A) typical short crack regime showing microstructural arrest events and the build up of crack closure, B) typical long crack growth and C) closure and microstructural interaction free behaviour.

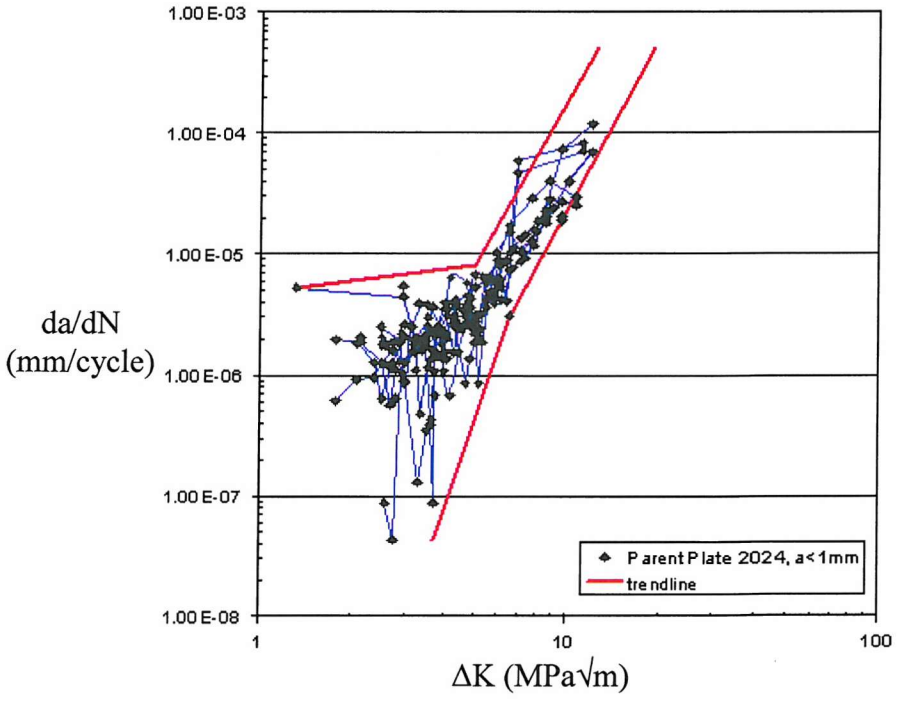

Figure 94 2024-T351crack growth date obtained at Southampton, showing scatter band used in growth rate calculation[113].

Chapter 5: 25mm Gauge Welds

5.1 Materials

5.1.1 Weld Conditions

The results in the following sections have been obtained from two 700x300mm plates, with a welded length of ~670mm, provided by Airbus UK. The plates were both 2024-T351 in 25mm gauge, with single partial penetration friction stir welds (to a depth of ~19mm) using a proprietary tool design. The plates were non-destructively assessed by Airbus prior to release, with the results of this assessment showing that both of the welds were sound to a minimum defect size of 1.2mm.

The two plates of interest are identified as "fast" and "slow" on the basis of weld feed rate, see Table 7. Calculated "weld pitch" values are also shown, which are defined by Seidel and Reynolds[124] as the tool advance per rotation (welding speed/rotational speed). This parameter may be shown to be linked to specific weld energy (joules/meter), where welds with a higher relative weld pitch are associated with colder processing conditions. In the first instance it may then be seen from Table 7 that the "slow" weld may be associated with a higher weld temperature, having a 23% lower weld pitch than the fast weld. When the expression of Midling and Rørvik[57] (Section 2.2.3) for energy input per mm for a friction stir weld, is applied to the current welds (see Table 7 column 6) the fast weld is seen to have approximately 6% lower energy input per mm than the slow weld. The equation in this case takes account of tool rotational speed, traverse speed, vertical force

and the diameter of the weld tool shoulder rather than the weld pitch which only considers feed rate and rotational speed.

Weld	Feed rate (mm/min)	Rotational speed (rpm)	Vertical force (kN)	Weld pitch (mm/rev)	Energy per unit length (J/mm)
Fast	60	195	49	0.31	44.5
Slow	40	170	40	0.24	47.5

Table 7 Welding parameters for 25mm welds.

5.1.2 Macrostructure: 25mm welds

Given the work carried out previously on the 13mm 2024-T351 friction stir welded plate (Chapter 4), where the presence of flow discontinuities on the crown surface of the fatigue specimens was closely identified with crack initiation, an initial study of the crown surface material flow features of the 25mm welds was carried out. Figure 95a) and b) shows typical etched macrostructures of the crown surfaces of the fast and slow welds respectively, skimmed by 1.8mm (close to the test depth. No macroscopic flow discontinuities were seen in either weld, at least in a form that was visible under equivalent imaging conditions to those used previously. The advancing (sharp) side of both welds can easily be identified, with the fast weld exhibiting a wider and more defined weld structure than the slow weld.

Figure 96 shows a transverse etched cross sections from each of the three welds that have been studied (i.e. the fast and slow 25mm welds and the 13mm weld discussed in Chapter 4). It may be noted that crown surfaces of the 25mm welds have been skimmed by 1mm from the original parent plate thickness in the images, as this was the supplied form of the materials. It is clear that the flow arm and nugget structure of the 13mm weld is not as evident in either of the 25mm welds. There was no well defined onion ring banding in the

25mm gauge welds, however both the fast and slow welds exhibited a roughly elliptical swirl pattern at the weld centreline (points A and B in Figure 96a) and b) respectively), which is set somewhat deeper into the weld in the fast weld than the slow weld. The slow weld also appears to have more defined vertical banding features (point C in Figure 96b)). The flow features that are present in the slow weld between the near surface region and material deeper into the weld are also more distinct than those in the fast weld (particularly the flow apex at X in Figure 96b)). The pattern of grain rotation in the TMAZ regions is also slightly different between the 25mm welds. The grains in the first 3mm below the crown surface of the fast weld (bearing in mind the 1mm skimmed off the parent plate thickness) appear to have a general upwards rotation on both sides of the weld (see D and E in Figure 96a)). In the slow weld the grains on the retreating side appear to rotate upwards towards the surface (see point G in Figure 96b)), whilst on the advancing side of the weld the grain rotation is generally downwards (see F in Figure 96b)).

5.1.3 Hardness Characteristics

Figure 97 shows hardness traces taken 2mm below the crown surface of each of the 25 welds and the trace taken from 2mm below the crown surface of the 13mm weld. The similar general trend is seen for all 3 measurements, with characteristic minima on either side of the weld centre and a moderately hard central plateau. The 25mm welds however exhibit a narrower plateau compared to the 13mm weld. It is also clear from Figure 97 that the fast weld has a harder plateau across the central weld region and less severe minima in the TMAZ/HAZ region compared with the slow weld.

Figure 98 shows hardness traces for both the fast and slow welds taken 7mm from the root surface, corresponding to the base of these non-penetrating welds. It is evident from the

figure that whilst these measurements are well within the weld region, there is no distinct plateau in hardness at the centre, i.e. the weld itself actually represents the hardness minima in these profiles. It is also clear from Figure 98 that the fast weld root is approximately 10Hv harder than the slow weld across most of the profile.

Hardness maps have been produced for both of the 25mm welds, as shown in Figure 99 for the fast weld and Figure 100 for the slow weld (a transverse section of the weld centre is shown in both diagrams). In Figure 99 and Figure 100 it is clear that the soft band (shown in yellow) surrounding the weld is not expressly linked to the grain structure. This is most evident at the root of the weld where the soft band extends right across the nugget of the weld, with no clear indication of a weld/TMAZ interface in the hardness values in this region. Figure 101 highlights a hardness trace taken at the interface between the nugget and TMAZ some 5mm from the crown surface of the fast weld. It is again clear that the drop in hardness does not occur directly at the change in grain structure from the fine structure of the nugget to the deformed TMAZ structure, with the minima occurring well beyond the fine grained region, i.e. in the TMAZ, in keeping with observations made in the 13mm weld. A similar trend is seen in Figure 102 for the retreating side of the weld; however the edge of the weld nugget is less sharply defined, and the slope of the hardness drop is more linear and less severe than for the advancing side.

It is clear from Figure 99 and Figure 100 that hardness levels in the weld centre are generally greater in the fast weld at all depths. The through thickness hardness variations measured at the centre line for both weld speeds is shown in Figure 103. A gradual decrease in hardness is seen through the depth in both cases, with a hardness minimum arising towards the weld root. Hardness levels then clearly rise for measurements made in

the material immediately below the actual weld nugget (bearing in mind these are only partial penetration welds). A significant difference between the 25mm welds reported here and the 13mm weld studied previously is clearly the soft region of fine grained weld root material of both the fast and slow welds which was not present in the 13mm weld.

5.1.4 Differential Scanning Calorimetry: 25mm welds

DSC results shown in Figure 104 are taken from two locations within each weld; firstly from the flow arm, 2mm below the plate crown surface, corresponding to the "top surface" of the fatigue specimens (labelled as Flow Arm), and secondly close to the weld root ~ 7mm from the base of the plate (labelled as Weld Root), this corresponds to the surface used for the "root face" testing, see Sections 5.1 and 5.3. It may be seen that strength levels scale reasonable well with the zone dissolution energy content (endothermic reaction between ~150 and 250°C) consistent with final strength at the weld centre being determined by the Cu and Mg solution content available for precipitation after the weld pass, although differences in higher temperature precipitation reactions are also evident between the various materials (in particular, a general decease in precipitation reaction energies around the sharp S/S` formation peak of the parent material, consistent with varying levels of resolutionising). Evidence of a higher temperature phase is also seen (around 300°C) consistent with the formation of Ω phase on slow cooling, as noted in the 13mm weld data[108].

In terms of higher temperature thermal effects, Figure 105 shows evidence of changing incipient melting conditions in the 5 material conditions shown. In particular, the slow weld flow arm specimen shows the most distinct change, with no clear incipient melting peak arising in this material/location combination.

5.1.5 Microstructure: 25mm welds

- ***Grain Structure***

Figure 106 shows the locations of selected micrographs for both the fast and slow weld regions (transverse sections). It is clear from the series of optical images shown in Figure 107 that the grain size of the fast weld is generally coarser than that of the slow weld at all depths. The grain size reduces in both welds moving down through the weld region; this becomes particularly significant at a depth of ~16mm in the case of the fast weld and at ~14mm in the slow weld. Some banding of regions of coarse and fine grains is seen in both welds, particularly at depths of ~14mm into the welds. There are also intermetallic particle bands present in both welds (bands of the order of ~50μm in length): these are more generally prevalent in the slow weld but are still distinct deep into the fast weld (the largest intermetallics are ~<2μm). These bands of particles were not particularly evident in the 13mm welds, as seen from the optical images of the weld nugget in Chapter 4.

The grain structure was also assessed via EBSD at 4 locations through the thickness of the fast and slow weld, (2, 7, 12 and 17mm from the crown surface), as shown in Figure 108. Both materials are seen to exhibit a similarly high angle boundary dominated structure, with limited evidence of sub-structure. It is again clear that the fast weld has a larger grain size than the slow weld at all depths. The average intercept diameters and aspect ratios of the grain structures are shown for both welds in Figure 109a) and b) and Table 8. The grain size generally gets finer with increasing depth, however there is a slight increase in grain size at 12mm for both weld speeds. In terms of aspect ratio changes with depth, in the case of the fast weld, the aspect ratio increases to 0.96 at a depth of 12mm (i.e. the

grains become more equiaxed), however at 17mm the trend is reversed and the aspect ratio increases to 0.61. The slow weld on the other hand shows the opposite trend, starting with a drop in aspect ratio up to 0.69 at 12mm from the crown surface, followed by a rise to 0.76 at 17mm.

Distance from crown surface (mm)	Fast weld		Slow Weld	
	Average Intercept (μm)	Aspect Ratio	Average Intercept (μm)	Aspect Ratio
2	4.7	0.71	2.8	0.98
7	3.7	0.90	2.3	0.82
12	4.1	0.96	3.0	0.69
17	2.5	0.61	1.9	0.76

Table 8 Transverse section grain dimensions measured in 25mm weld materials at weld centreline.

Figure 110 shows EBSD maps taken 2mm below the surface of both welds at 0, 2 and 5mm from the weld centre. It is again clear from the figure that the fast weld has a coarser grain structure than the slow weld at all positions. However there is little change in overall grain size moving away from the weld centre as shown by Table 9 and Figure 111 (confirmed for both sides of the weld).

Distance from weld centre (mm)	Fast weld		Slow Weld	
	Average Intercept (μm)	Aspect Ratio	Average Intercept (μm)	Aspect Ratio
-2	4.6	0.91	3.4	0.85
0	4.7	0.70	2.8	0.98
2	4.5	0.83	3.0	0.72
5	4.4	0.88	3.4	0.67

Table 9 Transverse section grain dimension variation with distance from weld centre towards the advancing side

Figure 112 shows typical EBSD maps obtained from sections 2mm below the crown surface in the weld direction (parallel to the L-S plane of the parent plate) parallel to the welding direction. It is clear that the grains are also essentially equiaxed in this plane with the fast weld again having a coarser structure than the slow weld

5.1.6 Summary

Macroscopically, the 25mm welds do not exhibit the well defined nugget region and onion ring structure that was seen previously in the 13mm weld. The hardness results show a similar trend near the crown surface (2mm below crown surface) as observed previously for the 13mm weld, with a characteristic hardness plateau in the weld centre, and minima on either side of the plateau just outside of the fine grained region of the weld. However, at the root of both of the 25mm welds a soft band was seen which was not present in the 13mm weld. Hardness measurements for the fast weld are generally higher than those for the slow weld.

DSC results indicate that the weld roots are essentially overaged microstructures in keeping with their low hardness levels for both of the 25mm welds. Distinct changes in apparent incipient melting behaviour were also noted in the weld material in relation to the parent alloy, particularly in the slow weld flow arm material.

The microstructure of each weld was studied in detail using both optical microscopy and EBSD; the fast weld generally exhibits a coarser grain structure at all positions through the weld. Grain size was not seen to vary significantly with distance from the weld centre. There was however significant variation in grain size with depth from the crown surface, with the finest grain size arising at the weld root for both welds.

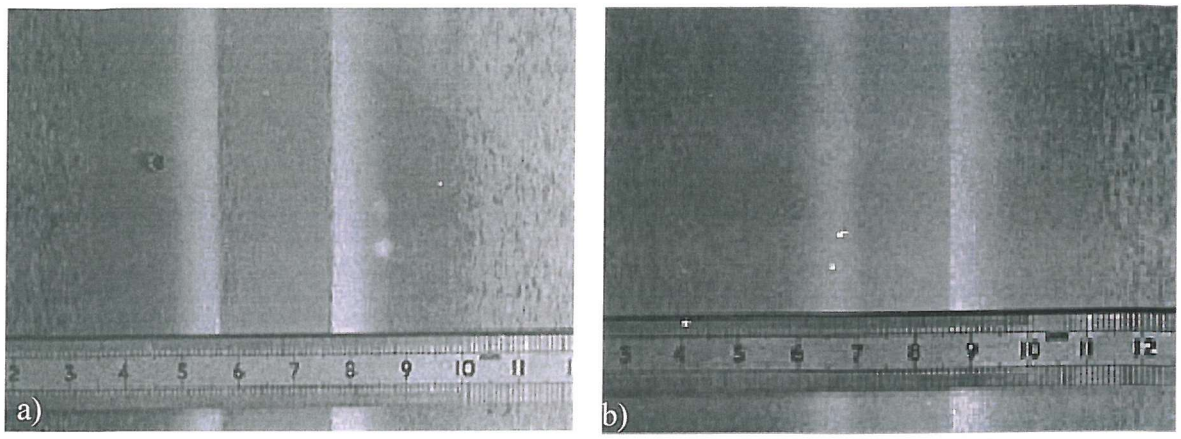

Figure 95 Typical macrographs of the top surface of 25mm plates weld a) fast weld and b) slow weld.

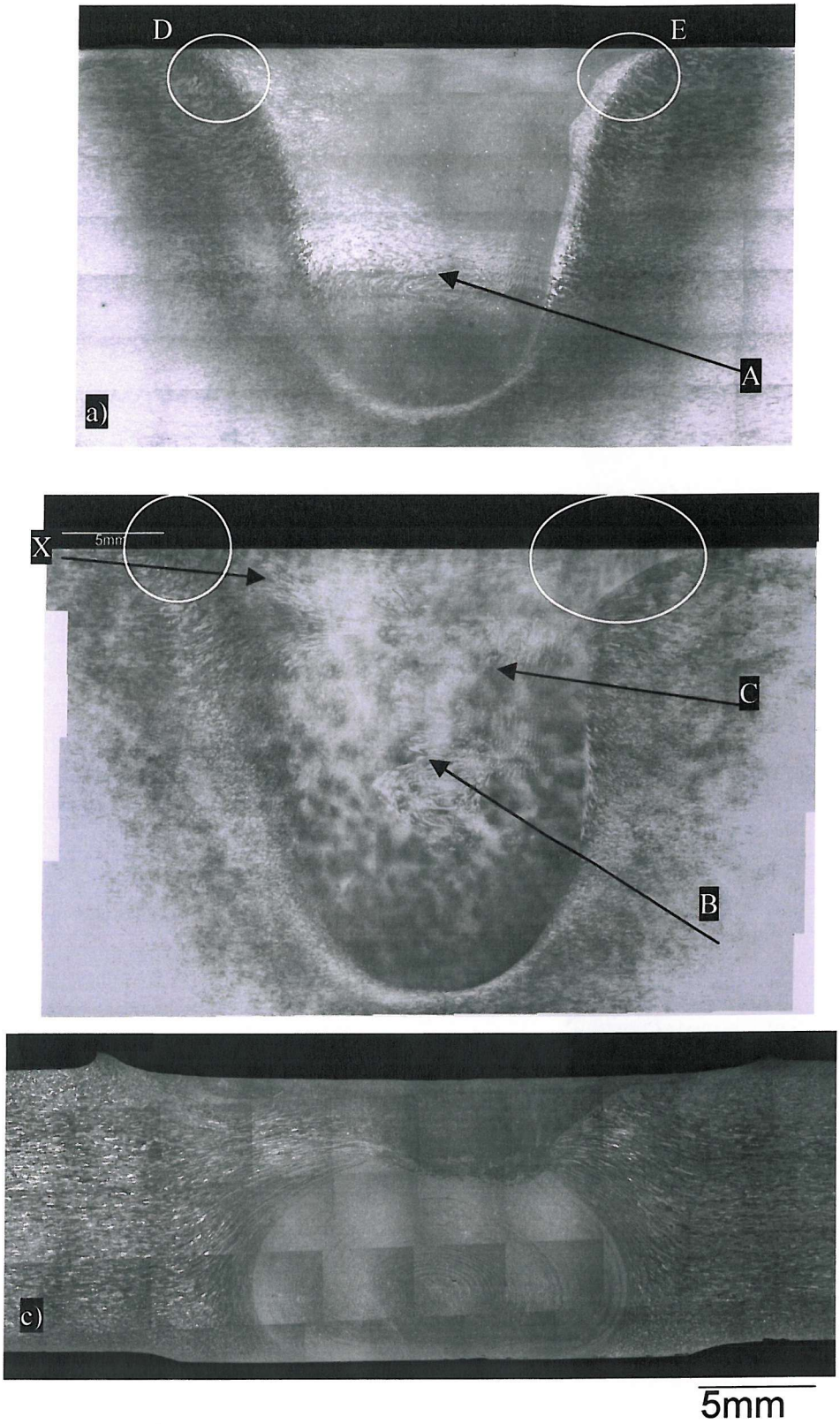

Figure 96 Transverse macrographs of a) fast weld in 25mm plate, b) slow weld in 25mm plate and c) 13mm welded plate.

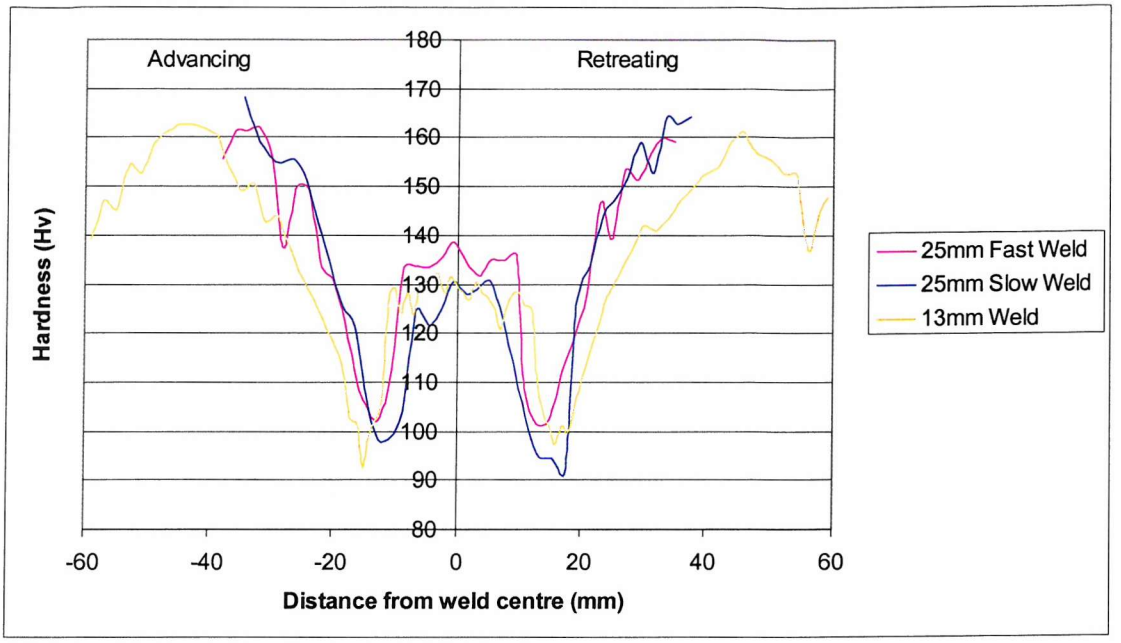

Figure 97 Hardness traces taken 2mm below crown surface (fatigue test depth) for the 13 and 25mm welds.

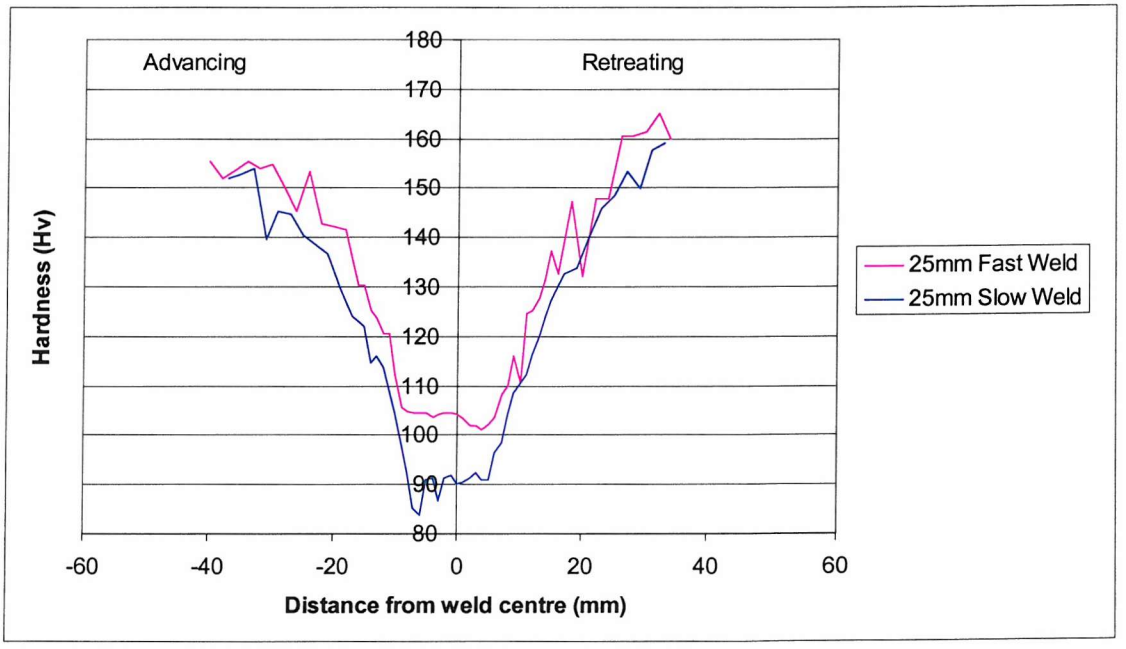

Figure 98 Hardness traces taken 7mm from root surface for the fast and slow welds in 25mm plate.

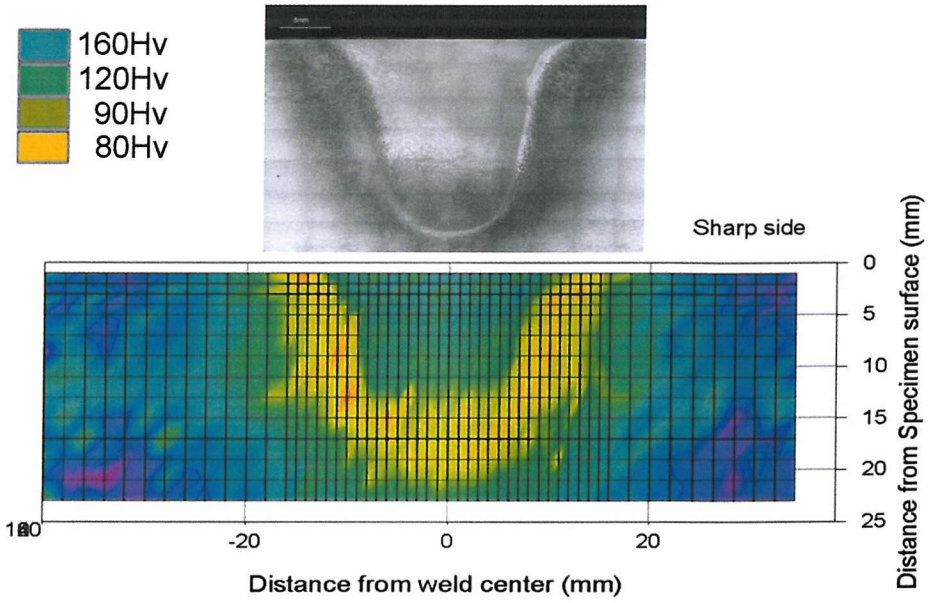

Figure 99 Hardness map of the fast weld, shown with an optical macrograph through the weld, plotted to same scale.

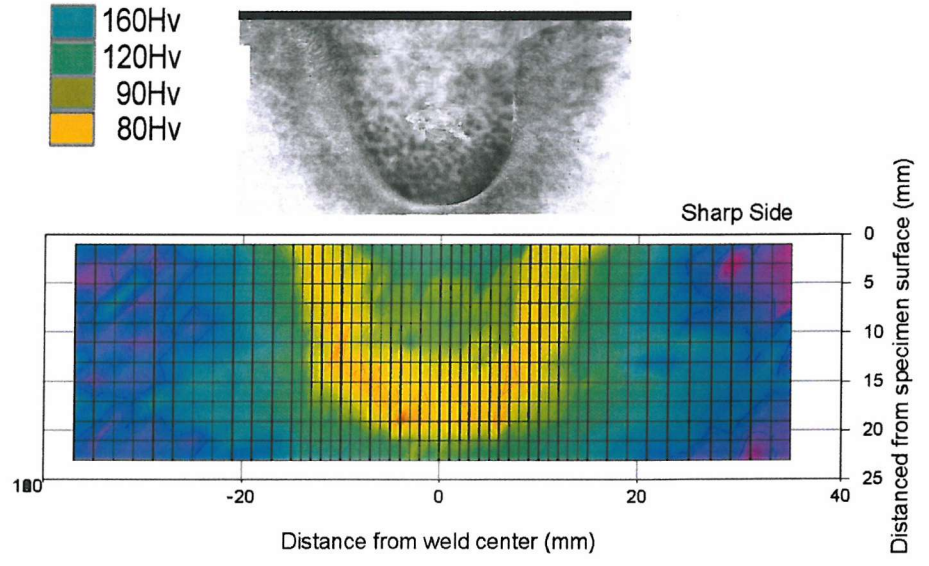

Figure 100 Hardness map of the slow weld, shown with an optical macrograph through the weld, plotted to same scale.

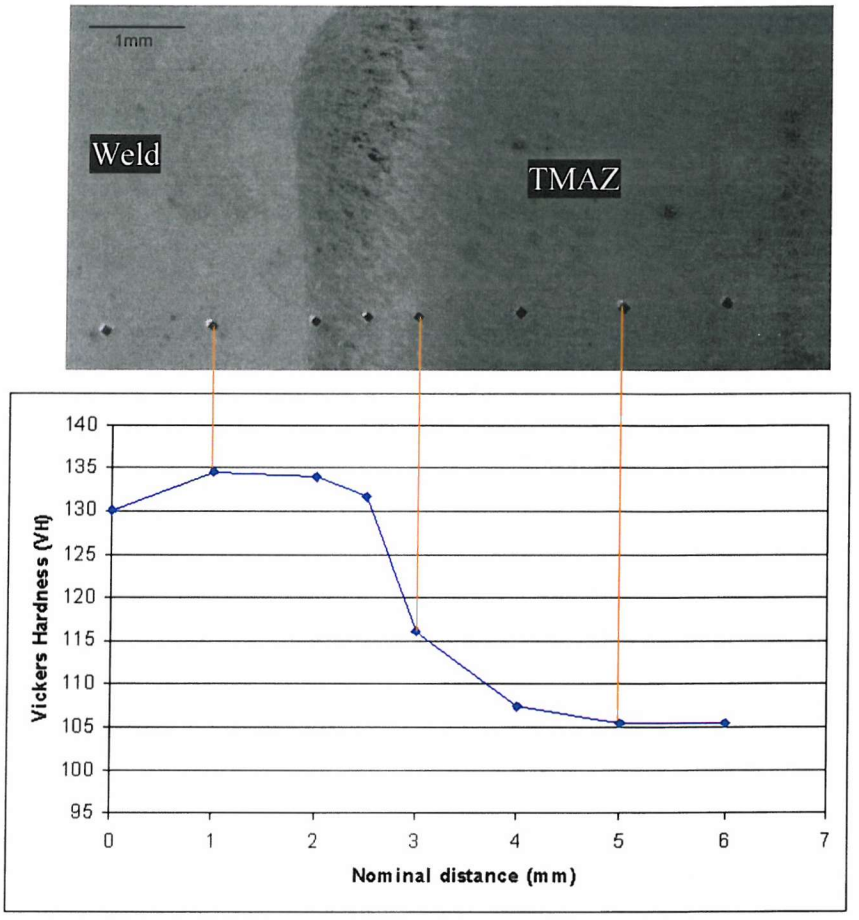

Figure 101 Hardness variation at the interface between nugget and TMAZ on the advancing side of the fast weld.

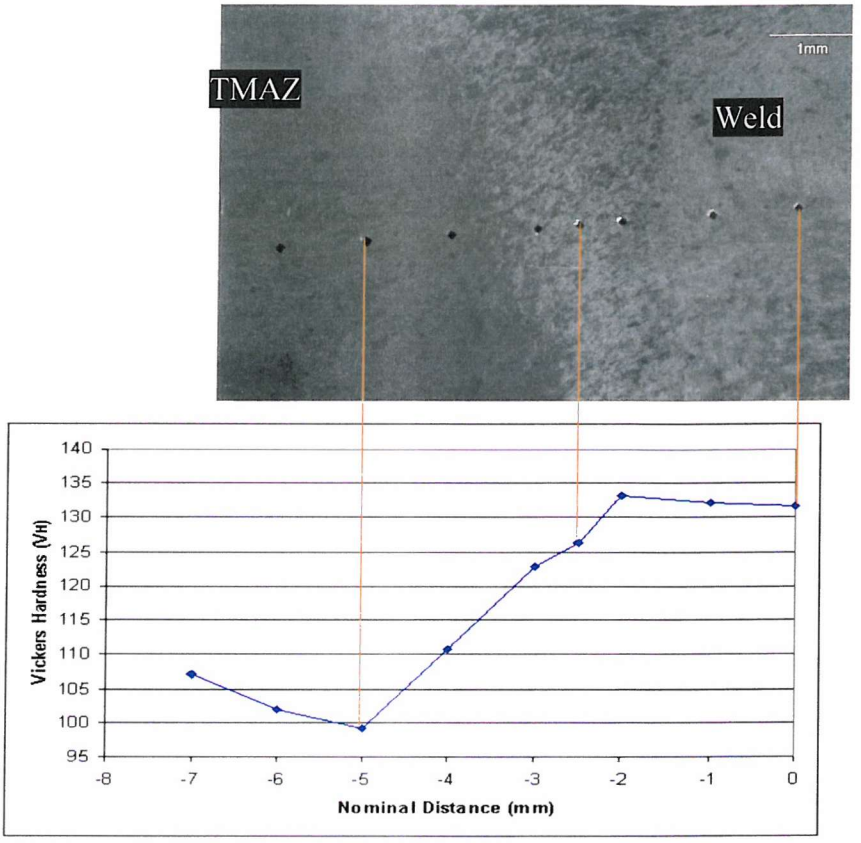

Figure 102 Hardness variation at the interface between nugget and TMAZ on the retreating side of the fast weld.

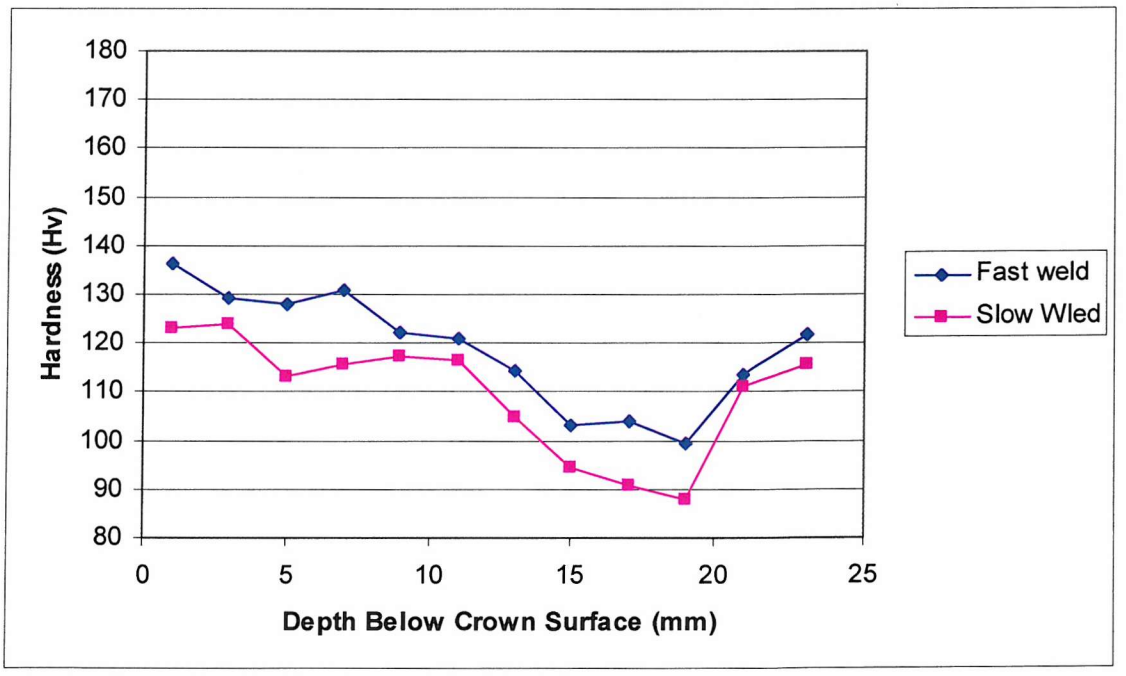

Figure 103 Through thickness hardness traces at the weld centre line for 25mm welds.

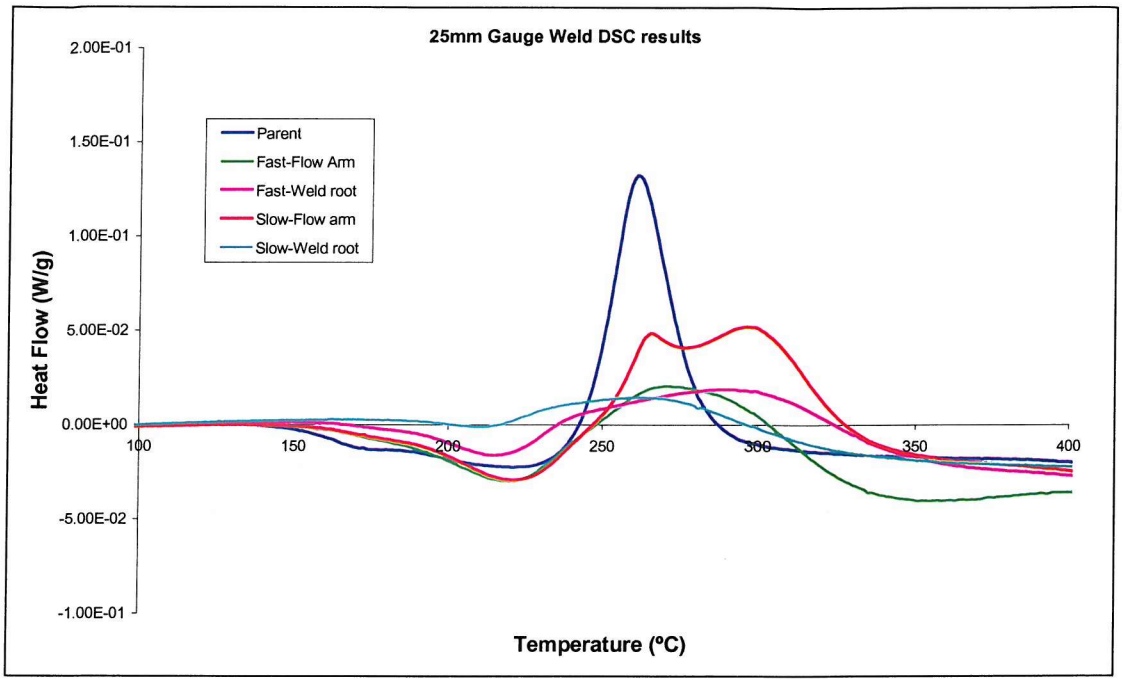

Figure 104 DSC result from 100-400°C for fast and slow welds and parent plate.

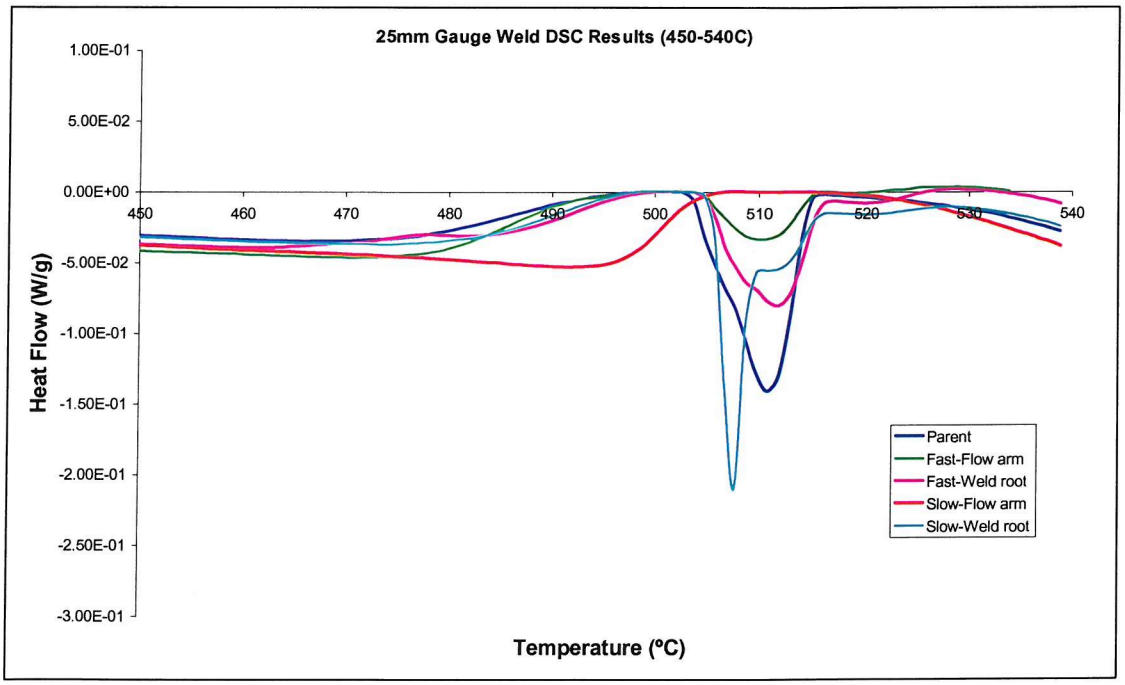

Figure 105 DSC results from 450-540°C for parent and weld materials.

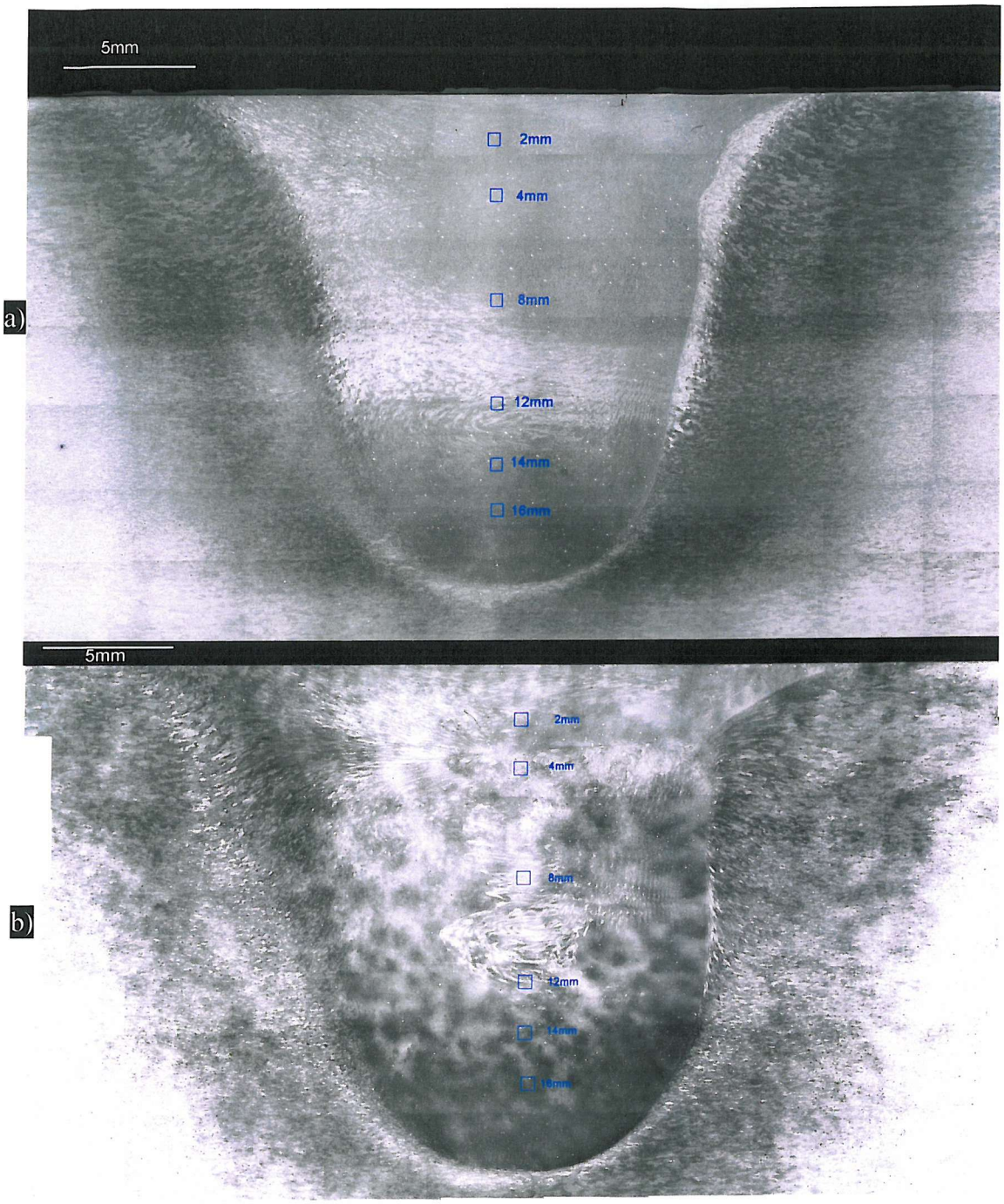

Figure 106 Transverse macrographs to locate the grain size micrographs in Figure 107: a) fast weld and b) slow weld.

Fast Weld	Depth into weld	Slow Weld
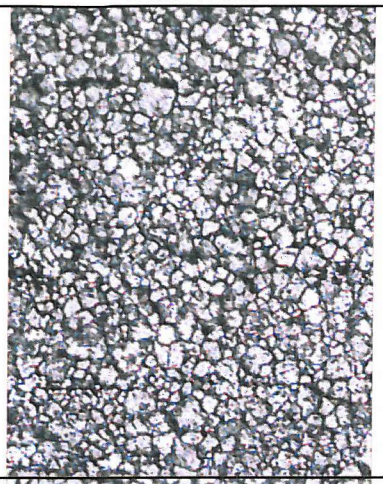	2mm	
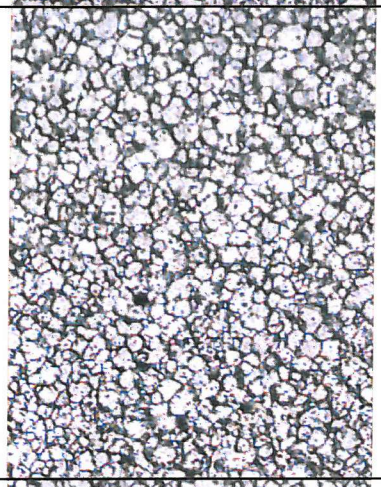	4mm	
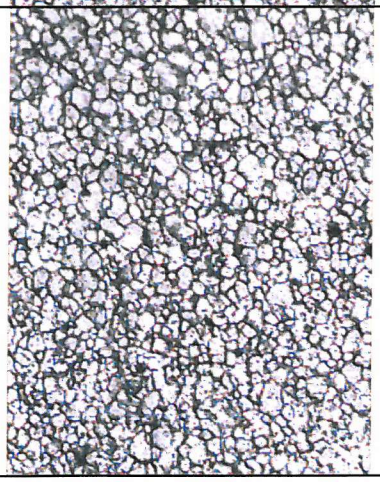	8mm 50µm	

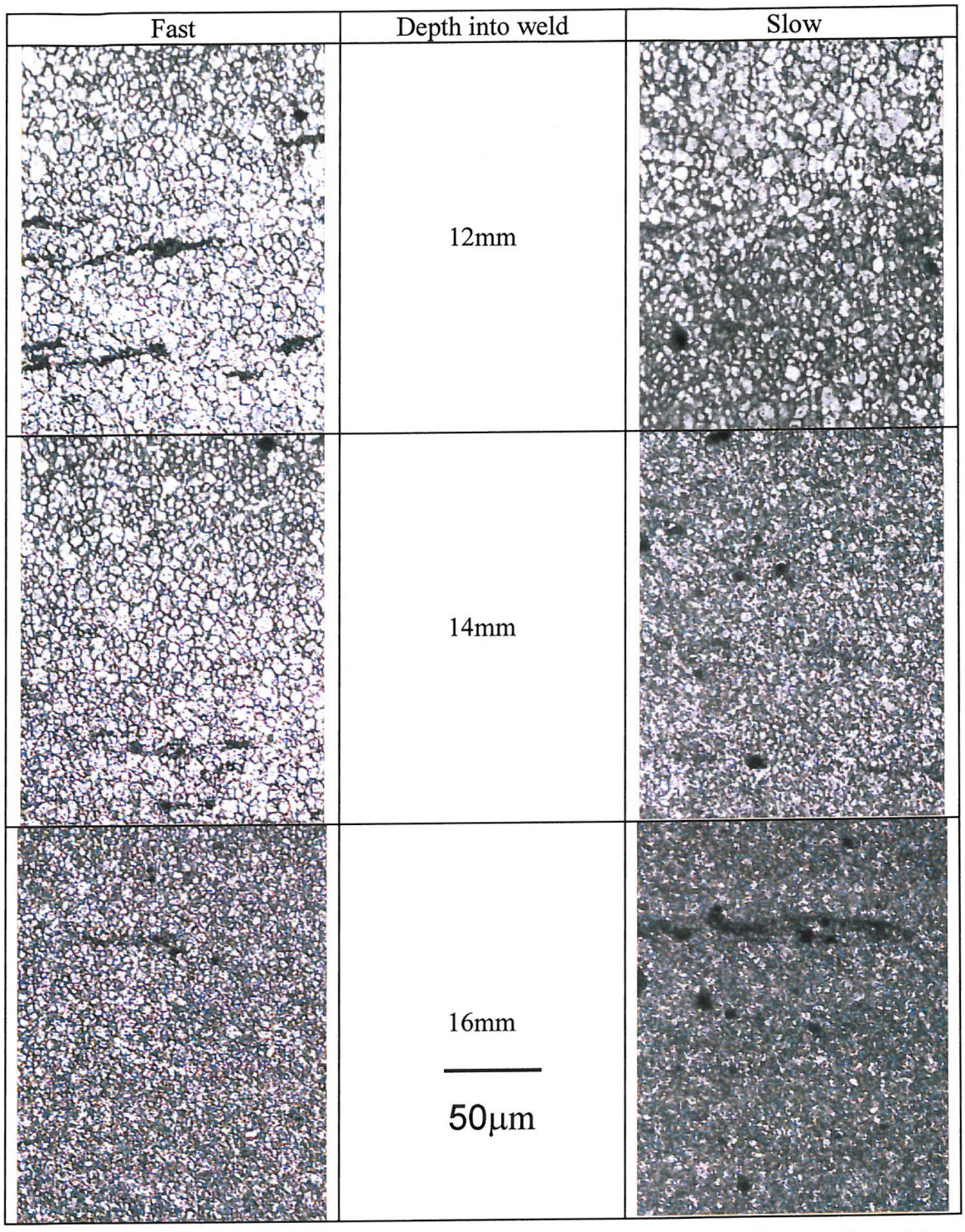

Figure 107 Optical micrographs of grain structures at varying depths through the weld region (transverse section).

Fast Weld	Slow Weld
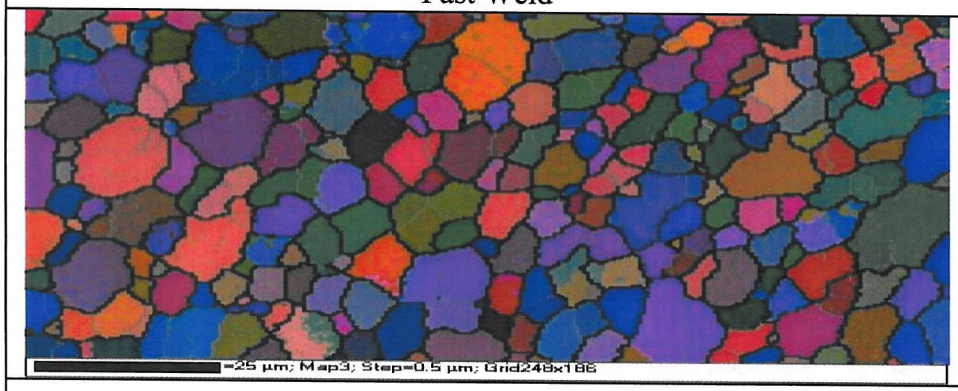	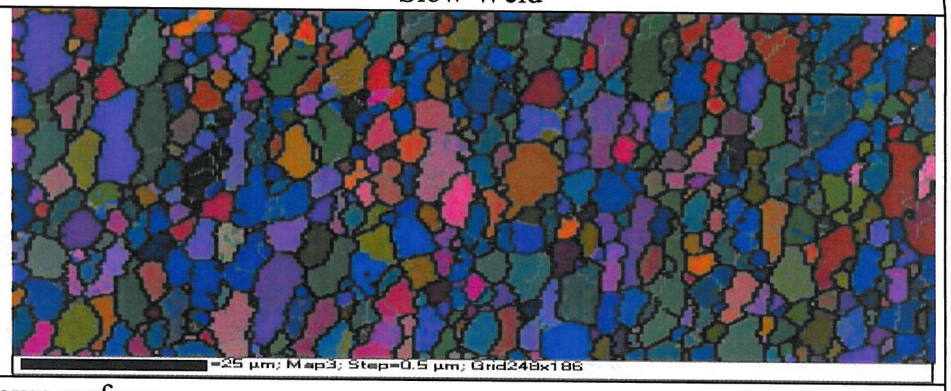
2mm from crown surface	
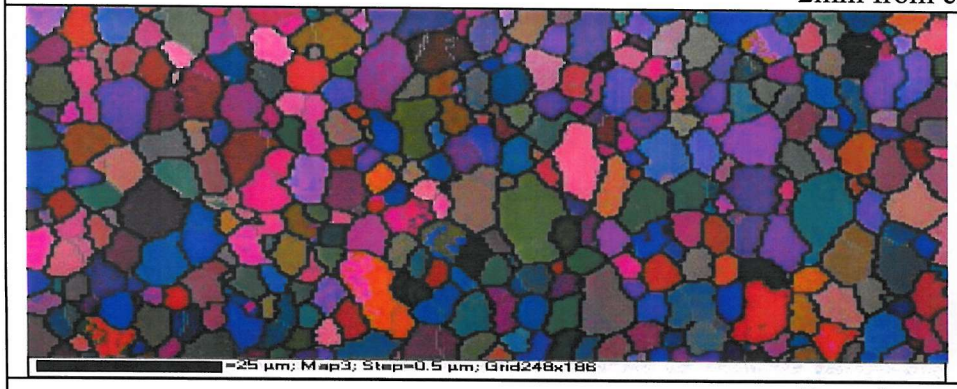	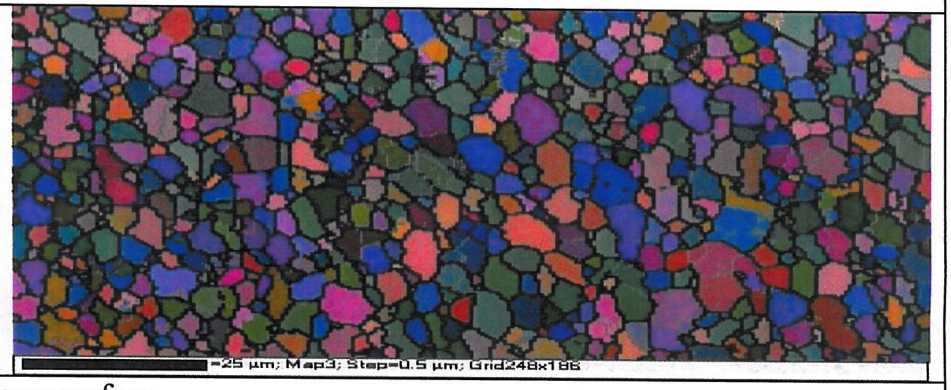
7mm from crown surface	

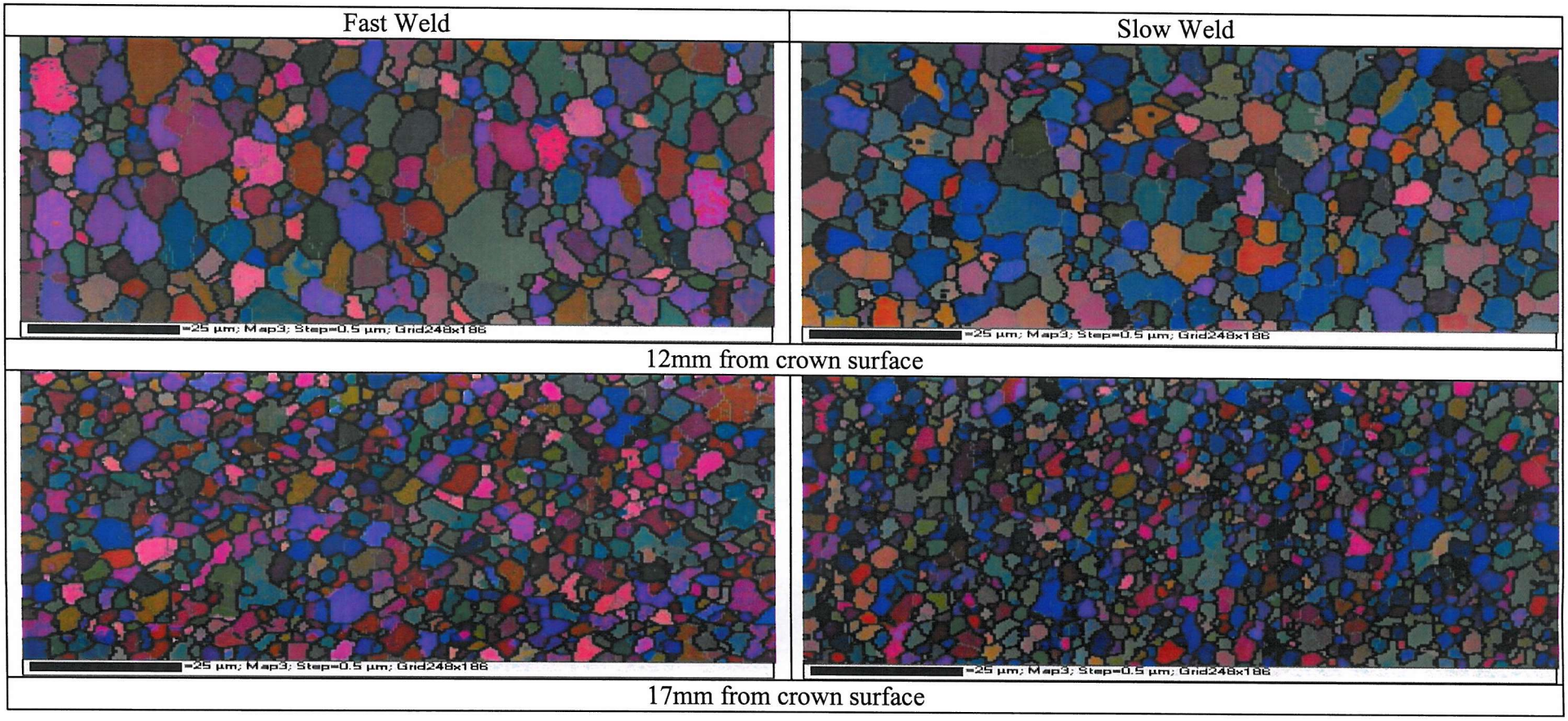

Figure 108 EBSD results from transverse sections through the fast and slow welds; taken at 2, 7, 12 and 17mm from the crown surface.

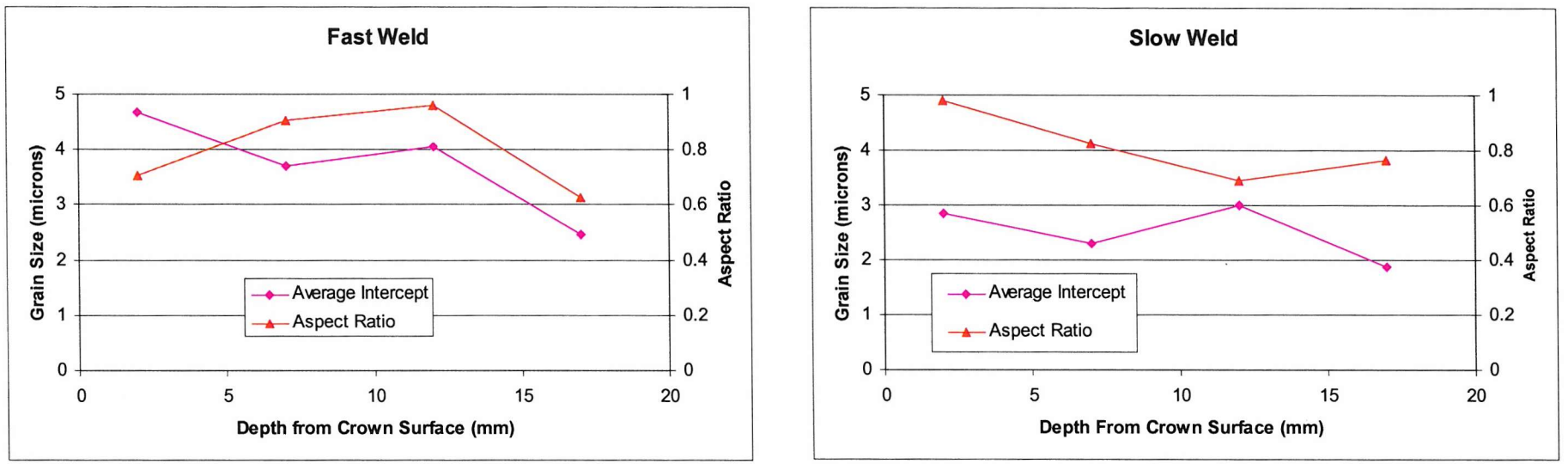

Figure 109 Graphs showing through thickness grain size variation (grain size calculated by linear intercept method).

Fast	Slow
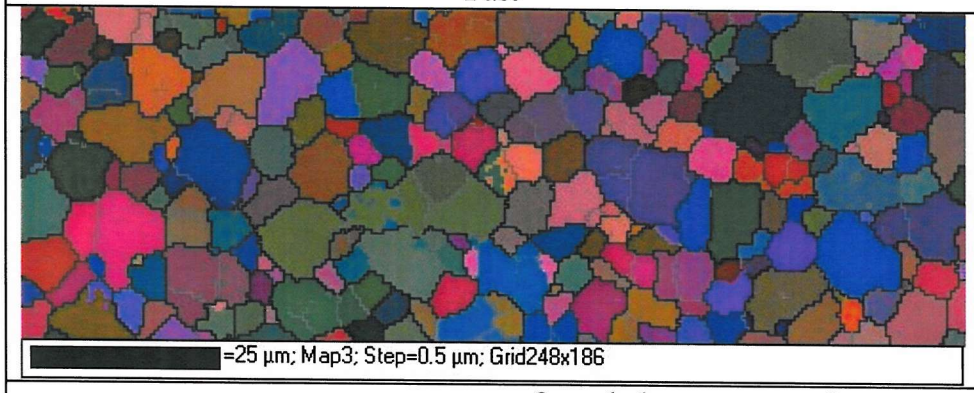	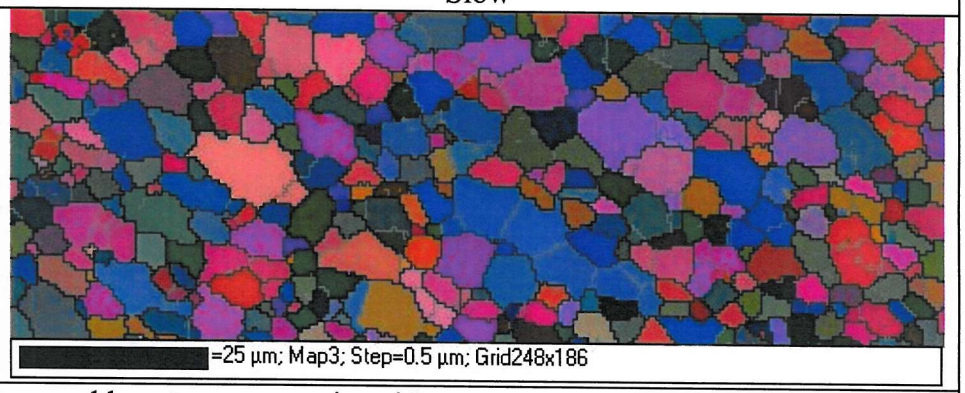
2mm below crown surface, 2mm from weld centre on retreating side	
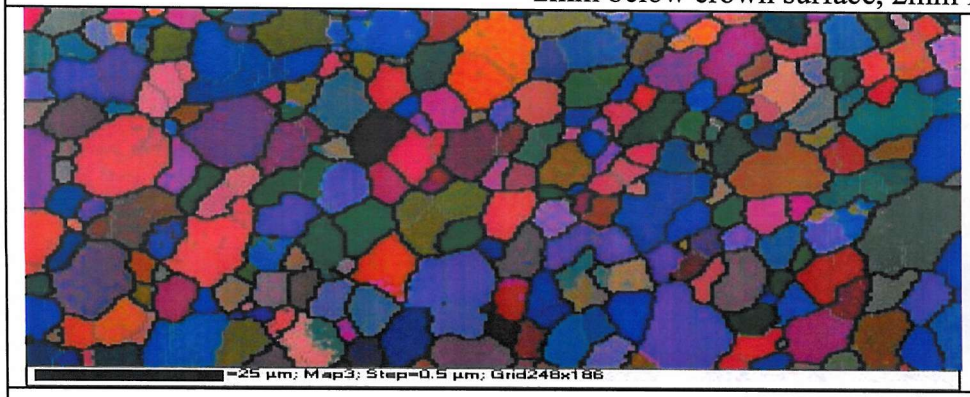	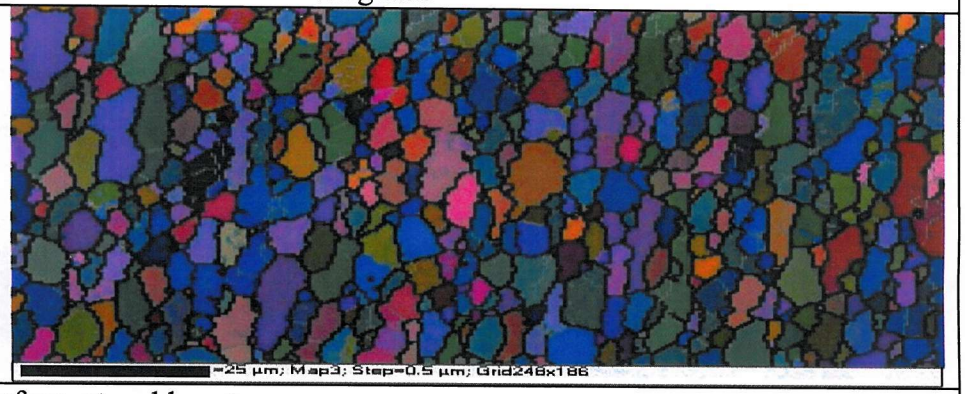
2mm below crown surface, at weld centre	

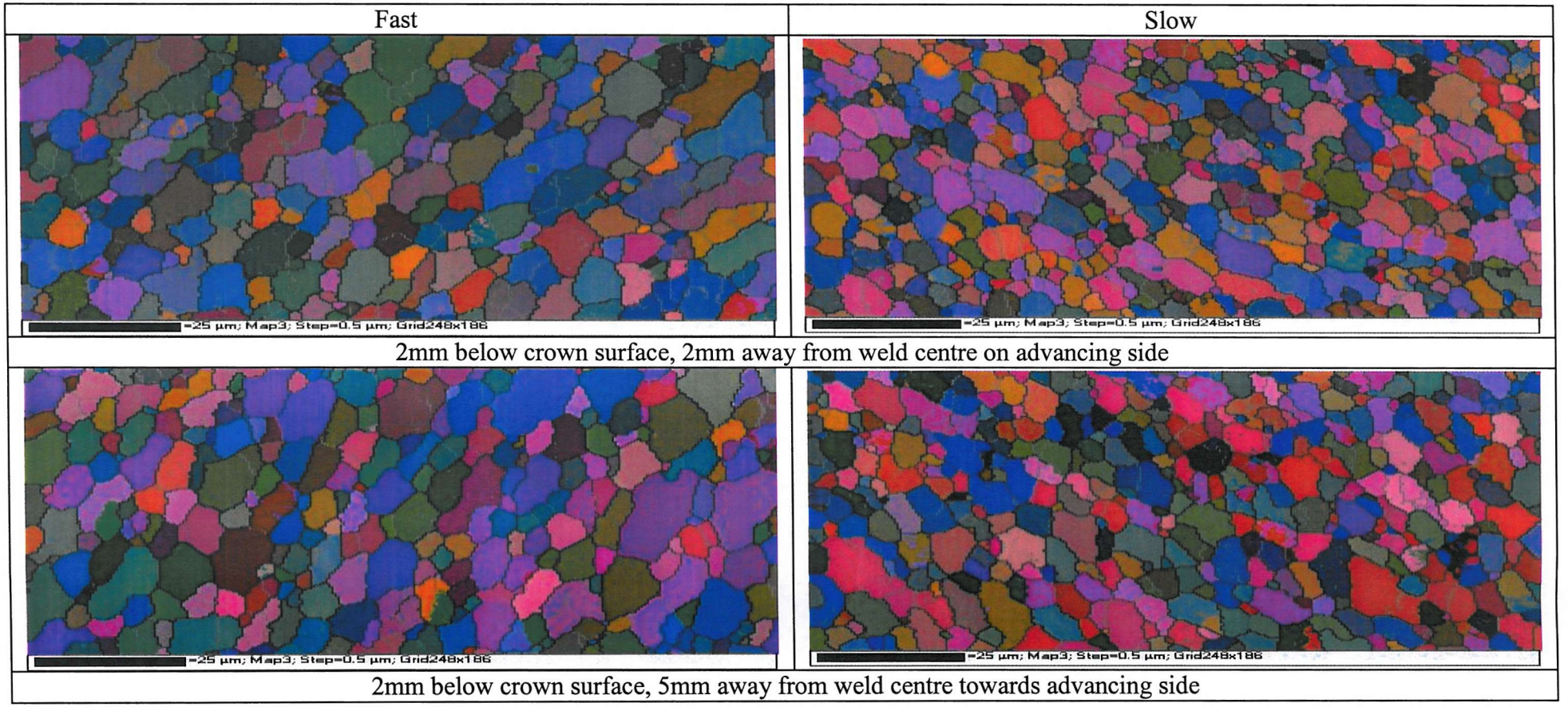

Figure 110 EBSD maps of fast and slow welds taken 2mm below the crown surface, at various locations across the weld width.

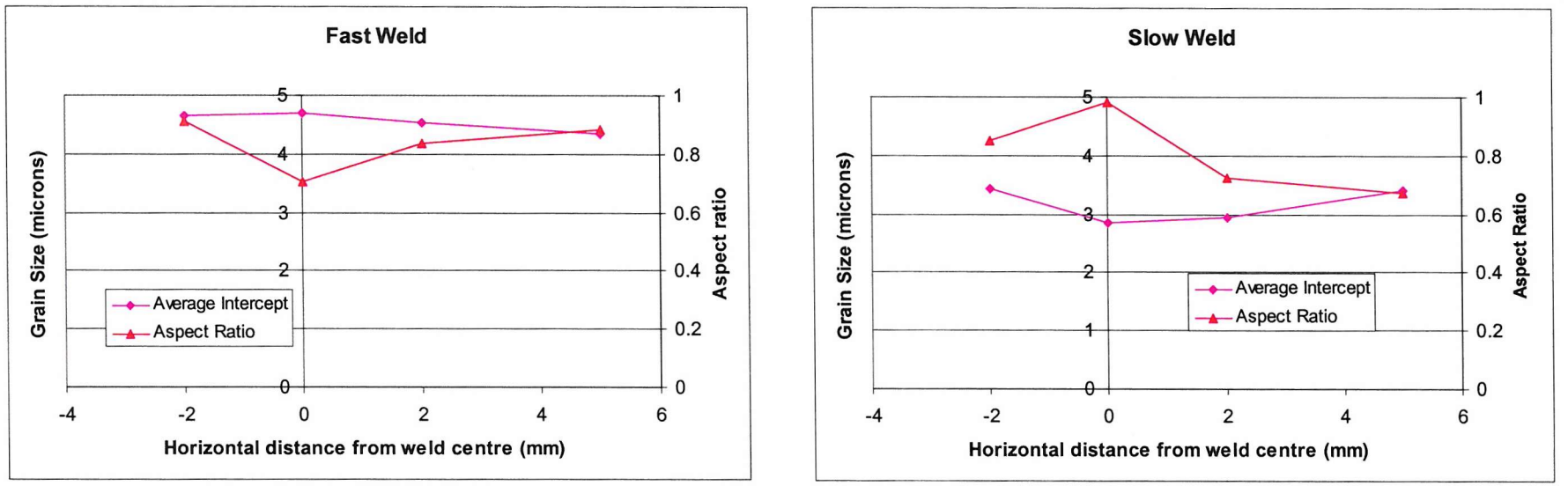

Figure 111 Grain size variation 2mm below crown surface across the weld width.

Fast	Slow
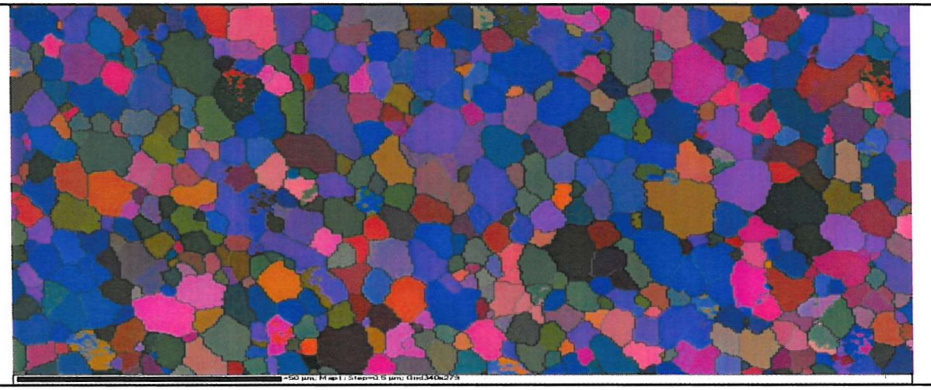	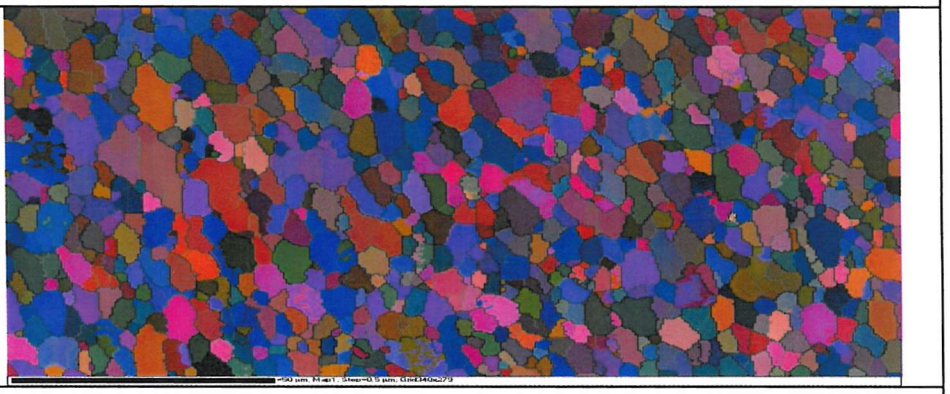

Figure 112 EBSD results for both the fast and slow weld at a depth of 2mm from the crown surface, sectioned parallel to the weld direction (corresponding to the L-S plane of the parent material).

5.2 Results: Crown Surface Tests

5.2.1 Fatigue Lives

Figure 113 shows the transverse S/N fatigue data obtained for the crown surface testing of the 25mm gauge welds, together with: (i) behaviour for literature data for 2024 plate tested at comparable R ratios, (ii) parent plate results obtained for similar stock 2024-T351 (same loading geometry as the previous weld tests), (iii) results for skimmed friction stir welded 2024-T351 obtained by Bussu *et al*[25] for 6mm gauge plate, and (iv) results of 13mm gauge friction stir welded plate (as reported in Chapter 4).

The 25mm weld results all fail within the wide parent plate scatter-band (from the literature). The results tend to fall on the lower bound of the literature data, and somewhat below the results obtained for parent plate with the same test geometry (i.e. "Southampton parent plate"), except at lower $\Delta\sigma$ (i.e. below 200MPa) where the fatigue life of both welds approaches the parent plate values. The weld speed does not appear to have a significant effect on the fatigue life of the 25mm welds (i.e. all results are within common levels of scatter in fatigue data). The 13mm plate results have been discussed previously (Chapter 4), however it is important to note the deleterious effect of failure over the nugget region on the fatigue life in the 13mm plate samples, and the generally poorer apparent fatigue performance of the 13mm material.

While the fatigue lives were generally comparable for the two weld speeds in the 25mm plate, the crack initiation locations varied, as shown in Table 10. The fast weld specimens

all failed outside the weld region; while a significant number of the slow weld specimens also exhibited crack initiation outside the weld region (in the HAZ), 2 specimens initiated within the weld nugget. The relationship between crack initiation location and hardness at each failure location is shown in Figure 114 for the various 25mm plate crown test specimens. The failures in the HAZ appear to occur close to, or at, the peak in hardness that occurs at the other edge of the HAZ.

Stress Range	Weld Speed	Cycles to failure	Failure location	
			Weld region	HAZ
200	Fast	6,000,000	Run Out	
225	Fast	364,000		X
250	Fast	116,000		X
250	Fast	101,000		X
250	Fast	194,000		X
200	Slow	5,679,000		X
225	Slow	237,000	X	
250	Slow	273,000		X
250	Slow	142,000	X	
250	Slow	153,000		X

Table 10 Fatigue results for 25mm welds: crack initiation locations

5.2.2 Failure Outside the Weld Region

- ***Macroscopic Behaviour***

The failures located outside the nugget region have all been identified with the HAZ (i.e. beyond any deformation from the welding process). Figure 115 shows a typical fracture surface of one of the failures in this region. The fracture surface shows relatively flat, conventional growth, with no significant (macroscopic) deflections from a nominal mode I path. Initiation was seen to occur at the top surface of the specimen in keeping with the majority of tests (1 corner initiation was seen).

- ***Fatigue Crack Growth Rate***

The fatigue crack growth rates plotted in Figure 116 are for failures outside the weld region for both the fast and slow welds. The growth rates for the two welded specimens appear to be reasonably comparable with each other and parent plate results at low ΔK (up to crack length of ~1mm) with some indication being seen of a classical short crack effect, where there is an increasing degree of growth rate scatter at low K levels and limited evidence of a threshold being reached. At intermediate K levels parent and weld growth rate curves converge, whilst the welds then appear to show improved growth resistance at higher K Values.

- ***Microscopic Behaviour***

SEM imaging of a typical HAZ failure is shown in Figure 117 a) and b). The fatigue features are clearly evident in Figure 117a) leading back to a region close to the surface; backscattered imaging of the initiation region is shown in Figure 117b), clearly highlighting a coarse intermetallic particle as the cause of initiation. In keeping with results in Section 4.2.3.2 for HAZ failures, a more ductile mode was evident with increasing crack lengths/K levels.

5.2.3 Failure Over the Weld Region (slow weld)

- ***Macroscopic Behaviour***

One of the most significant macroscopic features of the fatigue crack growth for failures over the nugget region (shown in Figure 118 and Figure 119) is the incidence of deflected crack growth. This is particularly prominent in the specimen shown in Figure 118: the surface crack growth is deflected by an angle of ~60° to the nominal growth plane at one

tip. The other crack tip is also deflected, but to a lesser extent. The crown surface of the other weld region failure is shown in Figure 119: the crack path at the surface does not show the same large scale deflection behaviour as that in Figure 118, however the overall growth plane was seen to be inclined at an angle to the nominal growth direction. It is significant to note that both failures have significant subsurface out-of-plane deflections (at up to 80° to the nominal growth plane), as shown Figure 120.

- ***Fatigue crack growth rates***

Fatigue crack growth rate results are presented in Figure 121 for the 2 cracks observed within the weld region for one of the over-weld region failures, together with growth rate results for the HAZ slow weld failure. Based on the available replica record it was possible to establish crack growth rates for one of the cracks from the nugget failure when it was relatively small (60-100μm identified in Figure 121 as the "second crack"), however subsequent growth was affected by shielding from a larger dominant crack, whilst the larger crack was also measured for crack lengths above ~500μm. There is evidence of classical short crack behaviour for the second crack, however but the extent is likely to have been limited by the available test records. The larger ("dominant") crack corresponds to the higher ΔK levels and mostly shows a classical long crack growth curve. It is important to note the distinctly different behaviour of the two tips of the larger crack, as one end undergoes sharp macroscopic deflection (highlighted in Figure 118), whilst the other tip only undergoes mild deflection from the nominal growth plane. As the crack grows, the difference between the ends of the dominant crack develops, with the severely deflected tip clearly growing more slowly (in terms of the *projected* length behaviour plotted in Figure 121). Standard stress intensity factor solutions clearly do not apply to such asymmetric deflected cracks: the dashed lines in Figure 121 indicate growth

behaviour using the projected crack lengths to give a general indication of the growth behaviour. In this context the growth rates for failure over the weld region are generally consistent with the slow weld growth rate established for failure outside the weld, and again growth is slower than that in parent plate growth for higher ΔK values.

- ***Microscopic Behaviour***

The fracture surface in Figure 122 shows a broadly similar microscopic failure morphology to the 13mm weld failures (viz. a ductile fine scaled fracture surface with little crystallographic character), however reasonably clear fatigue features are seen leading back to a distinct linear defect on the fracture surface. Assessment of the associated intermetallic distribution, as shown in Figure 123, shows little evidence of particularly coarse intermetallics or clustered intermetallics at the initiation point.

The initiation sites identified in Figure 124 (for the specimen without a marked surface deflection Figure 119) also clearly showed that initiation occurred from microscopic defects (either at, or just below, the surface) within the weld region. It is clear from Figure 122 and Figure 124 that there is a variation in initiation defect shapes (from linear to more complex shapes). The maximum length of the more linear defects extends to ~200μm, although the associated defect width is only of the order of 10-20μm.

The distribution of intermetallics at the crown surface in the region close to a weld initiation site is shown in Figure 125. There is clearly a degree of clustering of the intermetallics: Figure 126a) shows an SEM image of the crown surface around an actual initiation site, with the same area being shown in BEI mode in Figure 126b). The intermetallic clustering is still evident but this does not appear to be directly linked to the

initiation site. Figure 127a) and b) are images taken of the top surface of another initiation site; again clusters of intermetallics are present and but they are not obviously linked to the actual initiation. It may be noted that whilst the crack initiation point in Figure 127a) appears to be linked to a local perturbation in the particle flow/distribution pattern, such an effect was not apparent at the other initiation points.

The specimen surface grain structure around the crack initiation location for the specimen with a large deflection is shown in the EBSD orientation map in Figure 128 (the green line indicates the fracture edge). No evidence of a significant local variation in grain was noted in the initiation region within the welds.

Given the distinct crack turning of the slow weld failures, crack growth has been investigated with particular attention to the macroscopic crack deflections. Initially looking at the intermetallic distribution along the deflection, Figure 129a) and b) show that the growth is relatively flat and planar in nature; it is also suggests that there was limited interaction with intermetallic particles. There was no evidence of oxides either on the fracture edge or within the rest of the area covered by the micrographs. It is however clear that the crack growth is following the microstructural flow that is present in the intermetallic distribution within the weld, i.e. the crack growth is parallel to the general alignment of the intermetallics.

Looking in more detail at the fracture surface of the sub-surface deflection seen in both specimens, significant evidence of crack closure was present, see Figure 130, which shows the fracture surface to have significant quantities of oxide and rubbing damage due to surface contact during loading. Figure 131a) shows an area of the deflections that was not

subjected to closure damage; the growth appears to be predominantly ductile and transgranular in nature. Porosity was also occasionally present on the fracture surface (highlighted in Figure 131a); Figure 131b) shows that while intermetallics are present on the fracture surface, they are not as significant (at least in terms of point density) as those present in the 13mm weld during deflected growth around the weld nugget.

EBSD orientation map in the region of crack deflection[6] is shown in Figure 132; it is significant to note that there is a degree of grain alignment and banding in this region, with bands of finer grains lying parallel to the observed growth direction. The grain size banding is more evident in the feret maps shown in Figure 133, where the discontinuous nature of the bands is also evident, similar to the observations of the onion ring structure of the 13mm weld specimens.

A through thickness section along the weld line (L-S orientation of the parent material) is shown in Figure 134 highlighting the macroscopic banding that is present in the weld structure at the approximate location of the deflections seen in the weld failures: the bands are seen to extend to just below the top surface of the fatigue specimens, consistent with the more marked sub-surface crack deflections in the weld failures. The intermetallic density of the flow features is shown in Figure 135, showing that there are regions of high and low particle density present, similar to the banding in the 13mm weld. It should be noted that unlike the 13mm weld the flow features in the 25mm slow weld appear to be associated with micro-porosity (up to ~5μm diameter) as well as an intermetallic variation: the bands with less coarse intermetallics were identified with a higher density of such

[6] EBSD mapping was carried out on the crown surface of the specimen with the large surface deflection

pores. Micro-hardness assessment of the banding features as shown in Figure 136, showing an increase in hardness of ~6Hv between the dark and light bands.

5.2.4 Residual Stress Measurements

Transverse surface residual stress measurements from fatigue test coupons of the fast and slow welds are shown in Figure 137. It should be noted that results were also obtained for outside the weld regions (i.e. beyond ±10mm from the weld centre) however the intensity of the texture present in the 2024 plate made obtaining accurate results outside the weld region difficult. Hence the following discussion is confined to the weld central region where the fine grain size and reduced texture significantly improve the accuracy of the data acquired. For the fast weld shown in Figure 137a) it is evident that residual stresses in the flow arm region are slightly compressive (~25MPa) for approximately 6mm on either side of the weld centre. The slow weld, shown in Figure 137b), shows more fluctuation in residual stress across the weld centre region, with a tensile stress of ~30MPa at the weld centre and a compressive dip on either side (maximum compression of ~50MPa).

Figure 138 also shows the longitudinal residual stresses measured in the slow weld crown. The longitudinal residual stress in the weld region appears to be compressive with higher stresses at the weld centre. The stresses are relatively low (<~60MPa) for all locations within the weld. It is also interesting to note in Figure 138 that the residual stresses appear to be maintained even relatively close to the specimen edge (i.e. to within 5mm).

5.3 Results: Weld Root Tests

5.3.1 Fatigue Lives

It is clear from Figure 139 that the fatigue lives of the root face specimens (obtained at a fixed stress level of 250MPa) were consistent with the crown surface results, with no evidence of a weld speed effect on fatigue life (see Table 11 also). It is also clear that the results are within the scatter of the crown surface specimens. For the same applied surface maximum stress, all of the specimens failed in the HAZ well outside the weld region, at a minimum of 25mm from the weld centre. A hardness trace for the root of both welds with the horizontal location of the various failure locations is shown in Figure 140; it is clear that initiation in all cases is approximately at the peak in hardness between the parent plate and the weld region, similar to the HAZ failures in the crown tests.

Weld speed	Cycles to failure	Failure Location	Distance from weld centre (mm)
Fast	109,000	Retreating	34
Fast	117,000	Advancing	30
Fast	177,000	Advancing	25
Average	134,000		
Slow	113,000	Advancing	45
Slow	117,000	Advancing	32
Slow	151,000	Advancing	36
Average	127,000		

Table 11 Fatigue results for 25mm welds root face tests: crack initiation locations, all test carried out at 250MPa

- ***Macroscopic Behaviour***

Macroscopic fracture surfaces were very similar in each case, see Figure 141a) and b) for examples of fast and slow weld failure respectively. Fracture surfaces were reasonably flat, i.e. showing simple mode I dominated behaviour

- ***Fatigue Crack Growth Rates***

The short fatigue crack growth data obtained for the slow weld failure is shown in Figure 142: this is reduced to a scatter band for the subsequent diagrams: a dense band of data points is shown as a number of small cracks were identified for crack length measurements. Classical scattered short crack growth rate behaviour is clearly seen in Figure 142, with Figure 143 showing a comparison with equivalent data from a fast weld test. The growth rates for both weld speeds are consistent with parent plate values for moderate K levels (up to ΔK ~9MPa$\sqrt{m}$). The growth rates of both welds then fall below the parent plate rate, in a similar manner to that seen for the crown surface testing.

- ***Microscopic Behaviour***

Figure 144 and Figure 145 show examples of typical initiation sites from the fast and slow weld root failures respectively. It is clear from both sets of figures that the river line features lead back to a point on the surface. This was identified using BEI and EDX as a coarse intermetallic in all cases; see Figure 144b) and Figure 145b).

5.3.2 Residual Stress Measurements

It is clear from Figure 146 that the transverse residual stresses in the root of the slow weld are low (<~50MPa), although again it was not possible to clearly identify the residual stresses in the region around the crack initiation location due to the high level of error developed by the anisotropy (texture) present in the parent plate.

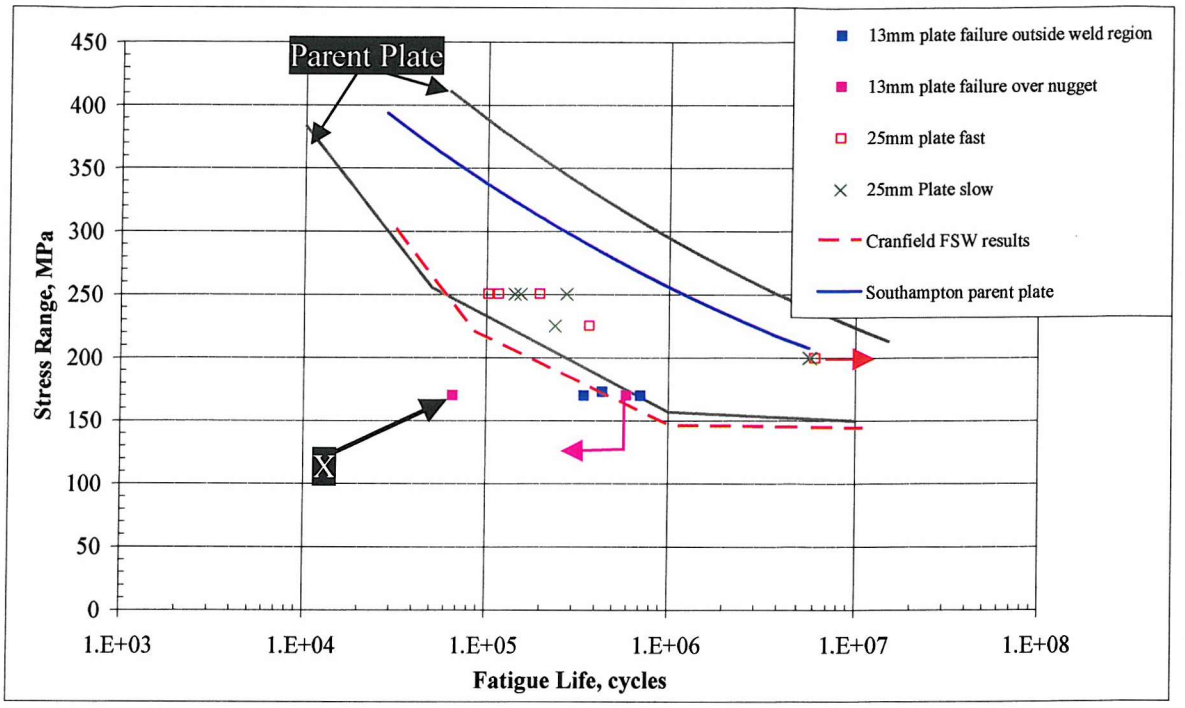

Figure 113 S/N data for 2024-T351 FSW plates, with parent plate results.

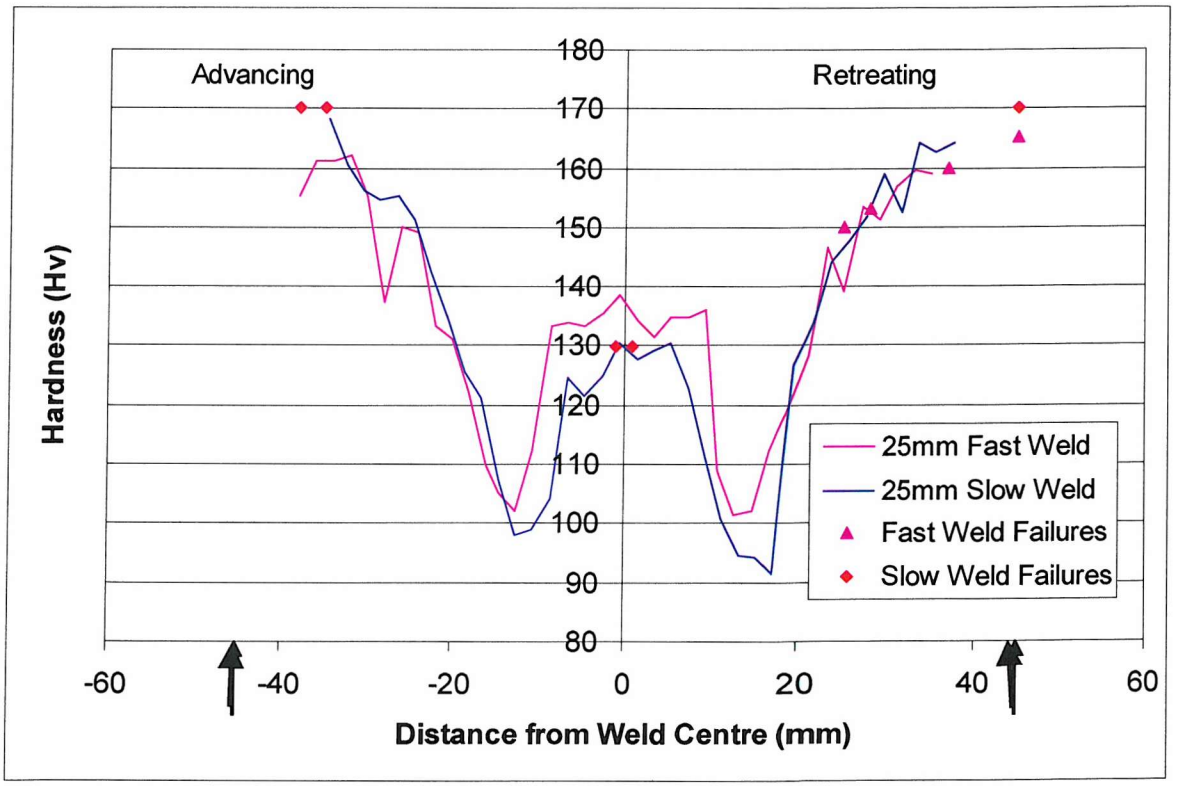

Figure 114 Hardness traces for the crown test surface of the 25mm gauge fast and slow welds with the corresponding failure locations indicated.

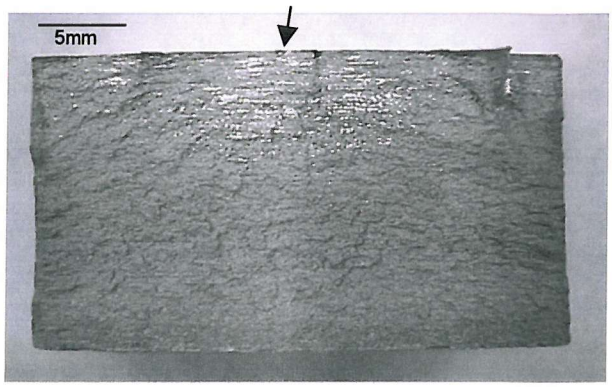

Figure 115 Macrograph of parent/HAZ fracture surface, 25mm gauge, fast welding speed.

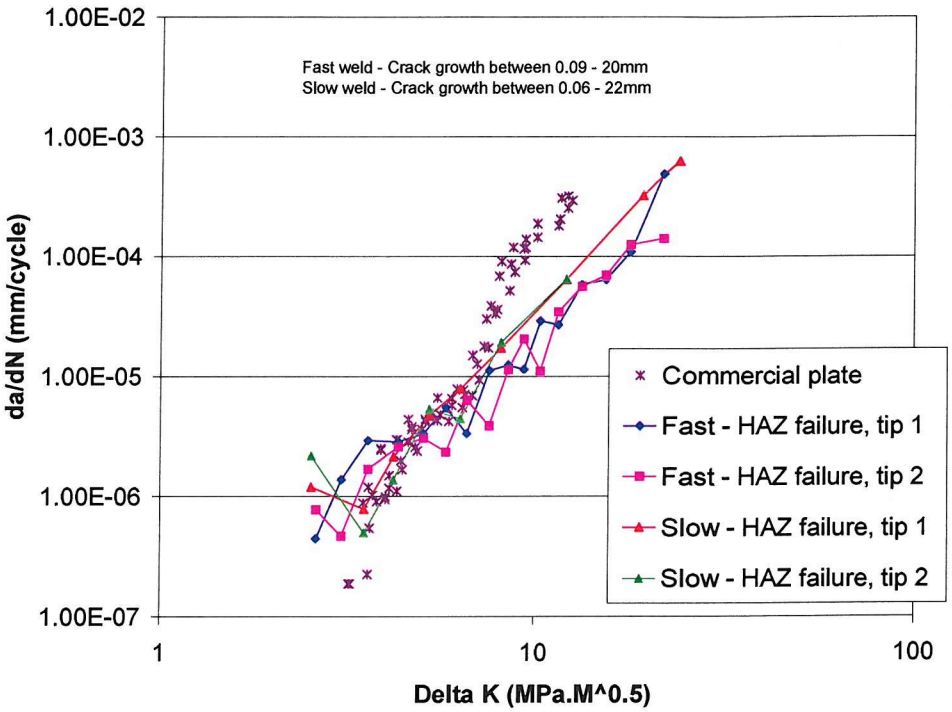

Figure 116 da/dN data for growth surface failure outside the weld region (HAZ failure) including parent plate data[111].

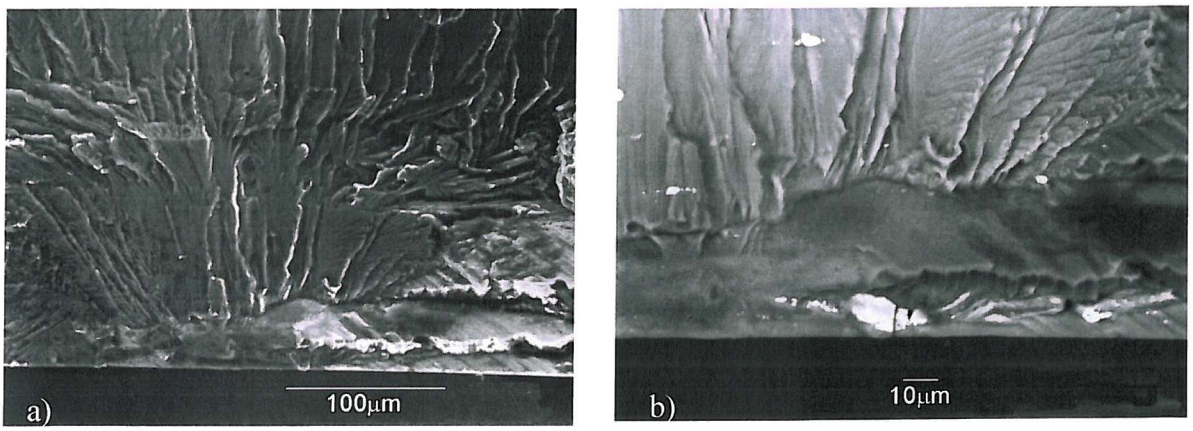

Figure 117 SEM images of initiation site for failure in the parent/HAZ region a) SEI (secondary electron image) and b) BEI (backscattered electron image).

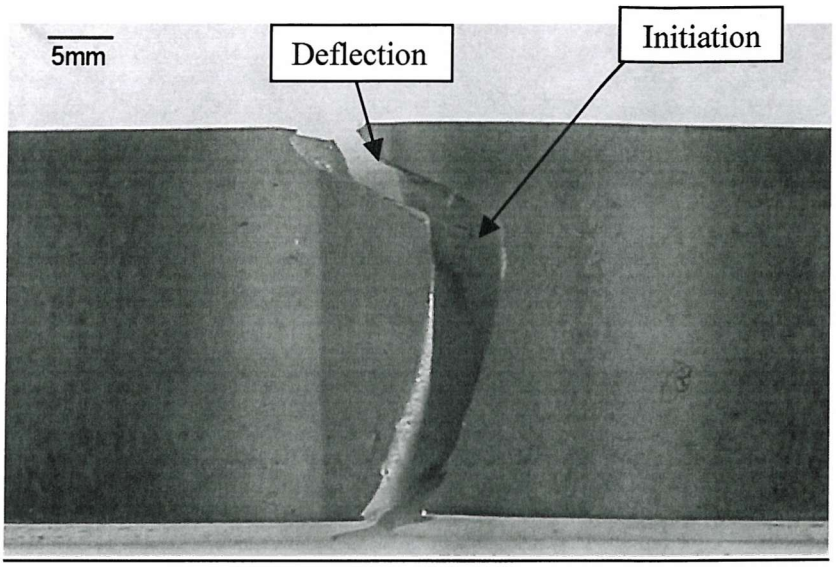

Figure 118 Macrograph of weld failure at the top surface of the slow weld specimen exhibiting large surface crack deflection (dominant initiation site is highlighted).

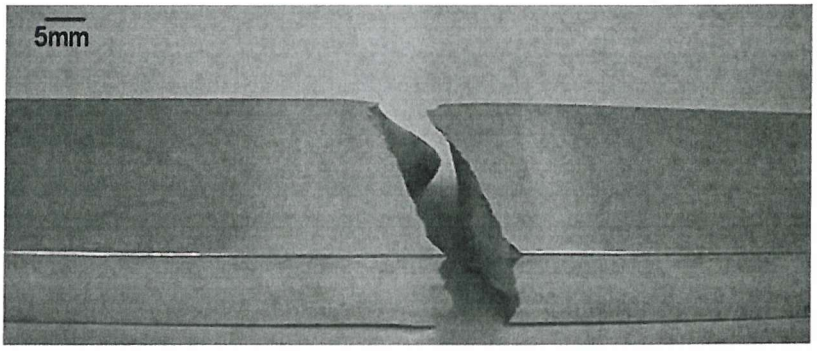

Figure 119 Macrographs of weld failure of the slow weld specimen without marked surface crack deflection.

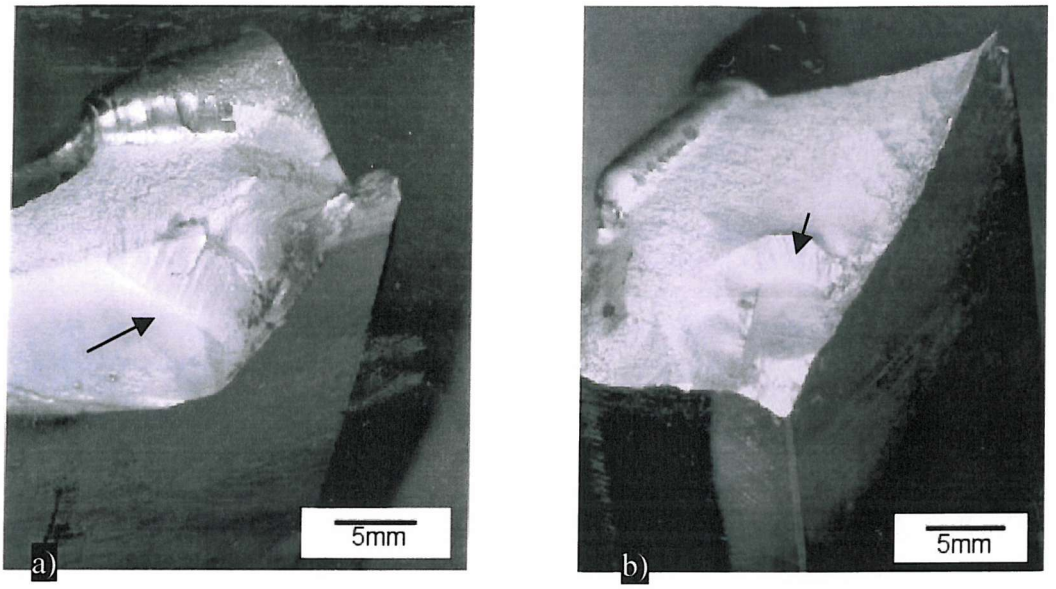

Figure 120 Macroscopic crack path deflections in the weld region a) sample with large surface crack deflection and b) sample without large surface crack deflection (deflections below surface).

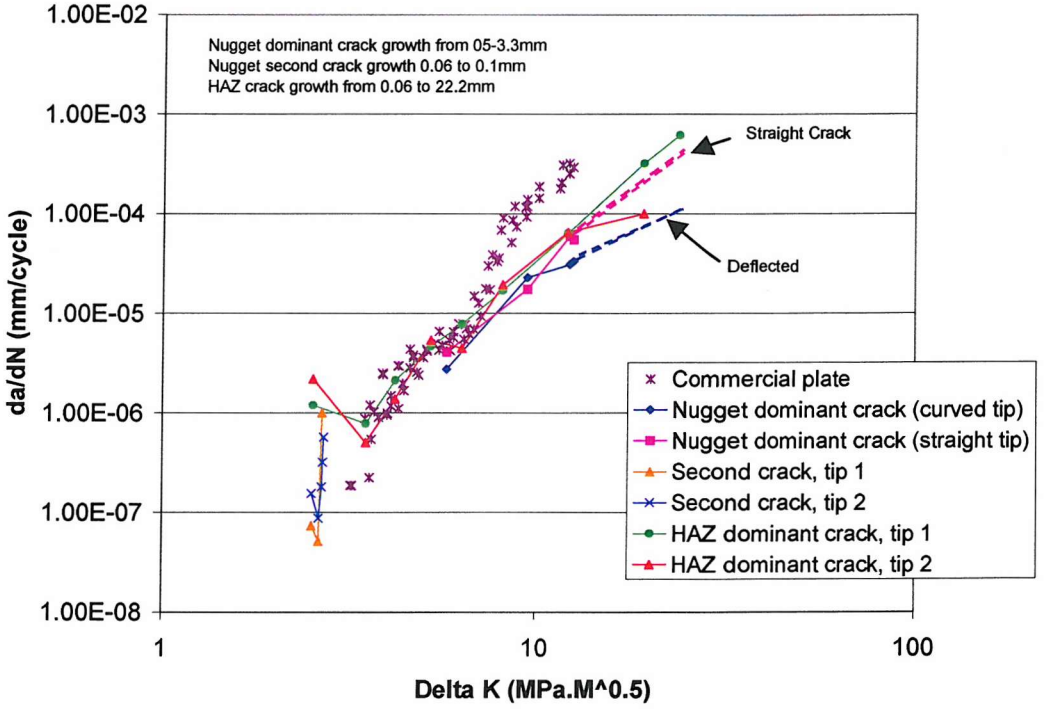

Figure 121 da/dN results for failure over the weld region (slow weld), including parent plate data[111].

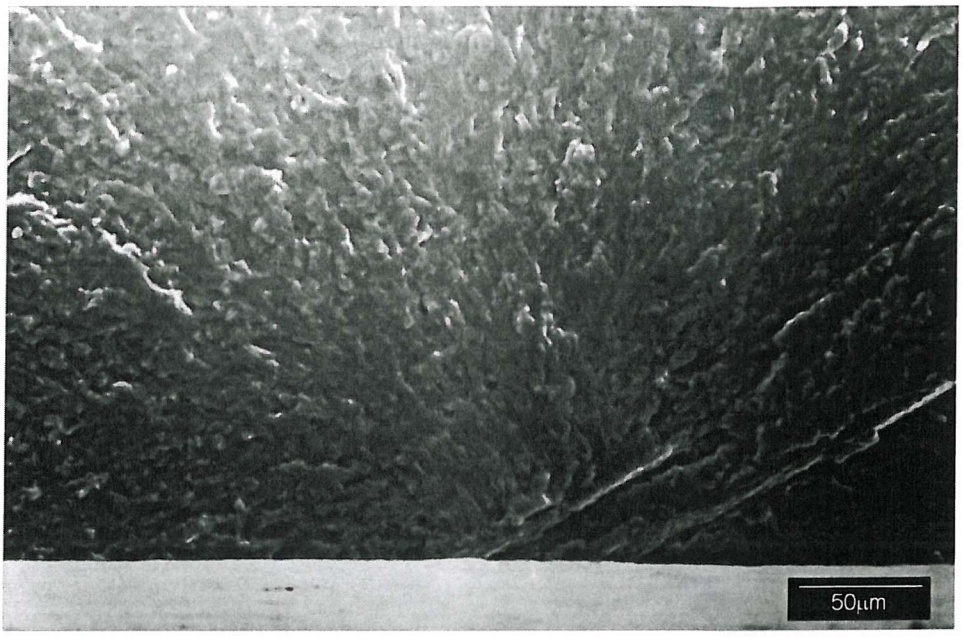

Figure 122 SEI micrograph showing fracture surface features leading back to the weld failure initiation site for the slow weld specimen with marked crack surface deflection.

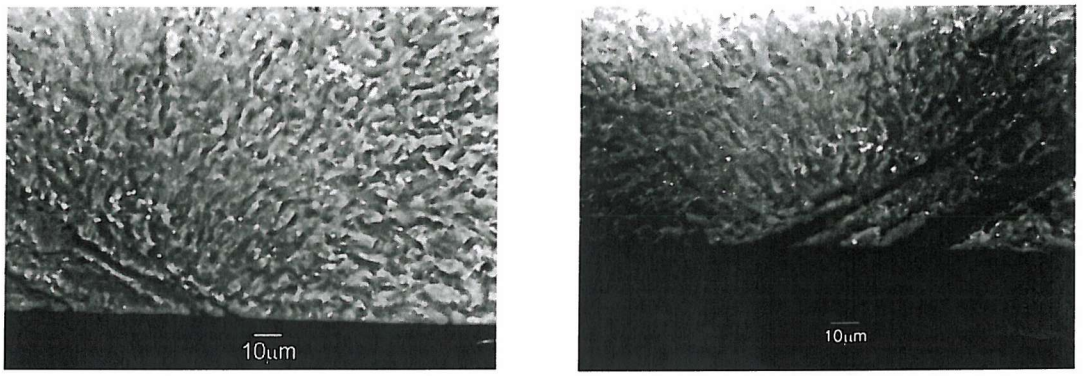

Figure 123 BEI micrographs of specimen with marked surface crack deflection showing the intermetallic distribution around initiation site for both faces of the failure (matching faces).

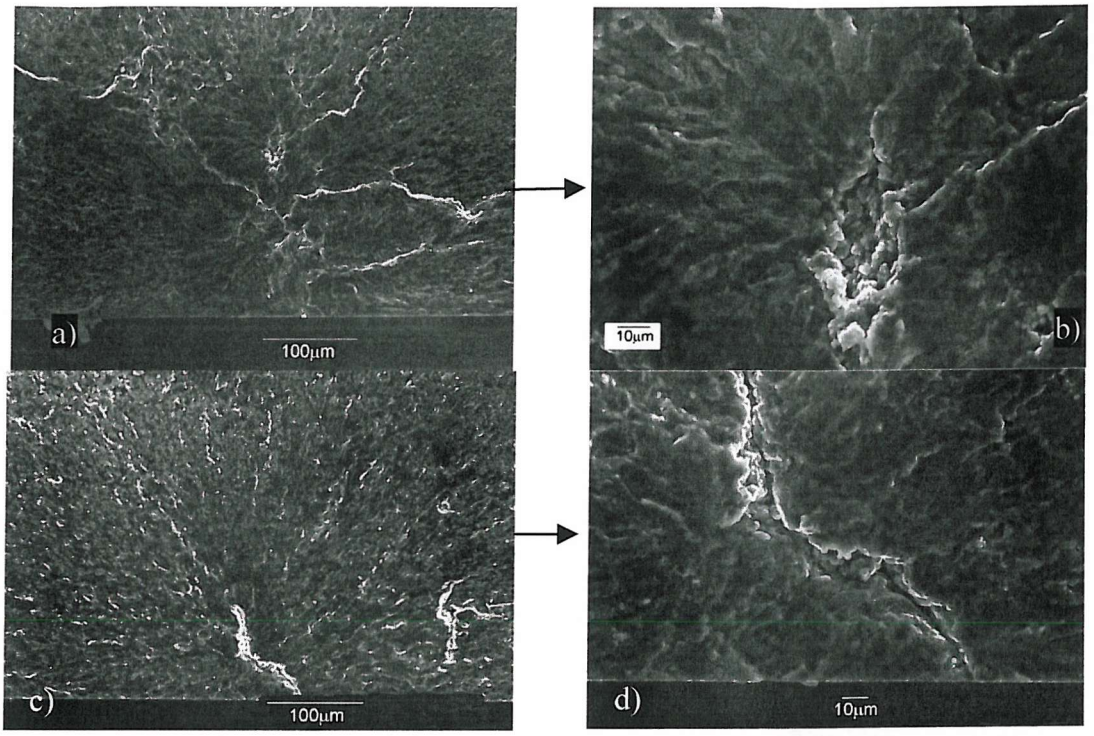

Figure 124 SEM micrographs of initiation sites found for the slow weld specimen without marked surface crack deflection: a) shows multiple initiations sites close together just below the surface, b) shows a more detailed image of one of the initiation sites from a), c) secondary initiation site, with surface features leading back to a linear defect, highlighted in d).

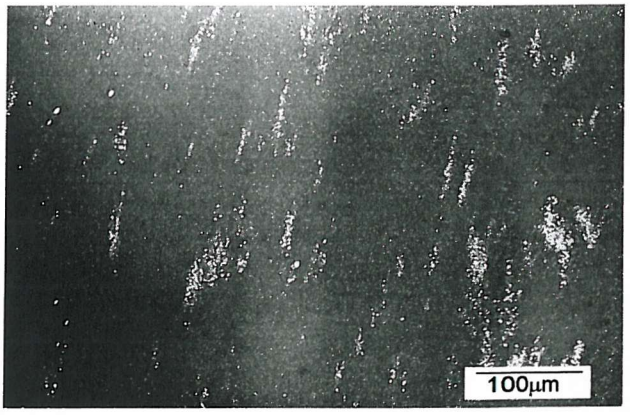

Figure 125 BEI image of a slow weld specimen top surface close to crack initiation site.

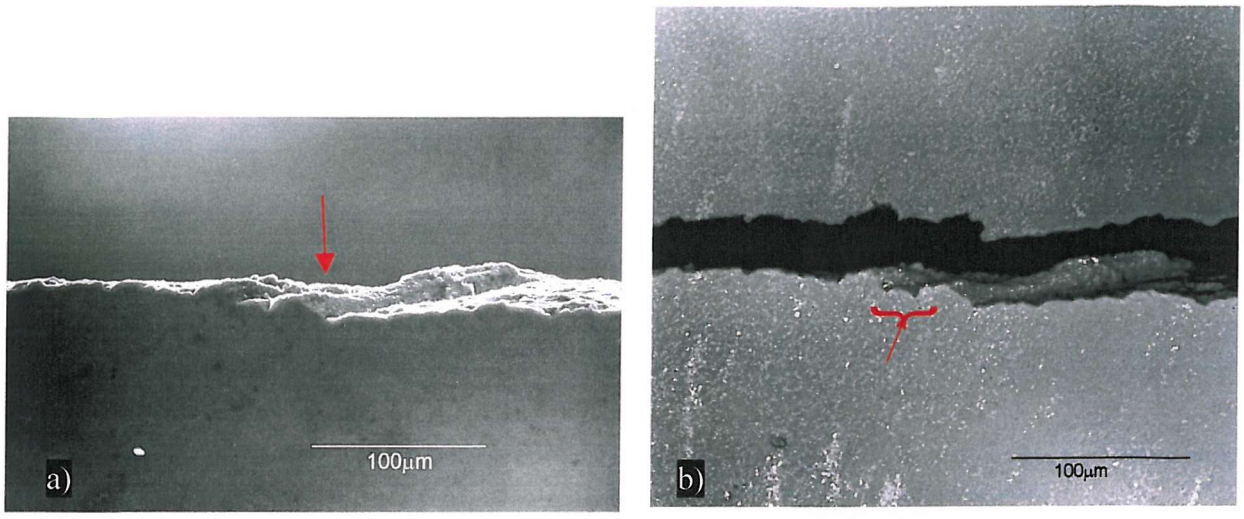

Figure 126 Top surface of the slow weld sample with a marked surface crack deflection a) SEI of one side of the failed sample and b) BEI of both sides of the failed specimen (arrows highlight the crack initiation site).

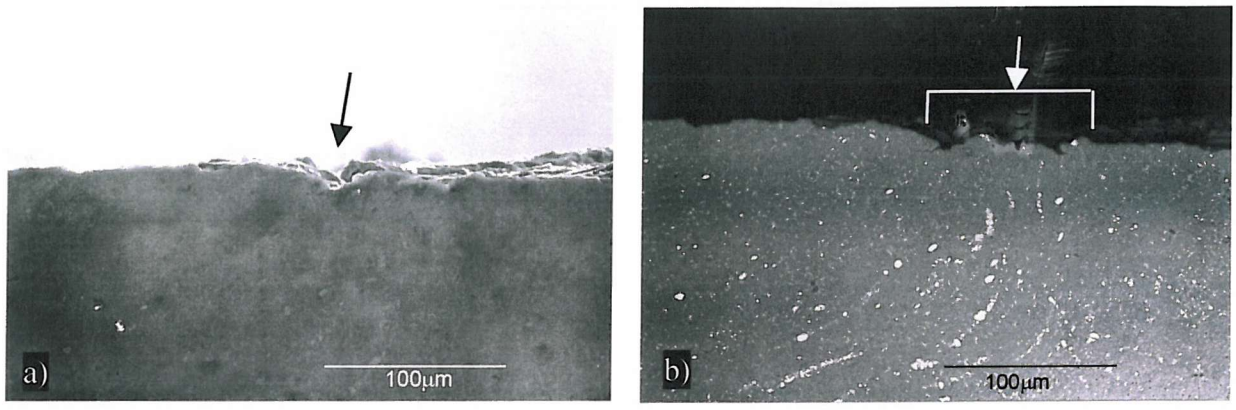

Figure 127 Top surface of slow weld specimen without marked surface crack deflection a) SEI and b) BEI (initiation location highlighted).

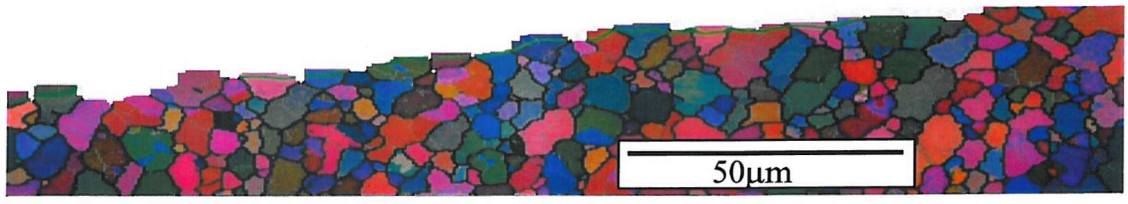

Figure 128 EBSD orientation map around initiation of slow weld specimen with marked surface crack deflection.

a)

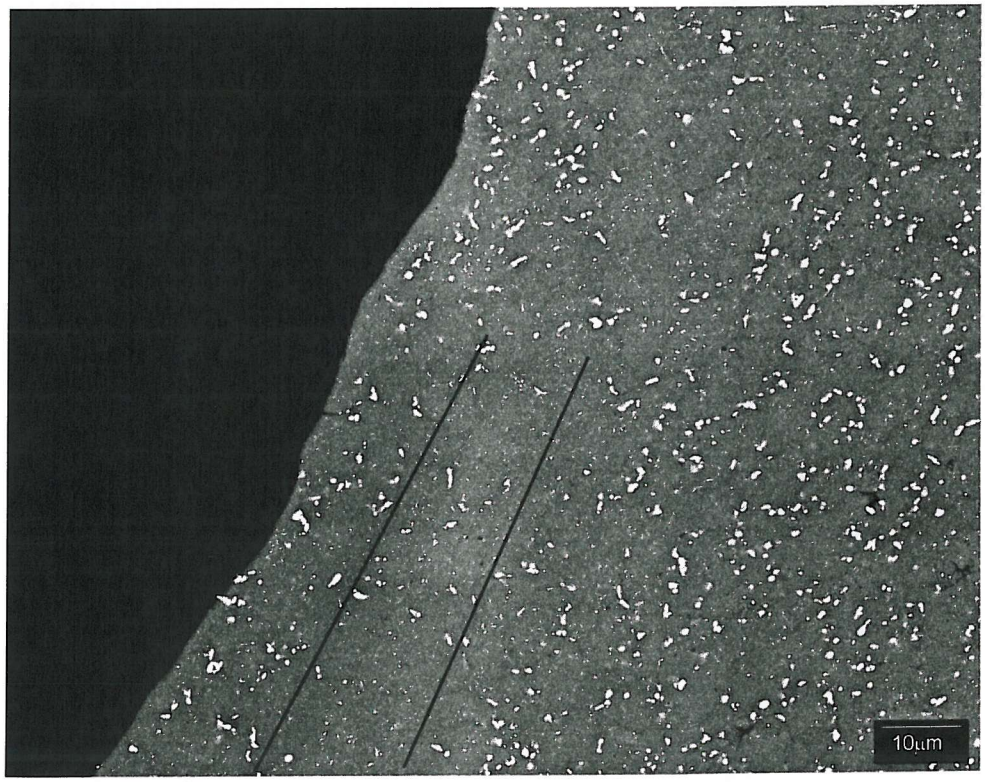

b)

Figure 129 BEI images of slow weld deflected crack growth, a) low magnification and b) higher magnification: regions of low particle density are highlighted in both images.

Figure 130 Fracture surface of subsurface crack deflection showing significant oxide debris and rubbing indicative of closure.

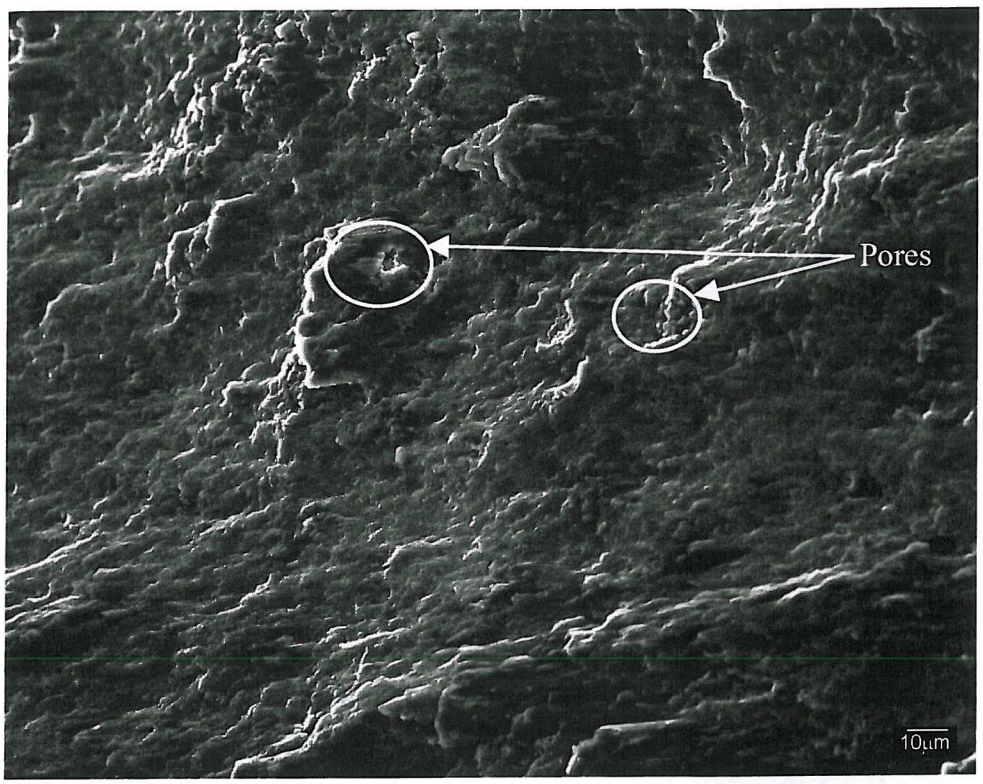

a)

b)

Figure 131 Deflected fracture surface features, a) SEI (pores circled) b) BEI.

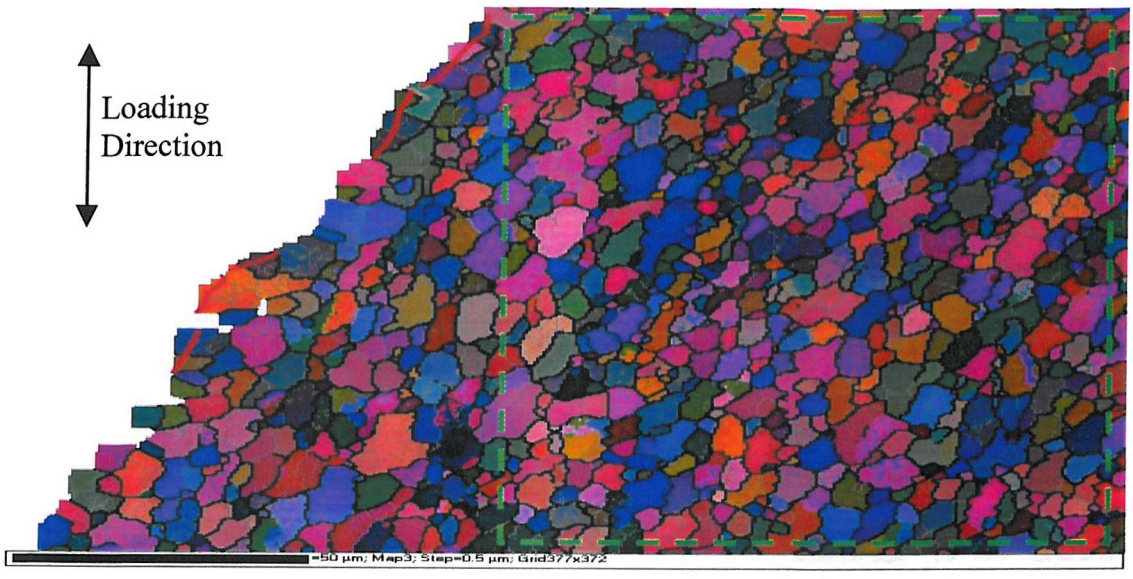

Figure 132 Specimen top surface EBSD map of deflected crack growth: red line marks actual crack front and feret measurements show in Figure 133 correspond to the region surrounded by green rectangle.

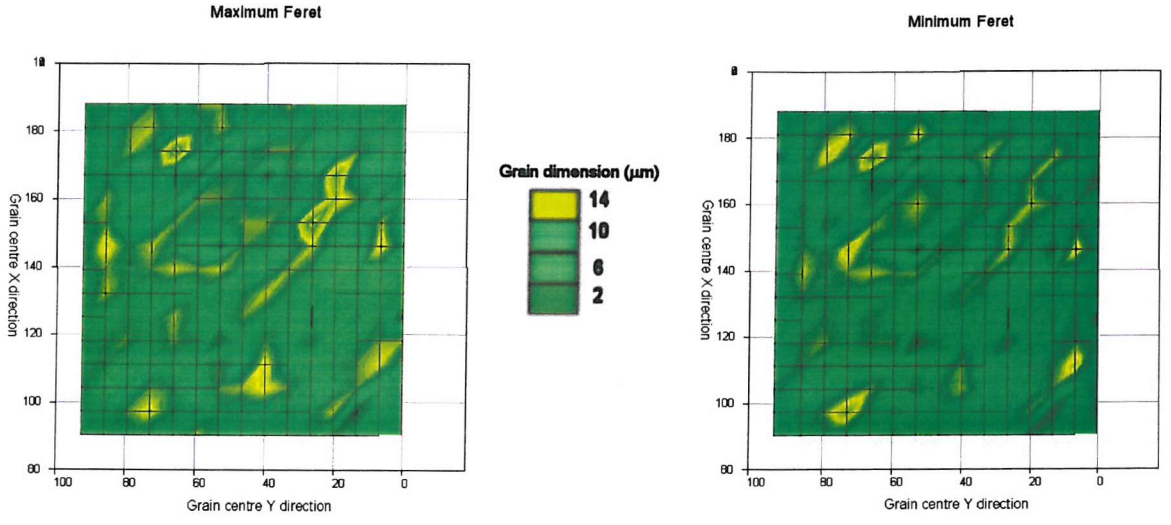

Figure 133 Grain feret diameters measurements obtained from indicated region in Figure 132, a) maximum feret and b) minimum feret.

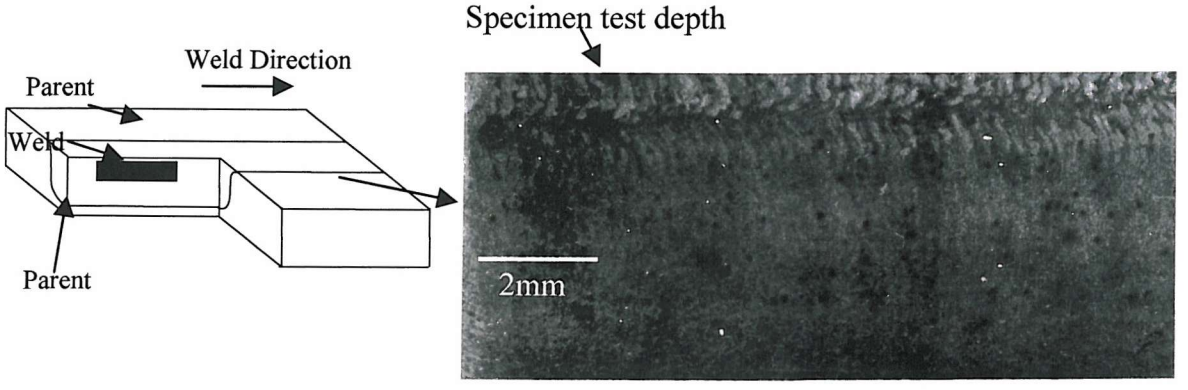

Figure 134 Vertical weld flow features observed in slow weld specimens (plane parallel to welding direction and plate through thickness).

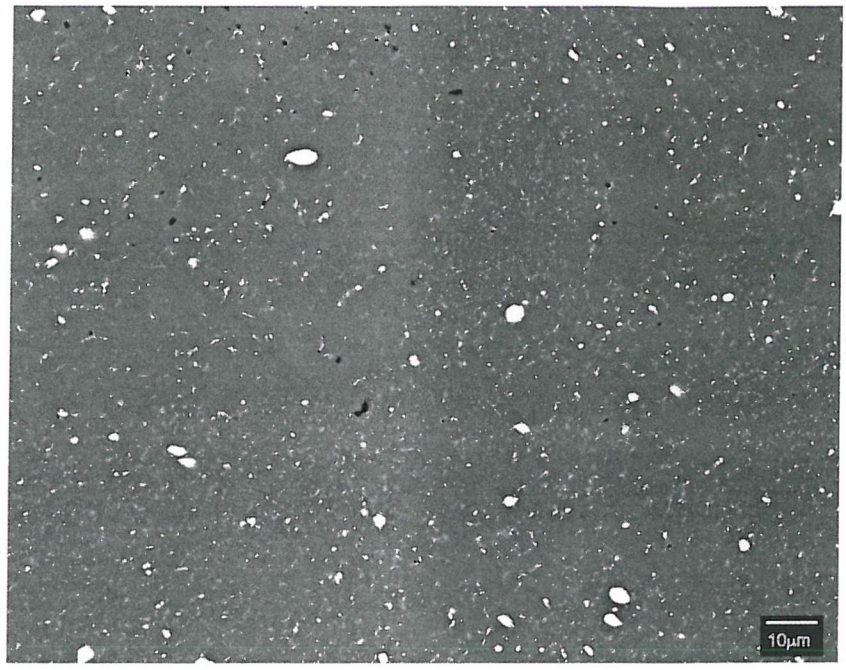

Figure 135 BEI of flow features in Figure 134.

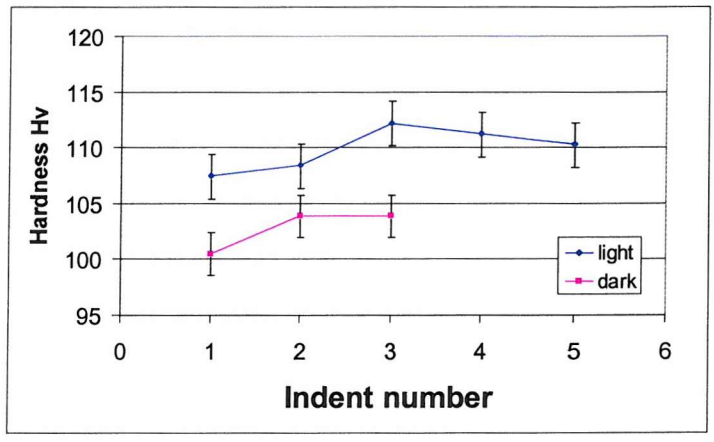

Figure 136 Hardness variations associated with banded structure of the slow weld, lines correspond to light and dark regions illustrated in Figure 134.

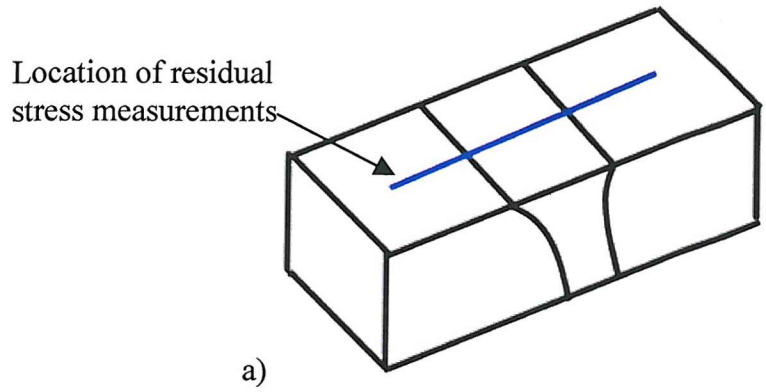

a)

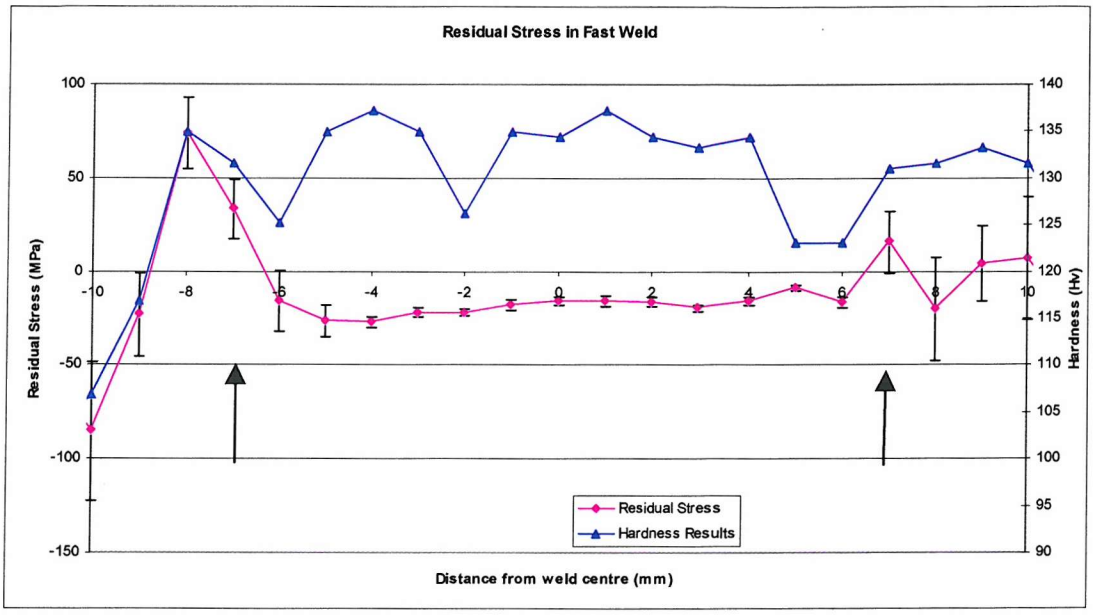

b)

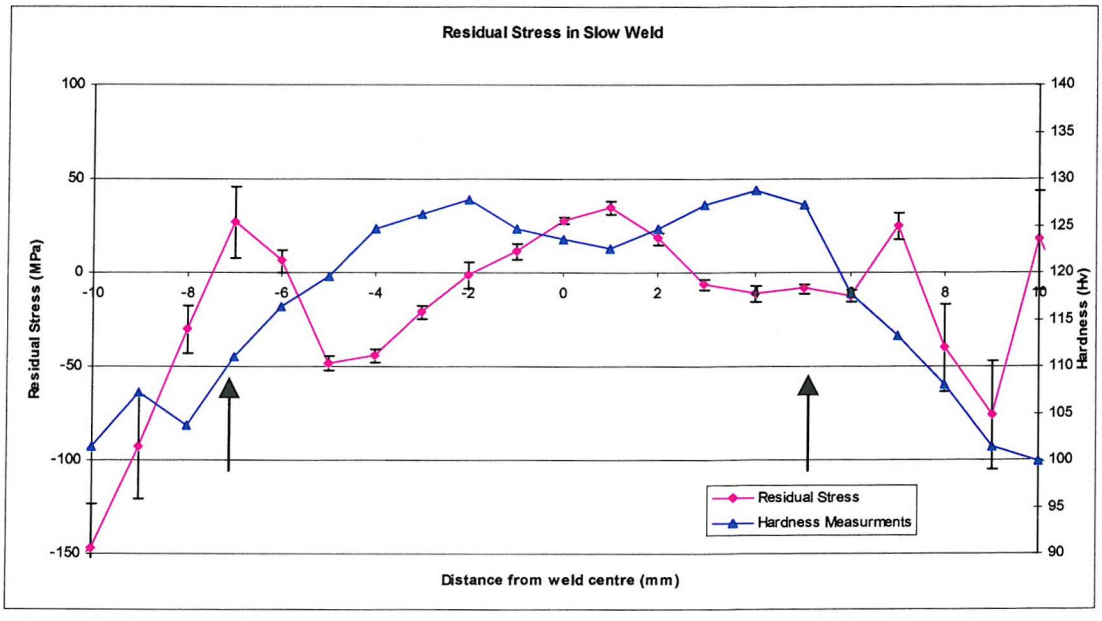

c)

Figure 137 Transverse residual stress profiles obtained across the 25mm gauge weld regions, and corresponding hardness profiles; a) shows measurement locations within the fatigue test coupons, b) fast weld results and b) slow weld results: arrows indicated edge of weld region.

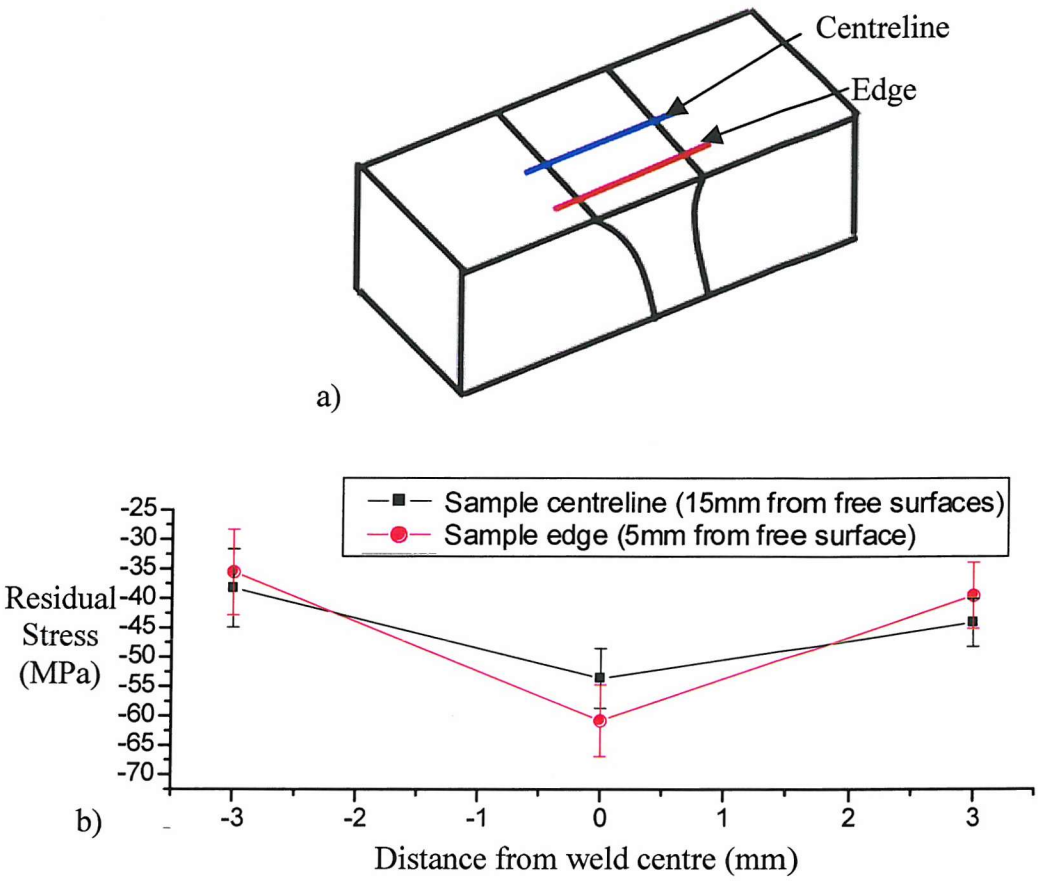

Figure 138 Longitudinal residual stress assessment in the slow weld flow arm region: measurements made on weld centreline and 5mm from sample edge; a) shows measurement locations within the fatigue test coupon and b) shows residual stress results.

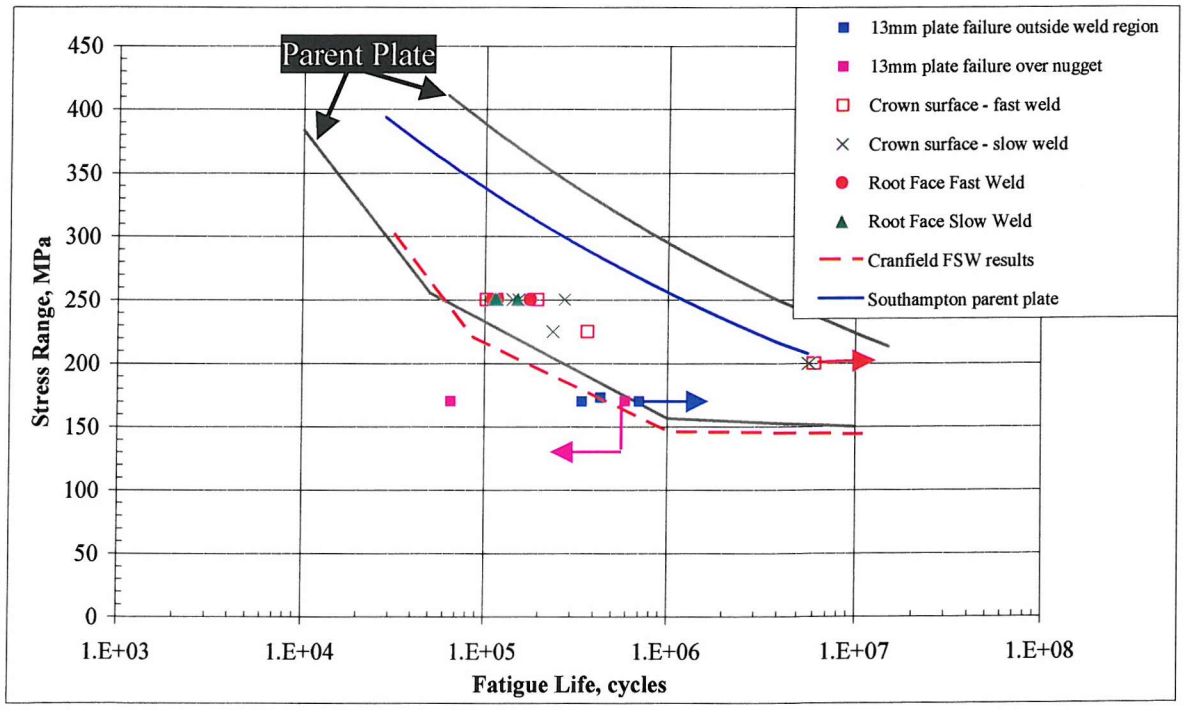

Figure 139 S/N data obtained from weld root testing, plus crown surface and parent plate results.

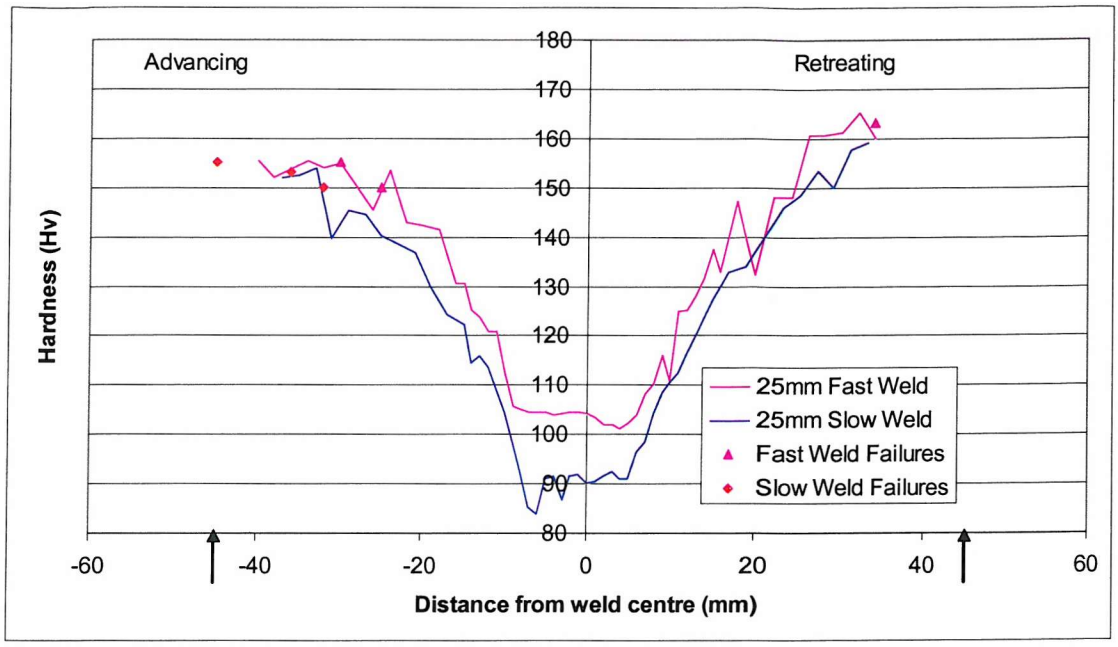

Figure 140 Weld root hardness traces for fast and slow welds with the locations of crack initiations indicated.

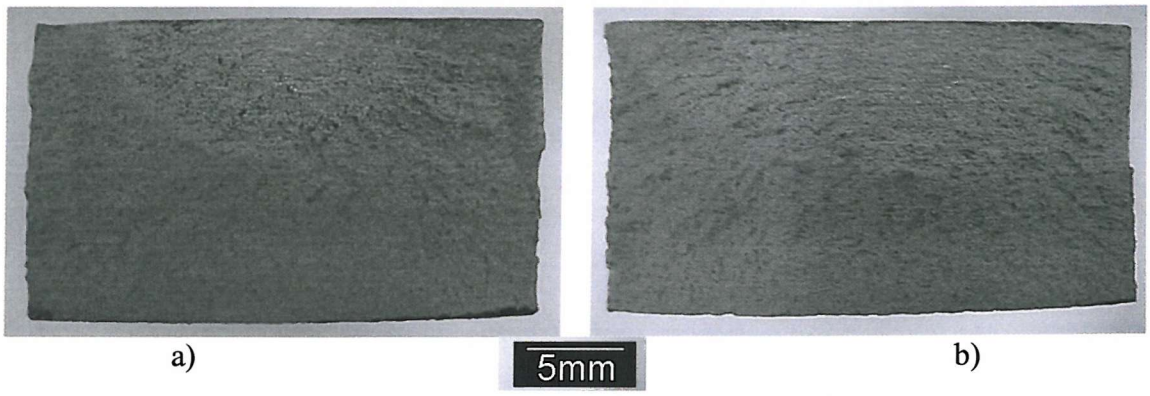

Figure 141 Macroscopic failures of root surface testing; a) fast weld and b) slow weld

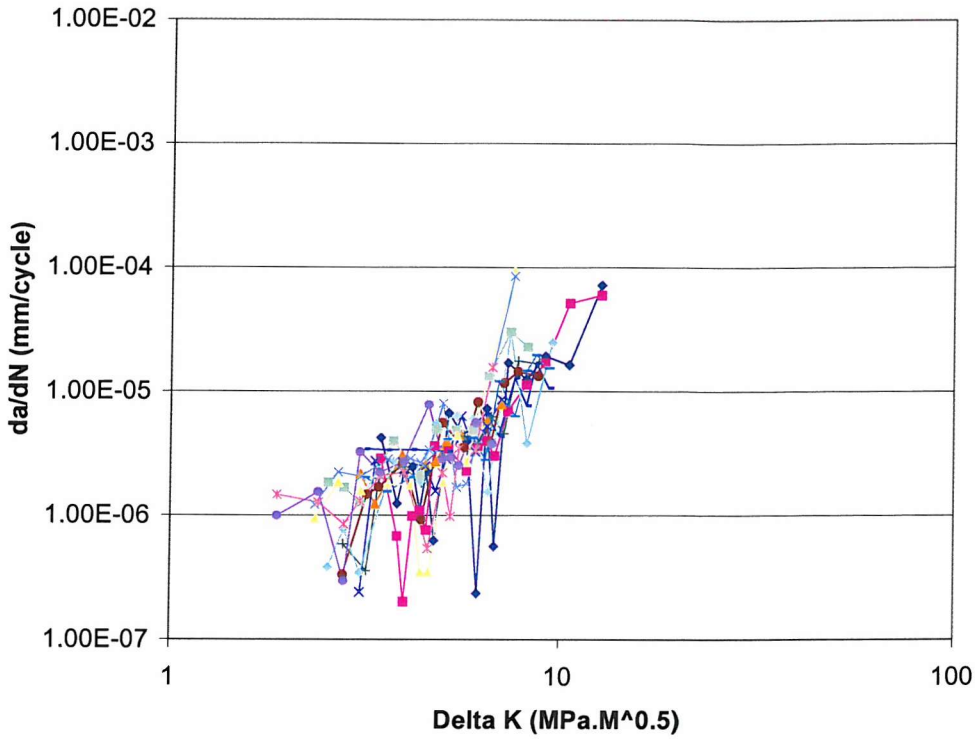

Figure 142 Slow weld root growth rate data scatter, based on multiple short crack measurements (0.05-4μm crack lengths).

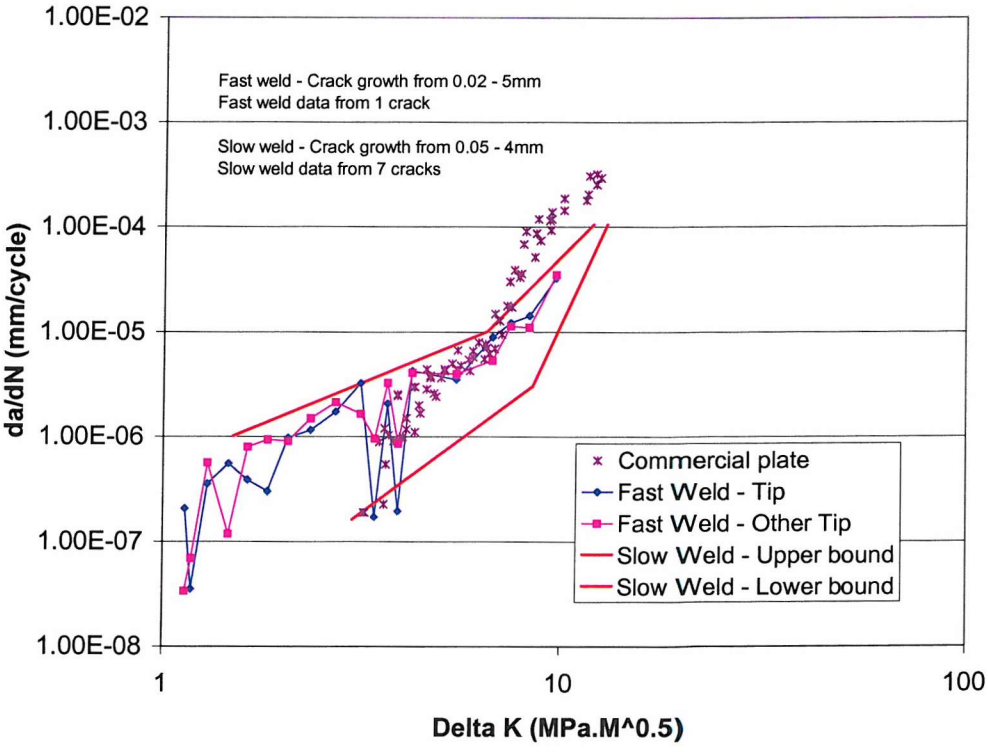

Figure 143 Fast and slow weld growth rate data for root surface testing, together with parent plate data[111].

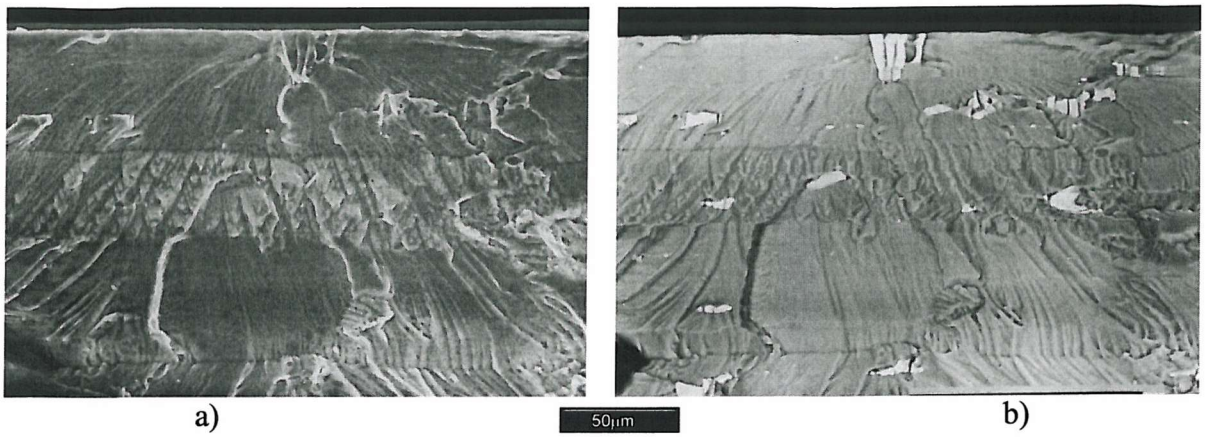

Figure 144 SEM images of microscopic failure of fast weld root failure, with river lines leading back to initiation; a) SEI and b) BEI.

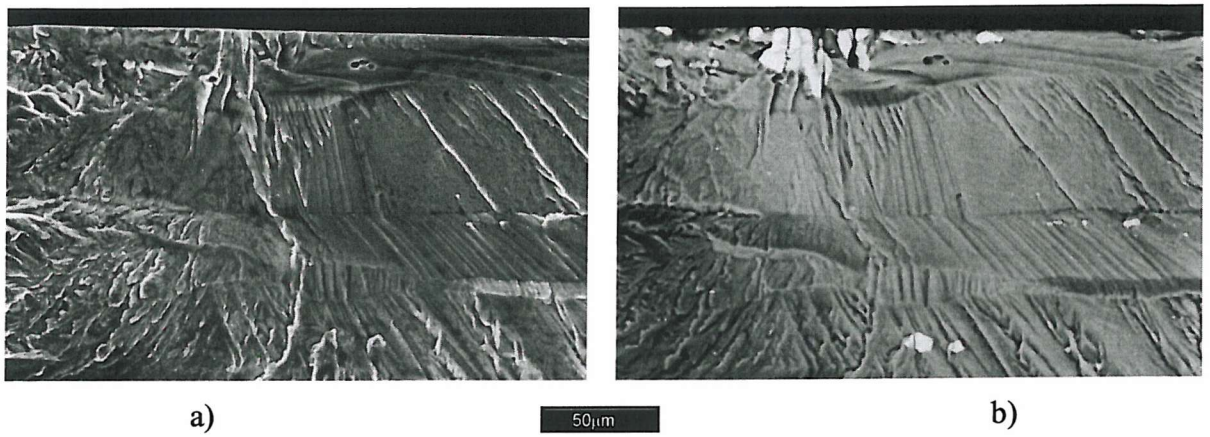

Figure 145 SEM images of microscopic failure of slow weld root failure, with river lines leading back to initiation; a) SEI and b) BEI.

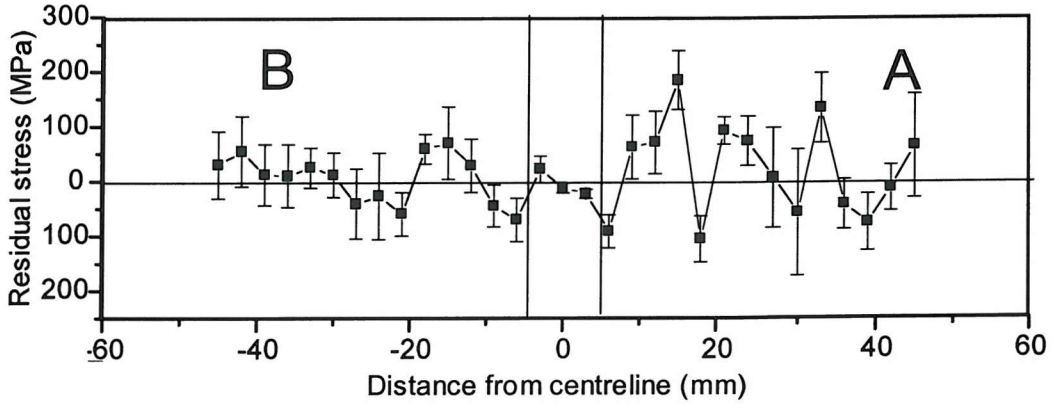

Figure 146 Transverse residual stress measurements at weld root of slow weld (weld region edges highlighted at ±5mm).

5.4 Discussion

5.4.1 Microstructure

The grain size variation between the welds is perhaps surprising; *viz* the slow weld has a finer grain size than the fast weld. The weld tool and specimen, are shown alongside the weld pitch values in Table 7. It would therefore be expected that the slow weld would be hotter than the fast weld; more grain growth might then be expected[124]. This is supported by the work of Hassan *et al*[61] (7010-T7651 friction stir welds in 6.35mm gauge plate) where a change in weld pitch from 0.32 from 0.53 mm/rev for a cold weld to 0.21 mm/rev for a relatively hot weld resulted in a factor of 2 grain size change near to the weld top surface (2.5μm for the cold weld to 6μm for the hot weld). However in the current work the observed grain size variation is not consistent with the observations of Hassan *et al*[61]: the fast weld has a higher weld pitch value than the slow weld, (0.31 and 0.24 mm/rev for the fast and slow welds respectively), with the fast weld exhibiting a grain size that is ~1.9μm coarser than the slow weld (4.7μm to 2.8μm respectively).

Considering the nominal heat input via the expression of Midling and Røruik may then help clarify the origins of the grain structure changes between the present fast and slow welds. As shown in Table 7, when frictional effects are considered in addition to the feed rate and rotation speed, the difference in heat input between the two welds becomes relatively small (~6%). Whilst approximately equivalent heat inputs may be identified with the present fast and slow welds, differences in heating and cooling rate will arise, with a faster thermal transient arising from a higher feed rate.

Hassan *et al*[125] found in their 7010-T651 partial penetration weld (15mm weld in 40mm gauge plate) that the grain size reduced through the thickness due to the higher cooling rates at the weld root, this is supported by the current partial penetration 25mm gauge welds; the grain size at the weld roots of the fast weld is finer than at the crown. They also suggest that for full penetration welds (7010-T7651, 6.4mm gauge plate) that the higher the energy input per unit length of weld (i.e. the lower the weld pitch) the more uniform the through-thickness grain size due to a more uniform temperature distribution within the weld. This is also supported in the current work; the slow weld has a more uniform through-thickness grain size than the fast weld.

Biallas *et al*[126] noted an increase in the nugget hardness with increasing rotation speed and feed rate. They used a constant weld pitch for each set of welding parameters that they used of 0.1mm/revolution, and, as such it, would be expected that the energy input per unit length would be the same for each set of parameters, it is therefore clear that the heating, cooling and strain rates are particularly important for overall weld region properties. Hassan *et al*[61] found that in the 7010 alloy they studied that the high temperatures experienced in the nugget region cause effective resolutionising of the alloying elements leaving relatively few coarse particles. In the case of the 7010 alloy the slower the cooling rate the more equilibrium η phase was formed. In the current work it may be seen that the present weld strength levels generally scaled with zone content levels, consistent with the observed heterogeneous precipitation within the weld nugget/flow arm being a limiting factor in weld strength as the more rapid thermal transient of the fast weld reduces the Cu and Mg solute loss to such coarse particles.

5.4.2 General Fatigue Behaviour

The fatigue lives of the present 25mm gauge weld specimens have been shown to be independent of crack initiation location, i.e. outside the weld region or over the weld region. This is somewhat surprising after the results seen previously in chapter 4 for the 13mm gauge specimens where initiation over the weld nugget region was associated with a marked drop in fatigue life. However in the 25mm welds, initiation of the failures over the weld region was not associated with the presence of a macroscopic flow discontinuity, which was identified with all of the failure over the nugget region in the 13mm plate (the over nugget failures are discussed in more detail in section 5.2.3). It is also clear from Figure 113 that the fatigue lives of the welded specimens are closer to the equivalent parent plate result (the Southampton parent plate data) than the 13mm gauge weld results discussed in chapter 4, independent of failure location in either gauge

Considering the influence of aging condition on the fatigue life in the first instance: given the 2 locations of fatigue crack initiation (i.e. outside the weld region and over the weld region) and the different thermal histories of the region it is worth examining any heat treatment effects that may affect the fatigue life. It is clear from Figure 147[127], which shows the dependence of fatigue resistance of 2024 on commercial temper conditions, that the fatigue life is in fact not dramatically affected by the temper condition (factor ~3 in fatigue life at 250MPa), which is within the scatter band of the present data.

Considering the general influence of weld process conditions on fatigue life, it is significant to note that Biallas *et al*[126] reported an increase in fatigue life with an increase in rotational and traverse speed for as welded (i.e. weld features still present) 2024-T3

friction stir welds: this was not seen in the current surface skimmed tests. Biallas *et al*[126] attributed the increase in fatigue life to the increase in the hardness of the nugget region, with crack initiation being linked to weld toe features caused by the welding process. The exact shape of these may however be expected to change with welding parameters with the work of Bussu et al highlighting the effect such weld toes may have on fatigue life when comparing skimmed and non-skimmed specimens. As such, the present work may be identified as a more "fair" indication of intrinsic effects of weld process parameters on fatigue behaviour. It may further be noted that the present weld root tests explicitly show a limited effect of nugget hardness on weld behaviour, as very much softer weld material was effectively tested in the root face experiments.

Ericsson *et al*[76] tested 6082-T6 in the as-welded condition and reported initiation for transverse specimens from within the weld, but only for high load levels (exact load level is not given, ~ 165MPa R=0.5). This finding is difficult to support or otherwise with the current work's limited number of over weld failures. One of the present over weld failures occurred at $\Delta\sigma$ of 225MPa and the other at 250MPa. However the specimen tested at lowest $\Delta\sigma$ failed outside the weld region.

5.4.2.1 Failure Outside the Weld Region

- ***Initiation***

The cause of crack initiation in the failures outside the weld was identified in all cases as occurring at intermetallics. This type of initiation was also seen in the 13mm weld failures outside the weld region in Chapter 4, and is the typical initiation mechanism for 2024-T351 parent plate. Initiation predominantly occurred well away from the weld in a region

that was affected by only minor heating and may be considered to be artificially aged to only a moderate level, c.f. the material close to the weld, as indicated by the hardness traces in Figure 114 and Figure 140 as the locations of the initiation are close to, or just inside the hardness maximum of the HAZ. The DSC traces for the equivalent region of the 13mm gauge welds clearly show a progression from zone strengthened material in the parent plate to material of increasing S/S` precipitation, with little to no zone content. There appears to be no difference in the initiation mechanism between the fast and slow welds and crown and root tests. For failures outside the weld region, this is consistent with the failure regions in question having very similar hardness levels and the same parent plate grain structures.

The lack of TMAZ initiation in the 25mm welds, as seen in the 13mm weld, is of course interesting in terms of microstructural influences on fatigue, similar hardness and grain structure characteristics were essentially present in the TMAZ of the 25mm gauge weld, in that the lower part of the hardness slope down from the central hardness plateau was located in mildly deformed region of the parent plate it is however valuable to consider residual stress distributions measured in the 25mm welds. Literature results indicate that tensile transverse residual stresses may be present across the weld nugget, and out to the locations of the 13mm gauge weld TMAZ failures; however in the 25mm welds the present residual stress measurements suggest that the transverse stresses across the nugget are infact predominantly compressive. The literature residual stress measurements available to date have all been obtained for full penetration friction stir welds in relatively thin gauge materials (7mm gauge maximum)[96]. It is clear however that the residual stress in the 25mm gauge partial penetration welds do not follow the same general trends in

residual stress with compressive stresses being present in the weld region rather than a tensile stress. There are several possible explanations for the differences in residual stress, including a more effective heat sink effect of the parent plate due to a relatively larger amount of material surrounding the weld process volume. This will also alter the mechanical boundary conditions due to the increased relative stiffness of the surrounding parent plate (parent plates are thicker compared to weld volume), whilst in a transverse sense in particular, the weld tunnel of these non-penetrating 25mm gauge welds could be seen to allow bending of the weld plate that could relax the tensile stresses in the transverse direction. Not withstanding the origins of residual stress changes between thicker and thinner, penetrating and non-penetrating welds, it may be seen that lower indeed compressive transverse residual stresses in the immediate vicinity of the 25mm non-penetrating welds are a likely contribution to the more distant HAZ failures of these specimens.

- ***Propagation***

For the failures outside the weld region there is essentially no difference in grain structure between the 2 welding conditions, and the grain structure is essentially the same as the parent plate. The intermetallic density is also not expected to be significantly different between the welds. It is therefore not surprising that the fatigue crack growth rate for both welds is essentially the same and similar to the parent plate data for the early growth. The crack growth rates obtained for the 13mm gauge weld (see Chapter 4) show that the fatigue crack growth in the mildly deformed HAZ region of the 13mm gauge is higher than in the current 25mm gauge welds (see Section 5.2), consistent again with residual stresses having a more direct influence on the outside weld failures of the 13mm gauge welds.

In terms of varying heat treatment conditions between the 25mm gauge HAZ failure location, the 13mm gauge TMAZ failure locations, and the behaviour of parent material, it is valuable to note the results of Bray *et al*[128] for a wide range of ageing conditions in 2024 plate material (from T351 to a reasonably overaged 48 hours at 190°C). It is difficult to directly link the results of Bray *et al*[128] to the complex, partially reverted condition of the 13mm gauge weld TMAZ failures, however the far HAZ material of the 25mm gauge weld failures would appear to be more comparable to simple low temperature treatments. Bray *et al*[128] showed that the fatigue crack growth resistance of 2024-T3 initially improves by a factor of ~2 for aging up to 0.2 hours for ΔK levels of 5 and 7.5 MPa$\sqrt{m}$ and R=0.1 in a moist air environment. However for the highest ΔK tested by Bray *et al*[128](15 MPa$\sqrt{m}$) no variation in crack growth rates was measurable going from the naturally aged condition to the most overaged material. The cause of the drop in crack growth rate for short aging times was thought to be due to the production and growth of solute clusters during the early stages of artificial aging with the later increase in growth rate being attributed to the dissolution of the clusters and the precipitation of S/S` phase. In the current work the aging condition in the 25mm gauge weld HAZ failure is identified as mostly overaged with significant S/S` content. As described above Bray *et al*[128] reported that the *da/dN* should have reached a minimum and returned to approximately the parent T351 level, hence the aging condition is unlikely to have any significant effect on the low and intermediate ΔK fatigue crack growth rate in the current welds. At ΔK ~10MPa$\sqrt{m}$ (corresponding to a crack length of ~2mm) the growth rates of the HAZ failures drops below that of the parent plate, which would not then appear to be an ageing effect.

A further factor that may of course have a marked influence on the fatigue crack propagation is the presence of residual stresses. The results obtained for the present 25mm welds are unfortunately unsatisfactory for the material outside the fine grained weld region. Furthermore, effects on longer crack growth may be associated with changes in residual stress with increasing depth into the sample as shown by Webster *et al*[95], which would not be measured by laboratory X-ray methods

5.4.2.2 Failure over the Weld Region

- ***Initiation***

The initiation sites in the over weld failures of the 25mm gauge specimens were easily identified as defects, some surface and some subsurface. The defect shape was variable but the defects tended to extend into the plate thickness, see Figure 124.

There are a number of features that can be identified as possibly influencing the failure over the weld region, including: strength variation, residual stress changes, grain structure, intermetallics and defect density. Comparing the hardness maps for the two welds shows a hardness difference in the weld centre, with the slow weld being slightly softer than the fast weld. This is indicative of a slight drop in strength in the weld region of the slow weld which could be considered to assist crack initiation however as suggested by Biallas et al. As noted earlier, hardness effects do not appear significant when considered in relation to the fatigue resistance of the soft weld root materials. It is also clear from the residual stresses presented in Figure 137, that the fast weld has a mainly compressive stress in the weld centre; this would be expected to discourage crack initiation by

suppressing quasi-static failure modes such as particle cracking or interface decohesion. The slow weld however has a tensile peak which corresponds to a drop in hardness which could be detrimental to fatigue crack initiation resistance.

The grain size in both weld cases is very fine with the slow weld being finer by ~40% at the test depth; using the Hall-Petch type equation for endurance limits after Turnbull and De Los Rios[129] for commercially pure aluminium it is possible to estimate the effect that the change in grain size between the welds will have on fatigue life, suggesting a 30% increase in endurance limit for the slow weld material. As such it would appear that the grain structure variation of the two weld speeds is not a direct contribution to the nugget failures.

In terms of intermetallic particle contributions to weld failure in the 25mm gauge specimens, it is clear that the normal "direct" contribution of intermetallics to initiation (i.e. via cracking or decohesion) is not relevant in this instance, as cracks clearly evolved from other large weld defects in the slow welds. It is still valuable to note that intermetallic clusters were evident in the 25mm gauge welds, but were clearly not severe enough to cause crack initiation (particles within the clusters were still relatively small).

The literature generally reports low defect content for friction stir welds. Figure 148 shows results from a systematic measurement of defect content across the roots and crown of the present 25mm gauge. It is clear from Figure 148 that the pore density in the weld centre of the slow weld in particular is higher than that of the rest of the slow weld. The micrographs included in Figure 148 are representative of the pore distributions in the weld

regions indicated. It may be noted that the location of the increased pore density corresponds to the tensile peak location in residual stress in the slow weld, which may then be seen as a particularly damaging combination. However crack initiation factors must still be finely balanced in these tests, as not all slow weld specimens failed within the weld region. In the first instance it may be identified that variability in pore population (evident in the variable morphology of the defects that cracks came from) is a significant contribution to specimen-to-specimen changes in initiation location.

The exact mechanism for the formation of the pores in friction stir welds is not fully understood to date. Gould and Feng[56] for example suggest that welding at a relatively cold temperature (i.e. increased traverse speed for the same rotation and force) can result in pores; this seems unlikely to be a major effect in the current weld as the energy input per unit length in the welds was fairly similar, with the slow weld energy being the slightly higher of the two.

A selection of the pores that are found on the crown surface around the weld centre of the slow weld specimens are shown in Figure 149. The complex nature of the pores is evident in the images. What is also evident in Figure 149 are the intermetallics which appear to decorate the edges of the pores with many showing evidence of a local particle free zone in their immediate surroundings (Figure 149a) in particular). While there has been little work reported on porosity in friction stir welds it is a well known problem for fusion welds, resulting from a number of processes including shrinkage during solidification and liquation. The solid state nature of friction stir welds is thought to remove solidification problems, i.e. bulk material does not reach the melting point. It has however been

suggested by several authors that incipient melting may occur during friction stir welding[36,55], however no direct evidence has been produced to support this idea. Incipient melting or liquation is common in the partially melted zone (the region between the HAZ and the fusion zone) of fusion welds and in super-plastic deformation[130]. Liquation has for example been seen to occur at large θ (Al_2Cu) particles, along grain boundaries and at numerous isolated points within 2219-T851 by Huang and Kou[131] for Gas Melt Arc (GMA) welding. Such melting may occur before the equilibrium solid plus liquid region of the phase diagram if the heating rate is sufficiently fast to prevent the θ particles from dissolving. Prangnell and Norman[132] studied 2024 TIG welds. They identified incipient grain boundary melting in all specimens; this was associated with a PFZ being formed and coarse spherical particles of equilibrium S phase. 2024 was identified as particularly susceptible to incipient melting due to the wide freezing range (~140°C) and the ability of 2024 to form low melting point eutectic phases at around 500°C.

In order to assess the potential for liquation in the current welds, DSC was carried out on specimens taken from the weld centre at both the weld crown and weld root fatigue testing locations, the results of which are shown in Figure 104 for the temperature range 100-400°C and Figure 105 for the temperature range 450-540°C. At this point it is worth re-emphasising the difference in the high temperature thermal effects evident in Figure 105 above 490°C. For all but the slow weld-flow arm trace an endothermic reaction occurs at around 505°C.

Given the obvious differences between the DSC locations a series of short high temperature heat treatments were carried out on specimens of 2024 parent in the DSC to

assess conditions under which incipient melting may occur and effects on subsequent DSC traces: Table 12 shows the test matrix used for the high temperature thermal treatments. The maximum controllable heating rate achievable by the DSC was 200°C/min, whilst the cooling rates that were achieved were in excess of 200°C/min to below 300°C. The heating rate achieved during the welding process is reported in the literature to be ~1000°C/min whilst cooling rates may be of the order of ~500°C/min (depending on exact welding conditions and alloy): while the current heat treatment experiments clearly do not represent the exact weld thermal cycle they may provide useful information about the effect of exposure to a high temperature cycle on the phases present. After the heat treatment cycle a normal DSC temperature scan was performed for indications of melting effects (experimental details given in chapter 3).

Looking at the high temperature dissolution endotherm shown in Figure 150, it is clear for the majority of the traces that low temperature phase dissolution is completed by ~500°C. The exception is the 490°C trace where the dissolution is still not complete and a particularly strong melting peak occurs at an onset temperature of ~505°C. Looking closely at the high temperature incipient melting endotherms in Figure 150, distinct variation in onset temperature is evident with evidence of two reactions (i.e. two peaks). While it is not possible to identify all possible reactions for a complex commercial material, likely ones that are readily identifiable with the lower bound of the apparent melting point include[133]:

$Al_2CuMg + Al_2Cu + Al\alpha \rightarrow L$ 504°C

$Cu_2FeAl_7 + Al_2CuMg + Al_2Cu + Al\alpha \rightarrow L$ 505°C

The particularly strong melting peak of the 490°C trace may then be attributed to the ternary Al-Cu-Mg reaction at 504°C as the relevant thermogram showed incomplete dissolution of low temperature phases which would be expected to include Al_2CuMg and Al_2Cu.

Considering the lower temperature of the two apparent melting reactions in Figure 150, it may be seen that this peak is "removed" for prior treatment to a temperature of 510°C. For treatment to 530°C this lower temperature melting effect returns. The true maximum temperature in any friction stir weld will always be difficult to establish directly, particularly in terms of material directly under the tool shoulder, however the high apparent GPB/zone content of the two weld crown materials do suggest that temperatures of the order of the alloy solution temperature have been reached during welding. Furthermore, whilst prior heat treatment may be seen to enhance the incidence of incipient melting via non-equilibrium melting (as seen in Figure 150 for the 490°C treatment material), it is difficult to identify a mechanism by which a short thermal exposure to temperatures less than or equal to the materials solutionising temperature (495°C) can remove phases associated with incipient melting. It is clear that the present heat treatment experiments cannot provide a simple maximum temperature "calibration" for the DSC traces of the 25mm weld materials (as in Figure 105), however it is evident that short exposures to temperatures of the order of 510°C can cause the initial incipient melting reaction to be removed. Bearing in mind the fact that:

a) pores in the slow welds were linked to the presence of intermetallic particles (Figure 149),
b) the slow weld had the highest heat input,

c) porosity was evident in the hottest material of the weld (i.e. the crown), and

d) incipient melting in other high temperature/high strain processes such as super-plastic forming is identified with void formation/cavitation[134,135,136],

then a likely origin of increased porosity (and hence nugget failure) in the 25mm gauge slow weld would appear to be incipient melting, highlighting the careful balance of process control that may be necessary for optimum weld performance.

While the elongated shapes of some of the defects makes an estimate of associated approximate K levels difficult, using a nominal dimension of 100μm for a semi-circular surface crack at 250MPa load level, it is possible to estimate a K level of the order of ~4MPa√m, which is clearly significant for the present materials given the fact that the long crack threshold is of the order of 3-4MPa√m at R=0.1 for conventional 2024.

Run number	First stage	Second Stage
Parent	-	-
1	5-480°C at 200°C/min	480-490°C at 20°C/min
2	5-500°C at 200°C/min	500-510°C at 20°C/min
3	5-520°C at 200°C/min	520-530°C at 20°C/min

Table 12 Thermal cycles for high temperature exposure tests

- ***Propagation***

The crack growth rates shown in Figure 121 show that the growth rate for a crack growing through the weld region is reasonably comparable with a slow weld failure outside the weld region. A significant feature of the crack growth over the weld region is of course the crack deflection that occurred in both cases (in one case up to 60° to the nominal crack growth direction). There were also subsurface out of plane curved deflections that can be

seen in Figure 120 on both failures. These appear similar to the failure around the nugget region seen in the 13mm weld in Chapter 4, but of very different orientation within the weld. It is clear in Figure 121 that the crack growth rate of the deflected crack tips of the dominant crack is reduced compared with the other end which did not suffer such a significant crack deflection. This reduction in crack growth rate is likely to be due to the crack tip driving force being reduced by the deflection as can be seen in Figure 151, which shows two boundary conditions for deflected crack growth: firstly when the entire crack is growing at an angle to the applied stress representative of the deflected crack section being large relative to the original straight crack section and secondly, with a infinitesimal crack tip deflection on straight/mode I macroscopic crack (similar to the situation when the crack starts to turn). The graph represents the proportional change in crack driving force that may be expected for the angled crack tip compared to an equivalent sized straight crack, where the mixed mode stress intensity conditions of the angled crack tip are expressed in terms of equivalent strain energy release rate, (ΔK_{EQ}), where $\Delta K_{EQ} = \sqrt{\Delta K_I^2 + \Delta K_{II}^2}$. It is clear that at the maximum angle of ~60°, a much reduced portion of the original crack tip driving force is acting on the crack (30-60% depending on exact geometry considered), highlighting the genuinely weak path that must be present in this direction within the weld.

The 25mm welds do not have the same distinct onion ring structure identified with the 13mm weld, however similar flow features and associated variations in local microstructure were identified when the weld was sectioned parallel to the welding direction along the weld centre line. The flow features in the fast weld occur significantly further into the weld than the slow weld ~6mm and ~0.5mm respectively. The depth of

the features correlates reasonable well with the location of the curved features seen on the fracture surfaces.

EBSD results show that the grain structure is elongated approximately parallel to the growth direction which may have assisted the deflected growth that occurred via some degree of intergranular failure. This is consistent with the 13mm weld where the crack was aligned with the fibring of the grain structure in the nugget region in Chapter 4. Similarly, bands of intermediate sized intermetallics manifested at the fracture surface were also evident.

While pores were linked to the initiation of the cracks over the weld and a number of pores were seen on the fracture surfaces it is thought that the density of pores is not high enough to cause a significant deflection ($\sim<1\%$ of the overall fracture surface). It is also evident from Figure 148 that the pore density reduces with distance from the weld centre; it is therefore unlikely that porosity had a major effect on the crack path.

Oxide entrapment was suggested as a possible cause of the deflection seen in the 13mm welds and again it cannot be ruled out in the case of the 25mm welds, however no evidence of oxide particles was found.

In summary it would appear that there is no one significant factor causing the crack to deflect: it is therefore considered to be a combination of the microstructural factors:

1. alignment of microstructure (grains structure and intermetallic particles),
2. porosity,

3. local hard-soft band influences.

The observed crack deflection shows that even in welds where the widely identified "onion ring" features of a friction stir weld are absent, flow features of the joining process may still exert a strong influence on failures in such welds.

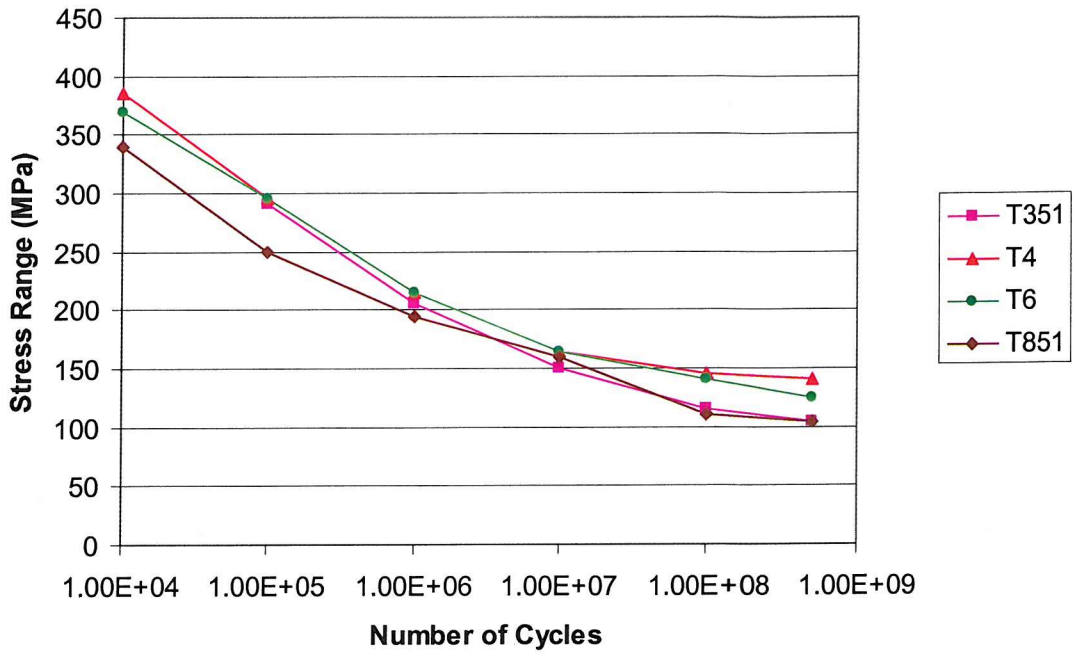

Figure 147 Rotating bend fatigue results for commercial tempers for 2024[127].

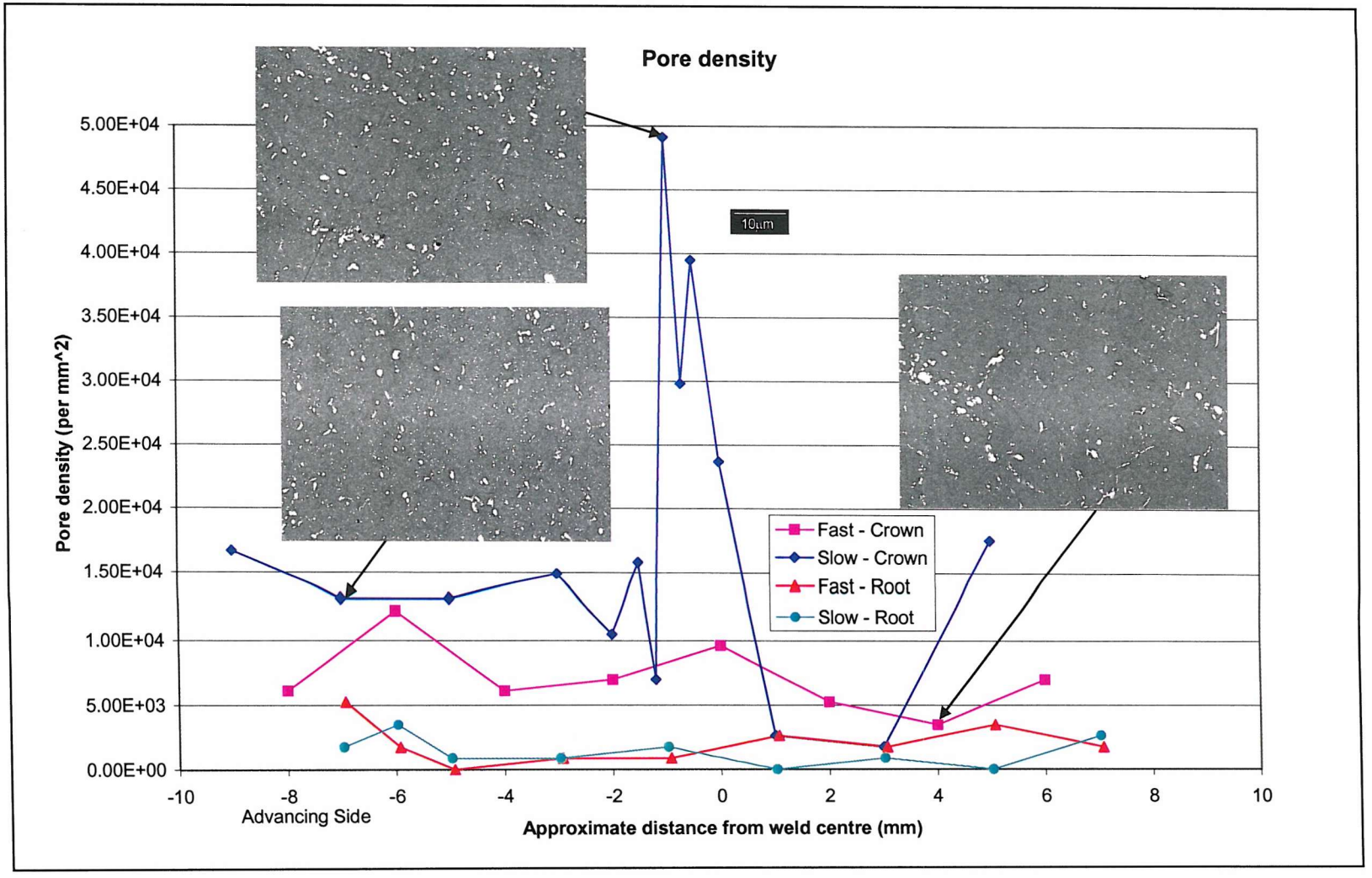

Figure 148 Variation in pore density with distance from weld centre line for fast and slow welds.

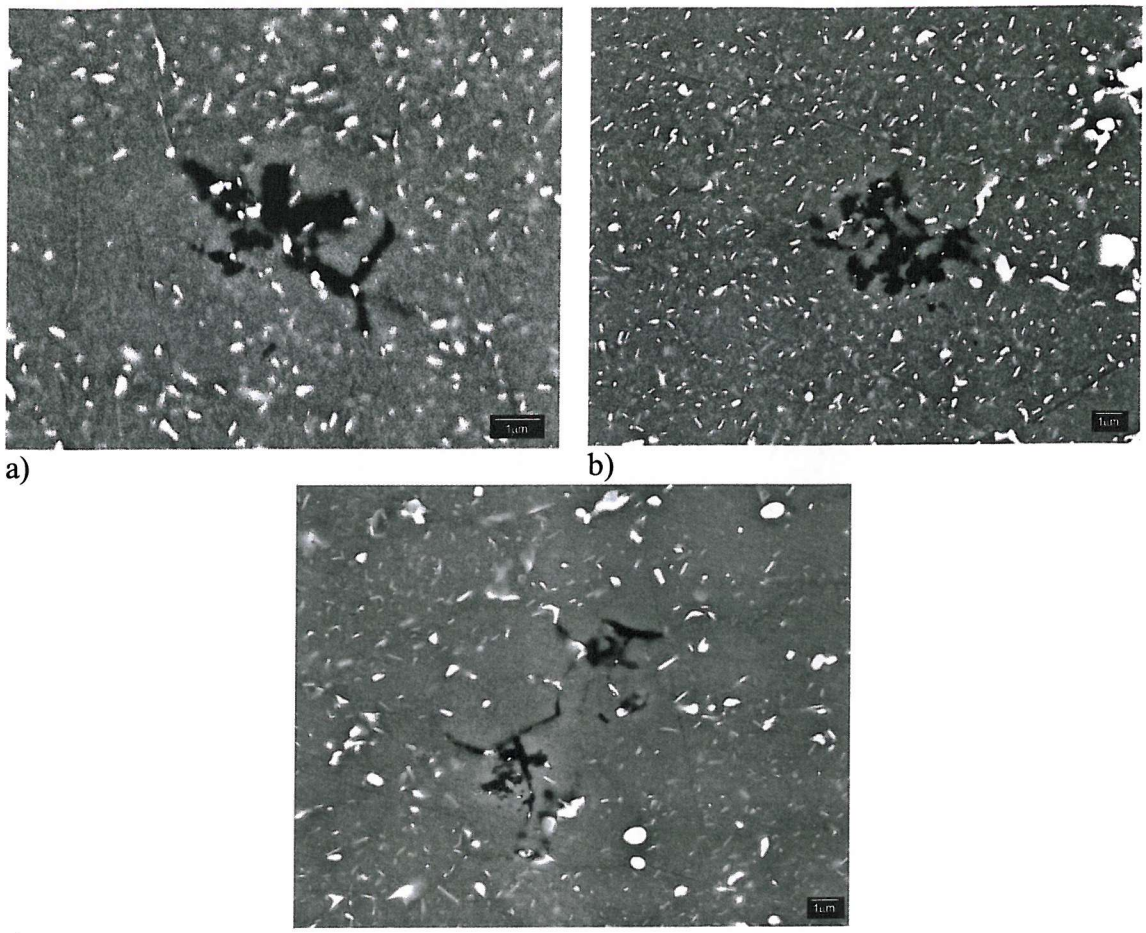

Figure 149 BEI images of complex pores geometries present in slow weld region.

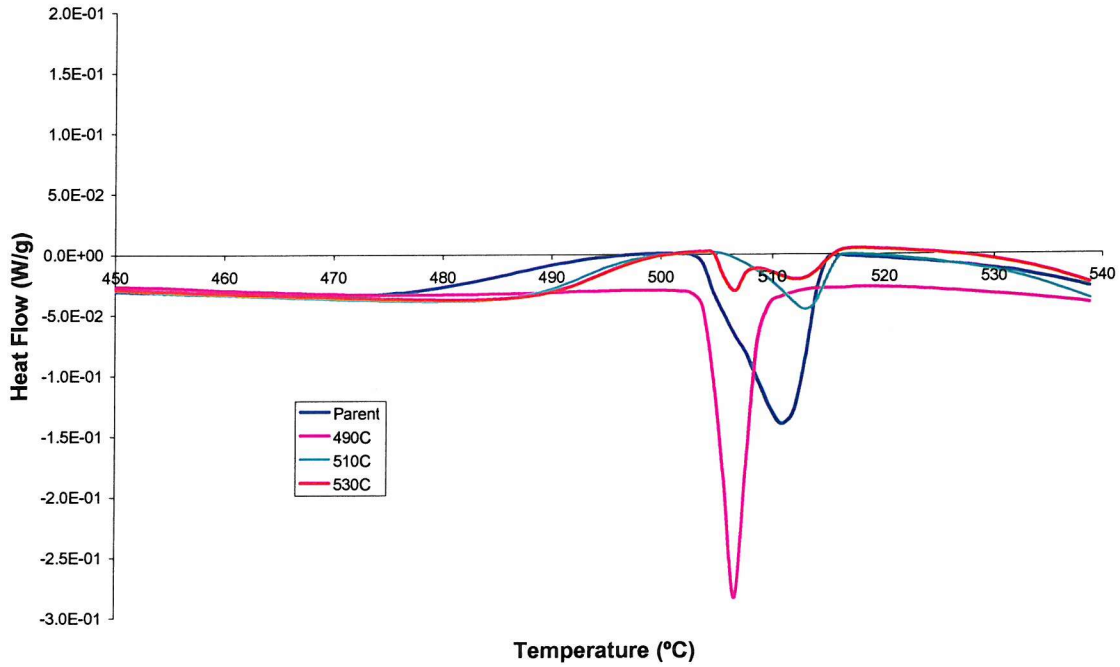

Figure 150 DSC results for short exposure experiments, 450-540°C.

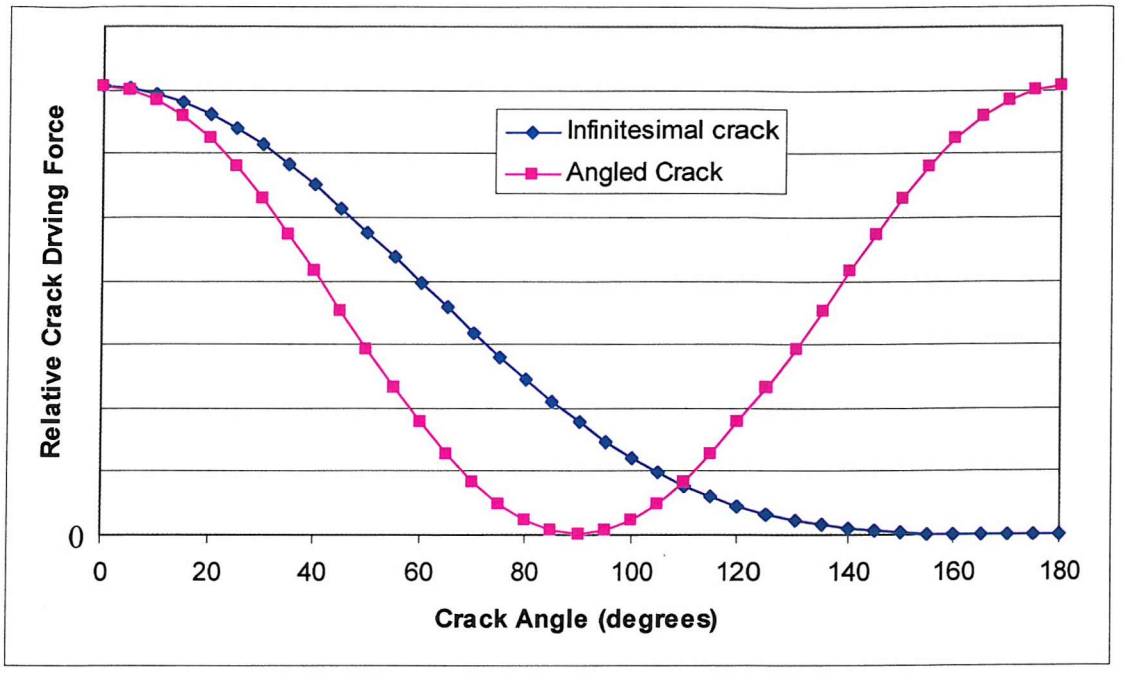

Figure 151 Graph showing the relative change in crack tip driving force with crack angle for a) an entirely angled crack and b) for an infinitesimally deflected crack tip on a macroscopic crack.

Chapter 6: Conclusions

6.1 13mm Weld

1. The weld nugget is identified as inherently resistant to fatigue crack initiation. This is in the first instance attributed to the very fine grain size which inhibits slip band formation, fine intermetallics which have been shown to reduce crack initiation probability significantly, low defect content, and reasonable strength.
2. Crack initiation occurs preferentially at discontinuities in the weld region material flow; the discontinuities have been associated with a change in intermetallic size, density and distribution. The significant factor from an initiation point of view is the increased intermetallic size (<~20μm).
3. The bands that form the onion ring structure in the nugget region have been attributed to changes in both intermetallic size and nature; with the dark bands (when etched and viewed optically) having a higher density of intergranular precipitates and less intragranular precipitates, while the light bands show the converse. However, obvious grain structure variation was seen between the bands, although the grains in the nugget region do show some alignment with the onion rings.
4. The incidence of distinct deflection around the nugget region has been attributed to a combination of the banding present in the intermetallics and the hardness difference seen between the bands. These effects are consistent with the literature.
5. The short fatigue life associated with weld nugget failure, together with the location of the failures in the TMAZ suggests the influence of a residual tensile

stress in the weld region. A tensile residual stress would limit the build up of closure during growth, hence accelerating growth. It is also likely to make the region just inside the hardness minimum more prone to fatigue crack initiation. Whilst residual stress data is not available for the current weld this is supported by the most complete literature studies.

6.2 25mm Welds

1. The weld region is again seen to be resistant to fatigue crack initiation, as seen in the 13mm welds, although it is evident from tests of the weld root that the strength of the weld nugget material is not in fact critical to the apparent fatigue resistance.
2. Crack initiation was observed over the nugget region for the slow weld transverse speed. Initiation occurring at pore type defects with a maximum dimension of up to 100μm. The associated weld flow arm has a clearly higher pore density in the weld centre than either of the weld roots or the fast weld flow arm. The slow weld flow arm DSC analysis also exhibits an unusual absence of an incipient melting peak at around 500°C: this is thought to be the result of incipient melting during welding, resulting in an increased pore content.
3. The centre of both weld roots was seen to be very soft, supporting the idea that the ageing condition is the primary controller of strength rather than grain structure. Although the weld root is very soft, crack initiation of the weld root specimens did not occur in this region rather it occurred around the region of maximum hardness.

4. The residual stresses present in the 25mm welds have been measured using X-ray diffraction. Whilst the results for the fine grained weld region appear reasonable consistent and are therefore thought to be believable, the results for outside this region show marked scattering due to the texture and large grain size of the plate, hence these results are not thought to be representative of the true stress present. What is clear is that the transverse residual stresses in the weld centre are in this case compressive, unlike the tensile stress suggested by the literature. This change may be attributable to a number of facts: different weld tools, different weld parameters, different plate gauges and the difference in weld tool penetration. The compressive residual stress measured in the weld region may then account for the increase fatigue life of the over nugget failure and the short crack arrest events seen, and may also account for the location of failure well outside the nugget region close to the maximum hardness rather than close to the weld region in the TMAZ (c.f. 13mm weld behaviour).
5. Significant crack deflections seen in the nugget failures have been linked with microstructural flow features which occur in the welding direction. The grain structure and intermetallics show alignment parallel to the crack growth direction.

5.3 Overall Conclusions

1. The nugget region has been shown to be intrinsically fatigue resistant in the absence of any major crack initiating features such as increased pore density or a flow discontinuity with associated coarse intermetallics.

2. Flow heterogeneities lead to distinctly preferred crack paths within the weld. This is particularly evident in the slow 25mm weld, with the nominal crack tip driving force falling by up to 60% due to the crack deflections. It should be noted that while in the current transverse loading configuration this is not a significant problem and may even increase fatigue life, it does suggest that the longitudinal crack growth resistance may be poor.
3. The weld hardness is primarily related to aging effects rather than grain structure effects.

Chapter 7: Future Work

- The current work has shown that incipient melting may occur during the welding process depending on the welding parameters with direct implications for weld behaviour. Further detailed assessment of thermal histories associated with varying weld conditions would clearly be valuable to quantify optimum weld conditions to avoid such effects.
- A more detailed assessment of the residual stresses present within the welds, using a high energy method such as Synchrotrons or neutrons together with the fatigue study would be beneficial.
- Given the clear effect that the banding of the nugget region had on fatigue crack propagation it would be interesting to extend this work to study Re-Stir welding[137], as this process gives very distinct bands when the weld tool is reversed.
- Sub-size, residual stress free specimen testing could provide a useful insight into the properties of the various weld regions.
- Longitudinal testing should also be carried out to assess the effect of the flow features that are present.
- FE modelling of the effect of hard and soft boundaries would prove useful to enable a fuller understanding of the mechanical effect of the banding present in the nugget region.

Appendix 1: Linear Elastic Fracture Mechanics (LEFM)

A1.1 Linear Elastic Fracture Mechanics

The following section provides a basic review of the principles of Linear Elastic Fracture Mechanics (LEFM). Much use has been made of the following reference textbooks for general background information: Fatigue of Materials 2nd Edition by S. Suresh and Fracture Mechanics by Anderson., with more specific references being made in the text as necessary

An early assessment of the influence of crack like defects on mechanical properties is provided by Inglis. This work used a stress analysis of an elliptical defect in an infinite plate, identifying the maximum stress at the tip of the major axis of an ellipse, σ_A, to be:

$$\sigma_A = \sigma\left(1+2\sqrt{\frac{a}{b}}\right) \qquad \textbf{Equation 8}$$

where: σ is the far field applied stress, $2a$ is the length of the ellipse perpendicular to the applied stress and $2b$ is the length of the ellipse parallel to the applied stress. When $a>>b$ the ellipse takes on the shape of a crack with the radius of curvature of the tip (ρ), being given by:

$$\rho = b^2/a \qquad \textbf{Equation 9}$$

Equation 1 then becomes:

$$\sigma_A = 2\sigma\sqrt{\frac{a}{\rho}}$$ **Equation 10**

Identifying a critical σ_A value as a fracture parameter fails when $\rho \rightarrow 0$, as any applied stress would then cause failure.

An alternative approach to the influence of defects on mechanical performance may be found via the assessment of energy. From the first law of thermodynamics it is noted that the state of a system will only change if it is energetically favourable, therefore a crack will only grow if a net reduction in energy is achieved. Griffith noted for crack extension to occur due to an applied stress the rate of decrease in potential energy of the system, as a result of the displacement of the outer boundaries and the change in stored elastic energy, must at least equal the rate of increase in surface energy due to crack extension, hence a materials resistance to fracture can be characterised through a critical value of energy release rate, G_c, which is a measure of fracture toughness.

Using the stress analysis of Inglis for an elliptical hole in an infinite elastic plate, Griffith derived an expression for the net change in potential energy, W_p, of the large plate shown in Figure 152.

$$W_p = -\frac{\pi a^2 \sigma^2 B}{E'}$$ **Equation 11**

where B is the plate thickness, a is the half crack length, and E' is given as:

$$E' = \frac{E}{1-\upsilon^2} \text{ for plane strain, and } E' = E \text{ for plane stress}$$ **Equation 12**

where E is Young's modulus and ν is Poisson's Ratio.

The surface energy, W_s of the crack system is

$$W_s = 4aB\gamma_s \qquad \textbf{Equation 13}$$

where γ_s is free surface energy per unit surface area of the material

Considering these terms as functions of crack extension, the resulting critical stress for fracture initiation is:

$$\sigma_f = \sqrt{\frac{2E'\gamma_s}{\pi a}} \qquad \textbf{Equation 14}$$

Irwin extended this energy-based approach to fracture to defining an energy release rate, G, which is a measure of the energy that is available for an increment of crack extension, which can be consider as the driving force for crack growth:

$$G = -\frac{dW_p}{dA} \qquad \textbf{Equation 15}$$

The above equations were derived for the brittle fracture of a sharp crack for which the near-tip stresses exceed the cohesive strength of the material. For real engineering materials this is not the case. Orowan extended the energy release concept of Griffith by adding a term for energy dissipated by plastic work, γ_p, particularly considering the case where plasticity is limited in scale in relation to the elastic stress fields, hence giving the expression:

$$\sigma_c = \sqrt{\frac{2E(\gamma_s + \gamma_p)}{\pi a}} \qquad \textbf{Equation 16}$$

A1.2 Linear Elastic Stress Analysis of Cracks

In practice, G is difficult to calculate for many loading configurations. This makes it difficult to apply as an engineering criterion. Adopting a stress-based description of crack tip conditions, Irwin used the solutions of Westergaad to derive a solution for the stress distribution ahead of a loaded crack tip. If we define a polar coordinate system with the origin at the crack tip as shown in Figure 153, then assuming, isotropic linear elastic material behaviour, it may be shown that:

$$\sigma_{ij} = \left(\frac{k}{\sqrt{r}}\right) f_{ij}(\theta) + \text{Higher order terms} \qquad \textbf{Equation 17}$$

where: $k = \sigma_{app}\sqrt{a}$, σ_{ij} is the stress tensor, and r and θ are defined in Figure 153.

As $r \rightarrow 0$ the leading term approaches infinity, while the other terms in the equation remain finite, the near tip stresses may be seen to be dominated by the $1/\sqrt{r}$ singularity. As such k may be seen to be a convenient scalar that defines the relationship between applied load and crack tip conditions in the region where the most critical failure events occur (i.e. at the tip). It is convenient to replace k with the `stress intensity factor`, K, where $K = \sigma_{app}\sqrt{\pi a}$.

In terms of realistic loading of cracks in real structures it may be noted that any arbitrary crack loading can be resolved into a combination of the 3 loading types shown in Figure 154. Each mode illustrated in Figure 154 may be shown to produce a $1/\sqrt{r}$ stress singularity at the crack tip. In terms of a general description of crack tip stress conditions,

independent stress intensity factors may be defined for the three primary crack loading modes, with equation 13 then becoming:

$$\sigma_{ij} = \left(\frac{K_I}{\sqrt{2\pi r}}\right) f_{ij}^{I}(\theta) + \left(\frac{K_{II}}{\sqrt{2\pi r}}\right) f_{ij}^{II}(\theta) + \left(\frac{K_{III}}{\sqrt{2\pi r}}\right) f_{ij}^{III}(\theta) + \text{Higher order terms} \quad \textbf{Equation 18}$$

For general conditions of mode I loading of a crack, it may be shown that:

$$K_I = \sigma\sqrt{\pi a}F \quad \textbf{Equation 19}$$

where F is a function of the crack and component geometries. Solutions for F have been produced over the years for different geometries using a variety of analytical and finite element methods.

By a virtual work argument it may be shown for linear elastic conditions that K and G are related to one another by:

$$G = \frac{K_I^2}{E'} \quad \textbf{Equation 20}$$

The above relationship then allows a critical stress intensity factor K_c to be defined which is equivalent to G_c and is a measure of fracture toughness. Within an elastic context it may be seen that K provides a powerful local and global description of crack behaviour, forming the basis of LEFM.

For LEFM to be applied strictly, materials should behave totally elastically. When a crack grows in any realistic structural metal there is a certain amount of plasticity at the crack tip. A fundamental assumption then exists in the practical use of LEFM for metallic structures, where it is noted that if the scale of plasticity is `small` in relation to the region

at the crack tip that is dominated by the $1/\sqrt{r}$ singularity, then the elastic singularity (quantified via K) will effectively quantify processes occurring within the plastic region, even though these processes are of necessity non-linear.

A1.3 Crack Tip Plasticity

Calculation of the scale of crack tip plasticity may be accomplished by a number of techniques, ranging from first order approximations, such as the Irwin approach, to involved finite element solutions accounting for elastic-plastic work hardening behaviour. The Irwin approximation (based on simple examination of elastic near-tip stresses) gives:

$$r_p = \frac{1}{\pi}\left(\frac{K_I}{\sigma_{YS}}\right)^2 \qquad \textbf{Equation 21}$$

where r_p is the diameter of an assumed circular plastic zone directly ahead of the crack tip and σ_{ys} is the yield stress. The above equation is modified by a factor of a third for the plane strain condition to account for constraint in through-thickness plastic flow.

Alternative estimates of plastic zone size may be obtained from the strip yield model of Dugdale. This assumes a crack in an elastic plate subjected to plain stress conditions, with a slender, near-zero height, plastic zone region ahead of both crack tips. The model is essentially a balance of the crack tip stresses, i.e. stress intensity from the remote tensile stress must balance with the effective traction of the plastic material. The plastic zone size predicted by this approach is:

$$r_p = \frac{\pi}{8}\left(\frac{K_I}{\sigma_{ys}}\right)^2 \qquad \textbf{Equation 22}$$

On inspection it is clear that the Dugdale approximation is about 20% larger than the Irwin approximation.

Stress states have a significant effect on crack tip plasticity in mode I loading for a given stress intensity factor (as noted above). It should be noted that the pure plane strain condition may exhibit high tensile hydrostatic stresses just ahead of the crack tip due to plastic flow constraint. This leads to an increase in local stress levels at the crack tip, hence the plane strain condition is generally thought to be the most significant for crack propagation.

As the scale of near-crack tip yielding increases, the crack tip condition may no longer be controlled by the $1/\sqrt{r}$ singularity and LEFM fails to describe the crack tip stress condition usefully. To describe the stress state where time-independent non-linear behaviour is exhibited, elastic-plastic fracture mechanics may be applied. Examples are Crack Tip Opening Displacement (CTOD, see below), and the J-integral.

A1.3 Crack Tip Opening Displacement (CTOD)

Within LEFM and elastic-plastic fracture mechanics, crack tip opening displacements (CTODs) are widely identified as a valuable indication of the strain `damage` associated with crack tips. Wells related CTOD to stress intensity factors for the case of limited crack tip yielding using the analysis of Irwin for the plane stress state, giving:

$$\delta = \frac{4}{\pi}\frac{K_I^{\,2}}{\sigma_{YS}E'} \qquad \textbf{Equation 23}$$

where δ is the CTOD

A similar expression can be found from the Dugdale model:

$$\delta = \frac{K_I^{\,2}}{\sigma_{YS} E'} \qquad \textbf{Equation 24}$$

Again, the Dugdale result is about 20% larger than the value predicted by the Irwin model. For plane strain loading conditions a number of expressions have been suggested for CTOD based on experimental, analytical and numerical investigations: a general solution suggested by Rice gives:

$$\delta \cong 0.5 \frac{K_I^{\,2}}{\sigma_{YS} E} \qquad \textbf{Equation 25}$$

A1.4 Plastic Zone Shape

Plastic zone sizes so far have been estimated for θ = 0 (i.e. directly ahead of the crack); other angles can be estimated with the application of a yield criterion, such as the Von Mises and Tresca, into the equations for the Mode I elastic stress fields and solving for r as a function of θ, giving:

$$r_y(\theta) = \frac{1}{4\pi} \left(\frac{K_I}{\sigma_{YS}} \right)^2 \left[1 + \cos\theta + \tfrac{3}{2} \sin^2 \theta \right] \qquad \textbf{Equation 26}$$

The plane stress plastic zone shape calculated using the above method is shown in Figure 155, along with the plane strain plastic zone shape. It is clear from the figure that there is a significant difference between the plastic zone shapes for plane stress compared to plane strain, with through-thickness constraint in the plane strain case giving a smaller plastic zone size.

Figure 155 is clearly simplified in obtaining plastic zone dimensions from elastic tip stress fields. A more accurate description of plastic zone shape may be obtained from the so called "HRR" fields, derived for elastic-power law plastic materials where stress and strain distributions may be shown to be given by.

$$\sigma_{ij} = \sigma_0 \left(\frac{EJ}{\alpha \sigma_0^2 I_n r} \right)^{\frac{1}{n+1}} \tilde{\sigma}_{ij}(n,\theta) \qquad \textbf{Equation 27}$$

$$\varepsilon_{ij} = \frac{\alpha \sigma_0}{E} \left(\frac{EJ}{\alpha \sigma_0^2 I_n r} \right)^{\frac{1}{n+1}} \tilde{\varepsilon}_{ij}(n,\theta) \qquad \textbf{Equation 28}$$

Where σ_0 is the reference stress, usually equal to the yield stress, α is a dimensionless constant, n is the strain hardening exponent, I_n is an integration constant that depends on n, and $\tilde{\sigma}_{ij}$ and $\tilde{\varepsilon}_{ij}$ are dimensionless functions of n and θ.

Figure 156 shows a comparison of plane strain plastic zone shape calculated using pure elastic stress fields (as noted above), along with a plastic zone shape calculated using elastic-plastic finite element analysis published by Dodds for material of a low to moderate work hardening capacity. The figure shows that, in the first instance, the elastic analysis gives a reasonable first order approximation of the extent of the plastic zone.

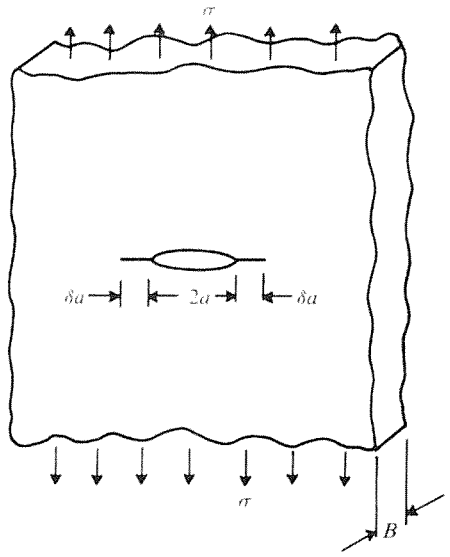

Figure 152 A large plate of an elastic material containing a crack of length 2a.[88]

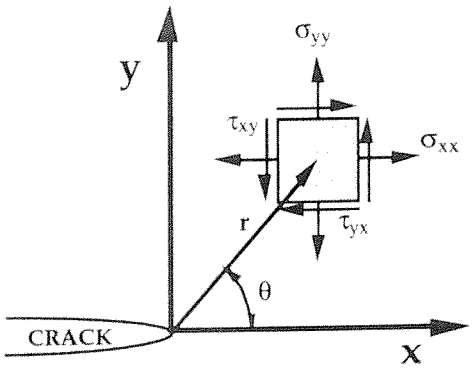

Figure 153 Definition of the coordinate axis ahead of a crack tip. The *z* direction is normal to the page.[138]

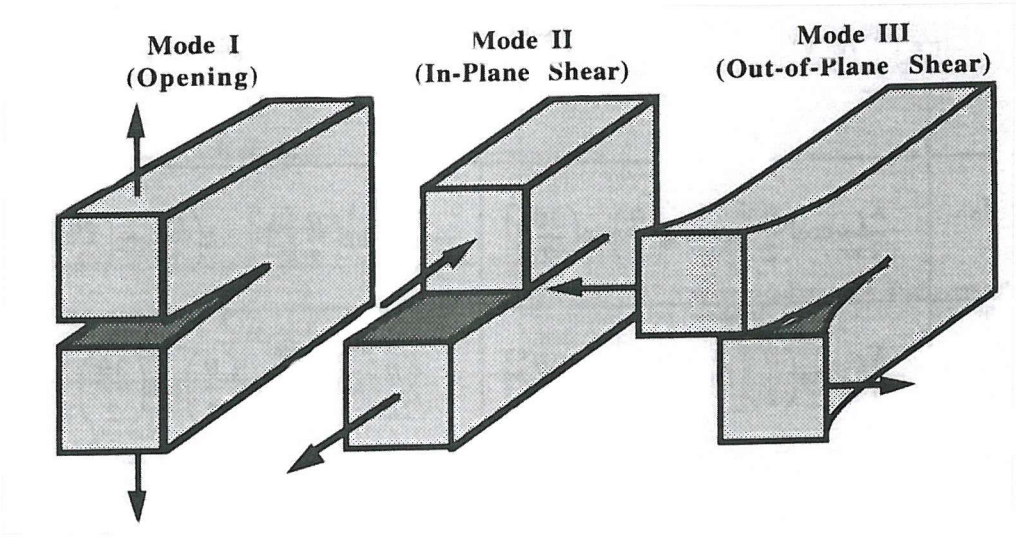

Figure 154 The three modes of loading that can be applied to a crack.[138]

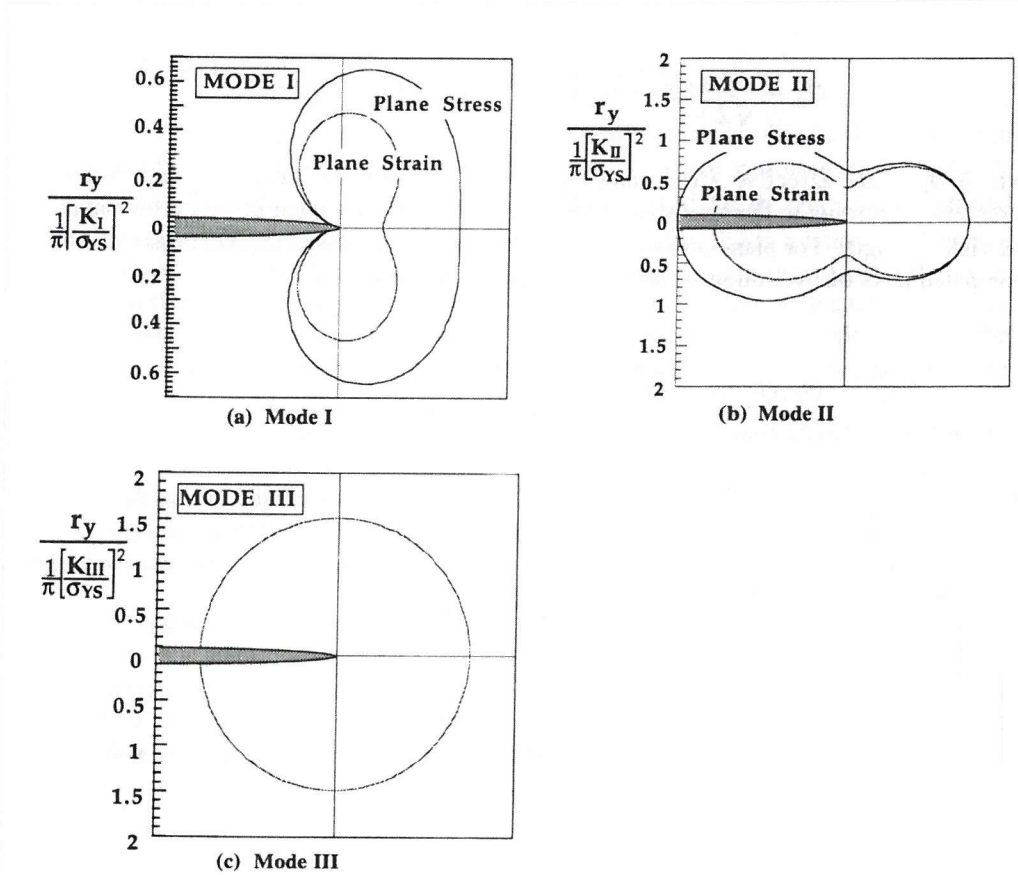

Figure 155 Crack tip plastic zone shapes estimated from the von Mises yield criterion and equation 22.[138]

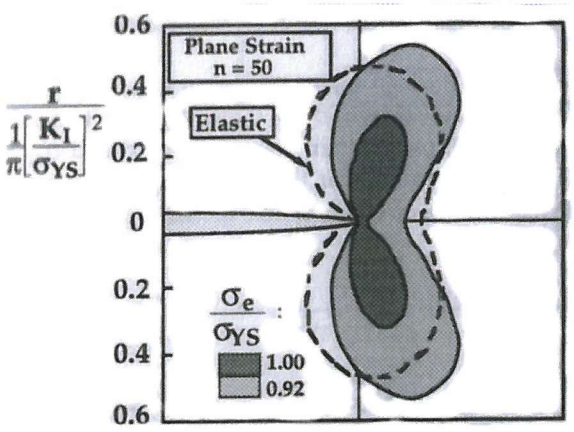

Figure 156 Contours of constant effective stress in Mode I, obtained from finite element analysis.[138]

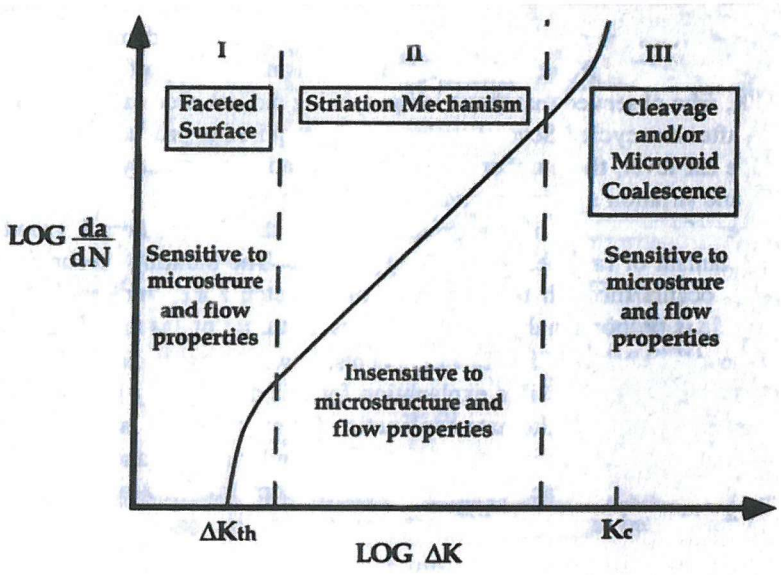

Figure 157 Micro-mechanisms of fatigue in metals.[138]

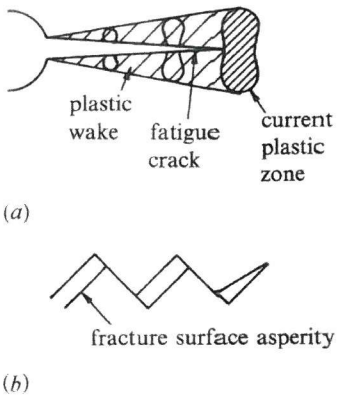

Figure 158 A schematic illustrations of the mechanisms which promote retardation of fatigue crack growth in constant amplitude fatigue a) plasticity induced crack closure: b) roughness induced crack closure.[88]

References

[1] R. Pedwell, H. Davies and A. Jefferson, 1999, Proc. 1st Int. Symposium on Friction Stir Welds, Thousand Oaks, California, 14th – 16th June.
[2] L.E. Murr, Y. Li, E.A. Trillo, B.M. Nowak and J.C. McClure, 1999, *Aluminium Transactions*, Vol.1, pp. 141-154
[3] J.E. Hatch, 1984, *Aluminium: Properties and Physical Metallurgy*, American Society of Metals
[4] I.J. Polmear, 1995, *Light Alloys, Metallurgy of the Light Metals*, 3rd Edition, Arnold.
[5] ASM Specialty Handbook, 1994, *Aluminium and Aluminium Alloys* ASM International
[6] M.A. Zaidi and J.A. Wert., 1989, *Treatise on Materials Science and Technology Vol. 31*, pp. 137-170
[7] E.A. Starke Jr. 1989, *Treatise on Materials Science and Technology Vol. 31*, pp35-63
[8] F.J. Humphreys, 1985, *Dislocations & Properties of Real Materials*, Proc. Cont 50th Anniversary of Dislocations of Crystals, London, IoM, Edited Loretto, pp 175-204
[9] A.J. Ardell, 1985, *Metallurgical Transactions A*, Vol.16A pp2131-2165
[10] C.Y. Kung and M.E. Fine, 1979, *Metallurgical Transactions A*, Vol. 10A, pp. 603-610.
[11] A. Zabett and A. Plumtree, 1995, *Fatigue and Fracture of Engineering Materials and Structures*, Vol. 18, No. 7/8, pp. 801-809
[12] P. Mulvihill and C.J. Beevers, 1986, *The Behaviour of Short Fatigue Cracks,* EGF Pub. 1, pp. 203-213.
[13] W.L. Morris, 1979, *Metallurgical Transactions A*, Vol. 11A, pp. 1117-1123.
[14] J. Lankford, 1982, *Fatigue of Engineering Materials and Structures*, Vol. 5, No. 3, pp. 233-248.
[15] R.J.H. Wanhill and L. Schra, 1992, In: *Proc. ESIS conference on Short Fatigue Cracks*, pp3-27
[16] Y.H. Zhang and L. Edwards, 1992, *Scripta Metallurgica et Materialia*, Vol. 26, pp 1901-1906, Pergamon Press Ltd.
[17] W.M Thomas and R.E. Dolby, 2002, Proc: *6th International Conference on Trends in Welding Research*, Callaway Gardens Resort, Pine Mountain, Georgia, USA, 15-19 April
[18] W.M. Thomas, E.D. Nicholas, J.C. Needham, Mg. Murch, P. Templesmith, and C.J. Dawes, 1991, *"Friction Stir Butt Welding" International Patent Application No. PCT/GB92/02203*
[19] C.J. Dawes and W.M. Thomas, 1996, *Welding Journal*, March, pp. 41-45
[20] G. Engelhard, T. Hillers and D. Pellkofer, 2001, Proc: *3rd International Symposium on Friction Stir Welding*, Kobe, Japan, 27-28 September
[21] K. Matsumoto and S. Sasabe, 2001, Proc: *3rd International Symposium on Friction Stir Welding*, Kobe, Japan, 27-28 September
[22] W.M Thomas, A.B.M. Braithwaite and R. John, 2001, Proc: *3rd International Symposium on Friction Stir Welding*, Kobe, Japan, 27-28 September
[23] K. Aota, H. Okamura, E. Masakuni and H, Takai, 2001, Proc: *3rd International Symposium on Friction Stir Welding*, Kobe, Japan, 27-28 September
[24] R. Pedwell, H. Davies and A. Jefferson, 1999, Proc. *1st International Symposium on friction stir welding*, Thousand Oaks, California, 14-16 June
[25] G. Bussu and P.E. Irving, 1999, Proc. *1st International Symposium on friction stir welding*, Thousand Oaks, California, 14-16 June
[26] F. Marie, 2001, Proc: *3rd International Symposium on Friction Stir Welding*, Kobe, Japan, 27-28 September
[27] D. Lohwasser, 2001, Proc: *3rd International Symposium on Friction Stir Welding*, Kobe, Japan, 27-28 September
[28] T. Shinoda, H. Tokisue, M. Enomoto, H. Hori, S. Koga, M. Kumagai, K. Matsumoto, H. Okamura and K. Tsuchiya, 2001, Proc: *3rd International Symposium on Friction Stir Welding*, Kobe, Japan, 27-28 September
[29] K. Colligan, K. McTernan and J.R. Pickens, 2001, Proc: *3rd International Symposium on Friction Stir Welding*, Kobe, Japan, 27-28 September
[30] G. Engelhard, T. Hillers and D. Pellkofer, 2001, Proc: *3rd International Symposium on Friction Stir Welding*, Kobe, Japan, 27-28 September
[31] B. Irving, 1997, *Welding Journal*, January, pp. 31-41
[32] M.W. Mahoney, C. G. Rhodes, J.G Flintoff, R.A. Spurling, and W.H. Bingel, 1998, *Metallurgical and Materials Transactions A*, Vol. 29A, pp. 1955-1964
[33] K.V. Jata, K.K. Sankaran, and J.J. Ruschan, 2000, *Metallurgical and Materials Transactions A*, Vol. 31A, pp. 2181-2192

[34] A. von Strombeck, J.F. dos Santos, F. Torster, P. Laureano, and M. Koçak, 1999, Proc. *1st International Symposium on friction stir welding*, Thousand Oaks, California, 14-16 June
[35] A.P. Reynolds, W.D. Lockwood and T.U. Seidel, 2000, *Materials Science Forum*, Vol. 331-337, pp. 1719-1724
[36] A.F. Norman, I. Borough, and P.B. Prangnell, 2000, *Materials Science Forum*, Vols. 331-337, pp. 1713-1718
[37] L.D. Oosterkamp, A. Ivankovic, and A. Oosterkamp, 2000, Proc. *2nd International Symposium on Friction Stir Welding*, Gotherenburg, Sweden, 26-28 June
[38] K. Colligan, 1999, *Supplement to the Welding Journal*, pp. 229-s – 237-s
[39] A.P. Reynolds, T.U. Seidal, and M. Simonsen, 1999, Proc. *1st International Symposium on friction stir welding*, Thousand Oaks, California, 14-16 June
[40] K. Colligan, 1999, Proc. *1st International Symposium on friction stir welding*, Thousand Oaks, California, 14-16 June
[41] H.S. Yang, 1998, Proc. *ICCA-6*, Vol. 3, pp. 1483-1488
[42] P. Colegrove, M. Painter, D. Graham, and T. Miller, 2000, Proc. *2nd International Symposium on Friction Stir Welding*, Gotherenburg, Sweden, 26-28 June
[43] B. London, M. Mahoney, W. Bingel, M. Calabrese and D. Waldron, 2001, Proc: *3rd International Symposium on Friction Stir Welding*, Kobe, Japan, 27-28 September
[44] G.J. Bendzsak, T.H. North, and C.B. Smith, 1999, Proc. *1st International Symposium on friction stir welding*, Thousand Oaks, California, 14-16 June
[45] C. Dalle Donne, G. Biallas, T. Ghidini, and G. Raimbeaux, 2000, Proc. *2nd International Symposium on Friction Stir Welding*, Gotherenburg, Sweden, 26-28 June
[46] T. Shinoda, 2001, Proc: *3rd International Symposium on Friction Stir Welding*, Kobe, Japan, 27-28 September
[47] Li Ying, L.E. Murr, and J.C. McClure, 1999, *Scripta Materialia*, vol. 40, No. 9, pp. 1041-1046
[48] K. Colligan, I. Ucok, K. McTernan, P.J. KonKol and J.R. Pickens, 2001, Proc: *3rd International Symposium on Friction Stir Welding*, Kobe, Japan, 27-28 September
[49] W. Tang, X. Guo, J.C. McClure, L.E. Murr and A. Nunes, 1998, *Journal of Materials Processing and Manufacturing Science*, Vol. 7, pp. 163-172
[50] M.J. Russell and H.R. Shercliff, 1999, Proc. *1st International Symposium on friction stir welding*, Thousand Oaks, California, 14-16 June
[51] T.H. North, G.J. Bendzsak, and C. Smith, 2000, Proc. *2nd International Symposium on Friction Stir Welding*, Gotherenburg, Sweden, 26-28 June
[52] Ø. Frigaard, Ø. Grong, and O.T. Midling, 2001, *Metallurgical and Materials Transactions A*, Vol. 32A, pp. 1189-1200
[53] A.J. Leonard, 2000, Proc. *2nd International Symposium on Friction Stir Welding*, Gotherenburg, Sweden, 26-28 June
[54] P. Dong, F. Lu, J.K. Hong, and Z. Cao, 1999, Proc. *1st International Symposium on friction stir welding*, Thousand Oaks, California, 14-16 June
[55] B.I. Bjørneklett, Ø. Frigaard, Ø. Grong, O.R. Myhr, and O.T. Midling, 1998, Proc. *ICAA-6*, Japan, pp. 1531-1536
[56] J.E. Gould and Z. Feng, 1998, *Journal of Materials Processing & Manufacturing Science*, Vol. 7, pp. 185-194
[57] O.T. Midling and G. Rørvik, 1999, Proc. *1st International Symposium on friction stir welding*, Thousand Oaks, California, 14-16 June
[58] C.G. Rhodes, M.W. Mahoney, W.H. Bingel, R.A. Spurling, and C.C. Bampton, 1997, *Scripta Materialia*, Vol. 36, No. 1, pp. 69-75
[59] H. Larsson, L. Karlsson, and L.E. Svensson, 1998, Proceedings of *ICCA-6*, Vol. 3, pp. 1471-1476
[60] C. Juričić, C. Dalle Donne and U. Drebler, 2001, Proc: *3rd International symposium on Friction Stir Welding*, Kobe, Japan, 27-28 September
[61] Kh. A. A. Hassan, A.F. Norman and P.B. Prangnell, 2001, Proc: *3rd International symposium on Friction Stir Welding*, Kobe, Japan, 27-28 September
[62] S. Tanaka and M. Kumagai, 2001, Proc: *3rd International Symposium on Friction Stir Welding*, Kobe, Japan, 27-28 September
[63] Y.S. Sato, M. Urata and H. Kokawa, 2002, *Metallurgical and Materials Transactions A*, Vol. 33A, pp. 625-635
[64] K.V. Jata and S.L. Semiatin, 2000, *Scripta Materialia*, Vol. 43, No. 8, pp.743-749

[65] F.J. Humphreys and M. Hatherly, 1996, *Recrystallisation and Related Annealing Phenomena*, 1st Edition, Pergamon.
[66] L.E. Murr, Y. Li, E.A. Trillo, R.D. Flores, and J.C McClure, *Journal of Materials Processing & Manufacturing Science*, Vol. 7, pp. 145-161
[67] O.V. Flores, C. Kennedy, L.E. Murr, D. Brown, S. Pappu, B.M. Nowak, and J.C. McClure, 1998, *Scripta Materialia*, Vol. 38, No. 5, pp. 703-708
[68] Y.S. Sato, H. Kokawa, K. Ikeda, M. Enomoto, S. Jogan, and T. Hashimoto, 2001, *Metallurgical and Materials Transactions A*, Vol. 32A, pp 941-948
[69] L.E. Svensson, L. Karlsson, H. Larsson, B. Karlsson, M. Fazzini, and J. Karlsson, 2000, *Science and Technology of Welding Journal*, Vol. 5, No. 5, pp. 285-296.
[70] A. Denquin, D. Allehaux, M. Campagnac and G. Lapasset, 2001, Proc: *3rd International symposium on Friction Stir Welding*, Kobe, Japan, 27-28 September
[71] Y.S. Sato, H. Kokawa, M. Enomoto, and S. Jogan, 1999, *Metallurgical and Materials Transactions A*, Vol. 30A, pp. 2429-2437
[72] P.S. Pao, S.J. Gill, C.R. Feng, and K.K. Sankaran, 2001, *Scripta Materialia*, Vol. 45, pp. 605-612
[73] B. Heniz, B. Skrotzki, an G. Eggeler, 2000, *Materials Science Forum*, Vol. 331-337, pp. 1757-1762
[74] G. Liu, L.E. Murr, C-S. Niou, J.C. McClure, and F.R. Vega, 1997, *Scripta Materialia*, Vol. 37, No. 3, pp. 355-361
[75] L.E. Murr, G. Liu and J.C. McClure, 1998, *Journal of Materials Science*, Vol. 33, pp. 1243-1251
[76] M. Ericsson, R. Sandström, J. Hagström, 2000, Proc. *2nd International Symposium on Friction Stir Welding*, Gotherenburg, Sweden, 26-28 June
[77] M. Strangwood, J.E. Berry, D.P. Cleugh, A.J. Leonard, and P.L. Threadgill, 1999, Proc. *1st International Symposium on friction stir welding*, Thousand Oaks, California, 14-16 June
[78] D.P. Field, T.W. Nelson, Y. Hovanski and K.V. Jata, 2001, *Metallurgical and Materials Transactions A*, Vol. 32A, pp. 2869-2877
[79] M.A. Sutton, B. Yang, A.P. Reynolds and R. Talyor, 2002, *Materials Science and Engineering A*, Vol. A323, pp. 160-166
[80] K.N. Krishnan, 2002, *Materials Science and Engineering A*, Vol. A327, pp. 246-251
[81] G. Biallas, R. Braun, C. Dalle Donne, G. Staniek and W.A. Kagsser, 1999, Proc. *1st International Symposium on friction stir welding*, Thousand Oaks, California, 14-16 June
[82] H. Larsson, L. Karlsson, S. Stoltz and E-L. Bergqvist, 2000, Proc: *3rd International symposium on Friction Stir Welding*, Gothenburg, Sweden, 26th-28th June
[83] M.A. Sutton, B. Yang, A.P. Reynolds and R. Talyor, 2002, *Materials Science and Engineering A*, Vol. A323, pp. 160-166
[84] L. Magnusson and L. Källman, 2000, Proc. *2nd International Symposium on Friction Stir Welding*, Gotherenburg, Sweden, 26-28 June 2000
[85] M.G. Dawes, S.A. Karger, T.L Dickerson, and J. Przydatek, 2000, Proc. *2nd International Symposium on Friction Stir Welding*, Gotherenburg, Sweden, 26-28 June 2000
[86] Y. S. Sato, H. Kokawa, M. Enomoto, S. Jogan and T. Hashimoto, 2001, Proc: *3rd International Symposium on Friction Stir Welding*, Kobe, Japan, 27-28 September
[87] L. Edwards and Y.H. Zhang, 1994, *Act Metall. Mater.*, Vol. 42, No. 4, pp. 1413-1421.
[88] S. Suresh, 1998, *Fatigue of materials*, 2nd Edition, Cambridge
[89] R.A. Smith, 1977, *Int. J. Fract*, Vol.13, pp. 717
[90] T. Shinoda, H. Tokisue, M. Enomoto, H. Hori, S. Koga, M. Kumagai, K. Matsumoto, H. Okamura and K. Tsuchiya, 2001, Proc: *3rd International Symposium on Friction Stir Welding*, Kobe, Japan, 27-28 September
[91] K.V. Jata, 2000, *Materials Science Forum*, Vols. 331-337, pp 1701-1712
[92] M.G. Dawes, S.A. Karger, T.L Dickerson, and J. Przydatek, 2000, Proc. *2nd International Symposium on Friction Stir Welding*, Gotherenburg, Sweden, 26-28 June
[93] M. James, M. Mahoney, and D. Waldron, 1999, Proc. *1st International Symposium on friction stir welding*, Thousand Oaks, California, 14-16 June 1999
[94] L. Djapic Oosterkamp, P.J. Webster, P.A. Brown, G.B.M. Vaughan, and P.J. Withers, 2000, *Materials Science Forum*, Vols. 347-349, pp. 678-683
[95] P.J. Webster, L. Djapic Oosterkamp, P.A. Browne, D.J. Hughes, W.P. Kang, P.J. Withers, and G.B.M. Vaughan, 2001, *Journal of Strain Analysis*, Vol. 36, No. 1, pp. 61-70
[96] M.A. Sutton, A.P. Reynolds, D.Q. Wang and C.R. Hubbard, 2002, *Journal of Engineering Materials and Technology*, Vol. 124, pp. 215-221
[97] A.T.L. Anderson, 1994, *Fracture Mechanics, Fundamentals and Applications*, 2nd Edition, CRC Press

[98] P. Balke, 2002, PhD Thesis, *Dynamics of microstructures in metal sheets: an orientation imaging microscopy study*, Groningen University Press.
[99] P.E.J. Flewitt and R.K. Wild, 1994, *Physical Methods for Materials Characterisation*, Institute of Physics Publishing
[100] V. Randle and O. Engler, 2000, *Texture Analysis: Macrotexture, Microtexture and Orientation Mapping*, Gordon Breach.
[101] F.J. Humphreys, 2001, *Journal of Materials Science*, Vol. 36, pp. 3833-3854.
[102] N.C. Krieger Lassen, 1997, *Journal of Microscopy*, Vol. 190, Pt. 3 , pp. 375-391
[103] A.J. Wilkinson and P. B. Hirsch, 1997, *Micron*, Vol. 28, No. 4, pp. 279-308
[104] L.E. Murr, G. Liu and J.C. McClure, 1998, *Journal of Materials Science*, Vol. 33, pp. 1243-1251
[105] A.K. Jena, A.K. Gupta and M.C. Chaturvedi, 1989, *Acta Metallurgica*, Vol. 37, No. 3, pp. 885-895
[106] G.W. Smith, W.J. Baxter and R.K. Mishra, 2000, *Journal of Materials Science*, Vol. 35, pp. 3871-3880
[107] J. Koike, M. Mabuchi and K. Higashi, 1994, *Acta Metallurgica*, Vol. 43, No. 1, pp. 199-206
[108] F. Lefebvre, S. Wang, M.J. Starink and I. Sinclair, 2002, *Materials Science Forum*, Vols. 396-402, pp. 1555-1560
[109] L.M. Wang, H.M. Flower, and T.C. Lindley, 1999, *Scripta Materialia*, Vol. 41, Is. 4, pp. 391-396
[110] L. Reich, M. Murayama and K. Hono, Submitted to *Acta Materialia*
[111] Y. Xu, P.J. Gregson and I. Sinclair, 2000, *Materials Science Forum*, Vols. 331-337, pp. 1525-1530
[112] P.B. Prangnell and A.F. Norman, 1998, Proceedings of *ICAA-6*, Vol. 3, pp. 1501-1506
[113] F. Lefebvre, 2003, Thesis in preparation, University of Southampton
[114] R. Rishi, 1981, *Metallurgical Transactions A*, Vol. 12A, pp. 1089-1097
[115] Ø. Frigaard, Ø. Grong, S. Gulbrandsen-Dahl and O.T. Midling, 1999, Proc. *1st International Symposium on friction stir welding*, Thousand Oaks, California, 14-16 June
[116] H. Larsson, L. Karlsson, S. Stoltz and E-L. Bergqvist, 2000, Proc: *3rd International Symposium on Friction Stir Welding*, Kobe, Japan, 27-28 September
[117] S. Suresh, Y. Sugimura and E.K Tschegg, 1992, *Scripta Metallurgica,* Vol. 27, pp. 1189-1194
[118] P.D. Hobson, 1982, *Fatigue of Engineering Materials and Structures*, Vol. 5, No. 4, pp. 323-327
[119] L. Grabowski and J.E. King, 1992, *Fatigue and Fracture, Engineering Materials Structures*, Vol. 5, No. 6, pp. 55-606
[120] H. Bomas, T. Linkewitz and P. Mayr, 1996, *Fatigue and Fracture, Engineering Materials Structure*, Vol. 19, No. 2/3, pp. 299-307
[121] Y. Xu, 2001, PhD thesis University of Southampton
[122] P.J. Laz and B.M. Hillberry, 1996, *Fatigue 96*, eds G Lutjering and H Nowack (Oxford: Pergamon) vol2 p 1293
[123] K. Kor and I. Sinclair, 2002, Unpublished work, University of Southampton
[124] T.U. Seidel and A.P. Reynolds, 2001, *Metallurgical and Materials Transactions A*, Vol. 32A, Issue 11, pp. 2879-2884.
[125] Kh. A.A. Hassan, A.F. Norman, D.A. Price and P.B. Prangnell, 2003, *Acta Materialia*, Vol. 51, pp. 1923-1936
[126] G. Biallas, R. Braun, C. Dalle Donne, G. Staniek and W.A. Kaysser, 2000, Proc. *2nd International Symposium on Friction Stir Welding*, Gotherenburg, Sweden, 26-28 June
[127] J. Gilbert Kaufman, 1999, *Properties of Aluminium Alloys*, ASM International, pp277
[128] G.H. Bray, M. Glazov, R.J. Rioja, D. Li and R.P. Gangloff, 2001, *International Journal of Fatigue*, Vol. 23, pp S265-S276
[129] A. Turnball and E.R. De Los Rios, 1995, *Fatigue and Fracture, Engineering Materials Structures*, Vol. 18, No. 12, pp. 1455-1467
[130] P.B. Prangnell and A.F. Norman, 1998, *Proc. 6th International Conference on Aluminium Alloys*, Vol. 3, pp. 1501- 1506
[131] C. Huang and S. Kou, 2001, *Welding Research Supplement*, pp. 9s-17s
[132] A.F. Norman, V. Drazhner, N. Woodward and P.B. Prangnell, 1998, Proc. *7th International Conference on Joints in Aluminium*, Cambridge
[133] G.W. Smith, W.J. Baxter and R.K. Mishra, 2000, *Journal of Materials Science*, Vol. 35, pp. 3871-3880
[134] K. Higashi, T.G. Nieh and J. Wadsworth, 1995, *Acta Metallurgica Materialia*, Vol. 43, No. 9, pp. 3275-3282
[135] H. Iwasaki, M. Mabuchi and K. Higashi, 2001, *Acta Materialia*, Vol. 49, pp. 2269-2275
[136] C.L. Chen, M.J. Tan, 2002, *Materials Science and Engineering*, Vol. A338, pp. 243-252
[137] W. Thomas, D. Staines, I. Norris and E. Watts, 2003, *TWI – Connect*, Iss. 123, March/April, pp. 3

[138] AT.L. Anderson, 1994,, *Fracture Mechanics, Fundamentals and Applications,* 2nd Edition, CRC Press